Institut für Erd- und Umweltwissenschaften
Mathematisch-Naturwissenschaftliche Fakultät
Universität Potsdam

CLIMATE VARIABILITY AND EXTREME HYDRO-METEOROLOGICAL EVENTS IN THE SOUTHERN CENTRAL ANDES, NW ARGENTINA

FABIANA CASTINO

DISSERTATION

zur Erlangung des akademischen Grades

DOCTOR RERUM NATURALIUM
»DR. RER. NAT.«
in der Wissenschaftsdisziplin ALLGEMEINE GEOLOGIE

eingereicht an der
Mathematisch-Naturwissenschaftlichen Fakultät
der Universität Potsdam

Potsdam, im November 2016

Supervisor:
Prof. Manfred R. Strecker, PhD

Date of final exam: 10.05.2017

Published online at the
Institutional Repository of the University of Potsdam:
URN urn:nbn:de:kobv:517-opus4-396815
http://nbn-resolving.de/urn:nbn:de:kobv:517-opus4-396815

to Marí and Dino

Quae bene cognita si teneas, natura videtur
libera continuo, dominis privata superbis,
ipsa sua per se sponte omnia dis agere expers.
[Lucretius Titus Carus (99 – 55BC),
De Rerum Natura, Liber II]

[*Which well perceived if thou hold in mind,*
Then Nature, delivered from every haughty lord,
And forthwith free, is seen to do all things
Herself and through herself of own accord,
Rid of all gods.
Transl. by W. E. Leonard (1876 – 1944)]

ALLGEMEINE ZUSAMMENFASSUNG

Extreme hydro-meteorologische Ereignisse, wie langanhaltende Dürren oder Starkregen, gelten als Haupterscheinungsform der Klimavariabilität und haben einen entscheidenden Einfluss auf Umwelt und Gesellschaft. Dies gilt im Besonderen für die großen Gebirgsregionen dieser Erde. In einer extrem sensiblen Hochgebirgsregion wie den NW argentinischen Anden haben selbst geringe Veränderungen in der Intensität solcher Extremereignisse, sowie deren Häufigkeit und räumliche Verteilung, nicht nur einen großen Einfluss auf die Landschaftsentwicklung; flussabwärtsliegende Gemeinden sind zudem wirtschaftlich als auch humanitär einem hohen Risiko ausgesetzt. Die vorliegende Arbeit befasst sich im Wesentlichen mit der räumlich-zeitlichen Verteilung von Niederschlags- und Abflussmengen über den Zeitraum der letzten sieben Jahrzente, mit besonderem Fokus auf extreme hydro-meteorologische Ereignisse der subtropischen Zentralanden NW-Argentiniens. Um räumliche und zeitliche statistisch signifikante Trends der Niederschlags- und Abflussmengen bestimmen und quantifizieren zu können, finden in dieser Arbeit verschiedene Methoden Anwendung, in denen hochaufgelöste Zeitreihen von Niederschlags- und Abflussmengenstationen mit diversen Rasterdatensätzen von 1940 bis 2015 kombiniert werden. Über den betrachteten Zeitraum hinweg lässt sich eine allgemeine Intensivierung des hydrologischen Kreislaufes auf mittleren Höhen (500 - 3.000 m ü. NN) belegen. Diese Intensivierung steht einerseits im Zusammenhang mit dem Ansteigen von Extremwetterereignissen, besonders während der Regenzeit von Dezember bis Februar. Der beobachtete Anstieg in der Intensität dieser Wetterlagen deutet auf einen Zusammenhang der schweren Regenstürme und der Verlandung der Abflussbecken in der untersuchten, intermontanen Region hin. Ein rapider Anstieg in der Abflussmenge in Flüssen um bis zu 40% ist für den Zeitraum zwischen 1971 und 1977 dokumentiert. Dieser steht höchstwahrscheinlich mit der globalen Klimaverschiebung von 1976-77 in Zusammenhang, welche wiederum durch die Variabilität der Oberflächentemperatur des Pazifischen Ozeans beeinflusst wird. Nach diesem starken Anstieg können jedoch abnehmende Trends in Niederschlags- wie auch Abflussmengen auf niedrigen und mittleren Höhen der Ostflanken der Anden beobachtet werden. Im Gegensatz dazu belegen ein Anstieg der jährlichen Gesamtniederschlagsmenge sowie der Magnitude von extremen hydro-meterologischen Ereignissen in hohen Höhenlagen der trockenen Puna de Atacama Plateaus, dass niedrige, mittlere und hohe Sektoren der NW argentinischen Anden unterschiedlich auf Änderungen des Klimas reagieren. Schlussendlich kann die in der Region beobachtete, stark ausgeprägte Variabilität in der Hydro-meteorologie über jährliche Zeiträume zum größten Teil mit dem Südamerikanischen Monsunsystem erklärt werden. Jedoch sind große Anteile in der Variabilität der Abflussmenge auch stark an die Pazifische Dekaden-Oszillation (PDO) in Zeiträumen über mehrere

Jahrzehnte (~20 Jahre) gekoppelt und zu einem geringeren Anteil auch an die Meeresoberflächentemperatur-Anomalie des tropischen Südatlantiks (TSA) über mehrjährige Zeiträume hinweg (~2-5 Jahre). Interessanterweise wurden nur weniger stark ausgeprägte Zusammenhänge zwischen der Abflussvariabilität und El Niño-Southern Oscillation in unserem Untersuchungsgebiet gefunden.

ABSTRACT

Extreme hydro-meteorological events, such as severe droughts or heavy rainstorms, constitute primary manifestations of climate variability and exert a critical impact on the natural environment and human society. This is particularly true for high-mountain areas, such as the eastern flank of the southern Central Andes of NW Argentina, a region impacted by deep convection processes that form the basis of extreme events, often resulting in floods, a variety of mass movements, and hillslope processes. This region is characterized by pronounced E-W gradients in topography, precipitation, and vegetation cover, spanning low to medium-elevation, humid and densely vegetated areas to high-elevation, arid and sparsely vegetated environments. This strong E-W gradient is mirrored by differences in the efficiency of surface processes, which mobilize and transport large amounts of sediment through the fluvial system, from the steep hillslopes to the intermontane basins and further to the foreland. In a highly sensitive high-mountain environment like this, even small changes in the spatiotemporal distribution, magnitude and rates of extreme events may strongly impact environmental conditions, anthropogenic activity, and the well-being of mountain communities and beyond. However, although the NW Argentine Andes comprise the catchments for the La Plata river that traverses one of the most populated and economically relevant areas of South America, there are only few detailed investigations of climate variability and extreme hydro-meteorological events.

In this thesis, I focus on deciphering the spatiotemporal variability of rainfall and river discharge, with particular emphasis on extreme hydro-meteorological events in the subtropical southern Central Andes of NW Argentina during the past seven decades. I employ various methods to assess and quantify statistically significant trend patterns of rainfall and river discharge, integrating high-quality daily time series from gauging stations (40 rainfall and 8 river discharge stations) with gridded datasets (CPC-uni and TRMM 3B42 V7), for the period between 1940 and 2015. Evidence for a general intensification of the hydrological cycle at intermediate elevations (~ 0.5 – 3 km asl) at the eastern flank of the southern Central Andes is found both from rainfall and river-discharge time-series analysis during the period from 1940 to 2015. This intensification is associated with the increase of the annual total amount of rainfall and the mean annual discharge. However, most pronounced trends are found at high percentiles, i.e. extreme hydro-meteorological events, particularly during the wet season from December to February. The observed increase of extreme-events magnitude reflects substantial changes, particularly in the magnitude of rainstorms affecting the NW Argentine Andes. Importantly, variations in extreme hydro-meteorological events, such as heavy rainstorms, might represent the climatic driver of widespread aggradation of sediments presently observed in the intermontane sedimentary basins of NW Argentina. Here, I present a new approach for the

quantitative evaluation of erosion rates in fast-eroding environments on different timescales with the aim to better understand the link between extreme hydro-meteorological events and surface processes.

An important outcome of my studies is the recognition of a rapid increase in the amount of river discharge during the period between 1971 and 1977, most likely linked to the 1976-77 global climate shift, which is associated with the North Pacific Ocean sea surface temperature variability. A quantitative evaluation of the changes in water volumes across this rapid increase shows that in the upper Rio Bermejo, a major tributary of La Plata river, mean annual discharge increased by 40% ± 15% over seven years. Interestingly, after this rapid increase, both rainfall and river discharge decreased at low and intermediate elevations along the eastern flank of the Andes. In contrast, during the same time interval, at high elevations, extensive areas on the arid Puna de Atacama plateau have recorded increasing annual rainfall totals. This has been associated with more intense extreme hydro-meteorological events from 1979 to 2014. This part of the study reveals that low-, intermediate, and high-elevation sectors in the Andes of NW Argentina respond differently to changing climate conditions.

Possible forcing mechanisms of the pronounced hydro-meteorological variability observed in the study area are also investigated. For the period between 1940 and 2015, I analyzed modes of oscillation of river discharge from small to medium drainage basins (10^2 to 10^4 km^2), located on the eastern flank of the orogen. First, I decomposed the relevant monthly time series using the Hilbert-Huang Transform, which is particularly appropriate for non-stationary time series that result from non-linear natural processes. I observed that in the study region discharge variability can be described by five quasi-periodic oscillatory modes on timescales varying from 1 to ~20 years. Secondly, I tested the link between river-discharge variations and large-scale climate modes of variability, using different climate indices, such as the BEST ENSO (Bivariate El Niño-Southern Oscillation Time-series) index. This analysis reveals that, although most of the variance on the annual timescale is associated with the South American Monsoon System, a relatively large part of river-discharge variability is linked to Pacific Ocean variability (PDO phases) at multi-decadal timescales (~20 years). To a lesser degree, river discharge variability is also linked to the Tropical South Atlantic (TSA) sea surface temperature anomaly at multi-annual timescales (~2-5 years). Interestingly, less pronounced evidence is found in the study area for links between discharge variability and ENSO.

Taken together, these findings exemplify the high degree of sensitivity of high-mountain environments with respect to climatic variability and change. This is particularly true for the topographic transitions between the humid, low-moderate elevations and the semi-arid to arid highlands of the southern Central Andes. Even subtle changes in the hydro-meteorological regime of these areas of the mountain belt react with major impacts on erosional hillslope processes and generate mass

movements that fundamentally impact the transport capacity of mountain streams. Despite more severe storms in these areas, the fluvial system is characterized by pronounced variability of the stream power on different timescales, leading to cycles of sediment aggradation, the loss of agriculturally used land and severe impacts on infrastructure.

CONTENTS

List of Figures ix

List of Tables xi

1 Thesis organization and author contributions 1

2 Introduction 5
- 2.1 Climate variability and high-mountain environments 5
- 2.2 Morphotectonic and climatic setting of the study area 13
- 2.3 Hydrology and sediment flux 16
- 2.4 Research questions 19

3 Rainfall variability and trends of the past six decades (1950-2014) in the subtropical NW Argentine Andes 21
- 3.1 Introduction 22
- 3.2 Climatic and geographic setting 23
- 3.3 Data and methods 26
- 3.4 Results 30
- 3.5 Discussion 36
- 3.6 Conclusions 43

4 River discharge dynamics in the southern Central Andes and the 1976-77 global climate shift 47
- 4.1 Introduction 48
- 4.2 Data and methods 50
- 4.3 Results 53
- 4.4 Discussion 53
- 4.5 Conclusions 58

5 Oscillations and trends of river discharge in the southern Central Andes and the link with modes of climate variability 59
- 5.1 Introduction 60
- 5.2 Data and methods 62
- 5.3 Results 70

5.4 Discussion 81
5.5 Conclusions 86

6 Determination limits for cosmogenic ^{10}Be and their importance for geomorphic applications 89
6.1 Introduction 90
6.2 State of the art 91
6.3 Determination limits 93
6.4 Testing the method 97
6.5 Results 100
6.6 Discussion 104
6.7 Conclusions 108

7 Discussion and conclusions 109
7.1 Rainfall and river-discharge trends during the last seven decades 110
7.2 Oscillations of river discharge in the southern Central Andes and large-scale modes of climate variability 115
7.3 Concluding remarks 116

References 119

Acknowledgments 143

LIST OF FIGURES

2.1	Disproportionality of mountain vs. lowland runoff	6
2.2	Predicted changes between 2081 and 2100	9
2.3	Southern Central Andes: Topography and rainfall	14
2.4	Vegetation cover in the NW Argentine Andes	15
2.5	Major rivers of the southern Central Andes	17
3.1	Topography and rainfall in the southern Central Andes	24
3.2	Spatial distribution of the rainfall stations in NW Argentina	28
3.3	Swath profile for topography and rainfall in NW Argentina	29
3.4	Rainfall trends for 1950-2014	33
3.5	Rainfall trends for 1979-2014	34
3.6	Rainfall trends for 1998-2014	35
3.7	Rainfall trends: mean vs. percentiles	40
4.1	Spatial distribution of the hydrological stations	49
4.2	River-discharge trends for 1940-2015	52
4.3	Annual and seasonal trends for discharge percentiles	56
5.1	Drainage basins and station positions	62
5.2	Time series for 1940-2015	64
5.3	IMFs for river discharge for 1940-2015	65
5.4	Statistical significance test results for river-discharge IMFs	68
5.5	EEMD-results summary for 1940-2015	71
5.6	TDIC of IMF4 for ENSO BEST and PDO	72
5.7	TDIC-results summary for the period 1940-2015	74
5.8	EEMD-results summary for 1956-2015	76
5.9	TDIC-results the period 1940-2015: IMF4	78
5.10	TDIC-results the period 1940-2015: IMF5	78
5.11	TDIC-results the period 1940-2015: IMF6	79
5.12	TDIC-results the period 1940-2015: IMF7	80
6.1	Samples distributions for low and high ^{10}Be content	96
6.2	Probability density functions for low ^{10}Be content samples	98
6.3	Blank-correction methods differences	101
6.4	Error propagation and blank-correction methods	102

6.5 Blank-correction methods, LOD, and LOQ 104
6.6 Schematic overview of the proposed approach 106

7.1 Overview of the key results for the period 1940-2015 112
7.2 Overview of the key results for the period 1979-2014 114

LIST OF TABLES

3.1	List of climate rainfall indices	30
4.1	Main hydrological indices	51
5.1	Hydrological stations and stations metadata	61
5.2	Time series for discharge and climate indices	63
5.3	Summary of EEMD analysis for 1940-2015	70
5.4	Time-independent Pearson correlation for 1940-2015	71
5.5	Summary of EEMD analysis for 1956-2015	75
5.6	Time-independent Pearson correlation for 1956-2015	77
6.1	Long-term blank measurements at GFZ	99
6.2	LOD and LOQ evaluations	101

CHAPTER 1

THESIS ORGANIZATION AND AUTHOR CONTRIBUTIONS

This study constitutes a cumulative thesis that comprises two peer-reviewed, published articles, one manuscript in review, and an additional manuscript to be submitted for review to a scientific journal.

The principal aim of this study is to document climate variability in the southern Central Andes in NW Argentina during the past decades, with the goal to improve our understanding of the forcing mechanisms that modify hydrological variables and associated surface processes, with particular emphasis on extreme hydro-meteorological events. This attempt also includes deciphering the climate factors that contribute to changes in the spatiotemporal rainfall and river-discharge patterns in this semi-arid, highly vulnerable mountain environment. The thesis constitutes four independent, but thematically closely linked studies focused on climate variability; chapters 3 through 6 correspond to the individual studies. Below I provide a short summary for each chapter.

Chapter 2 – Introduction. This chapter illustrates the rationale and motivation of this study together with the identified research questions that guided me through the analysis of climate variability in NW Argentina. In addition, a brief overview of the morphotectonic and climatic setting is presented for the southern Central Andes, including a short description of the hydrological regime in NW Argentina.

Chapter 3 – Rainfall variability and trends of the past six decades (1950–2014) in the subtropical NW Argentine Andes. This chapter provides a comprehensive analysis of rainfall variability and trends in NW Argentina. Here I compare changes in extreme and total annual and seasonal rainfall, as well during the last six decades (1950-2014). This trend analysis is based on different datasets, integrating daily rain-gauge time series and gridded datasets, and it primarily focuses on changes in magnitude and frequency of extreme events using quantile regression. This chapter has been published by *Castino, F., B. Bookhagen, and M. R. Strecker* in the journal *Climate Dynamics (2017).* Fabiana Castino, Bodo Bookhagen, and Manfred R. Strecker contributed to the design of the study. Fabiana Castino, Bodo Bookhagen, and Manfred R. Strecker all contributed to organizing and conducting fieldwork in the Andes, visiting field sites and collecting metadata of hydro-meteorological stations in

NW Argentina. Fabiana Castino collected and analyzed the hydro-meteorological time series. All co-authors discussed the results of the analysis. Fabiana Castino wrote the manuscript, with additional contributions from all co-authors.

Chapter 4 – River-discharge dynamics in the southern Central Andes and the 1976-77 global climate shift. In this study, the evolution of the frequency distribution of river discharge in the Southern Central Andes was documented between 1940 and 1999. Quantile regression, combined with change-point analysis, was applied to daily river-discharge time series from small to medium-size drainage basins (10^2-10^4 km^2) from the eastern flank of the Southern Central Andes, in the transition between the tropics and subtropics. This chapter, submitted for publication by *Fabiana Castino, Bodo Bookhagen, Manfred R. Strecker,* has been published in the journal *Geophysical Research Letters (2016)*. Fabiana Castino, Bodo Bookhagen, and Manfred R. Strecker contributed to the design of the study. Fabiana Castino collected and analyzed the river-discharge time series, to document statistically significant changes during the period between 1940 and 1999. All co-authors discussed the interpretation of the results. Fabiana Castino wrote the manuscript, with contributions from Bodo Bookhagen and Manfred R. Strecker.

Chapter 5 – Oscillations and trends of river discharge and their linkages to climatic drivers in the southern Central Andes. This part of the study investigates magnitude and frequency of oscillatory modes that explain river-discharge variability and possible links with large-scale climate-mode oscillations. An innovative analysis combining the Ensemble Empirical Mode Decomposition and the Time-Dependent Intrinsic Correlation is applied using time series of monthly discharge anomalies relevant to small to medium montane drainage basins for the period between 1940 and 2015. The manuscript that forms the foundation of this chapter is currently in preparation for publication by *Fabiana Castino, Bodo Bookhagen, Manfred R. Strecker*. Fabiana Castino, Bodo Bookhagen, and Manfred R. Strecker contributed to the design of the study. Fabiana Castino analyzed the river-discharge observations, using the spectral decomposition of the collected discharge time series and different climate indices. All co-authors contributed to the interpretation of the results. Fabiana Castino wrote the manuscript with contributions from all co-authors.

Chapter 6 – Determination limits for cosmogenic ^{10}Be and their importance for geomorphic applications. This chapter describes a novel method to define the threshold above which samples for cosmogenic nuclide analysis can be reliably distinguished from blanks in cosmogenic radionuclide studies (specifically ^{10}Be) based on laboratory blank measurements. The manuscript has been submitted for publication by *Sara Savi, Stefanie Tofelde, Hella Wittmann, Fabiana Castino, and Taylor F. Schildgen* to *Quaternary Research* and is currently being revised. Sara Savi, Stefanie Tofelde, Hella Wittmann, and Taylor F. Schildgen contributed to the design of the study. Sara Savi prepared and analyzed the samples in the laboratory and

estimated the ^{10}Be samples concentration. Sara Savi and Fabiana Castino designed the procedure for statistically defining the Determination Limits. Sara Savi wrote the manuscript with contributions from all co-authors.

Chapter 7 – Discussion and Conclusions. This chapter summarizes and integrates the principal results of the individual studies. The chapter concludes with the identification of additional research questions addressing the problem of climate variability and its impact on the surface-process regime in high-mountain regions and discussing possible future efforts to solve them.

The Appendices from A1 to A4 of this thesis are available on the attached CD as electronic supporting information of Chapters from 3 to 6, respectively.

CHAPTER 2

INTRODUCTION

2.1 CLIMATE VARIABILITY AND HIGH-MOUNTAIN ENVIRONMENTS

2.1.1 GENERAL BACKGROUND

In most parts of our planet Earth's climate during the Holocene has been characterized by highly favorable conditions for societal and technological advancement. Climate is complex, however, and continually changes in response to orbital parameters, solar radiation, the interaction between atmosphere and oceans, and anthropogenic impacts on land use or atmospheric chemistry. Depending on the magnitude of these variations, climate may severely impact natural and human systems, especially in highly vulnerable regions, such as polar regions, dry subtropical areas, and high-mountain environments [*Füssel and Klein*, 2006; *Hare et al.*, 2011; *Field et al.*, 2014].

Deviations of climatic characteristics over a given time period (e.g., a month, a season or year) compared to long-term behavior are often referred to as *climate variability*. Alternatively, climate variability is defined as a variation in the mean state and other statistics of the climatic conditions on all temporal and spatial scales, beyond individual weather events [*Barros et al.*, 2012]. These variations are commonly termed *anomalies*. Statistically significant variations in either the mean state of the climate or in its variability and persisting for an extended period (i.e., typically decades or longer) are instead referred to as *climate change* [*Barros et al.*, 2012]. A short introduction to this terminology is important, because in the context of this thesis I will mainly address climate variability and anomalies.

As a result of the complexity of the processes influencing climate variability, anomalies in climate variables present both periodic and chaotic character on a large range of spatial and temporal scales [*Latif and Barnett*, 1994; *Saji et al.*, 1999; *Marshall et al.*, 2001]. A part of this variability can be modelled using simple frequency distributions; in addition, much of the spatial structure of this variability can be described as a combination of preferred patterns, which impact weather and climate on many spatial and temporal scales; these patterns are commonly called *modes of climate variability* [*Hartmann et al.*, 2013]. Among the dominant modes of climate variability, the El Niño Southern Oscillation (ENSO) strongly affects global and regional climate and the surface-process regime [*Horel and Wallace*, 1981;

Ropelewski and Halpert, 1987; *Wang et al.*, 2000; *Diaz et al.*, 2001; *Alexander et al.*, 2002]. For example, there is general agreement that ENSO modulates both Indian and South American Monsoon Systems, affecting particularly the magnitude and pattern of monsoonal precipitation at regional scale [*Webster and Yang*, 1992; *Garreaud and Battisti*, 1999; *Torrence and Webster*, 1999; *Marengo et al.*, 2012].

2.1.2 CLIMATE VARIABILITY AND EXTREME HYDRO-METEOROLOGICAL EVENTS

There is general consensus that the primary manifestation and impact of climate variability on human society and the natural environment is represented by extreme events [*Katz and Brown*, 1992; *Easterling et al.*, 2000]. Spatially large and long-lasting droughts, among the costliest and most widespread natural disasters, are generally linked to extremes in climate variability [*Verschuren et al.*, 2000; *Marengo et al.*, 2008; *Sheffield et al.*, 2009; *Cook et al.*, 2010]. Conversely, climate variability in high-mountain regions may be reflected by heavy rainstorms that result in floods and a variety of mass-movement types, impacting local infrastructure and landscape development [*Wolman and Miller*, 1960; *Plate*, 2002; *Korup and Clague*, 2009].

In the lowlands of the Indian subcontinent, the Arabian Peninsula and East Africa, for example, more than two billion people are directly influenced by extreme rainstorms often triggering floods and mass-movement events triggered by variability in the Asian Monsoon System [*Chang et al.*, 2000; *Cook et al.*, 2010; *Stager et al.*, 2011]. This variability in the spatiotemporal characteristics of rainfall patterns, floods, and droughts of this important circulation system has important socio-economic impacts in the Himalayan and East African-Arabian realms [*Krishna Kumar et al.*, 2004; *Goswami et al.*, 2006; *Malik et al.*, 2016].

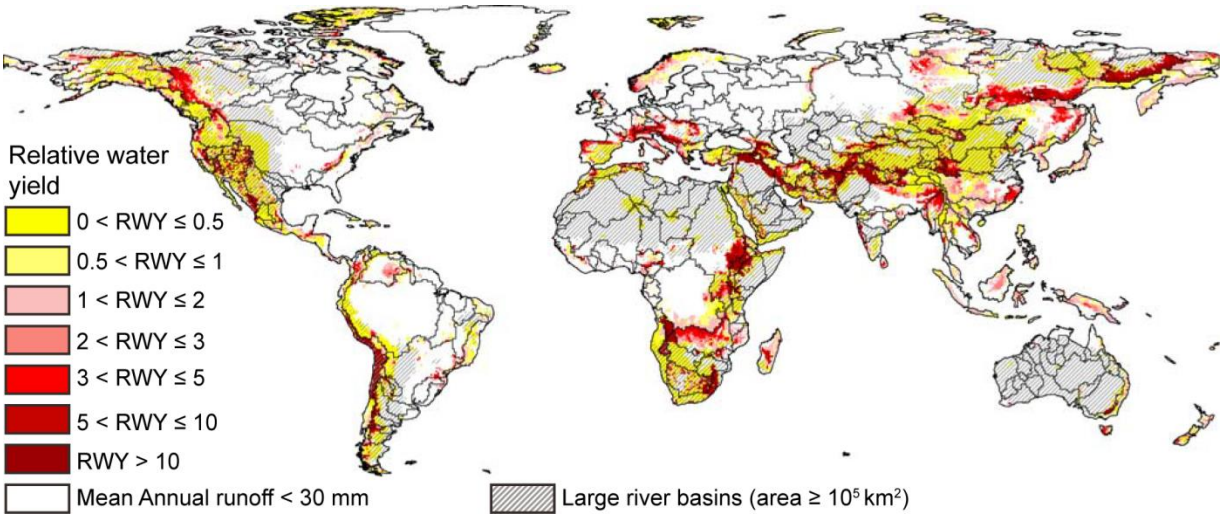

Figure 2.1 Disproportionality of mountain runoff relative to average lowland runoff (Relative water yield, RWY). Disproportionality in favor of runoff exists when RWY is greater than 1. The importance is marked for RWY > 2 and essential for RWY > 5 (after Viviroli et al. [2007]).

Similarly, downstream areas of the high-mountain environments of the South American Andes, where 70% of the population of South America lives, are increasingly affected and challenged by the effects of climate variability [*Garreaud et al.*, 2009; *Barros et al.*, 2015; *Boers et al.*, 2015b].

2.1.3 CLIMATE VARIABILITY IMPACTS ON HIGH-MOUNTAIN REGIONS

Climate variability strongly affects mountain regions: Small changes in climatic conditions in this sensitive environmental system (e.g., changes in the amount and frequency of precipitation) can have far-reaching impacts on human communities downstream and may lead to irreversible perturbations of the natural environment [*Beniston*, 2003; *Diaz et al.*, 2003].

Importantly, climate variability strongly modulates mountain hydrology, which is a key element of the water cycle [*Beniston et al.*, 1997; *Beniston*, 2003]. Mountain ranges are commonly referred to as the Earth's water towers, since they constitute one of the most important sources of renewable freshwater for the adjacent downstream areas (Figure 2.1) [*Bandyopadhyay et al.*, 1997; *Liniger et al.*, 1998; *Xu et al.*, 2008; *Immerzeel et al.*, 2010]. In case of pronounced seasonality, mountain belts may redistribute winter precipitation during the melting of snow and ice during spring and summer, naturally dampening the variability of runoff towards the lowlands during seasons with lower amounts of precipitation. More than 50% of world's mountainous areas has an essential or supportive role for the downstream areas (Figure 2.1) [*Viviroli et al.*, 2007], supplying freshwater for agriculture, hydropower, industrial manufacturing, nutrients, and potable water for human settlements. Therefore, against the backdrop of increasing worldwide water demand due to growing populations and developing economies, high-mountain environments have a crucial role as sources of natural freshwater [*Vörösmarty et al.*, 2000; *Tilman*, 2002; *Viala*, 2008].

In addition, mountain regions are characterized by pronounced climatic and surface-process gradients, coupled with exceptionally high degrees of biodiversity per unit area [*Kessler*, 2002; *Beniston*, 2003; *Martinelli*, 2007]. Precipitation, as a primary control on different types of mass movements within these regions may furthermore govern the occurrence, rates, and magnitudes of erosional processes, efficiently redistributing material through space and time [*Hallet et al.*, 1996; *Roe*, 2003].

The complex linkages between climate variability, erosion, sediment transport and storage have been addressed by numerous studies, revealing a rich relationship between precipitation patterns, runoff, fluvial discharge, and associated surface processes [*Wolman and Miller*, 1960; *Coppus and Imeson*, 2002; *Webster et*

al., 2011; *Carretier et al.*, 2012; *Pepin et al.*, 2013]. However, some of these studies suggest that the rate at which sediment is eroded from an orogen and transferred to foreland regions primarily depends on the magnitude and frequency of heavy rainfall and associated flooding events [*Coppus and Imeson*, 2002; *Bookhagen et al.*, 2005; *Webster et al.*, 2011]. Therefore, in high-mountain environments, extreme hydro-meteorological events are among the pivotal drivers of surface processes, which in turn control landscape evolution and biotic activity. Consequently, the episodic delivery of large amounts of sediment to the fluvial system driven by hillslope erosion and ultimately the character of rainfall events, may not only alter aquatic habitats and biodiversity [*Ryan*, 1991; *Henley et al.*, 2000], but also affect the operational life span or damage water reservoirs and hydropower infrastructures [*Trussart et al.*, 2002; *Garg and Jothiprakash*, 2008; *Houze et al.*, 2011]. For these reasons it is of utmost importance that we better recognize, characterize and predict the spatial and temporal patterns of climate variability and its possible impact on the environmental system.

2.1.4 CLIMATE VARIABILITY AND FUTURE CLIMATE PROJECTIONS

Against the backdrop of global change, climate variability is a phenomenon of global and regional significance, especially in light of possible forcing by teleconnections and impacts on erosional and depositional patterns. In fact, climate variability may strongly modulate the availability of freshwater resources at different spatial and temporal scales, exacerbating the vulnerability of areas already under water stress. This issue is particularly relevant in climatic threshold environments, such as the fringes of arid and semiarid regions, which are particularly vulnerable to seasonal water shortages or increased precipitation [*Viviroli et al.*, 2007].

Indeed, according to climate assessments for the near future, it has been proposed that at global scale the impact on evaporation and precipitation will likely result in an overall intensification (or acceleration) of the water cycle [*Huntington*, 2006; *Trenberth*, 2011; *Stocker et al.*, 2013] (Figure 2.2). In particular, a global increase in precipitation is expected, which should result, for example, in an increase of renewable freshwater-resource availability. This would potentially reduce the vulnerability to water scarcity in regions that are currently under water stress. Importantly, it is also suggested that the global intensification of the water cycle would be associated with an increase in the intensity and frequency of extreme hydro-meteorological events such as rainstorms, floods, and droughts [*Trenberth*, 2011; *Stocker et al.*, 2013], which would severely impact mountainous environments and beyond.

At regional scale, most of the future climate projections for the extra-tropics and particularly for subtropical regions, show that areas for which water demand is

already critical would likely experience a decrease in precipitation, significantly reducing the availability of freshwater [*Viviroli et al.*, 2011].

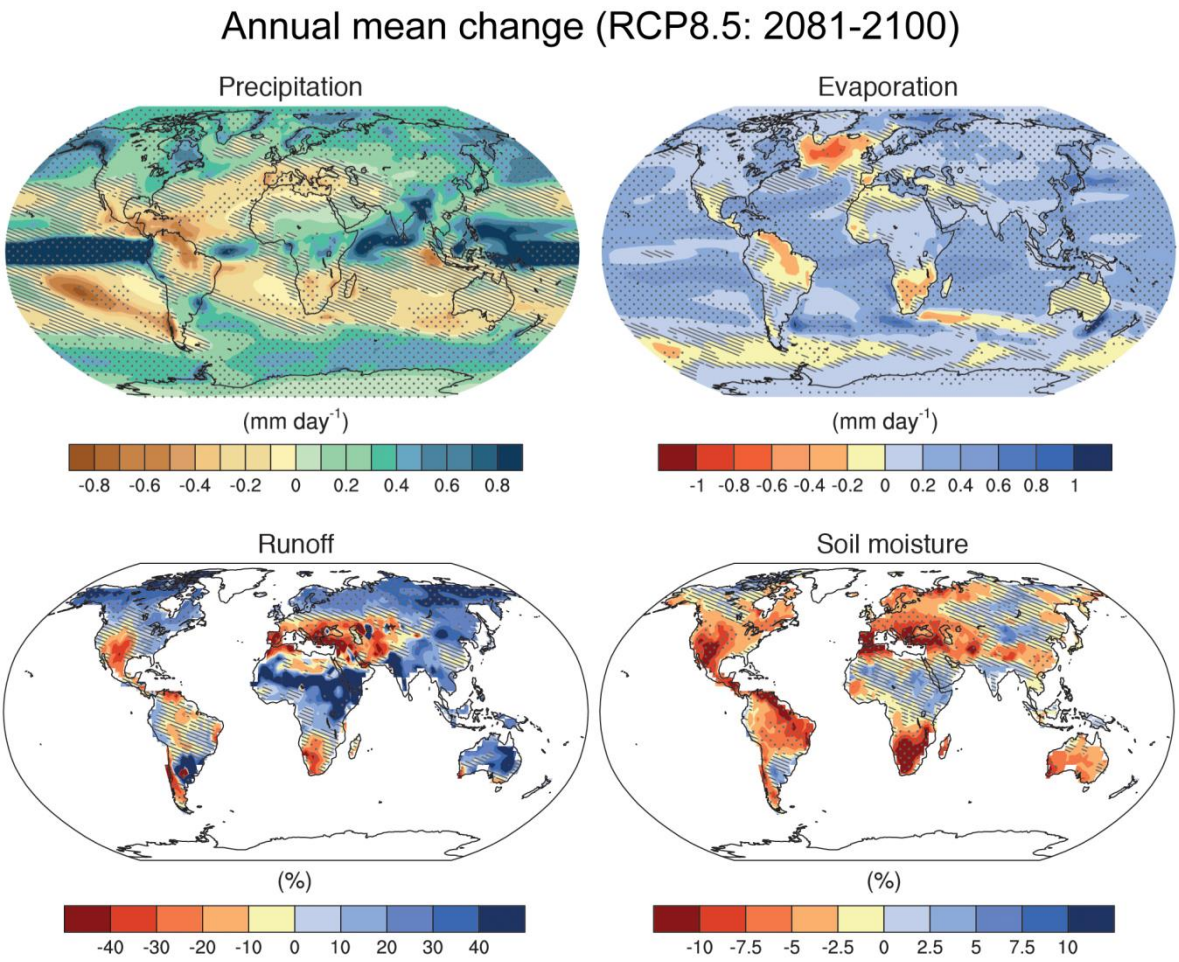

Figure 2.2 Predicted annual mean change in precipitation, evaporation, runoff, and soil moisture between 2081 and 2100 relative to 1986-2005 under the Representative Concentration Pathway RCP8.5 (mitigation scenario with radiative forcing target of about 8.5 Wm^{-2}) (modified after Stocker et al., [2013]).

For tropical areas, most of climate variability is controlled by the monsoonal systems. Although monsoonal circulation is expected to weaken, the monsoonal precipitation is likely to intensify at global scale, in association with a lengthening of the wet season and an increase of the area encompassed by monsoon systems [*Christensen et al.*, 2013]. Nevertheless, large uncertainties still affect future trends in monsoon intensity and timing in many parts of the world. Low confidence has been put into projections of many aspects of phenomena that influence climate change at regional scale, including changes in the amplitude and spatial patterns of the monsoonal system and of other modes of climate variability (e.g., El Niño Southern Oscillation, the North Atlantic Oscillation, or Pacific North American pattern) [*Stocker et al.*, 2013]. As a consequence, predictions of the future climate in the mountain environment are also fraught with large uncertainties and more detailed investigations are needed to improve predictions as to how the climate system will behave.

Therefore, rigorous, quantitative assessments of spatial and temporal patterns of climate variability are needed in high-mountain environments, particularly with respect to hydro-meteorological extreme events and their impact on the surface-process regime. The resulting data is needed to: 1) improve and secure freshwater resources and to aid flood-risk management; 2) better comprehend how landscape-shaping processes affect the evolution of mountain belts in an event-driven vs. a slowly operating process regime; and 3) implement effective measures anticipating future environmental impacts on natural systems and mitigating the effects of a warming climate on socio-economic activity.

2.1.5 MOTIVATION

Several studies have strived to decipher rates and processes related to variability and change in mountain climate, and large efforts have been devoted to providing reliable assessments on magnitude and timing [*Zeng et al.*, 2008; *Casassa et al.*, 2009; *Chevallier et al.*, 2012; *Hänggi and Weingartner*, 2012; *Miller et al.*, 2012; *Sorg et al.*, 2012; *Wulf et al.*, 2012, 2016; *Palazzi et al.*, 2013; *Zampieri et al.*, 2015; *Molina et al.*, 2015; *Malik et al.*, 2016]. These studies have revealed a large footprint of a warming climate, which is most visibly and dramatically manifested by glacial retreat. In high-mountain environments these trends cause reduced water-storage capacity and impact runoff variability in catchments, which in turn may strongly affect hillslope processes and increase associated geomorphic hazards [*Evans and Clague*, 1994; *Richardson and Reynolds*, 2000; *Jansson et al.*, 2003; *Barnett et al.*, 2005; *Vergara et al.*, 2007; *Keiler et al.*, 2010]. However, besides the diffuse signal of increased melting and retreat of glaciers, previous studies reveal a large degree of spatiotemporal heterogeneity in the response of the involved processes to the overall warming conditions. In this context, the high-elevation and foreland sectors of the Himalaya, the European Alps, and the Andes are among the most extensive, economically relevant, and densely populated mountain regions on Earth and constitute primary targets for investigating climate variability under the looming specter of Global Change [*Auer et al.*, 2007; *Scherler et al.*, 2011; *Boers et al.*, 2014b].

In the Himalaya, statistically significant precipitation trends have been observed in the central and eastern regions of the orogen, indicating decreasing annual total amounts during the last century [*Dimri and Dash*, 2012; *Palazzi et al.*, 2013]. On the other hand, extreme-event analysis shows enhanced rainstorm intensity in the northwestern Himalaya between 1951 and 2007, which has resulted in increased flood-related vulnerability [*Malik et al.*, 2016]. Furthermore, increased annual peak-flood discharge, associated with an increasing frequency of high-magnitude flood events, has been observed in few basins in the northwestern Himalaya from 1970 to 2000 [*Bhutiyani et al.*, 2008]. Streamflow measurements in these regions have revealed a complex spatial trend pattern in terms of annual volumes in the most prominent catchments. Despite these important observations, relatively large uncertainties

remain [*Immerzeel et al.*, 2010; *Moors et al.*, 2011]; this is because the streamflow-pattern heterogeneity is in part due to the dampening effect of increasing glacial melting [*Shahzad Khattak et al.*, 2011; *Miller et al.*, 2012; *Sharif et al.*, 2013] and local glacial mass gain [*Matsuo and Heki*, 2010; *Gardelle et al.*, 2012]. However, although less pronounced than in previous IPCC assessments [e.g., *Cogley et al.*, 2010], decreasing annual amounts and increased seasonality of streamflow are expected according to future climate projection as a result of increasing trends in precipitation extremes [*Bolch et al.*, 2012; *Kääb et al.*, 2012; *Palazzi et al.*, 2013].

In the European Alps, trend analysis shows increasing precipitation along the northern side of the mountain range during winter and spring in the period between 1800 and 2000 [*Brunetti et al.*, 2006]. The past century marked a general decline in snow depth and duration of snow cover at elevations below 1500 m in the French, Italian, and Swiss Alps; this was accompanied by increasing evapotranspiration in the Italian and western Austrian Alps [*Beniston*, 2012; *Bocchiola*, 2014; *Kormann et al.*, 2016]. During the same period, extreme hydro-meteorological events exhibit increased frequency and magnitude in Switzerland and northern Italy, confirming a widespread trend in Europe [*Brunetti et al.*, 2001; *Schmidli and Frei*, 2005; *Madsen et al.*, 2014]. Earlier spring peaks of river discharge by more than 2 weeks/century have been noticed for major Alpine river basins (i.e., Rhine, Danube, Rhone, and Po); this has been largely attributed to changing seasonality in the amount of total precipitation [*Zampieri et al.*, 2015]. Future climate projections predict substantial changes in the amount and degree of precipitation seasonality, associated with increases in heavy precipitation events and melting of permafrost regions [*Beniston et al.*, 2011; *Gobiet et al.*, 2014].

Running continuously from approximately 10° N to 55° S, the Andes traverse a great variety of climate environments - from humid, tropical settings in the north to arid sectors in the central part, and to humid-temperate conditions in the south. For the past century, the tropical Andes, which include the Northern Andes (10° N to 10° S) and the northern Central Andes (10° to 25° S), do not exhibit evidence of changing precipitation, except for southern Peru and western Bolivia, where a tendency towards slightly drier conditions and weaker seasonality has been observed [*Vuille et al.*, 2003; *Lavado Casimiro et al.*, 2013; *Seiler et al.*, 2013; *Molina et al.*, 2015; *Zubieta et al.*, 2016]. Therefore, the glacier retreat in the tropical and subtropical Andean regions cannot be solely associated with temperature change, as perhaps at higher latitudes, but the availability of moisture may constitute one of the primary forcing factors of glacial dynamics in this particular environment at present and the younger geological past [*Ramírez et al.*, 2001; *Haselton et al.*, 2002; *Vuille et al.*, 2003, 2008; *Bradley et al.*, 2006]. In the past 20 years trend analysis of streamflow of tropical and extra-tropical catchments in major South American rivers (i.e. Amazon, Negro, Orinoco, Tocantins, Parana) has not displayed a coherent hydrological pattern [*Marengo*, 1995;

García and Mechoso, 2005; *Marengo et al.*, 2009], except for an abrupt increase during the 1970s; this phenomenon has been associated with the 1976-77 global climate shift [e.g., *Graham*, 1994; *Carvalho et al.*, 2011; *Jacques-Coper and Garreaud*, 2015]. Interestingly, also the southern Andes (35° to 55° S) exhibit a trend pattern associated with glacier shrinkage during the past century [*Schneider et al.*, 2007; *Carrasco et al.*, 2008], associated with a decline in precipitation. However, the impact of precipitation changes on regional river flows remains poorly understood [*Barros et al.*, 2015]. Future climate projections indicate that, apart from an initial increased flow due to the glacial melt disequilibrium, freshwater supply from high-elevations catchments in the tropical and extra-tropical Andes will decrease, with anticipated severe impacts on the socio-economical activities of local communities [*Vuille et al.*, 2008; *Chevallier et al.*, 2011; *Barros et al.*, 2015]. However, quantitative assessments of trend patterns in mountain climate, including modifications of magnitude and frequency of extreme hydro-meteorological events, are rare for the Andean headwater basins, although this kind of data is critical for improving the reliability of future climate projections and the efficiency of mitigation and adaptation measures [*Barros et al.*, 2015].

The lacuna of detailed investigations of the modification of the climate in many parts of the Andes is particularly critical for the subtropical Andean catchments between 25° to 35° S. These areas comprise large catchments for important rivers (i.e. Rio de La Plata) and include densely populated and economically relevant areas [*Tucci and Clarke*, 1998; *Berbery and Barros*, 2002]. Located in the subtropical dry zone in the realm of the descending branch of the southern-hemisphere Hadley Cell during austral summer, this region would be arid were it not for the South American Monsoon System (SAMS). In addition, according to its latitudinal position and the conditions determined by the cold Humboldt Current along the Pacific coast, this region should be inherently dry, characteristic that makes this mountain area highly vulnerable. The SAMS advects large amounts of moisture from the Amazon basin southward along the Andean orogeny to these dry areas [*Zhou and Lau*, 1998; *Vera et al.*, 2006]. The NW Argentine Andean foothills are considered 'oases', humid regions whose source of surface- and groundwater is the monsoon-driven, orographic high-elevation rainfall and snowfall over the adjacent range (see below).

Field observations in the intermontane basins of NW Argentina during the past decade have revealed that high-elevation hillslope environments are subjected to pronounced incision and mass movements that might be related to the frequency and/or intensity of storminess. Sediment generated by these events is subsequently deposited in the narrow intermontane valleys, leading to widespread aggradation, which affects arable lands and infrastructure [Rivelli and Manuela, 2009; COBINABE, 2010]. These first-order observations call for a more rigorous analysis of the hydro-climatogical characteristics of this Andean sector to better constrain the role of

climatic variability on the surface-process regime and to mitigate the region's vulnerability to extreme hydro-meteorological events.

2.2 MORPHOTECTONIC AND CLIMATIC SETTING OF THE STUDY AREA

With a length of approximately 7000 km, the meridionally-oriented, tectonically-active Andean orogen achieves elevations between 5 and 7 km asl and forms a hemispheric-scale orographic barrier for atmospheric circulation systems. The study area comprises the foreland, the steep eastern flank, and the eastern sector of the high-elevation region of the southern Central Andes between 16° and 32° S (Figure 2.3). The foreland in the east is at about 0.5 km asl, whereas the high-elevation areas in the west reach peaks that are in excess of 6 km elevation. The western sector of the study area is an integral part of the internally drained Andean Plateau, the second largest plateau on Earth, with a mean elevation of about 4 km asl and low topographic relief (Figure 2.3). The Andean Plateau consists of the northern Andean Plateau (the Altiplano of Bolivia), located in the tropics, and the southern sector (the Puna de Atacama of Argentina) in the subtropics, approximately south of 20°S. The area between the foreland and the plateau constitutes a region of intermontane basins with steep topographic gradients and high relief contrasts that are parallel to the border of the Andean Plateau (Eastern Cordillera, Sierras Pampeanas and Santa Barabara ranges).

The rainfall pattern in the southern Central Andes is controlled by the interaction between topography and the hemisphere-scale atmospheric circulation patterns [*Gandu and Geisler*, 1991; *Campetella and Vera*, 2002; *Bookhagen and Strecker*, 2008; *Garreaud et al.*, 2010; *Insel et al.*, 2010]. Moisture transport along and into the southern Central Andes occurs during the wet season during the austral summer, dominated by the SAMS [*Zhou and Lau*, 1998; *Vera et al.*, 2006; *Silva and Carvalho*, 2007; *Marengo et al.*, 2012]. The onset of the SAMS begins between September and October and typically lasts until the end of the austral summer/fall in March, generating an efficient precipitation and erosional regime [*Silva and Carvalho*, 2007; *Bookhagen and Strecker*, 2008, 2012]. During the austral summer, strong convective heating over Amazonia and central Brazil initiates the monsoon. The monsoonal regime is part of a continental gyre, which transports moisture westward from the tropical Atlantic Ocean to the Amazon basin, where it is recycled and transported farther west towards the Andes [*Gandu and Silva Dias*, 1998; *Vera et al.*, 2006]. Due to the orographic effect of the orogen, moisture is partly released in form of intense rainfall at the eastern flanks of the tropical Andes and partly advected southward towards the subtropical areas of South America, driven by the South American Low-Level Jet (SALLJ) and the South Atlantic Convergence Zone (SACZ) [*Gandu and Silva Dias*, 1998; *Marengo et al.*, 2012; *Boers et al.*, 2015b].

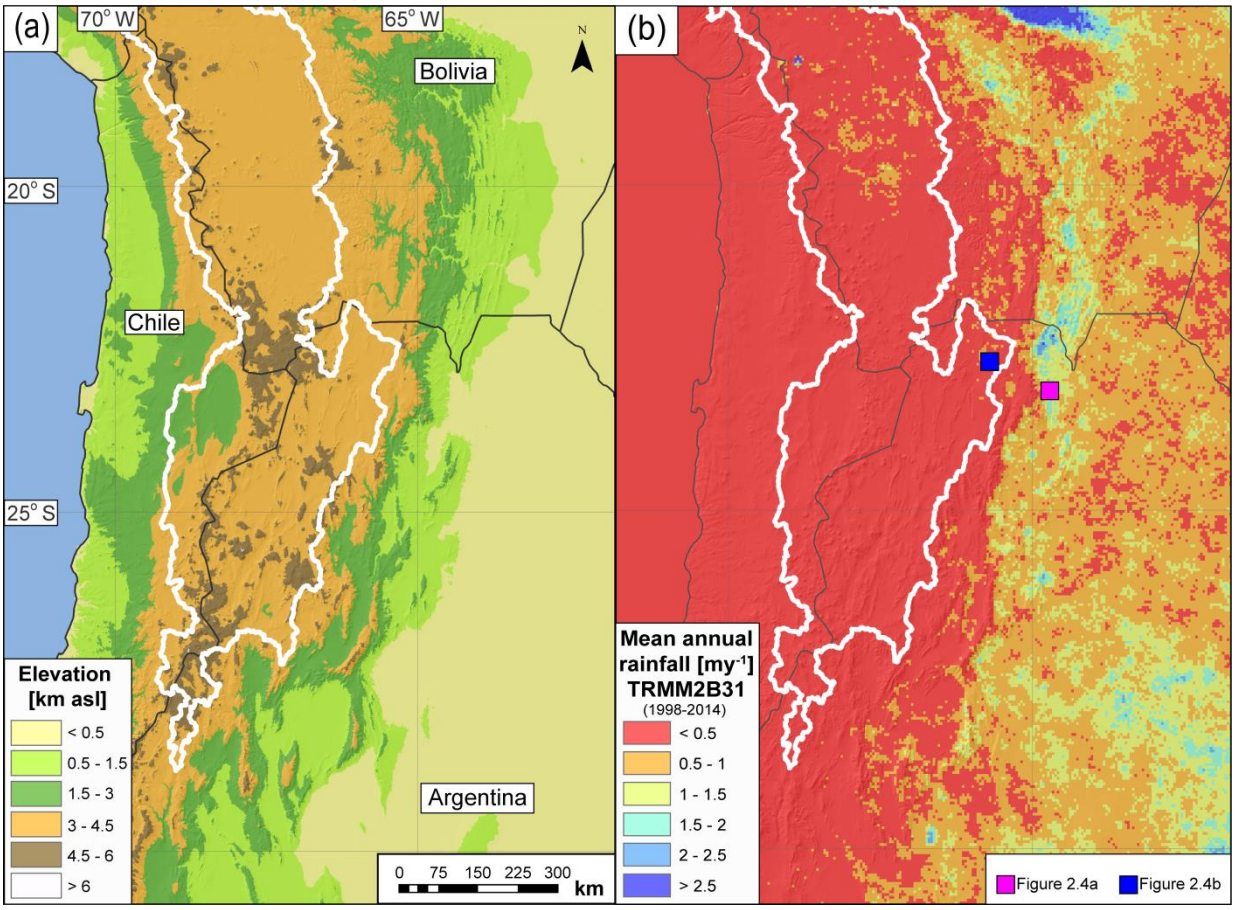

Figure 2.3 (a) Topography (SRTM) of the southern Central Andes. The border of the internally-drained Andean Plateau is outlined in white; thin dark-grey lines denote international borders. (b) Mean-annual rainfall data from TRMM 52 2B31 V7 (1998-2014) [Bookhagen and Strecker, 2008; Bookhagen and Burbank, 2010]. The distribution of rainfall is characterized by a pronounced gradient between low-elevation foreland at the eastern-flank areas and arid, high-elevation sectors of the internally drained plateau in the orogen interior. Magenta and blue squares show locations of Figure 2.4.

About 80% of the annual precipitation on the eastern flanks of the NW Argentine Andes falls during summer, between November and February [*Rohmeder*, 1943; *Halloy*, 1982; *Bianchi and Yañez*, 1992; *Garreaud et al.*, 2003, 2010]. The rainfall gradient is mimicked by the distribution, type and density of vegetation cover. Consequently, subtropical forest vegetation along a narrow strip on the eastern flanks of the orogen is substituted by a sparse cover of xerophytes in the semi-arid to arid intermontane valleys farther west (Figure 2.4). In contrast, the western flanks of the orogen, the Altiplano-Puna Plateau, and the intermontane valleys in the lee of the outermost eastern ranges are semi-arid to hyper-arid (Figures 2.3 and 2.4). During winter, due to the seasonal change in the tropospheric temperature gradient between low and mid latitudes, regional westward moisture transport beyond the orographic barrier is prevented, resulting in a drier climate [for a summary see *Vera et al.*, 2006; *Strecker et al.*, 2007].

Figure 2.4 Typical vegetation covers in two different areas in the NW Argentine Andes: (a) subtropical forest on eastern flank of the Eastern Cordillera, District of Orán (Salta province; see Figure 2.3b for location); (b) sparse shrubs and grass cover in the arid Puna plateau in the interior of the orogen, District of La Quiaca (Jujuy province; see Figure 2.3b for location).

The distribution of rainfall maxima at the windward flanks of the sub-tropical Central Andes is controlled by the geometry of the mountain range, with precipitation hotspots that may reach 6 m/y [*Seluchi and Marengo*, 2000; *Bookhagen and Strecker*, 2008; *Giovannettone and Barros*, 2009; *Espinoza et al.*, 2015]. Mesoscale convective systems (MCSs), forming locally and triggered by orographic uplift or atmospheric instability, are the primary source of intense rainfall events along the eastern flanks and within the central Andean Plateau, both in the tropical and

subtropical parts of the mountain range [*Maddox et al.*, 1979; *Garreaud*, 2000; *Romatschke and Houze*, 2013; *Boers et al.*, 2015b].

On interannual timescales, the rainfall patterns in the NW Argentine Andes may be modulated by the interplay between different atmospheric features, such as the Bolivian High (i.e., an upper-level (~200 hPa) anticyclone developing during austral summer over the Bolivian Altiplano, whose position and intensity controls for example the rainfall variability in the Amazon basin and wet and dry episodes over the Altiplano), the Chaco Low and the North-Western Argentinian Low (low-level thermal depressions localized over these regions, whose interaction with the South Atlantic Subtropical Anticyclone is frequently related to the penetration of air masses of tropical origin into the mid-latitudes) [*Schwerdtfeger*, 1976; *Gandu and Silva Dias*, 1998; *Salio et al.*, 2002; *Seluchi and Saulo*, 2003; *Carvalho et al.*, 2004; *Vuille and Keimig*, 2004; *Boers et al.*, 2014c]. In addition, different climate disturbances, such as the Madden-Julian Oscillation (MJO), the El Niño Southern Oscillation (ENSO) or the Pacific Decadal Oscillation, may substantially affect the overall rainfall pattern during the SAMS, especially by controlling the strength of the SALLJ [*Madden and Julian*, 1971; *Vuille et al.*, 2000; *Garreaud and Aceituno*, 2001; *Mantua and Hare*, 2002]. These changes may result in increased precipitation in the generally dry regions of the orogen interior, which in turn leads to increased runoff, erosion, and deposition in the intermontane basins [*Strecker et al.*, 2007; *Bookhagen and Strecker*, 2012].

2.3 HYDROLOGY AND SEDIMENT FLUX

In the southern Central Andes, the pronounced rainfall seasonality is reflected by the river discharge annual cycle of intermontane catchments, exhibiting homogeneous unimodal hydrographs with peak-discharge values between February and March [*Pasquini and Depetris*, 2007]. Major river catchments originating in this region are the Rio Bermejo (123 x 10^3 km^2 catchment size, 1060 km length) and the Rio Salado (124 x 10^3 km^2 catchment size, 2010 km length), both are tributaries of the Rio Paraná. In addition, the Rio Dulce (90 x 10^3 km^2 catchment size, 810 km length) drains into the Laguna Mar Chiquita, the largest Argentine salt lake [*SSRH*, 2004] (Figure 2.5a).

The Andean intermontane basins in this region mainly contain fluvio-lacustrine deposits, whereas basins in the adjacent Altiplano-Puna Plateau to the west contain fluvio-lacustrine, evaporitic, and volcanic strata, typically between 3 and 5-km thick [*Alonso et al.*, 1991; *Strecker et al.*, 2007]. The adjacent mountain ranges consists of easily erodible late Proterozoic metasedimentary rocks [e.g., *JeŽek et al.*, 1985], more resistant Cambro-Ordovician quartzites, and Paleozoic to Miocene intrusives that are covered by partially preserved Cretaceous and Neogene sedimentary rocks [*Salfity and Marquillas*, 1994].

In contrast to the tropical and southern Andes, there are virtually no glaciated peaks in this region [*Lliboutry*, 1998], resulting in a negligible contribution to streamflow from snow- and ice-melt compared to rainfall. This, however, was not the case during repeated glacial episodes in the Pleistocene, when the arid mountain tops of NW Argentina were repeatedly glaciated, most likely due to increased westward moisture transport [*Rohmeder*, 1943; *Haselton et al.*, 2002; *Vizy and Cook*, 2007; *Zech et al.*, 2009].

Drainage basins in the sector encompassing the intermontane valleys have small to medium-size catchments (10^2 to 10^4 km^2), with headwaters located at elevations above 4 km asl, which results in steep river gradients. Along the course of these rivers, a large amount of sediment eroded from the hillslopes is transported, but often transiently deposited in the intermontane valleys, before it is remobilized and further transported toward the foreland [*Marcato et al.*, 2009; *COBINABE*, 2010].

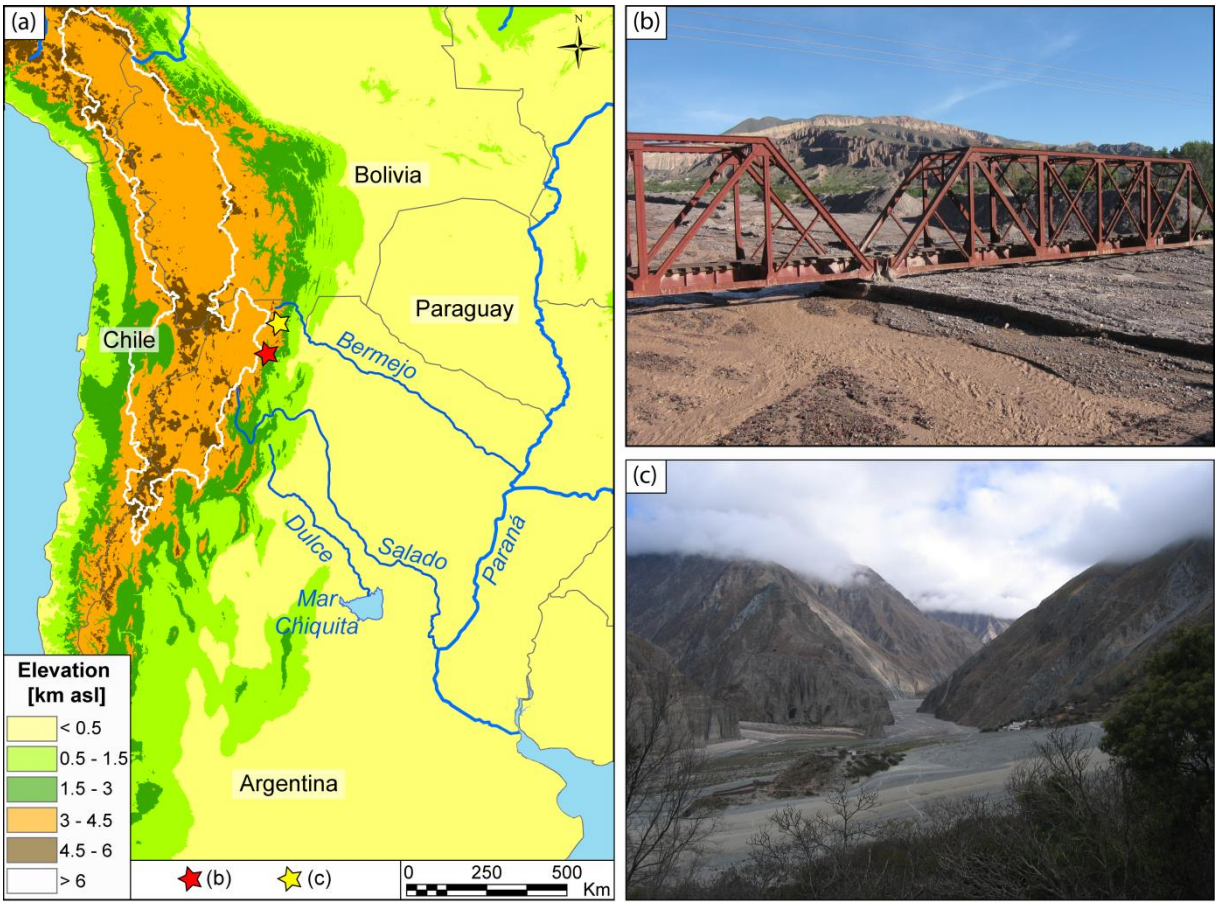

Figure 2.5 (a) Major rivers originating in southern Central Andes: Rio Bermejo and Rio Salado, tributaries of the Rio Paraná, and Rio Dulce draining into the Laguna Mar Chiquita. Red and yellow stars mark locations of (b) and (c) (Humahuaca basin and Rio Iruya, respectively). Aggradation in the intermontane valleys of the upper catchment areas of the upper Rio Bermejo; (b) Rio Grande in the Quebrada de Humahuaca. The river bed has aggraded during the past decades by approximately 8 m (estimation obtained by field observations); (c) Rio Iruya in the northeastern sector of the Eastern Cordillera. The river has aggraded its bed during the past decades aided by mudflow activity that has been responsible for the partial burial of the village of Las Higueras.

During the last decade, enhanced erosion from the orogen interior and transient sediment accumulation in the intermontane basins of NW Argentina have created major problems because of flooding agriculturally-used lowlands and basic infrastructure maintenance such as road and railway lines, despite continual efforts to rebuild at higher levels (Figure 2.5b-c).

River-sediment flux observations are often used to estimate sediment transport and erosion rates in drainage basins at decadal time scale; these evaluations are also important for better understanding the link between climate variability and sediment transfer and depositional processes at short or inter-event timescales [Wulf et al., 2010; Carretier et al., 2012]. However, the limited accessibility of high-elevation mountain regions, often also densely vegetated, complicate the implementation and maintenance of gauging networks, resulting in spatially non-homogeneous and poorly populated sediment flux datasets.

In the southern Central Andes coarse and fine-sediment flux observations are available for several catchments with headwaters located in the intermontane ranges for the past two decades [*COBINABE*, 2010]. However, operational constraints relevant to these gauging stations, including heterogeneous sampling frequencies during the period of activity, critically impact the reliability of sediment-transport budgets and erosion rates derived from these data.

An alternative method, widely applied to estimate erosion rates at river-basin scale on centennial to millennial time scale, is based on geochemical tracers, e.g. cosmogenic radionuclides inventories (CRNs) [*Bierman and Steig*, 1996; *Granger et al.*, 1996; *von Blanckenburg*, 2005]. This method associates denudation rates of the rock source with the concentration of radionuclides stored in eroded sediment and produced by the interaction with cosmic rays reaching the Earth's surface [*Nishiizumi et al.*, 1989; *Lal*, 1991]. Based on the hypothesis that, as the principal climatic drivers of surface processes in NW Argentina, are rare, extreme hydro-meteorological events that determine erosional efficiency, CRN inventories provide a natural average of the rates of landscape evolution, since they integrate several surface-shaping events over centennial to millennial timescales [*Kirchner et al.*, 2001; *von Blanckenburg*, 2005].

A recent study has documented the strong influence of the steep east-to-west climatic gradient affecting erosion in the southern Central Andes [*Bookhagen and Strecker*, 2012]. Relying on basin-wide erosion rates derived from cosmogenic radionuclides (CRNs) inventories, this study shows that the spatial erosional pattern at centennial to millennial time scale largely mimics present-day mean annual rainfall across the Andean orogen. Erosion rates thus vary by one order of magnitude between the humid basins on the eastern flank of the mountain range (~ 1 mm/y) and the semi-arid intermontane valley to the west (< 0.1 mm/y) [*Bookhagen and Strecker*, 2012]. Interestingly, the analysis of alluvial-fan deposits of the Del Medio catchment in the

Humahuaca intermontane valley (Figure 2.5), it was observed that, in comparison to the rest of the region, river catchments located within the humid sector or at the climatic transition zone between the sub-humid and sub-arid conditions, may experience relatively rapid surface-process rates, as landslides or mud-flows preferably impact this environment [*Savi et al.*, in press].

Climate settings characterized by relatively fast surface-process rates, i.e. those regions characterized by relatively low CRNs concentrations, may represent the critical end-member environment for estimating reliable exposure ages or erosion rates, since the CRNs concentrations could be comparable to the detection limit of the methodology. However, a rigorous and universally accepted definition of those limits is not yet available, although it is essential for correctly interpreting the evaluations obtained by CRNs inventories in these particular climate settings. Therefore, this lacuna underscores the need of further investigations to quantitatively define these limits for the determination of reliable cosmogenic radionuclides concentrations in rock and sediment samples.

2.4 RESEARCH QUESTIONS

This thesis primarily focuses on climate variability in the subtropical Central Andes of NW Argentina, with a particular emphasis on extreme hydro-meteorological events. Aided by the availability of a unique dataset of long-term time series of high-quality rainfall and river-discharge measurements, rigorous statistical analysis is performed to evaluate the spatiotemporal variability of rainfall and discharge of the past six decades. The main aim of this study is therefore directed toward deciphering if, and to which degree rainfall and discharge have changed in NW Argentina over this timespan. This approach also serves to detect if such changes may be related to variations in magnitude and/or frequency of extreme hydro-meteorological events - which are here associated with rainfall and river discharge high percentiles (>90th). Furthermore, these variations will be analyzed to identify periodic components, which might be linked to large-scale modes of climate variability (e.g., ENSO). In addition, since variations in extreme hydro-meteorological events might represent the climate driver of the observed aggradation in some drainage basins, effort is also dedicated to improve the quantitative evaluation of erosion rates on different timescales.

These overarching goals are addressed by answering the following, thematically linked research questions that will guide me through this process to better understand the role of climate variability in high-mountain environments of the southern Central Andes:

1. *Is there any statistically significant trend that has characterized the spatiotemporal pattern of rainfall in the southern Central Andes during the*

last decades? Has the magnitude and frequency of rainstorm events changed during this period? (Chapter 3)

2. *Has river discharge changed in magnitude during the last decades? Has the frequency distribution of river discharge shown differential trend values depending on the percentiles? (Chapter 4)*

3. *Is there any evidence of a link between river-discharge variability in the southern Central Andes and large-scale modes of climate variability such as ENSO or PDO? (Chapter 5)*

4. *How can the limit of concentrations for the determination of CRNs in rock and sediment samples be defined? How can statistically rigorous guidelines be developed for reliably estimating CRN concentrations in fluvial sediments to help assess the efficiency of the erosional regime? (Chapter 6).*

CHAPTER 3

RAINFALL VARIABILITY AND TRENDS OF THE PAST SIX DECADES (1950-2014) IN THE SUBTROPICAL NW ARGENTINE ANDES

Fabiana Castino[1], Bodo Bookhagen[1], and Manfred. R. Strecker[1]

[1] Institute of Earth and Environmental Science, University of Potsdam

Climate Dynamics (2016), doi: 10.1007/s00382-016-3127-2

ABSTRACT

The eastern flanks of the Central Andes are characterized by deep convection, exposing them to hydrometeorological extreme events, often resulting in floods and a variety of mass movements. We assessed the spatiotemporal pattern of rainfall trends and the changes in the magnitude and frequency of extreme events (≥95th percentile) along an E-W traverse across the southern Central Andes using rain-gauge and high-resolution gridded datasets (CPC-uni and TRMM 3B42 V7). We generated different climate indices and made three key observations: (1) An increase of the annual rainfall has occurred at the transition between low (< 0.5 km) and intermediate (0.5 – 3 km) elevations between 1950 and 2014. Also, rainfall increases during the wet season and, to a lesser degree, decreases during the dry season. Increasing trends in annual total amounts characterize the period 1979-2014 in the arid, high-elevation southern Andean Plateau, whereas trend reversals with decreasing annual total amounts were found at low elevations. (2) For all analyzed periods, we observed small or no changes in the median values of the rainfall-frequency distribution, but significant trends with intensification or attenuation in the 95th percentile. (3) In the southern Andean Plateau, extreme rainfall events exhibit trends towards increasing magnitude and, to a lesser degree, frequency during the wet season, at least since 1979. Our analysis revealed that low (< 0.5 km), intermediate (0.5 – 3 km), and high-elevation (> 3 km) areas respond differently to changing climate conditions, and the transition zone between low and intermediate elevations is characterized by the most significant changes.

KEYWORDS

Extreme rainfall, South American Monsoon System, Central Andes, quantile regression, rain gauges, CPC-uni, TRMM, orographic barrier

3.1 INTRODUCTION

Extreme hydrometeorological events are important drivers for a variety of natural hazards, including floods, landslides, and other mass movements (White and Haas 1975; Caine 1980), often associated with severe damages and high costs. In light of a suspected worldwide increase of such events, it has been argued that this trend may be a result of global warming (e.g., Trenberth et al. 2003; Seneviratne et al. 2012). Several studies have shown an increasing magnitude and/or frequency in extreme rainfall events in a wide variety of environments (e.g., Haylock and Nicholls 2000; Goswami et al. 2006; Malik et al. 2011). This is partly in agreement with predictions and future climate projections in the context of continued global change (e.g., Trenberth et al. 2003; Giorgi and Lionello 2008).

High-elevation regions are particularly sensitive to the effects of global warming and are considered the sentinels of climate change, since they are thought to respond rapidly and intensely to changing environmental conditions (e.g., Beniston et al. 1996; Pepin et al. 2015; Vuille et al. 2015). Several synoptic-scale studies have addressed changes of rainfall extremes in areas including mountain ranges, such as the Himalaya and the Andes, from which fundamental impacts on the landscape and the human habitat can be expected [*Marengo*, 2004; *Penalba and Robledo*, 2010; *Espinoza et al.*, 2012; *Barros et al.*, 2013; *Skansi et al.*, 2013; *Robledo et al.*, 2015; *Malik et al.*, 2016]. However, these studies are generally limited to station data recorded at low elevations aimed at capturing mainly synoptic-scale spatial patterns at low resolution (>100 km). Furthermore, synoptic-scale studies cannot provide reliable insights into the spatiotemporal specifics of climate variability in a mountain belt, since the pronounced orographic and relief gradients strongly impact both total and extreme rainfall patterns.

Moreover, several recent studies have analyzed extreme rainfall events in the Central Andes, [*Romatschke and Houze*, 2010; *Boers et al.*, 2014b, 2015b; *Rohrmann et al.*, 2014; *de la Torre et al.*, 2015; *Espinoza et al.*, 2015]. However, none of these investigations have addressed changes in rainfall patterns at the scale of the entire mountain belt, although the Central Andes comprise the catchments for the Amazon and La Plata rivers, including the most populated and economically relevant areas in South America [*Tucci and Clarke*, 1998; *Berbery and Barros*, 2002; *Gloor et al.*, 2013; *Lavado Casimiro et al.*, 2013].

Our study provides a comprehensive analysis of rainfall variability and trends in the subtropical Central Andes of NW Argentina, comparing changes in

extreme, total annual and seasonal rainfall along an E-W oriented elevation transect across the Andes. We test if the spatiotemporal rainfall pattern has undergone statistically significant changes during the last six decades (1950-2014), and if so, to which degree magnitude and/or frequency of heavy rain and extreme events account for precipitation variations at annual and seasonal scales. Carefully taking into account both strengths and limitations of the different datasets, we integrate (1) daily, high-quality rain-gauge time series for the period 1950-2014, including stations located both at low and high elevations, and (2) high-spatiotemporal resolution gridded datasets for the period 1979-2014, based on interpolated ground-station observations or remotely-sensed estimations. We define a set of climate indices relevant to both extreme and total rainfall and we analyze their spatiotemporal changes for different time periods starting in 1950. We perform rigorous statistical analyses on rainfall time series, focusing on changes in magnitude and frequency of extreme events using quantile regression [*Koenker and Bassett Jr.*, 1978; *Cade and Noon*, 2003], with a particular emphasis on the 95thpercentiles.

3.2 CLIMATIC AND GEOGRAPHIC SETTING

The study area lies at the eastern flank of the southern Central Andes between 16° and 32° S (Figure 3.1), across the boundary between the tropics and subtropics. This region is characterized by strong contrasts in topography, with lowlands in the east at about 0.5 km asl and high-elevation areas in the west with peaks in excess of 6 km. The western study area is part of the internally drained Andean Plateau, the second largest plateau on Earth, with a mean elevation of about 4 km asl and low topographic relief (Figure 3.1)). The Andean Plateau can be divided into the northern Andean Plateau (Altiplano), located in the tropics, and the southern Andean Plateau (Puna de Atacama) in the subtropics, roughly below 20°S. In contrast, the area between the eastern low and western high elevations constitutes a region with steep topographic gradient and high relief.

We distinguish between three main topographic areas with distinctive climatic environments that we define as followed from east to west: (1) the *low elevations* (< 0.5 km) with low topographic slopes and low relief values; (2) the *intermediate elevations* (also referred to as the mountain front) describes the area with steep slopes and high relief values that abuts the eastern low elevations of the Andean foothills with elevations roughly between 0.5-3 km; (3) the *high elevations* above 3 km to the west of the mountain front with steep slopes and high relief. The *intermediate elevations* are characterized by a very dynamic surface-process regime, where steep topographic, environmental, and climatic gradients coincide.

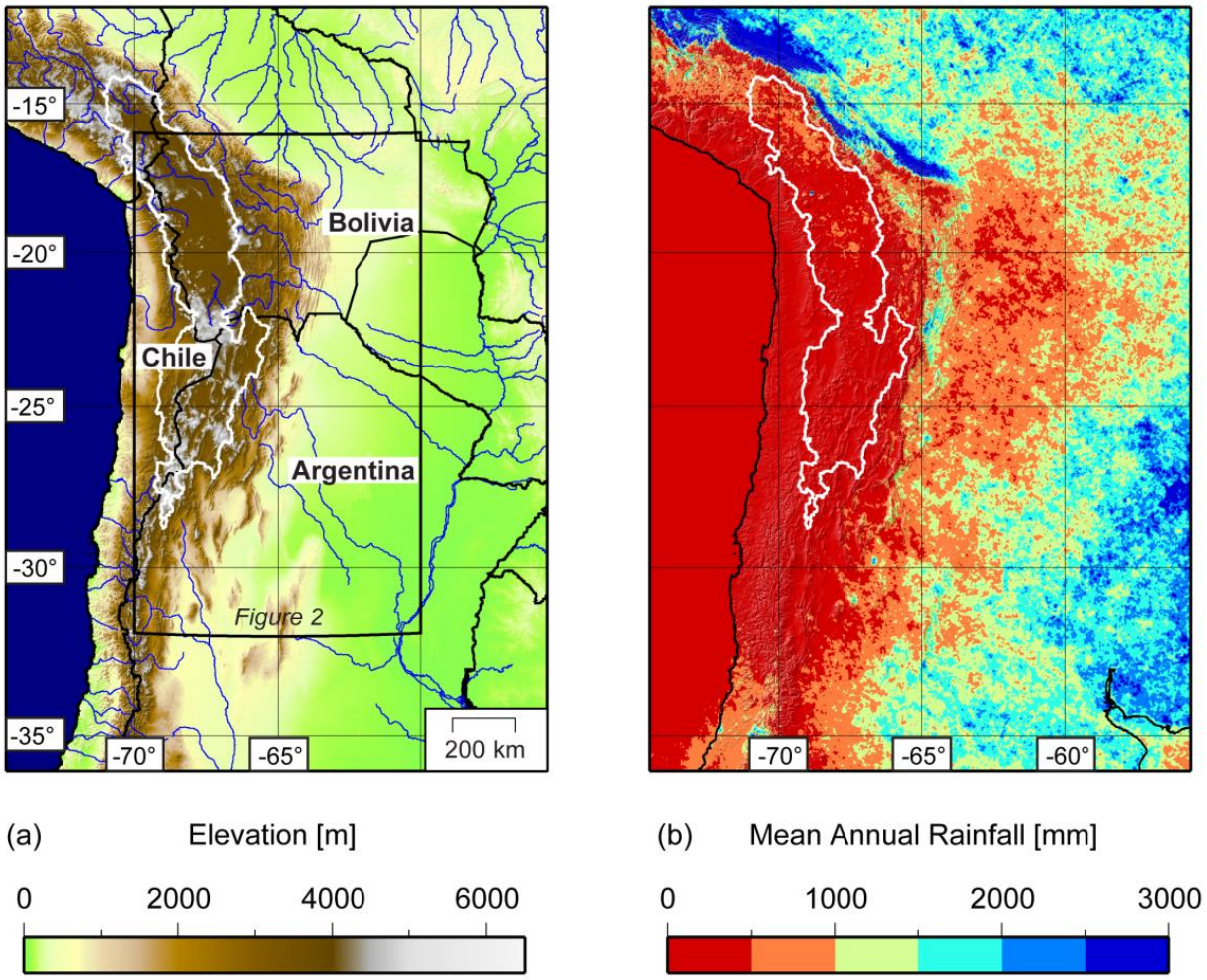

Figure 3.1 Topographic and climatic characteristics of the southern Central Andes. (a) Topography is derived from SRTM data; boundary of the internally-drained Altiplano (northern Andean Plateau) and Puna de Atacama (southern Andean Plateau) is outlined in white. Major rivers are marked in blue, black lines denote political borders. Black box outlines the study area in NW Argentina (cf. Figure 3.2), with lowlands at < 0.5 km asl in the eastern, the mountain front to the west (0.5-3 km asl) and the high-elevation regions (< 3 km asl) further west near the drainage divide of the Andean Plateau, with peaks elevations in excess of 6 km; (b) mean annual rainfall data derived from TRMM 2B31 over the period 1998-2014 [*Bookhagen and Strecker*, 2008; *Bookhagen and Burbank*, 2010]. Rainfall is characterized by a pronounced gradient between low-elevation frontal areas and arid, high-elevation areas of the internally drained plateau.

The rainfall pattern in the southern Central Andes is controlled by the interaction between topography and the large-scale atmospheric circulation [*Gandu and Geisler*, 1991; *Campetella and Vera*, 2002; *Bookhagen and Strecker*, 2008; *Garreaud et al.*, 2010; *Insel et al.*, 2010]. Moisture transport along and into the southern Central Andes occurs during the wet season, dominated by the South American Monsoon System (SAMS) [*Zhou and Lau*, 1998; *Vera et al.*, 2006; *Silva and Carvalho*, 2007; *Marengo et al.*, 2012]. Due to the orographic effect of the Andean orogen, moisture is partly released in form of intense rainfall at the eastern flanks of the tropical Andes and partly advected southward by the South American Low-Level

Jet (SALLJ), towards the subtropical areas of South America [*Gandu and Silva Dias*, 1998; *Marengo et al.*, 2012; *Boers et al.*, 2015b]. Triggered by the interaction between moisture-laden wind and the orographic barrier, intense precipitation occurs also at the eastern flank of the subtropical southern Central Andes in NW Argentina, resulting in a steep E-W rainfall gradient between the humid low-elevation and semi-arid to arid high-elevation regions (Figure 3.1). Here, on average, about 80% of the total annual rainfall occurs between December and March, when the SAMS is at its mature phase (Rohmeder 1943; Halloy 1982; Bianchi and Yañez 1992; Boers et al. 2015b).

The distribution of rainfall maxima at the windward flanks of the tropical and sub-tropical Central Andes is controlled by the geometry of the mountain range, its orientation, and small-scale topographic structures, with observed precipitation hotspots that may reach 6 m/yr [*Seluchi and Marengo*, 2000; *Garreaud et al.*, 2003; *Bookhagen and Strecker*, 2008; *Giovannettone and Barros*, 2009; *Espinoza et al.*, 2015]. Intense rainfall events along the eastern mountain flanks and on the central Andean Plateau both in the tropical and subtropical parts of the mountain range are mainly associated with mesoscale convective systems (MCSs), forming locally and triggered by orographic uplift or atmospheric instability [*Maddox et al.*, 1979; *Garreaud*, 2000; *Romatschke and Houze*, 2013; *Boers et al.*, 2015b]. To a lesser degree, MCSs formed in other source areas may propagate to the eastern flanks of the Central Andes [*Cohen et al.*, 1995; *Durkee et al.*, 2009; *Boers et al.*, 2015b]. For example, frontal systems originating from the central Argentine lowlands and fed by moisture advected by the SALLJ generate intense rainfall events in the subtropical drainage basins, including the Andean Plateau.

The overall rainfall pattern can be modulated by the interplay of different atmospheric features such as the South Atlantic Convergence Zone (SACZ), the Bolivian High or the Chaco Low [*Gandu and Silva Dias*, 1998; *Salio et al.*, 2002; *Carvalho et al.*, 2004; *Vuille and Keimig*, 2004; *Boers et al.*, 2014c]. Also, different climate disturbances such as the Pacific Decadal Oscillation (PDO), the El Niño Southern Oscillation (ENSO), or the Madden-Julian oscillation (MJO) can substantially affect the overall rainfall pattern during the SAMS, by controlling the strength of the SALLJ [*Madden and Julian*, 1971; *Vuille et al.*, 2000; *Garreaud and Aceituno*, 2001; *Mantua and Hare*, 2002]. Consequently, anomalously large amounts of moisture can be transported toward subtropical South America, deeply affecting the local rainfall pattern and often resulting in flooding and mass-movement events at the eastern slopes and in the intermontane valleys [*Houston*, 2006; *Vera et al.*, 2006; *Boers et al.*, 2014b].

Hence, in this region any changes in the rainfall pattern during the summer wet season will also have a strong impact on water-resource, infrastructure or hydrological risk management. Therefore, in our study we focus our analysis on the

summer season (DJF) while the results for the other seasons are available in the Appendix A1.

3.3 DATA AND METHODS

We rely on daily-rainfall time series derived from both synoptic meteorological and hydrological stations from the southern Andean Plateau, the eastern flanks of the mountain belt, and the foreland (Figure 3.2). To achieve higher spatial and temporal resolution, we included both rain-gauge derived and remotely-sensed gridded datasets retrieved from multiple sources, with different characteristics in spatiotemporal resolution. The data used in this study are:

1. Daily hydrological time series from 1925 to the present, made available in NW Argentina by the Argentine National Weather Forecast Service (Servicio Meteorológico Naciónal, SMN, 592 stations) and by the Department of Water Resources (Subsecretaría de Recursos Hídricos de la Nación, Banco Nacional Hídrico, BNH, 83 stations). Although most of the recording stations are located at the Andean mountain front, several stations also exist in the orogen interior. Unfortunately, during the last two decades a majority of the stations of the SMN network were abandoned due to a reorganization of the monitoring network (Figure 3.2). Among a total of 675 rain gauges, a set of 40 high-quality time series was selected in the investigated area. The selection depended on whether the data were continuous with at least 80% of the expected number of data available over the last three decades (1979 – 2014) [*Haylock et al.*, 2006; *Isotta et al.*, 2014] and met the standard-quality requirements, assessed using WMO validation standards [*WMO*, 2008; *Rodda*, 2011; *Antolini et al.*, 2015]. Time-series homogeneity was tested by visual inspection [*Haylock et al.*, 2006; *Longobardi and Villani*, 2009], since constructing a suitable reference time series was often not possible, given the excessive difference in elevation and/or relative distance between station locations. Among the 40 selected stations, 13 stations operated continuously over the period 1950-2014 (Figure 3.2). Table A1.1 in the Appendix A1 summarizes the selected station locations and time-series duration in a metadata table.
2. Climate Prediction Center (CPC) unified gauge (CPC-uni): the National Oceanic and Atmospheric Administration (NOAA) CPC unified gauge provides daily rainfall values from 1979 to the present at 0.5° x 0.5° spatial resolution over the global land areas [*Xie et al.*, 2007; *Chen et al.*, 2008]. High-quality gauge reports are collected from multiple sources and used to build a daily analysis based on an optimal interpolation technique, which reprojects precipitation synoptic reports to a grid.

Several studies on rainfall climatology, testing the performance of climate modeling or comparing different rainfall datasets have used CPC-uni [*Higgins et al.*, 2000; *Silva et al.*, 2007; *Jones et al.*, 2012; *Bombardi et al.*, 2013; *Jones and Carvalho*, 2014; *Ruscica et al.*, 2014; *Rao et al.*, 2015].

3. Tropical Rainfall Measurement Mission (TRMM 3B42 V7): the TRMM Multi-satellite Precipitation Analysis (TMPA) provides 3-h rainfall estimates from January 1998 to September 2014 at 0.25° x 0.25° spatial resolution [*Huffman et al.*, 2007]. The gridded rainfall algorithm uses an optimal combination of TRMM 2B31 and TRMM 2A12 data products, SSM/I, Advanced Microwave Scanning Radiometer (AMSR), and Advanced Microwave Sounding Units (AMSI) [*Kummerow et al.*, 1998, 2000]. Here we used the research-grade version, which is calibrated at monthly scale using land-surface precipitation-gauge analysis based on the GCPC dataset [*Huffman et al.*, 2007]. Previous studies used TRMM 3B42 data to analyze rainfall variability providing high-quality estimates in South America and other regions [*Carvalho et al.*, 2012; *Chen et al.*, 2013; *Xue et al.*, 2013; *Boers et al.*, 2015a] to identify rainfall-extreme events and their impact on river discharge, to develop a method for predicting extreme floods in the eastern Central Andes. Furthermore, these data were used to spatially characterize and identify the origin of rainfall over South America [*Bookhagen and Strecker*, 2011; *Boers et al.*, 2013, 2014a, 2014b, 2015a, 2015b]. TRMM 2B31 data with 5 km x 5 km spatial and approximately daily resolution were also used to relate topographic characteristics and orographic rainfall along the eastern Andes [*Bookhagen and Strecker*, 2008].

A ~100-km-wide and 390-km-long longitudinal swath profile (22°-23°S, 66°-62°W) shows the pronounced topographic and rainfall gradients across the Andes, detected by station data and CPC-uni and TRMM products (Figure 3.3). Previous studies showed that the TRMM 3B42 V7 and CPC-uni data provide a statistically robust description of the main features of the SAMS [*Carvalho et al.*, 2012; *Boers et al.*, 2015b]. However, there are significant uncertainties in the characterization of extreme precipitation events using the coarser gridded climatic datasets [*Ensor and Robeson*, 2008; *Carvalho et al.*, 2012].

Based on the collected data, we estimated annual and seasonal values (SON, DJF, MAM, JJA) of several indices (Table 3.1), for the rainfall-data parent distribution and for the extreme values, both at yearly and multi-decadal scales (mean values for climatological normals (CLINO, [*World Meteorological Organization*, 2011]) 1961-1990 and 1981-2010) for different time periods (1950-, 1979-, 1998-2014), for which the selected datasets were available. For the daily datasets, we define *wet days* as all occurrences larger than 0.5 mm/d and for the 3-h dataset *wet hours* as those

occurrences exceeding 0.1 mm/3h. Our statistical analysis was performed using years/seasons with less than 20% missing data.

We focused our analysis on the temporal evolution of these indices evaluating yearly deviations from the CLINOs as absolute anomalies. Given the index X, the yearly (annual/seasonal) absolute anomaly is defined as $AX_i = X_i - \langle X \rangle$, where X_i are the annual/seasonal estimation for X in the i-th year (i=1, ..., N, N = length of the time series in year), and <X> the relevant CLINO estimation. We also analyzed normalized values of the climate indices by the mean CLINO values to achieve an unambiguous interpretation of differences in the rainfall pattern between wet and dry areas. In the following, we will refer to *mean-normalized* anomaly as defined by: $ANX_i = 100*AX_i/\langle X \rangle$ and expressed in %/yr.

Despite recent advances in the calculation of the distribution of rainfall extremes (e.g., AghaKouchak and Nasrollahi 2010; Papalexiou and Koutsoyiannis 2013; Serinaldi and Kilsby 2014), drawbacks regarding the evaluation of power-law exponents for these distributions still exist, especially related to model regressions based on low-populated samples.

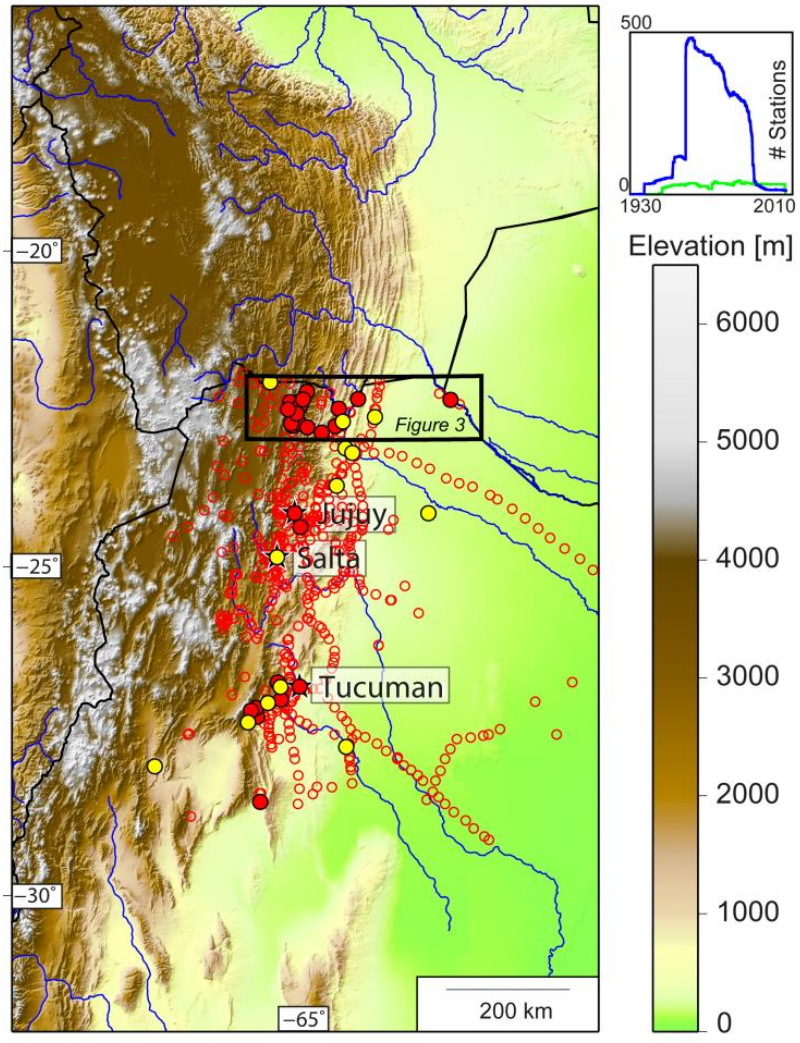

Figure 3.2 Topography of the study area and spatial distribution of 675 meteorological stations measuring daily rainfall (592 from SMN and 83 from BNH) in the provinces of Jujuy, Salta, Tucumán, Catamarca, and Santiago del Estero in NW Argentina (for location see Figure 3.1). Unfilled red circles indicate the location of rainfall stations that have been in operation during the period 1925-2014; Filled red circles represent the location of 40 rainfall stations that have been operating continuously between 1979 and 2014, among which 13 have continuous rainfall time series back to 1950 (yellow filled circles). Graph in right upper corner depicts temporal evolution of the number of active stations operating in the target area during the last 90 years (blue: SMN; green: BNH). Significantly less station data were collected in the last two decades. The black rectangle denotes the area of the swath profile in Figure 3.3.

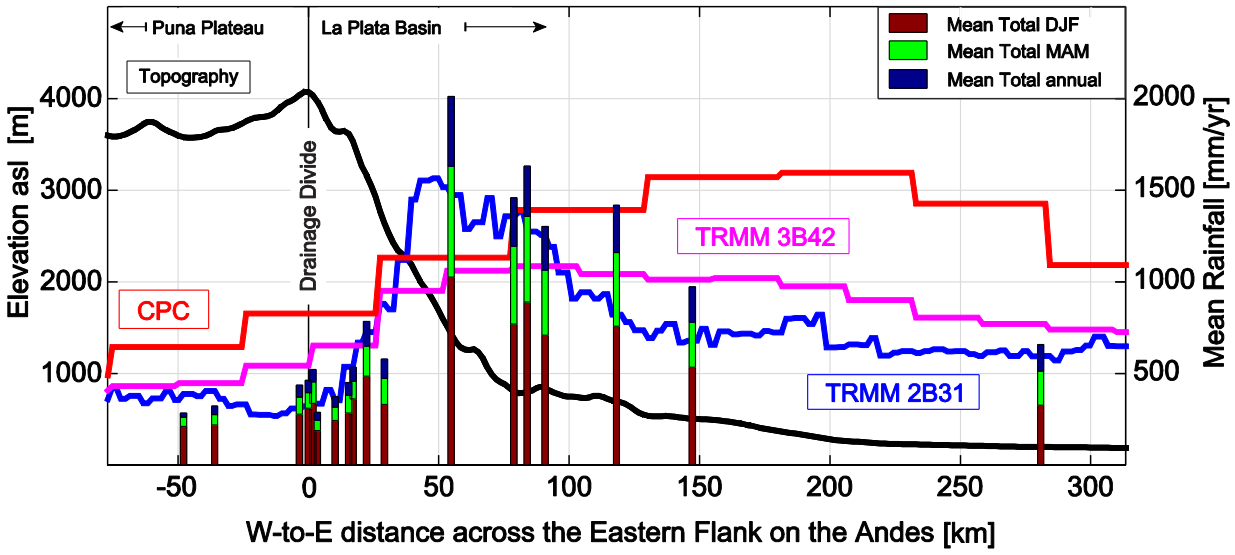

Figure 3.3 Swath profile (100 km wide, 390 km long) showing longitudinal variability of rainfall and topography (cf. Figure 3.2 for swath location). Rainfall data show annual average amounts from both station data (CLINO 1981-2010) and gridded datasets (CPC, red, 1979-2014; TRMM 3B42, magenta; and TRMM 2B31, blue, 1998-2014). Note strong E-W rainfall gradient, best depicted by rain-gauge and high-spatial resolution TRMM 2B31 data: mean annual rainfall increases up to 2000 mm/yr when the first orographic barriers are reached at ~50 km distance from the drainage divide. Rainfall rapidly decreases to <500 mm/yr in the lee of the orographic barriers. Seasonal contributions to annual mean totals for austral summer (DJF) and autumn (MAM) show that these two seasons alone account for at least 70% of the annual totals. Quantitative and qualitative comparison reveals that TRMM 2B31 estimations are in good agreement with station-derived values (Bookhagen and Strecker 2008, and this study), whereas the lower spatial resolution TRMM 3B42 data is less capable to correctly detect the location of rainfall maxima at the orographic barrier.

In our study, instead of evaluating distribution fitting parameters, we applied quantile regression analysis [*Koenker and Bassett Jr.*, 1978; *Cade and Noon*, 2003] to the wet days subsets of the raw data, to detect if rainfall-frequency distributions underwent statistically significant changes in the mean/median values as well as in the higher extremes during the past decades. In the appendix a short description of the quantile regression methodology is provided.

We estimated several percentiles (Table 3.1) focusing on extreme wet days and defined in the statistical sense *low-moderate* and *extreme* rainfall events as those occurrences below the 50th and exceeding the 95th percentiles, respectively [*Wulf et al.*, 2012; *Boers et al.*, 2014b; *Espinoza et al.*, 2015].

For deciphering and interpreting the evolution of both rainfall-frequency and intensity for semi-arid to arid environments, we estimated climate indices, including percentiles, restricting the analysis to the wet days/hours subsets, adopting the standard practice commonly applied to climate studies (e.g., Tank et al. 2009; Rajczak et al. 2013; Sillmann et al. 2013; Kendon et al. 2014). Additional information can be found in the Appendix A1.

Abbreviation	Parameter	Units
TS	Total amount	mm/yr
TSF (TSF%)	Absolute (percentage*) fraction due to the seasonal totals to the annual amount	mm/yr (%/yr)
#WD	Number of wet days (>0.5mm/d)/hours (>0.1mm/3h)	#/yr
MRd	Mean daily/3-hourly rainfall for wet days/hours	mm/d mm/3h
IthPrct	ith percentiles of wet days (i = 1, 5, 10, 25, 50, 75, 90, 95, 99, 99.5 99.9)	mm
#IthPrct (%IthPrct)	Number (percentage with respect to the total number of wet days/hours) of wet days/hours exceeding the Ith percentile	#/yr (%/yr)
TPIthPrct (TP%IthPrct)	Absolute (percentage*) fraction of TS accounted for by wet days/hours exceeding the ith percentile	mm/yr (%/yr)

Table 3.1 List of climate indices evaluated for analyzing climate spatiotemporal variability in NW Argentina. All indices were estimated at annual as well as seasonal (SON, DJF, MAM, JJA) scale (*The percentage is estimated dividing the absolute value by the relevant total amount (year/season)).

We analyzed the evolution of the percentiles of the wet days/hours frequency distributions using normalized wet days/hours subsets of data, to allow for a spatial comparison in a region characterized by pronounced spatial variability. We will refer to it below as *median-normalized*, having divided each original wet days/hours sub-datasets by the 1981-2010 median of the frequency distribution of the wet days/hours. For the TRMM dataset (1998-2014) no CLINO values could be estimated and the normalization was obtained using the 1998-2014 median values. We emphasize that only in the case of the percentile indices the median-normalization was performed.

Except for percentiles, trends associated with every climate index were estimated applying iteratively re-weighted least squares with a bisquare-weighting function [*Holland and Welsch*, 1977; *Huber*, 1981]. In the following we will refer to the latter analysis as *robust regression*. For all indices, including percentiles, trends are represented by the slope of the regression line and the statistical significance was verified applying a two-tailed t-Student test at the 95% confidence level [*Gosset*, 1908; *Yue and Pilon*, 2004].

3.4 RESULTS

3.4.1 TREND ANALYSIS FOR THE PERIOD 1950-2014

Rainfall time series are available for this time period only from rain gauges. Although some time series start in the 1920s, we performed our statistical analysis

starting in 1950, for which a sufficiently populated statistical ensemble can be configured with 13 stations located in the humid and arid regions. All analyses were conducted on annual and seasonal time scales; in the data presentation DJF trends are shown for all 13 rain gauges, revealing a complex spatiotemporal pattern (additional data plots are in the Appendix A1, Figure A1.2-13).

Our study confirms that the steep orographic rainfall barrier in the southern Central Andes results in a pronounced rainfall gradient across the Andean orogen (Figure 3.3) [*Bookhagen and Strecker*, 2008; *Rohrmann et al.*, 2014]. The mean rainfall pattern in NW Argentina is associated with strong seasonality, with summer and fall seasonal totals (6 months) on average accounting for at least 70% of the annual values (Figure 3.3) (e.g., Vera et al. 2006; Bookhagen and Strecker 2008; Espinoza et al. 2015; Boers et al. 2015b).

Approximately half of the analysed stations provided statistically significant ($p<0.05$) trends for DJF (Figure 3.4). The data show a rather coherent spatial pattern for DJF total amount and number of wet days indices, with most of the significant trend signal observed at the transition zone between low and intermediate elevations (0.3 – 1.5 km) (Figure 3.4 and Figure A1.5). Total amount and number of wet days indices increased during the period 1950-2014 at the transition zone between the low and intermediate elevations, whereas low elevations exhibited a more mixed pattern (Figure 3.4a-b). Mean daily rainfall showed positive trends at high elevations, but there were negative trends at the mountain front (Figure 3.4c). Quantile regression indicated negative trend values for the 50th percentile at the transition zone between the low and intermediate elevations and positive values at low elevations (Figure 3.4d). Fewer stations provided significant trends for the 95th percentile, with positive trends at the northernmost stations at high elevations and at the transition zone between the low and intermediate elevations, whereas almost no trend is found for the frequency of events exceeding the 95th percentile (extreme events). In the following, we denote the area where the northernmost stations are located as *the northernmost NW Argentine provinces*. Though based on few stations, both magnitude and frequency of the 95th percentile presents non-significant trends at low elevations, whereas a positive trend is found at high elevations (Figure 3.4e-f).

3.4.2 TREND ANALYSIS FOR THE PERIOD 1979-2014

Both rain-gauge time series (40 stations) and the CPC-uni dataset (hereafter referred to CPC) are available for this time period. Station data showed mostly no significant trends for the total amount for DJF. On the contrary, the frequency of wet days exhibited negative trend values at low elevations, a more mixed pattern at the mountain front, and mostly no significant values at high elevations (Figure 3.5a-b). CPC indicated similar trend patterns of the number of wet days at low elevations, with mostly significant negative trends as low as -3 %/yr in the lowlands. CPC also

exhibited large areas at high elevations (between 20° and 17°S and between 30° and 25°S) with significant positive trends of up to 5 %/yr or more particularly for the total amount. For mean daily rainfall, few stations provide significant results, exhibiting a mixed pattern of significant trends at the mountain front for the southernmost stations and negative trends at high elevations for the northernmost ones. CPC for this index showed positive trends both at low and high elevations, with more pronounced and coherent trends in the high-elevation regions up to 5 %/yr (Figure 3.5c). Quantile regression for rain gauges documented relatively low trend values for the 50th percentile; the 95th percentile exhibits a more mixed pattern with no significant trend at low elevations, mainly negative at high elevations, and positive in the transition between the low and intermediate elevations, where also the frequency of extreme events showed positive trends (Figure 3.5d-f).

For CPC, we observed that for DJF the 95th percentile trend pattern exhibits extensive regions characterized by positive trends both at low and high elevations (up to more than 0.25-0.5 times the value of the median in a year), associated with a less coherent and more mixed trend pattern of the frequency of extreme events (≥95th Prct) for DJF (Figure 3.5f). On the contrary, the 50th percentile exhibited trend values of low significance (Figure 3.5d). Acceptable agreement is found between rain gauges and CPC results at low elevations and at the mountain front, but there are significant differences at high elevations (Figure 3.5b,c,f).

3.4.3 TREND ANALYSIS FOR THE PERIOD 1998-2014

TRMM 3B42 V7 data (hereafter referred to TRMM) were used to analyze rainfall-trend patterns for the period 1998-2014. TRMM were aggregated at daily scale (12UTC-12UTC) to obtain the same time resolution of the stations and CPC data sets, and the same methodology was applied to both 3-h (raw-data time resolution) and daily rainfall datasets. Daily and 3-h datasets exhibited analogous spatiotemporal patterns (Figure A1.14). In the following, results obtained for the 3-h dataset will be shown. As in the previous cases, trend analyses were conducted at annual and seasonal scale (Table 3.1) and results for the summer (DJF) are shown (see Appendix A1 for complete results).

Total amount, number of wet hours, and mean 3-hourly rainfall climate indices display different patterns, especially at high elevations (Figure 3.6a-c): the total amount shows significant trends mainly in the northernmost part of the study area (23° - 17°S) and mostly positive (with values exceeding 5 %/yr), whereas the number of wet hours exhibits significant trends mainly concentrated in the southernmost area (below 23°S), and generally negative (with values <-5 %/yr). As a consequence, the mean 3-hourly rainfall shows mainly positive trends, especially at high elevations up to more than 5 %/yr. In the low-elevation regions few grid cells exhibited statistically significant trends for these indices.

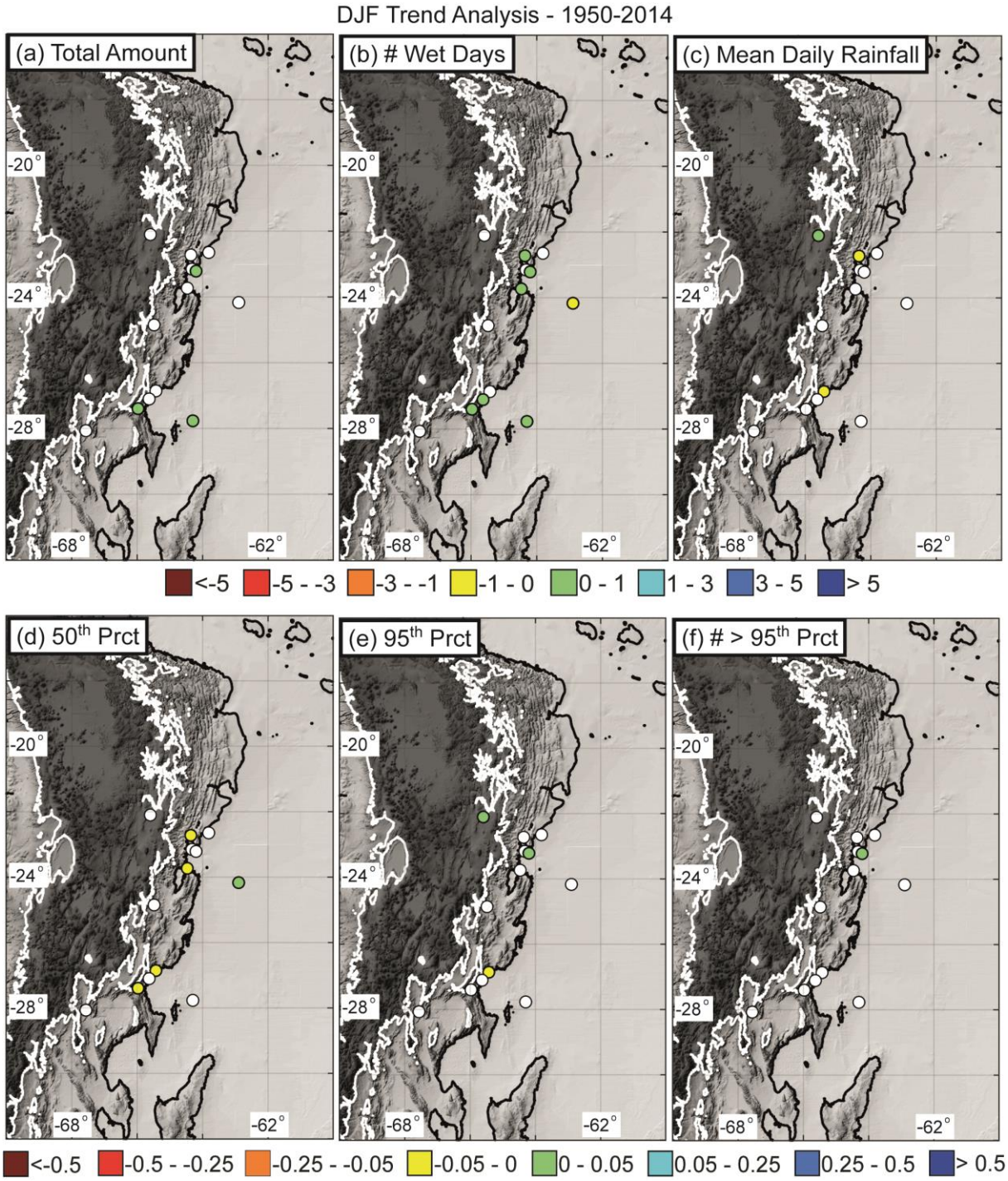

Figure 3.4 Trend analysis of daily rainfall estimation from rain gauges for DJF for the period 1950-2014 (for this period 13 stations were available). Black and white lines are elevation contours at 500 and 3000 m asl, respectively, roughly separating the eastern lowlands from the intermediate and high-elevation areas to the west. Shown are the mean-normalized climate indices (a) total amount, (b) number of wet days, (c) mean daily rainfall ([% yr^{-1}]); the median-normalized climate indices (d) 50th percentile, (e) 95th percentile ([yr^{-1}]), and (f) the mean-normalized number of events exceeding the 95th percentiles ([% yr^{-1}]). Full circles are statistically significant trends at $p<0.05$ confidence level, empty circles are non-significant values; approximately half of the stations presents statistically significant results (see also Figure A1.6A).

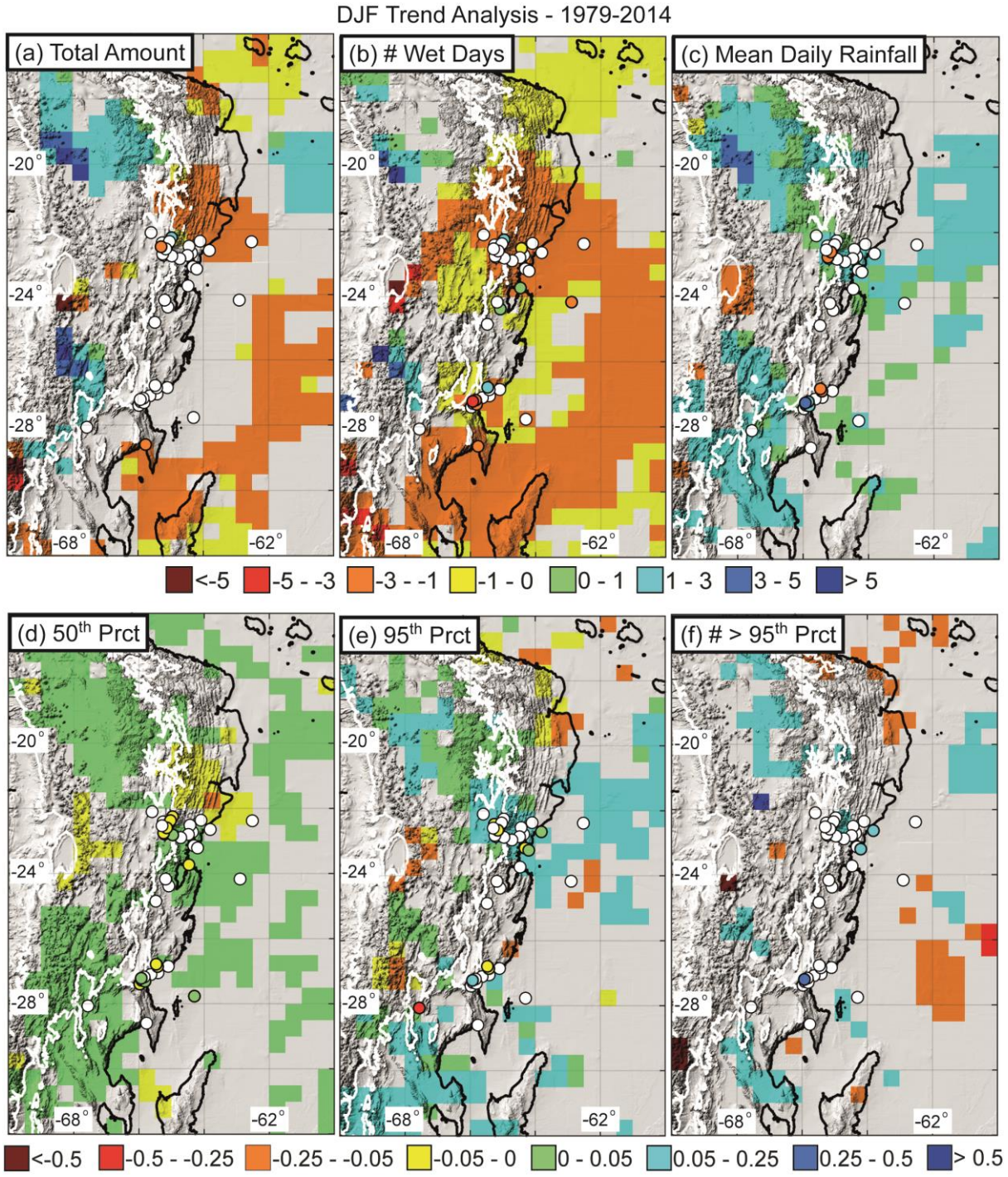

Figure 3.5 Trend analysis of daily rainfall estimation from rain gauges for DJF for the period 1979-2014 (for this period 40 stations are available) and CPC dataset. Black and white lines are elevation contours at 500 and 3000 m asl, respectively, roughly separating the eastern lowlands from the intermediate and high-elevation areas to the west. Shown are the mean-normalized climate indices (a) total amount, (b) number of wet days, (c) mean daily rainfall ([% yr^{-1}]); the median-normalized climate indices (d) 50th percentile, (e) 95th percentile ([yr^{-1}]), and (f) the mean-normalized number of events exceeding the 95th percentiles ([% yr^{-1}]). Rain gauges: Full circles are statistically significant trends at $p<0.05$ confidence level, empty circles are non-significant values; few stations provided statistically significant results (approximately ¼ of the stations). CPC dataset: only statistically significant trends are shown ($p<0.05$; blank grid cell are non-significant trends); between 17% and 58% grid cells provide significant results (FigureA1.6B).

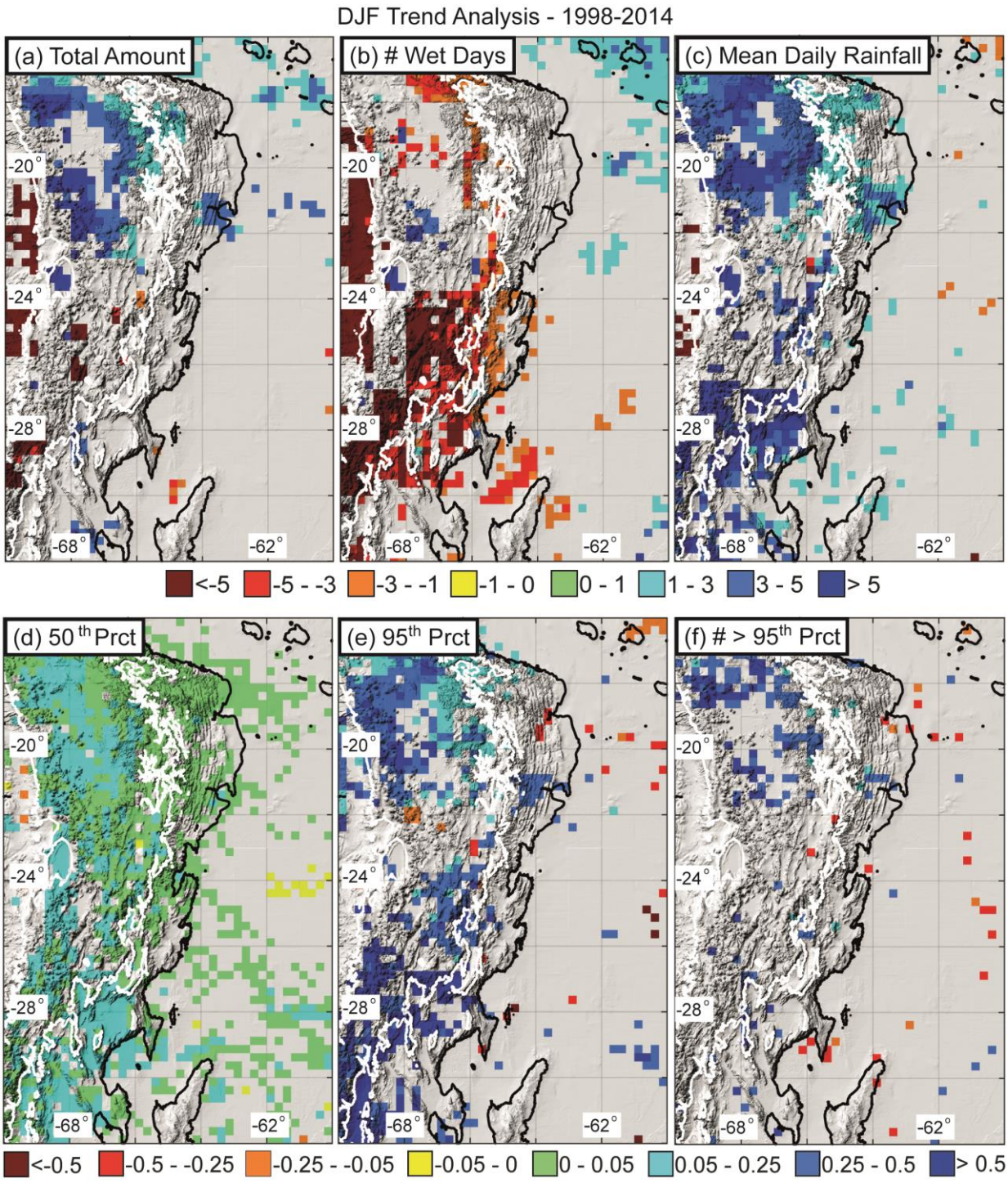

Figure 3.6 Trend analysis of 3-hr rainfall estimation from TRMM 3B42 dataset for DJF over the period 1998-2014. Black and white lines are elevation contours at 500 and 3000 m asl, respectively, roughly separating the eastern lowlands from the intermediate and high-elevation areas to the west. Shown are the mean-normalized climate indices (a) total amount, (b) number of wet days, (c) mean daily rainfall ([% yr^{-1}]); the median-normalized climate indices (d) 50^{th} percentile, (e) 95^{th} percentile ([yr^{-1}]), and (f) the mean-normalized number of events exceeding the 95^{th} percentiles ([% yr^{-1}]). Only statistically significant trends are shown ($p<0.05$; blank grid cell are non-significant trends); between 17% and 28% grid cells provide significant results.

In particular, total amount and number of wet hours showed positive trends in the northernmost part of the study area (above 23°S), whereas the southernmost region (below 25°S) is characterized by mostly negative trends.

For the wet hours frequency distribution, we observed that during DJF the 50th percentile exhibits mostly no or relatively low significant trends (Figure 3.6d); in contrast the 95th percentile records a coherent trend pattern with large regions characterized by positive trends, especially in the high-elevation regions (up to more than 0.5 times the value of the relevant percentile in a year, Figure 3.6e). We observed that the overall pattern of the 95th percentile generally mimics mean daily rainfall (Figure 3.6c). During DJF the frequency of extreme rainfall events (≥95th Prct) exhibits few significant, but mainly positive trends at high elevations.

3.5 DISCUSSION

3.5.1 CAVEAT

Gridded-rainfall data are a useful source of information for several types of studies, particularly for an assessment of climate variability and climate-change analyses [*Dai et al.*, 1997; *Sen and Habib*, 2000; *Roy and Balling*, 2004; *Carvalho et al.*, 2012; *Boers et al.*, 2014b, 2015b], because they avoid the limitations of point observations with uneven spatial distribution or missing data [*Daly et al.*, 1994; *Liebmann and Allured*, 2005; *Daly*, 2006; *Ensor and Robeson*, 2008]. However, it has been long recognized that ground-station based gridded rainfall data have limitations as well, especially at high temporal resolution. In particular, the spatial density of the original rain gauges is reflected in the quality of the interpolated values [*Ensor and Robeson*, 2008; *Carvalho et al.*, 2012].

For the CPC dataset it has been observed that, besides good agreement between annual and seasonal total amounts (TS), the frequency of low-magnitude events is overestimated, whereas both frequency and magnitude of heavy-rain events are usually underestimated [*Ensor and Robeson*, 2008]. This behavior will affect the wet days frequency distribution, will shift the percentiles towards lower values, and may also impact the total amount at annual and seasonal scales. We argue that by shifting the frequency distribution towards low values, lower variability will characterize the rainfall gridded dataset, implying potentially lower trends than provided by the original rain-gauge time series. Although it is not the aim of this study to test the degree of agreement between the rain gauges and the CPC datasets, we still need to take into account these limitations for correctly interpreting the outcomes of the statistical analysis.

We also point out that, as a consequence of the limited number of measuring stations in remote mountainous areas such as in our study area, the gridded and

interpolated rainfall patterns may be misrepresented, especially at high elevations, including the Puna de Atacama Plateau and mountain-front areas, characterized by steep climatic and topographic gradients [*Bookhagen and Strecker*, 2008, 2012]. Figure 3.3 illustrates this constraint with a longitudinal swath profile, highlighting the rainfall gradient across the NW Argentine Andes. Visual inspection reveals that the high-spatial resolution TRMM 2B31 estimations are in good agreement with station-derived values [*Bookhagen and Strecker*, 2008]. With decreasing spatial resolution, however, we are less capable to correctly detect the location of rainfall maxima at the orographic barrier. In particular, the CPC dataset is less precise in localizing the rainfall maxima at the mountain front, and it overestimates rainfall amounts in the arid, high-elevation region. Here, rainfall peaks in the lee of the eastern ranges record values twice as high as station estimates. We argue that trend-analysis results based on the CPC dataset may be affected by lower absolute trends and that spatial location of maximum and minimum estimations may be misrepresented, particularly within topographic transitions, compared to the rain-gauge dataset.

Furthermore, although based on calibrated remotely-sensed measurements, research-grade TRMM estimations can be potentially affected by bias errors in remote high-elevation regions as well. In fact, among other sources of uncertainty affecting TRMM evaluations, the calibration strongly depends upon the density of the ground stations [*Huffman et al.*, 2007], which is limited in high-elevation areas. Several studies have addressed this issue (e.g., Condom et al. 2011; Heidinger et al. 2012; Zulkafli et al. 2014; Nerini et al. 2015; Wulf et al. 2016). Most of these studies analyzed the performance of satellite observations for hydrological applications at drainage-basin scale, which requires continuous and high-quality rainfall estimates. It has been shown that TRMM data overestimate rainfall compared to rain-gauge measurements in areas of pronounced relief. Thus, post-processing and rainfall adjustment in combination with ground observations are an approach to rescale these data for hydrological applications (e.g., Wulf et al. 2016). At the same time, the comparison of the performance of TRMM with other rainfall-gridded datasets reveals that TRMM sufficiently captures the major features of SAMS with respect to the other datasets [*Carvalho et al.*, 2012; *Boers et al.*, 2015a]. Also, Boers et al. (2015b) have shown that TRMM allows detecting the propagation of extreme events from the southeastern sectors of South America towards the eastern Central Andes, whereas reanalysis datasets at coarser resolution, such as ERA-Interim [*Dee et al.*, 2011] and MERRA [*Rienecker et al.*, 2011], could not reproduce this mechanism. Thus, depending on the specific application, particular caution must be used to correctly interpret results based on TRMM data. We emphasize that in the present study, we relied on normalized indices to analyze changes in the rainfall field, which should filter out systematic overestimations.

Station data from high-elevation environments have inherent limitations as well, mainly related to uneven spatial distribution of rain gauges, a problem often dictated by maintenance and infrastructure conditions in these regions. Despite the fact that rain gauges provide high-quality observation, in some cases the rainfall stations used in our study are located at valley bottoms, particularly in the transition between low and high-elevation areas. These stations may not represent an area average, but are only representative of the climatic conditions for a restricted area.

In our analyses, we carefully took into account the strengths and limitations of the various datasets. With these boundary conditions in mind, we aimed at testing whether trends in rainfall patterns in the NW Argentine Andes were detectable and to what degree the collected datasets were able to exhibit this signal.

3.5.2 RAINFALL TREND AT SEASONAL SCALE DURING THE PERIOD 1950-2014

We observed that total rainfall amount and number of rainy days generally exhibit a positive trend during DJF at the transition zone between the low and intermediate elevations. Importantly, this trend was also found for MAM (Figure A1.6), implying that in this area the wet season tends to get wetter, with both increasing total amount and frequency of rainfall events. On the other hand, we observed either no change or a decrease of total amount and event frequency during SON and JJA (Figure A1.6), suggesting that the dry season tends to get drier, which is also evident when plotting the seasonal trends vs. elevation (Figure A1.5). This behaviour has been defined as 'the wet get wetter, the dry get drier' mechanism [*Held and Soden*, 2006; *Carvalho and Jones*, 2016]. However, at the transition zone between the low and intermediate elevations the net annual budget exhibits the trend towards a wetter general condition (Figure A1.5-6), in good agreement with results obtained for South America from previous studies [*Barros et al.*, 2000; *Haylock et al.*, 2006]. Barros et al. (2000) found positive DJF total amount trends for most of the Argentine territory, more pronounced in the northern study area and during the period 1956-1991, which they related to a decrease of the mean meridional gradient of temperature affecting atmospheric circulation. Their results were also confirmed by Haylock et al. (2006) with a comprehensive study of rainfall trends in South America during the period 1960-2000, suggesting wetter conditions at annual scale for northern Argentina.

3.5.3 RAINFALL TREND AT SEASONAL SCALE DURING THE PERIOD 1979-2014

We have performed a trend analysis for a shorter period (1979-2014), for which we could rely on a denser rain-gauge network (40 stations) and on the CPC dataset. In contrast, for the period 1950-2014, station data show no trends or a

decrease of total amount and number of wet days both at high and low elevations at annual and seasonal scales for 1979-2014 (Figure 3.5 and Figure A1.5). However, the wet season (DJF and MAM) also exhibits a trend of increasing rainfall (both total amount and number of wet days) at a few localities at the mountain front (Figure 3.5). These findings are partially corroborated by the CPC trend analysis, which displays the general trend towards drier conditions for the same period (1979-2014) during DJF, except at high elevations (Figure 3.5), where we observed extensive areas of increasing rainfall totals (between 17°S and 20° and between 25°S and 30° and), in part on the Puna de Atacama Plateau. Although for a shorter time period (1998-2014), the TRMM dataset exhibits similar features at high elevations during DJF (Figure 3.6), with an area of increasing rainfall on the Puna de Atacama Plateau (between 23°S and 20°S). Unfortunately, no station data are available for these areas at high elevation exhibiting significant trends. However, since TRMM data show a coherent trend signal over a wide region, we suggest that this signal represents a real trend towards increasing rainfall at high elevations. Nevertheless, we observed that the local maxima trend values shown by TRMM at high elevations appear to be displaced southward compared to the CPC outcomes. Such dislocation in the position of maxima and minima trend values is not surprising, since it was recognized that the CPC dataset is affected by such limitations due to the scarcity of rain gauges in the transition between the low and high elevations and the Puna de Atacama Plateau (see Caveat section).

Concerning the remaining seasons, both station data and CPC datasets document a trend pattern for Autumn (MAM), which mimics the summer trend, whereas for the dry season (JJA and, to a lesser degree, SON) the tendency towards drier conditions was even more pronounced compared to the period 1950-2014 (Figure A1.5-6).

In summary, for the last three decades (1979-2014) we observed a general trend towards drier conditions at low elevations during the wet season and locally wetter conditions at the mountain front. On the contrary, we found evidence for extensive areas exhibiting a trend of increasing total seasonal rainfall amount in the arid Puna de Atacama Plateau region.

Interestingly, the aforementioned positive trend revealed in our study appears to be in contrast with rainfall projections for a different emission scenario for the northern Andean Plateau (Altiplano) obtained during recent studies [*Urrutia and Vuille*, 2009; *Minvielle and Garreaud*, 2011; *Thibeault et al.*, 2012]. In particular, Urrutia and Vuille's (2009) projections for DJF rainfall in the tropical Andes during the period 2071-2100 exhibits a rather incoherent pattern, with increasing, as well as decreasing total rainfall amounts compared to the period 1961-1990. On the Bolivian Altiplano the projection showed a significant total-amount decrease.

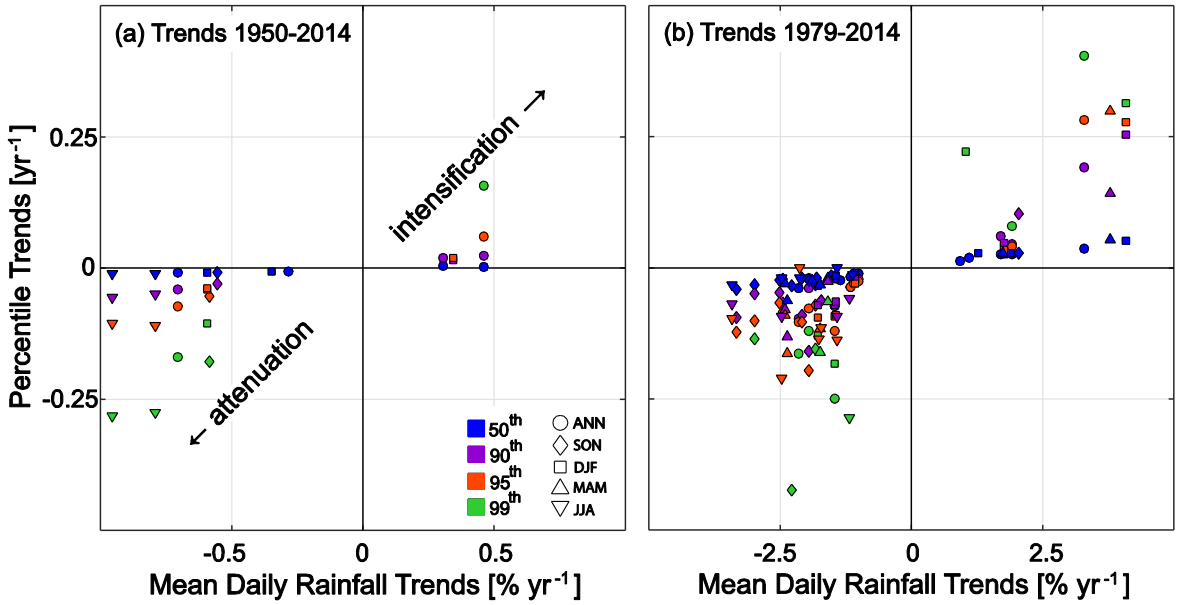

Figure 3.7 Trend analyses for rain gauges (only statistically significant trends, $p<0.05$, are shown): (a) mean daily rainfall (MRd) trends vs. percentile (Prct) trends for the period 1950-2014. The rainfall spatial variability exhibits a complex pattern, reflected both in the mean daily rainfall and in the percentile analysis, with either positive (intensification) or negative (attenuation) trends. All analyzed stations show the same trend for their mean daily rainfall and the frequency distribution percentiles, implying that an intensification of the mean daily rainfall is accompanied by either no change or an intensification of the uppermost percentiles. (b) Same as (a) but for the period 1979-2014, indicating similar features. In both periods, attenuation is mostly associated with the dry season, whereas the wet season reflects both attenuation and intensification of rainfall events.

We emphasize that our study area was only partially included in their investigated region. Urrutia and Vuille (2009) suggest that the rainfall decrease expected for DJF by the end of the century could be linked to the weakening of the easterlies in the middle and upper troposphere. It has been recognized that easterly wind anomalies at high tropospheric levels are associated with deep convection on the Altiplano by transporting moist air from the interior of the continent. This phenomenon has been called the 'easterly/wet – westerly/dry relationship' [*Garreaud and Aceituno*, 2001; *Thibeault et al.*, 2010]. Minvielle and Garreaud (2011) analyzed the predicted change in rainfall pattern in the Central Andes (15°-25°S) for the end of the 21st century (2070-99), confirming a significant decrease in total amounts linked to the change in the middle and upper troposphere circulation with respect to 1970-99. Unfortunately, their study does not include statistically significant results for NW Argentina. Thibeault's et al. (2012) projections also suggested a decrease of rainfall on the Bolivian Altiplano, starting already in 2020, although the implications for the precipitation on the southern Andean Plateau were not discussed.

To summarize, several studies have suggested a general decrease of rainfall-total amount starting by 2020 for the wet season in the tropical Central Andes. The authors are not aware of similar studies extending their investigation areas southward, including the Puna the Atacama plateau (southern Andean Plateau) in NW Argentina, which has different climatic characteristics than the Bolivian Altiplano (northern Andean Plateau), in particular concerning the characteristics of rainfall convective systems [*Romatschke et al.*, 2010; *Romatschke and Houze*, 2013; *Rohrmann et al.*, 2014]. However, the CMPI5 projections for rainfall in South America for the end of this century proposed by Carvalho and Cavalcanti (2016) exhibit a more complex pattern for the areas including the northern and southern Andean plateaus. These projections show an overall weak signal of change for the entire wet season (October-March), a negative signal in the Chilean part, and locally a positive signal on the Argentine side. Additionally, Carvalho and Cavalcanti (2016) suggested an intensification of the SAMS poleward of 20°, accompanied by a reduction of up to 40% of DJF rainfall in Chile. This confirms the different dynamic climatology of the northern Altiplano, located in the tropics, and the subtropical Puna de Atacama Plateau, although both areas are characterized by similar elevations and orography.

Finally, we observe that for the period 1950-2014 there is no clear pattern at low elevations, in contrast with the coherent negative trend for the period 1979-2014. We tested the hypothesis if this change in the trend pattern is related to the 1970s climate shift [*Minetti and Vargas*, 1998; *Rusticucci and Penalba*, 2000; *Carvalho et al.*, 2011; *Jacques-Coper and Garreaud*, 2015]; detailed information on this test is provided in the Appendix A1. However, based on our station dataset it is not possible to unambiguously identify the 1970s climate shift as a forcing factor of the changing rainfall trend in our study region.

3.5.4 TREND OF DAILY RAINFALL MAGNITUDE-FREQUENCY DISTRIBUTION

As previously pointed out, daily station data showed that DJF mean daily rainfall for the period 1950-2014 recorded few significant values; they are negative at the transition between the low and intermediate elevations, and positive at high elevations (Figure 3.4). In contrast, a rather incoherent spatial pattern was observed for 1979-2014 (few significant values, both negative and positive, Figure 3.5). On the other hand, both CPC and TRMM results exhibit a coherent signal toward an intensification of the mean-rainfall amount per event, which was particularly pronounced at high elevations (Figure 3.5 and Figure 3.6). This intensification is associated with a diffuse reduction in the frequency of rainfall events, except for restricted areas at high elevations (see section 5.3*)*. Thus, to decipher whether such changes in the mean-rainfall amount per event are due to changes in mean/median and/or to the extreme rainfall values, we analyzed the trends of the different percentiles of the frequency distributions.

The spatial pattern of the percentile trends is in good agreement with the trend shown by the mean daily rainfall-climate index (for station data: Figure 3.7, for CPC data: Figure 3.5; for TRMM data: Figure 3.6. An intensification (or attenuation) of the mean daily rainfall is accompanied by an intensification (or an attenuation) of the percentiles at any order, particularly at high orders (≥90th) (Figure 3.7). We also observed that often small or no changes in the median values of the wet days frequency distributions were associated with significant trends, either towards local intensification or attenuation in the 95th percentiles (Figure 3.7and Figure A1.3).

In the high elevations of the Puna de Atacama Plateau in the northernmost NW Argentine provinces, DJF extreme events (≥95thPrct) increased in magnitude, but not in frequency during the period between 1950 and 2014, whereas the low-medium events (<50thPrct) exhibit no changes (Figure 3.4 and Figure A1.11). This results in increased mean daily rainfall without strongly affecting the total amount and frequency of wet days. At the mountain front, few stations provided significant results and the overall trend signal is mixed and not significant. Nevertheless, we observe that, despite a decrease of low-medium events intensity, at few locations in the northernmost NW Argentine provinces both frequency and magnitude of extreme events increased, which is reflected by the total amount and frequency of rainy days. In the southernmost stations, both low-moderate and extreme events exhibit a decreased magnitude, but it is the increased frequency of low-moderate events (Figure A1.11) that accounted for the increased total amount and frequency of wet days. At low elevations, non-significant patterns were detected. Taken together, these observations suggest that in the northernmost NW Argentine provinces for the period 1950-2014, extreme (≥95thPrct) events increased in magnitude at high elevations on the Puna de Atacama Plateau and locally at the transition zone between the low and intermediate elevations.

Except for minor discrepancies, the gridded datasets from the periods 1979-2014 and 1998-2014 record increasing magnitude and frequency of extreme events at the mountain front; these trends, do not affect the total amount and number of wet days. Good agreement exists also at low elevations, where the decrease of total amount and number of wet days is not related to changes in extreme events. At high elevations few station data show significant, decreasing magnitudes of extreme events. This result contrasts with findings obtained from CPC and TRMM data, documenting a coherent pattern of increasing magnitude of extreme events for extensive areas on the Puna de Atacama Plateau (between 22° and 20°S and below 24°S). Given that station data provide few significant results for the high elevations among mostly non-significant trends, we suggest that in this context stations represent only locally the changing character of precipitation, whereas the gridded dataset provides a regional-scale signal of changes of the rainfall pattern.

In summary, our results suggest that at the transition zone between the low and intermediate elevations and in the semi-arid/arid high-elevation areas of the southern Central Andes extreme rainfall events have been increasing in magnitude and, to a lesser degree, in frequency during the wet season beginning in 1979. Starting from 1950, we found an increase in rainfall at the transition zone between the low and intermediate elevations, partly reflected by the magnitude of extreme events in the northernmost NW Argentine provinces, whereas no trend signal was found for the same period at low elevations.

These observations partially agree with previous studies, showing changing extreme rainfall events for Argentina and other continental regions [*Frei and Schär*, 2001; *Krishnamurthy et al.*, 2009; *Penalba and Robledo*, 2010; *Skansi et al.*, 2013; *Malik et al.*, 2016]. In particular, Penalba and Robledo (2010) analyzed the trend of the frequency of rainy days and of events exceeding the 75th frequency distribution percentile in Argentina. These authors found a general positive signal for all seasons for the period 1961-2000, except for the austral winter (JJA). At continental scale, Skansi et al. (2013) reported increasing trends in heavy precipitation events for the period 1950-2010, accompanying a significant wetting and intensified rainfall. These findings are in agreement with our results at the mountain front and at high elevations, but not at low elevations, where we did not observe any significant trend signal.

The observed increase in rainfall, both in total amount and extreme-event intensity, is consistent with the findings by Hsu et al. (2011). These authors showed that total monsoon precipitation has had significant positive trends during the past 30 years related to an increase in global mean-surface temperatures. Carvalho and Cavalcanti (2016) observed that the reanalysis products (CFSR and NCEP/NCAR) indicate a progressive increase in low-level tropospheric temperatures over tropical South America during the monsoon season. This can potentially alter ocean-land differential heating affecting the monsoonal circulation and moisture transport from the tropics to the subtropics. In fact, enhanced monsoonal circulation could affect the strength of the SALLJ and/or the SACZ, which are the most important features controlling moisture advection in the subtropics and the precipitation systems affecting the southern Central Andes. Interestingly, our results suggest that mountain front and high-elevation areas in the southern Central Andes respond more readily to changes in large-scale circulation.

3.6 CONCLUSIONS

We analyzed rainfall variability and trend patterns in the southern Central Andes (70°-60°W, 16°-32°S) at different spatiotemporal scales. We based our analysis on daily rain-gauge observations (40 gauges) and two gridded datasets (CPC-uni, TRMM 3B42 V7). We defined a set of six climate indices, covering the entire rainfall-

frequency distribution at annual and seasonal scales, for three different time periods: 1950-2014, 1979-2014, and 1998-2014. In particular, we analyzed magnitude and frequency trends of different rainfall events, from low-moderate (<50th percentile) to the extremes (>95th percentile), and the rate of change at annual and seasonal scales. We focused our analysis on the wet season from December to February (DJF), contributing at least 40% to the annual total rainfall amount, but we furnish additional insights for both the entire year and the dry season. Our study distinguishes between three geographic areas characterized by pronounced topographic, environmental, and climatic differences. These are the low-elevation regions in the eastern part of the study area, the mountain front (intermediate elevation) bordering the Andean mountain chain immediately to the west, with elevations between 0.5-3 km, and the high-elevation areas (> 3 km) farther west in the southern Andean Plateau. In the following, we summarize our key findings:

1. Station data for the period 1950-2014 show an increase of the annual total rainfall amount and wet days frequency at the transition zone between the low and intermediate elevations, accompanied by a trend characterized by a wetter wet season and, to a lesser degree, a drier dry season. For the period 1979-2014 rain-gauge measurements exhibit a significant trend at low elevations towards decreasing annual rainfall total amounts. Decreasing annual rainfall total amounts were also detected at low elevations with the CPC dataset for the period 1979-2014 and TRMM data for 1998-2014. At high elevations, both the CPC and TRMM datasets indicate that extensive areas on the arid southern Andean Plateau (Puna de Atacama) as well as at the mountain front (between 20°S and 23°S and between 25°S and 30°S) record increasing annual rainfall total amounts and, to a lesser degree, frequency of wet days. At seasonal scale, we observed for the dry season an even more pronounced trend towards drier conditions, whereas for the wet season extensive areas exhibited increasing trends in seasonal rainfall total amount on the Puna de Atacama Plateau. This supports previous findings of 'the wet get wetter, the dry get drier' mechanism.
2. Daily rainfall frequency distribution analysis often revealed small or no changes in median values of the wet days/hours magnitude, but a significant tendency towards either local intensification or attenuation in the 95th percentiles (extreme rainfall events). This observation holds true for all datasets and strongly impacts the trends of rainfall total amounts. For the period 1950-2014, rain-gauge measurements showed that for the wet season extreme (≥95thPrct) events have undergone a significant increase in magnitude, but not in frequency at the transition zone between the low and intermediate elevations as well as at high elevations in the northernmost NW Argentine Provinces. This accounts for most of the rate of change in the total amount, particularly at the transition zone between the low and

intermediate-elevation areas of the southern Central Andes. Starting in 1979 at high elevations on the Puna de Atacama Plateau, all gridded datasets reveal large areas with increasing magnitude of extreme rainfall events during DJF.

3. Discrepancies between the results of the three datasets were found and are related to the magnitude of trends and spatial localization of minima/maxima trend values. This is particularly true for the high-elevation areas both for annual rainfall totals and extreme events. We ascribe such discrepancies to the limitation of the CPC dataset, characterized by relatively low spatial resolution and scarcity of rain-gauge measurements within the transition between the low and high elevations, as well as on the arid Puna de Atacama Plateau. Besides these discrepancies, the CPC and TRMM datasets showed similar rainfall patterns, both clearly recording opposite trends between low and high elevations. Analysis of CPC and TRMM datasets exhibited some important similarities with the results obtained from rain gauges. Although the rain-gauge measurements do not display a strong coherent pattern as observed in the gridded datasets, we detected indications pointing toward an increasing magnitude of extreme rainfall at the mountain front areas by the station dataset. We suggest that the spatial inconsistency of the trend pattern from the station dataset is the lack of coherent significant results obtained at high elevations. Hence, the station data only partly support the trend towards increasing amounts and frequencies on the Puna de Atacama Plateau as observed by the gridded CPC and TRMM dataset.

ACKNOWLEDGMENTS

This investigation was carried out with funds from the Leibniz Fund of the German Science foundation (DFG) to M.S. (STR373/19-1) and additional funds by the German Federal Ministry of Education and Research provided to the PROGRESS initiative on Climate Change, Georisk and Sustainability at Potsdam University to M.S. and B.B. The authors thank the Servicio Meteorológico Nacional (SMN), Argentina, and the Subsecretaría de Recursos Hídricos (BDHI), Argentina, for providing rain-gauge time series. The authors thank in particular M. García (SMN), D. Cielak (BDHI), Ricardo N. Alonso (UN Salta), Arturo Villanueva (UN Tucumán), and E. Marigliano (EVARSA, Argentina) for their valuable support during this study. The CPC-uni and TRMM 3B42 V7 data are available at https://climatedataguide.ucar.edu/climate-data/cpc-unified-gauge-based-analysis-global-daily-precipitation and http://disc.sci.gsfc.nasa.gov/gesNews/trmm_v7_multisat_precip respectively. Furthermore, the authors thank the three anonymous reviewers for their insigntful comments and suggestions.

APPENDIX A1

The supporting information of this chapter is available in the attached CD.

CHAPTER 4

RIVER DISCHARGE DYNAMICS IN THE SOUTHERN CENTRAL ANDES AND THE 1976-77 GLOBAL CLIMATE SHIFT

Fabiana Castino[1], Bodo Bookhagen[1], and Manfred. R. Strecker[1]

[1] Institute of Earth and Environmental Science, University of Potsdam

Geophysical Research Letters (2016), doi: 10.1002/2016GL070868

KEY POINTS

- Change point for increase in discharge between 1971 and 1977 linked to the 1976-77 climate shift
- Most pronounced discharge increase observed in high percentiles for the Southern Central Andes across the change point
- Discharge increase of 40% in the NW Argentine Andes between 1971 and 1977

ABSTRACT

Recent studies have shown that the 1976-77 global climate shift strongly affected South American climate. In our study, we observed a link between this climate shift and river-discharge variability in the subtropical Southern Central Andes. We analyzed daily river-discharge time series between 1940 and 1999 from small to medium mountain drainage basins (102-104 km2) across a steep climatic and topographic gradient. We document that the discharge frequency-distribution changed significantly, with higher percentiles exhibiting more pronounced trends. A change point between 1971 and 1977 marked an intensification of the hydrological cycle, which resulted in increased river discharge. In the upper Rio Bermejo basin of the northernmost Argentine Andes, the mean annual discharge increased by 40% over seven years. Our findings are important for flood risk management in areas impacted by the 1976-77 climate shift; discharge-frequency distribution analysis provides important insights into the variability of the hydrological cycle in the Andean realm.

4.1 INTRODUCTION

There is increasing evidence that a global climate shift occurred between 1976 and 1977, associated with sea-surface temperature variability in the North Pacific Ocean [*Graham*, 1994; *Miller et al.*, 1994]. This change strongly affected the South American climate [*Marengo*, 2004; *Agosta and Compagnucci*, 2008; *Kayano et al.*, 2009; *Carvalho et al.*, 2011; *Jacques-Coper and Garreaud*, 2015]. *Marengo* [2004] suggested that an intensification of moisture advection from the Tropical Atlantic into the Amazon basin may have increased rainfall in southern Amazonia starting from 1975-1976. Modifications to the low-level atmospheric circulation occurred during the mid-1970s and were documented in southern South America, resulting in lower mid-latitude cyclonic activity [*Agosta and Compagnucci*, 2008]. During the same period, rapid changes in temperature and rainfall patterns were observed throughout South America [*Kayano et al.*, 2009; *Jacques-Coper and Garreaud*, 2015].

The spatiotemporal rainfall pattern in tropical and subtropical South America is controlled by the South American Monsoon System (SAMS). On average, southward moisture transport by the SAMS occurs between late October and late April [*Zhou and Lau*, 1998; *Vera et al.*, 2006; *Marengo et al.*, 2012]. *Carvalho et al.* [2011] showed that, starting from 1971-1972, the onset (demise) of the SAMS has been occurring earlier (delayed). This has resulted in a prolongation of the wet season (approximately 25 days) related to the 1976-1977 climate shift. Furthermore, the acceleration of glacial retreat in tropical South America between the mid-1970s and early 1980s was linked with Pacific Ocean warming associated with this climate shift [*Francou*, 2003; *Rabatel et al.*, 2013; *Hanshaw and Bookhagen*, 2014].

Several studies have documented a rapid increase in mean river discharge in large South American rivers (i.e., the Amazon, Negro, Orinoco, La Plata, Paraná, Paraguay) during the 1970s [*García and Vargas*, 1998; *Genta et al.*, 1998; *Robertson and Mechoso*, 1998; *Labat et al.*, 2004; *Marengo*, 2004; *García and Mechoso*, 2005; *Pasquini and Depetris*, 2010]. However, these studies mostly linked river-discharge variability to the El Niño Southern Oscillation, while *Marengo* [2004] and *Labat et al.* [2004] ascribed the observed changes to the 1976-1977 climate shift. To our knowledge, no study has analyzed how the magnitude frequency distribution of river discharge changed in response to the climate shift. This information would be necessary, however, to better understand pronounced changes in sediment flux and fluvial behavior in the Andean foreland and intermontane basins.

In this study, we examined how the frequency distribution of river discharge evolved between 1940 and 1999 in the Southern Central Andes, using standard and quantile regression [*Koenker and Bassett Jr.*, 1978] combined with change-point

analysis [*Taylor*, 2000]. Our study area encompassed the eastern flank of the Central Andes between 21° and 28° S, in the transition between the tropics and subtropics (Figure 4.1). Strong contrasts in topography, rainfall, and vegetation cover characterize this area, with low elevation in the east at about 0.5 km asl and high elevations in the west with peaks in excess of 6 km [*Bookhagen and Strecker*, 2012]. We relied on daily river-discharge time series from small to medium-size drainage basins (10^2-10^4 km^2) for the period 1940-1999 (Figure 4.1). These catchment sizes are more sensitive to climate change than large drainage basins such as the Amazon or La Plata basins, which contain large floodplains that dampen discharge trends [*Dunne and Mertes*, 2007; *Melack et al.*, 2009].

In a previous study, we documented a trend reversal in 1979 towards decreasing mean annual rainfall at the topographic transition between low regions in the east and intermediate elevations (0.5 – 3 km asl) [*Castino et al.*, 2017]. At the same time, an increasing magnitude of extreme rainfall events (>90th percentile) at high elevations (> 3 km asl) was detected.

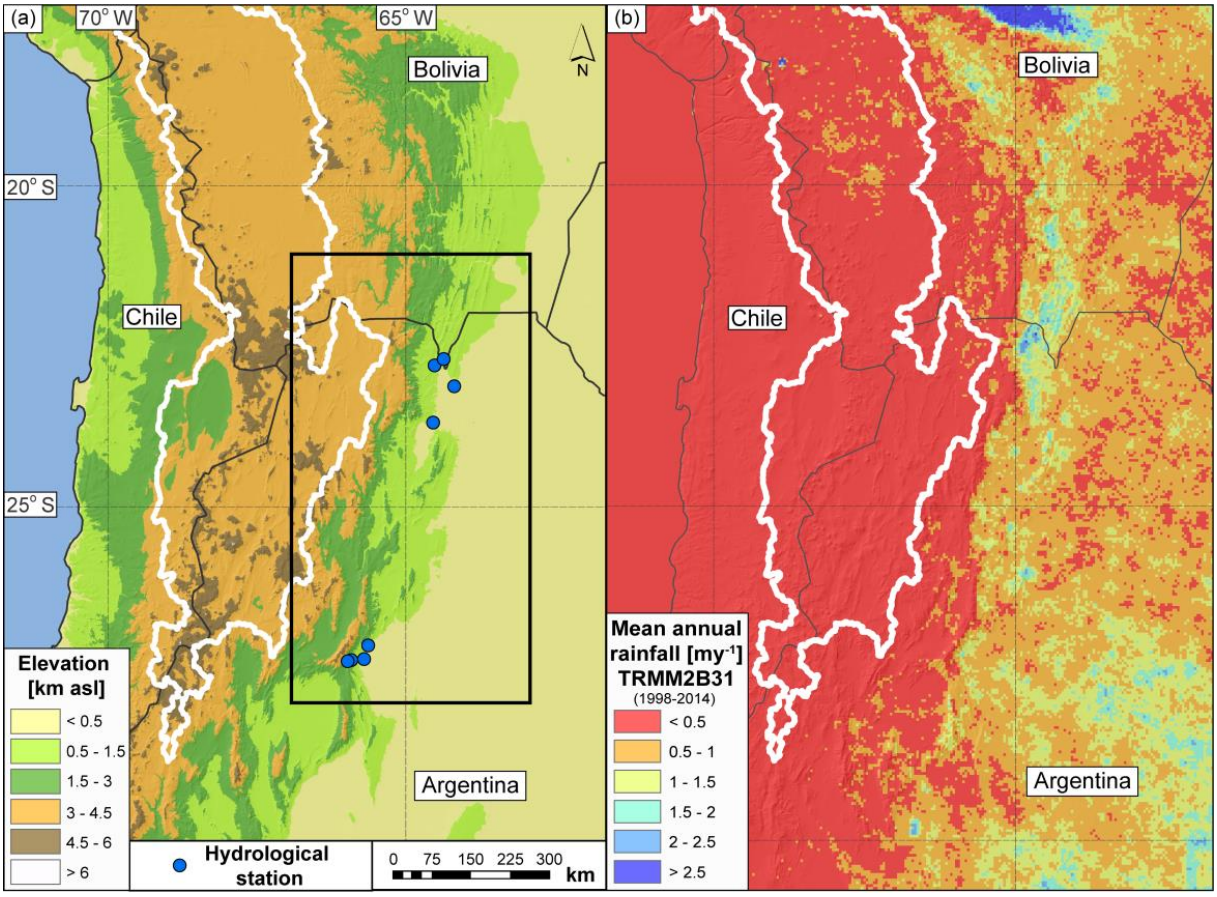

Figure 4.1 (a) Topography (SRTM) of the Southern Central Andes. The boundary of the internally-drained central Andean Plateau is outlined in white; the thin dark-grey line denotes international borders. The black rectangle delineates the study area in NW Argentina where discharge time series (n = 8, blue dots) are available (cf. Figure A2.1). (b) Mean annual rainfall data derived from TRMM 2B31 V7 (1998-2014) [*Bookhagen and Strecker*, 2008; *Bookhagen and Burbank*, 2010]. Rainfall is characterized by a pronounced gradient between low-elevation frontal areas and arid, high-elevation areas of the internally-drained plateau in the orogen interior.

However, no statistically significant link between the trend reversal in 1979 and the 1976-1977 climate shift was observed, most likely because of the high stochasticity and intermittency of rainfall-related processes.

In this study, we used river discharge to decipher the impact of the 1970s climate shift on the hydrological cycle. This is paramount not only for improving water resources and flood-risk management, but also for understanding sediment-transport processes that impact infrastructure and landscape development in different compartments of the Andean orogen.

4.2 Data and Methods

We relied on eight daily discharge time series derived from hydrological stations at the eastern flanks and foreland of the Southern Central Andes in NW Argentina (Figure 4.1). The time series, starting in 1914, were made available to us by the National Department of Water Resources (Subsecretaría de Recursos Hídricos de la Nación, Banco Nacional Hídrico, BNH). The gauged drainage basins differ in basin size (10^2 - 10^4 km^2) and climatic conditions (from predominantly humid to semi-arid environments, cf. Appendix A2, Figure A2.1, section A2.1 [*WMO*, 2008]). Data density is higher and data are more reliable for the period 1940-1999, so we focused our analysis on this time period. The investigation was performed on annual and seasonal scales (DJF – December through February and MAM – March through May), because the wet season contributes up to 90% to the total annual discharge on average (Figure A2.1).

We used several statistical indices (Table 4.1) to characterize discharge dynamics and trends (cf. Appendix A2, section A2.2 [*Compagnucci et al.*, 2000]). We primarily focused on NAQ_y^{season}, which is the normalized annual (ANN) or seasonal (DJF, MAM) discharge anomaly with respect to the mean discharge of the reference period 1970-1999, and the $PINQ_d^{season}$, which is the I-th percentile (I = 5, 10, …, 90, 95) of the normalized daily discharge Q_d^{season} with respect to the 50th percentile of the reference period 1970-1999.

The spatial variability of discharge in the study area between 1940 and 1999 was analysed by cross correlating the time series. The high values of cross-correlation for each station pair (rho> 0.5, p<0.001) reveal a high, spatially coherent discharge pattern, with a maximum time lag of one day (Figure A2.2).

Because of the high correlation between the time series, we stacked the eight normalized time series (i.e., the spatial mean of the eight time series of normalized daily discharge), and in the following sections we refer to the stacked mean time series as the *multi-station mean*. Single-station results are available in the Appendix A2.

We used the multi-station mean time series to identify discharge trends, taking a two-tiered approach:

1. To test for a linear trend, we applied both linear and quantile regression analysis [*Koenker and Bassett Jr.*, 1978; *Cade and Noon*, 2003; *Yu et al.*, 2003] to normalized discharge anomaly and to normalized daily discharge, respectively. Trend values were expressed in y^{-1} of the normalizing factor (for linear regression: $\overline{Q_{ref}^{season}}$; for quantile regression: $(P50Q_d^{season})_{ref}$, season = ANN, DJF, MAM). t-Student and Mann-Kendall tests at 5% significance level were used to determine whether each time series had a statistically significant trend [*Mann*, 1945; *Kendall*, 1948].
2. To test for non-linear trends, we used change-point analysis [*Taylor*, 2000], applied to both normalized discharge anomaly and the percentiles of normalized daily discharge. Statistical significance of the identified change points was verified using a bootstrapping technique at the 5% significance level (Appendix A2, section A2.3). Uncertainties associated with change-point timing were estimated by combining change-point analysis and bootstrapping within the percentile errors (±1σ) (percentile standard error estimated following *Evans*, [1942]), resulting in non-symmetric uncertainties. We emphasize that the change-point timing is independent of the normalization reference period (Figure A2.5).

Index	Definition	Expression
NAQ_y^{season}	Normalized (N) annual (ANN) or seasonal (DJF, MAM) discharge anomaly with respect to the mean discharge of the reference period 1970-1999	$NAQ_y^{season}(i) = \frac{Q_y^{season}(i) - \overline{Q_{ref}^{season}}}{\overline{Q_{ref}^{season}}}$ $Q_y^{season}(i)$: mean annual (ANN) or seasonal (DJF, MAM) discharge of the i-th year, i = 1, … , Ny; Ny: length of the time series in years; $\overline{Q_{ref}^{season}}$: mean annual (ANN) or seasonal (DJF, MAM) discharge for the reference period 1970-1999
$PINQ_d^{season}$	I-th percentile (I = 5, 10, …, 90, 95) of the normalized (N) daily discharge Q_d^{sc} with respect to the 50th percentile of the reference period 1970-1999	$Q_d^{season}(j) = \frac{Q_d(j)}{(P50Q_d^{season})_{ref}}$ $Q_d(j)$: daily discharge of the j-th day, j =1, … , n; n: the length of the annual (ANN) or seasonal (DJF, MAM) time series in days; $(P50Q_d^{season})_{ref}$: annual (ANN) or seasonal (DJF, MAM) median (50th percentile) of daily discharge for the reference period 1970-1999 season = ANN, DJF, MAM

Table 4.1 Main hydrologic indices used in this analysis: normalized discharge anomaly (NAQ_y) and percentiles of normalized daily discharge ($PINQ_d$).

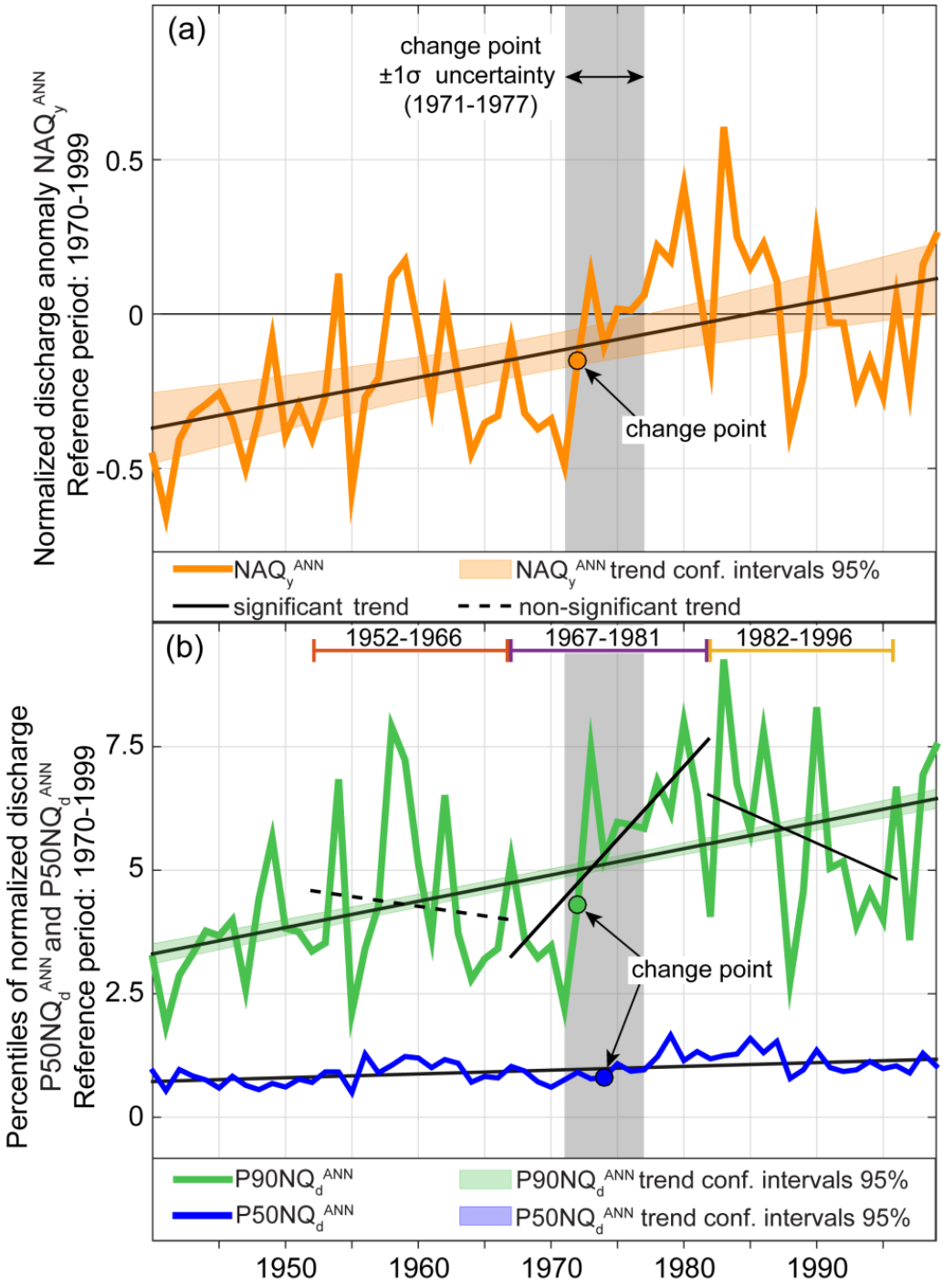

Figure 4.2 Results of linear regression and change-point analysis for the annual multi-station time series. (a) Annual normalized discharge anomaly NAQ_y^{ANN} (orange): statistically significant change point ($p<0.05$) results in 1972 (orange circle); statistically significant trends were observed for the complete time series (1940-1999, positive, black solid line; shading: confidence intervals at 95%, cf. Table A2.8). (b) Daily normalized discharge at the 50th percentile ($P50NQ_d^{ANN}$, blue) and at the 90th percentile ($P90NQ_d^{ANN}$, green): Statistically significant change points were found in 1974 (blue circle) and 1972 (green circle), respectively; $P50NQ_d^{ANN}$ and $P90NQ_d^{ANN}$ also exhibited a statistically significant positive trend for the complete time series (1940-1999, black solid line). Horizontal color bars indicate the 15-year periods before (1952-1966), across (1967-1981), and after (1982-1996) the change point; trend analysis was also conducted for these as well (c.f. Figure 4.3). Light grey polygons represent the ±1σ uncertainty of change-point timing (1971-1977) based on a bootstrap analysis (Figure A2.10).

4.3 RESULTS

Linear regression analysis applied to NAQ_y^{ANN} revealed statistically significant ($p<0.05$) positive trends on the annual scale for the period 1940-1999 for the multi-station mean time series (+0.008 ± 0.002 y^{-1}) (Table 4.1 and Figure 4.2a).Similar results were obtained for the wet season. Quantile regression also showed a statistically significant trend for the multi-station mean time series: The trend of the median normalized discharge ($P50NQ_d^{ANN}$: +0.008 ± 0.001 y^{-1}) and the trend for the 90th percentile of normalized discharge ($P90NQ_d^{ANN}$: +0.053± 0.003 y^{-1}) indicate a higher trend magnitude for the higher percentile (Table 4.1, Figure 4.2b).

We detected a statistically significant ($p<0.05$) change point during the period 1940-1999 for the annual and seasonal multi-station mean time series of NAQ_y^{season} (season = ANN, DJF, MAM), indicating a rapid increase in mean discharge in 1972 (Figure 4.2a and Figure A2.6). Similar results were obtained for the percentiles of normalized daily discharge $PINQ_d^{season}$, with change points between 1972 and 1977 (±1σ uncertainty: 1971-1977) (Figure 4.2b and Figure A2.10). In the following, we will refer to this as the *1971-1977 change point*.

Changes to the discharge frequency distribution were evaluated within three 15-year periods: before (1952-1966), across (1967-1981), and after (1982-1996) the change point. The linear trend analysis of NAQ_y^{ANN} before (1952-1966) and after (1982-1996) the change point revealed no statistically significant trends when t-Student tests were used, whereas significant results were found using the Mann-Kendall test. Statistically significant positive trends were found across the change point (1967-1996) (+0.045 ± 0.009 y^{-1}). Results from quantile regression applied to Q_d^{ANN} for the 90th percentile ($P90NQ_d^{ANN}$) suggest a statistically significant positive (+0.296 ± 0.029 y^{-1}) trend across and a statistically significant negative (-0.122 ± 0.023 y^{-1}) trend after the change point (Figure 4.2b). The complete results are shown in Table A2.8. The number of events exceeding the 90th percentile of normalized daily discharge ($P90NQ_d^{ANN}$) and the fraction of total discharge accounted for by the 10 largest discharge events also revealed a statistically significant change point during the early 1970s that yielded higher values (Figure A2.9). The detailed results of the trend and change-point analyses are shown in the Appendix A2 (section A2.4).

4.4 DISCUSSION

Over the past 20 years, several studies have addressed streamflow variability in South America, documenting a spatially and temporally heterogeneous pattern [*Marengo*, 1995, 2009; *Compagnucci and Vargas*, 1998; *Robertson and Mechoso*, 1998; *García and Vargas*, 1998; *Genta et al.*, 1998; *Compagnucci et al.*, 2000; *Piovano et al.*, 2002; *Callede et al.*, 2004; *Labat et al.*, 2004; *García and Mechoso*, 2005; *Pasquini and Depetris*, 2007]. *Marengo* [1995] did not observe a clear trend

pattern in streamflow during the period between 1903 and 1992 in some of the largest river basins of tropical South America (in Peru, Brazil, Argentina, and Venezuela), and attributed long-term variations in the Amazon river to decadal and multi-decadal modes of climate variability [*Marengo*, 2009]. In the sub- and extra-tropics, both *Genta et al.* [1998] and *Robertson and Mechoso* [1998] found relatively low mean discharge values until 1940 and increased values after 1970 for the main drainage basins in southeastern South America (SESA). Increased discharge after 1970 was also reported by *García and Mechoso* [2005], associated with rapid changes in the mean values between 1970 and 1972 in the largest drainage basins of South America. These trends had been previously observed in the Rio de La Plata by *García and Vargas*, [1998]. Similar results were also found for rivers in the Cuyo region in the Argentine Andes between 30°and 40°S [e.g., *Compagnucci et al.*, 2000] suggesting a change from decreasing to increasing discharge trends around 1977. An increase in the water level of the Laguna Mar Chiquita, a saline lake located in the Pampean plains of central Argentina (30.5°S, 62.7°W), was also observed starting in 1972, documenting a change towards wetter conditions [*Piovano et al.*, 2002]. *Pasquini and Depetris* [2007] analyzed trends based on the monthly mean discharge time series of Andean rivers between 15 and 50°S, including the Rio Bermejo, which was also considered in our study for approximately the same period. Pasquini and Depetris [2007] documented a shift from a decreasing to an increasing trend in ~1950.

One of the most prominent results of the above studies is a discharge trend change during the 1970s [*García and Vargas*, 1998; *Genta et al.*, 1998; *Robertson and Mechoso*, 1998; *Compagnucci et al.*, 2000; *García and Mechoso*, 2005]. This finding is in agreement with our analysis, which showed a rapid change in the Southern Central Andes during 1971-1977 (Figure 4.2 and Figure A2.10). We documented a long-term increasing trend at all percentiles of daily discharge; this change was most pronounced for the uppermost percentiles (>70th, Figure 4.3a). This implies that the upper end of the discharge frequency distribution became heavier during 1940-1999 and suggests a general intensification of the hydrologic cycle.

The change point documented in the river discharge is statistically significant, temporally coherent, and documented at every percentile value and time scale (annual and seasonal) from 1971 to 1977 (Figure 4.3). This finding is also confirmed by the number of events exceeding the annual 90th percentile of normalized daily discharge ($\mathrm{P90NQ}_{\mathrm{d}}^{\mathrm{ANN}}$) and the fraction of total discharge accounted for by the 10 largest discharge events. Both exhibit a statistically significant change point towards higher values during 1971-1972 (Figure A2.9). This result is not only revealed by the multi-station mean, but also supported by single-station analysis (Text S4), confirming that a rapid change towards higher discharge occurred during the period 1971-1977.

We noted that the identified change point precedes the 1976-77 climate shift (Figure 4.2). Previous studies suggested that the duration of the SAMS changed during 1971-1972 and impacted the annual flow in the Parana River [*Carvalho et al.*, 2011]. Given the change point uncertainty of seven years, we could not distinguish the drivers of the hydrologic changes, but our analysis supports the timing of the 1976-77 climate shift affecting South America [*Agosta and Compagnucci*, 2008; *Kayano et al.*, 2009; *Carvalho et al.*, 2011; *Jacques-Coper and Garreaud*, 2015]. Importantly, our analysis clearly reveals a coeval intensification of the hydrologic cycle during 1971-1977.

To further investigate the link between the 1976-77 climate shift and discharge variability in the Southern Central Andes, we applied linear and quantile regression analyses to the multi-station mean time series for the periods before (1952-1966), across (1967-1981), and after (1982-1996) the change point. For the normalized annual discharge anomaly (NAQ_y^{ANN}), we observed mostly non-significant trends for the periods before and after the change point, whereas for the period across the change point (1967-1981), we documented statistically significant increasing trends (Table A2.8). Quantile regression showed a temporally coherent trend pattern with statistically significant positive (negative) trends across (after) the change point for all considered percentiles, with non-significant trends before the change point (Figure 4.3). Quantile regression of the single-station analysis suggested similar timing and therefore emphasized the coherent spatial pattern of this trend reversal across and after the change point (Table A2.8). This observation suggests that (normalized) mean discharge is not an adequate metric for deriving trends for these distributions over the considered time period; because of this we relied on quantile regression instead.

A potential explanation for the trend reversal across and after the 1971-1977 change point (from positive to negative) is attributable to large-scale climate oscillations. Several studies have addressed the link between discharge in major South American rivers and large-scale modes of variability, often linking discharge in tropical as well as subtropical South American rivers to ENSO cycles [*Marengo*, 1995; *Robertson and Mechoso*, 1998; *Compagnucci et al.*, 2000; *Pasquini and Depetris*, 2007; *Bookhagen and Strecker*, 2011]. Additional factors include solar activity [*Compagnucci et al.*, 2014; *Antico and Torres*, 2015] and Pacific Decadal Oscillation phase transitions [*Marengo*, 2004; *Jacques-Coper and Garreaud*, 2015], which is also interpreted as a possible controlling factor of the climate shift in extra-tropical South America [*Jacques-Coper and Garreaud*, 2015].

Our quantile regression analysis documented that the uppermost percentiles of normalized daily discharge presented the most pronounced trends, independent of the considered period (Figure 4.3). In a previous study analyzing rainfall-trend patterns in the Southern Central Andes for the period 1950-2014, *Castino et al.* [2017] documented significant trends for the uppermost percentile of daily rainfall, which were particularly pronounced in the wet season (DJF), whereas the median values

showed low or no significant trends. Interestingly, the frequency of events exceeding high percentiles did not show any statistically significant trends. These results were interpreted to be indicative of significant changes, particularly in the magnitude of rainstorms affecting the Southern Central Andes. Furthermore, two main results that are relevant for our analysis were shown [*Castino et al.*, 2017].

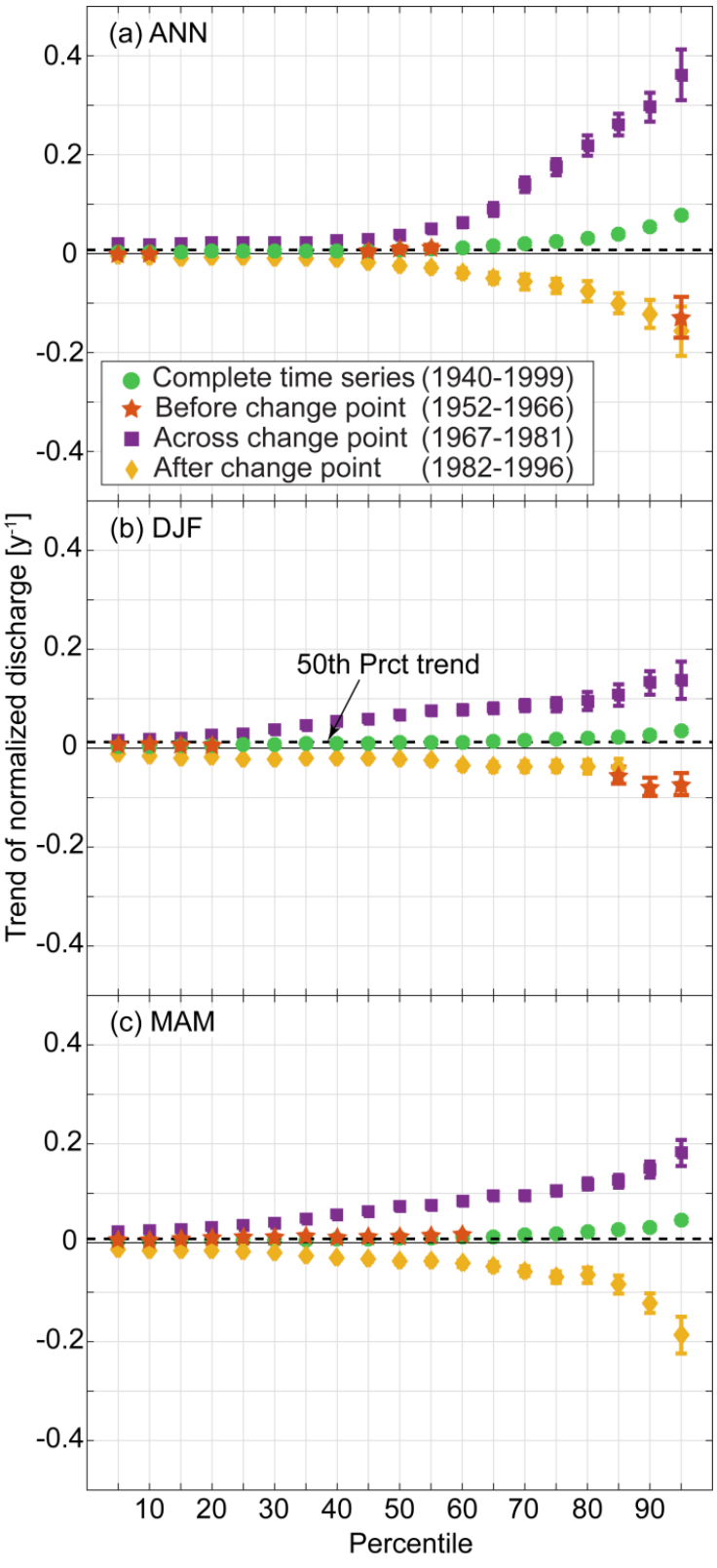

Figure 4.3 Discharge trends (±1 standard error, [*Evans*, 1942]) in the normalized daily discharge Q_d^{season} for different percentiles of the frequency distribution of the multi-station mean time series on (a) annual and (b-c) seasonal scales for the period 1940-1999, obtained through quantile regression. Trend values for the complete time series (green circles) and the periods before (1952-1966, red stars), across (1967-1981, purple squares), and after (1982-1996, yellow diamonds) the change point are shown. Absolute percentile trend magnitudes strongly dependent on the timescale of normalization: The values of the 50th percentile used for the seasonal scale (DJF and MAM) are approximately 2-3 times larger than those used for the annual scale.

Firstly, a pronounced increase in total rainfall amount during the period 1950-2014 confirmed the intensification of the hydrological cycle during this period. Secondly, a rainfall trend reversal towards decreasing rainfall amounts in the topographic transition zone between the low (<0.5km) and the intermediate (0.5 - 3 km) elevations to the west was observed after 1979. The drainage basins considered here are located at this topographic transition zone, and river-discharge analysis shows a similar trend reversal. The rainfall trend analysis did not reveal a spatiotemporally coherent change [*Castino et al.*, 2017], in contrast to the river-discharge trend during 1971-1977 presented in this study. We attribute this limitation to the high spatiotemporal stochasticity and intermittency of rainfall-related processes, associated with sparse and disparately distributed rainfall stations. The rainfall network therefore does not fully capture the small spatiotemporal scale of convective cells that partially control the rainfall pattern at the topographic transition zone at intermediate elevations during the wet season [*Romatschke and Houze*, 2010; *Rasmussen and Houze*, 2011; *Rohrmann et al.*, 2014]. In other words, the rainfall network does not capture the storm distribution, whereas the hydrologic stations do. In this context, it is conceivable that, despite the fact that the trend reversal is also observed in the rainfall pattern [*Castino et al.*, 2017], the timing and magnitude of the 1971-1977 change point are not properly detected by rainfall time series analysis (Figure A2.13, Text A2.5).

To provide a quantitative evaluation of the changes in water volumes across the change point, we used the upper Rio Bermejo catchment (the largest catchment with a discharge for the reference period 1970-1999: $13 \cdot 10^9$ m^3 y^{-1}, Table A2.2 and Figure A2.1) as an example. The mean annual discharge for this drainage basin increased by 40% (confidence interval 95%: ± 15%) across the change point, corresponding to an increase of $5.2 \pm 2.0 \cdot 10^9$ m^3 y^{-1} in seven years (1971-1977). A considerable fraction of this increase in water volume derived from the 10 largest events per year. During the ten years prior to the change point (1961-1970), these events contributed 12% of the total discharge on average, whereas after the change point (1978-1987), the mean annual contribution increased to 25% of the total, confirming that the uppermost percentiles underwent a pronounced increase. Since river discharge has a direct control on sediment transport capacity, a pronounced increase in discharge has a prominent impact on erosional hillslope processes, as well as on the remobilization of transiently stored coarse river sediments. Over the last decade, field observations in NW Argentina have shown that the downstream areas at elevations between 500-1000 m have been affected by aggradation processes [*Marcato et al.*, 2009; *COBINABE*, 2010]. We hypothesize that the increase in discharge in the intermediate elevation zone has resulted in increased sediment transfer, which ultimately caused aggradation in lower-lying areas, as the fluvial system was overwhelmed by the sustained influx of coarse sediment, causing

infrastructural damage and the loss of agricultural land [*Rivelli*, 1999; *Cencetti and Rivelli*, 2011; *Marcato et al.*, 2012].

4.5 CONCLUSIONS

We analyzed the dynamical evolution and the trends of river discharge in the Southern Central Andes during 1940-1999. We used a daily multi-station mean time series obtained by stacking eight river-discharge time series from catchments (10^2-10^4 km^2) located on the eastern flank of the Southern Central Andes along a steep topographic and climatic gradient. We estimated different indices on annual and seasonal scales, focusing our analysis on the wet season (DJF and MAM), and applied a two-tiered approach of standard and quantile regressions followed by change-point analysis to evaluate runoff trends between 1940 and 1999. We obtained two key results: First, quantile regression analysis revealed a spatially coherent and statistically significant positive increase in discharge for the period 1940-1999, with higher trends for the uppermost percentiles, suggesting an intensification of the hydrological cycle in this area; second, change-point analysis presented a rapid increase in discharge during the period 1971-1977, most likely linked to the 1976-1977 climate shift. We also observed positive (negative) trends across (after) the change point at most percentiles of daily discharge in every season. Our study provides evidence to support a link between hydro-meteorological drivers and sediment transport processes in semi-arid mountain environments. The decadal-scale increase in discharge at the higher percentiles has resulted in massive sediment transport, which continues to affect downstream infrastructure and agricultural areas.

ACKNOWLEDGEMENTS

Our study was supported by the Leibniz Fund of the German Science foundation (DFG) to M.S. (STR373/19-1) and the German Federal Ministry of Education and Research project PROGRESS (Climate Change, Georisk and Sustainability initiative at Potsdam University) to M.S. and B.B. The authors thank the Subsecretaría de Recursos Hídricos (BDHI), Argentina, for providing rain-gauge and discharge time series. We thank in particular D. Cielak (BDHI), Ricardo N. Alonso (UN Salta), Arturo Villanueva (UN Tucumán), and E. Marigliano (EVARSA, Argentina) for their valuable support during this study. We also thank two anonymous reviewers for their valuable comments.

APPENDIX A2

The supporting information of this chapter is available in the attached CD.

CHAPTER 5

OSCILLATIONS AND TRENDS OF RIVER DISCHARGE IN THE SOUTHERN CENTRAL ANDES AND THE LINK WITH MODES OF CLIMATE VARIABILITY

ABSTRACT

This study analyzed the discharge variability of small to medium drainage basins (10^2-10^4 km^2) in the southern Central Andes of NW Argentina. I applied the Hilbert-Huang Transform (HHT) to evaluate non-stationary and non-linear oscillatory modes of variability and trends, based on four time series of monthly normalized discharge anomaly between 1940 and 2015. I document statistically significant trends of increasing discharge during the past decades, documenting an intensification of the hydrological cycle during this period. An Ensemble Empirical Mode Decomposition (EEMD) analysis revealed that discharge variability in this region can be described by five quasi-periodic statistically significant oscillatory modes, with mean periods varying from 1 to ~20y. Furthermore, I show that discharge variability is most likely linked to phase of the Pacific Decadal Oscillation (PDO) at multi-decadal timescale (~20y) and, to a lesser degree, to Tropical South Atlantic SST anomaly (TSA) variability at shorter timescales (~2–5y). Previous studies highlighted a discharge change point in the southern Central Andes from 1971 and 1977, inferred to have been associated with the 1976-77 climate shift. These new results introduce important additional constraints to this phenomenon, which suggest that the discharge change point coincides with a long-term increasing trend and the periodic enhancement of discharge linked to PDO phase and TSA variability.

5.1 INTRODUCTION

In a recent study on river discharge variability in the southern Central Andes of NW Argentina during the time interval between 1940 and 1999, a rapid change towards increasing discharge amounts was observed between 1971 and 1977. This change involved up to a 40% increase of annual mean discharge within 7 years (Chapter 4). This is comparable to other investigations that have revealed a rapid increase in mean river discharge in large South American rivers (i.e., the Amazon, Negro, Orinoco, La Plata, Paraná, Paraguay) during the 1970s [García and Vargas, 1998; Genta et al., 1998; Robertson and Mechoso, 1998; Labat et al., 2004; Marengo, 2004; García and Mechoso, 2005; Pasquini and Depetris, 2010].

This step change in river discharge has been linked to the 1976-77 global climate shift that strongly impacted South American climate [e.g., *Graham*, 1994; *Miller et al.*, 1994; *Kayano et al.*, 2009; *Carvalho et al.*, 2011; *Jacques-Coper and Garreaud*, 2015]. Associated with this rapid change, a trend reversal in river discharge was also observed with increasing (decreasing) values across (after) the change point, documenting the pronounced temporal variability of run-off in this region.

Although few previous studies addressed the possible causes of spatiotemporal rainfall and river-discharge variability in South America, the physical processes that drive changes in the hydrologic system have remained unclear [e.g., *Robertson and Mechoso*, 1998; *Marengo*, 2004; *García and Mechoso*, 2005; *Antico and Kröhling*, 2011; *Antico and Torres*, 2015]. The drivers for hydro-meteorological change in mountainous catchments are complex, resulting in a pronounced non-stationary and non-linear character [e.g., *Compagnucci et al.*, 2000; *Khaliq et al.*, 2006; *Nourani et al.*, 2009]. Most studies in the Andean realm suggest that the El Niño Southern Oscillation (ENSO) exerts a first-order control on run-off in major tropical and extra-tropical South American river basins, whereas other investigations document links between river discharge and the Pacific Decadal Oscillation (PDO) [*Marengo*, 2004] and/or the activity of the South Atlantic Convergent Zone (SACZ). Importantly, these studies analyze discharge variability for large catchments, such as the Amazon or La Plata river basins, which contain large floodplains resulting in lag times that dampen discharge trends [*Dunne and Mertes*, 2007; *Melack et al.*, 2009].

In light of these issues I focused on three main points in my investigation: First, I identified magnitude and frequency of modes of oscillation at different timescales that may explain river-discharge variability; second, I documented long-term discharge trends; third, I strived to document linkages with large-scale modes of climate variability that might affect river discharge in southern Central Andes between 1940 and 2015. I used an innovative analysis combining the Ensemble Empirical Mode Decomposition (EEMD) [*Huang et al.*, 1998; *Huang and Wu*, 2009] and the Time-Dependent Intrinsic Correlation (TDIC) [*Chen et al.*, 2010]. These methods are

adaptive and are based on intrinsic information derived from the data; this approach is particularly appropriate for analyzing non-stationary geophysical time series that result from non-linear natural processes, providing not only the statistically significant intrinsic oscillatory modes that constitute the original time series, but also a statistically significant trend [*Wu et al.*, 2007].

I relied on four time series of daily normalized discharge anomaly from 1940 to 2015 obtained from small to medium montane drainage basins (10^2-10^4 km^2) in the Eastern Cordillera of the Andes of NW Argentina (Figure 5.1). Importantly, discharge from these catchments sizes is particularly sensitive to climate variability, because floodplain reservoirs either do not exist or they are very small compared to the more extensive drainage basins of the Amazon and La Plata rivers.

The catchments are characterized by different climatic conditions ranging from predominantly humid to semi-arid environments (Table 5.1). For a detailed description of the geographic and climatic setting of the study area, I refer the reader to chapter 2 of the thesis.

In addition, to test for a possible link between river discharge and large-scale climate forcing, I considered the monthly time series of four regional and global climate indices (Table 5.2).

Finally, after performing EEMD analysis, I identified the statistically significant intrinsic modes functions (IMFs) for discharge and the climate indices. Next, for each pair of statistically significant IMFs of discharge and each climate index relevant to the same timescale, I estimated the TDIC. The resulting values of TDIC were used to decipher possible linkages between river-discharge variations in the southern Central Andes and large-scale climate modes of variability. As a final outcome, I estimated the magnitude of the intrinsic trend for the time interval between 1940 and 2015 and compared it with analogous findings from previous studies.

Code	Basin	Station	Time series start	Time series end	Length [y]	Area [km^2]	Mean annual rainfall [mm]	Elevation range [m]
JU0016	San Francisco	Caimancito	19470901	20150831	68	22136	630	350-5900
SA0629	Pescado	Cuatro Cedros	19560901	20150831	59	1972	1440	480-4530
SA0604	Bermejo	Aguas Blancas	19440901	20150831	71	4885	1280	400-5030
SA0693	Bermejo	Pozo Parmiento	19400901	20150831	75	23782	1080	300-5100

Table 5.1 Hydrological stations and station metadata. Legend: Time series start/end: YYYYMMDD; Length: Time-series length [years]; Area = area of the drainage basin at the station location [km^2]; basin-wide mean annual rainfall derived from TRMM2B31 [*Bookhagen and Strecker*, 2008]; Minimum and maximum elevation values of each basin derived from SRTM data.

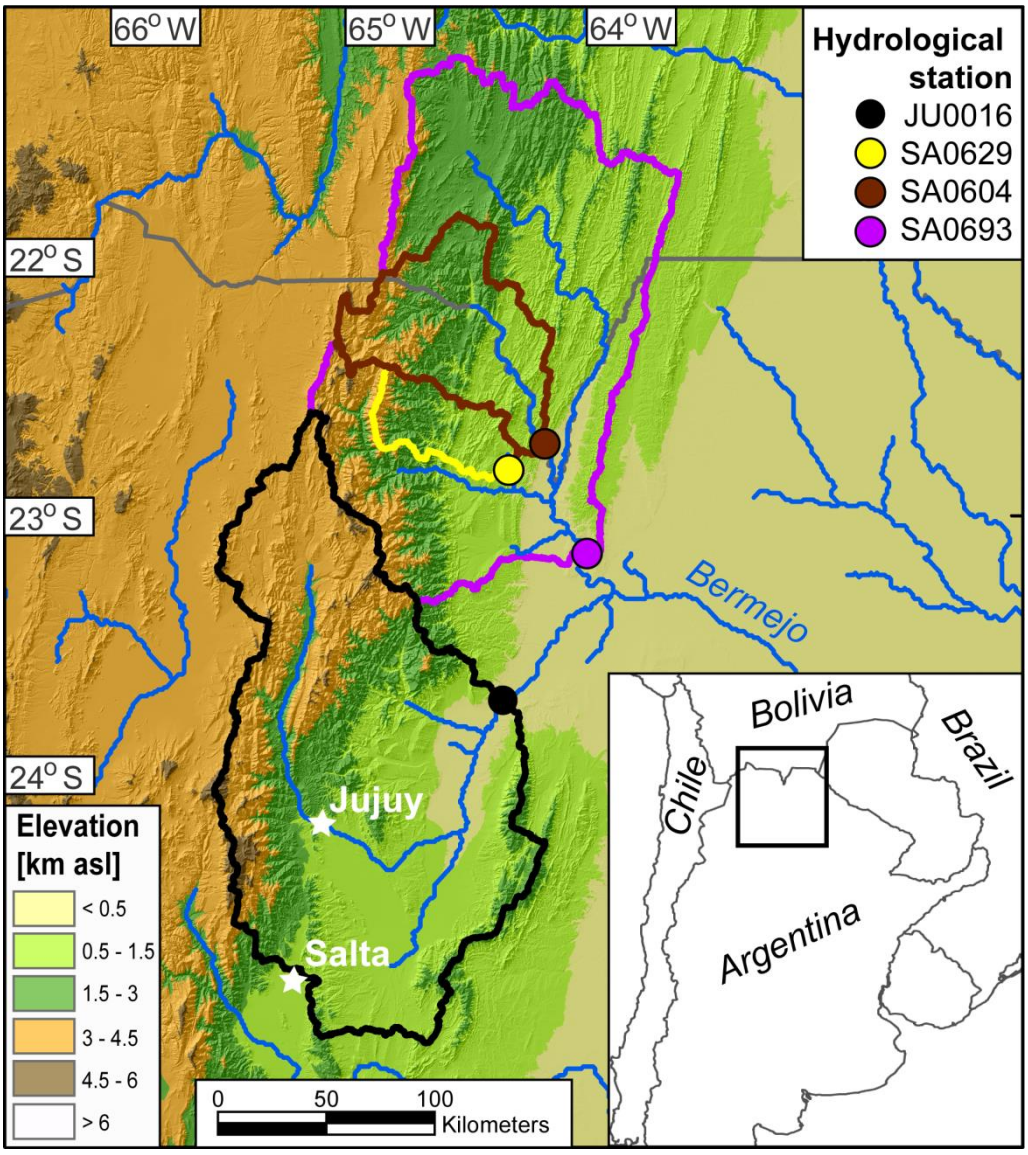

Figure 5.1 Digital elevation model of the study area with principal drainages; polygons represent the catchment areas at the station location and circles denote the four analyzed hydrological stations in the provinces of Jujuy and Salta. The white stars indicate the location of the cities of Jujuy and Salta. The grey lines indicate international boundaries. The black rectangle in the inset represents the study area in the Eastern Cordillera of the southern Central Andes of Argentina.

5.2 Data and methods

5.2.1 Data

Four time series of daily discharge were available for different time intervals starting from 1940 (Table 5.1). I analyzed two time intervals: (1) From September 1940 to August 2015 (75y) with one time series from the upper Rio Bermejo (Pozo Sarmiento, SA0693); (2) From September 1956 to August 2015 (59y) with four time series: two from the upper Rio Bermejo at Pozo Sarmiento and at Aguas Blancas (SA0604), one from a tributary of the upper Rio Bermejo (Rio Pescado at Cuatro

Cedros, SA0629), and one from a tributary of the Rio Bermejo (Rio San Francisco at Caimancito, JU0016) (Table 5.1).

I also considered four climate indices as proxies for large-scale coupled atmospheric-oceanic conditions: (1) the El-Niño Southern Oscillation BEST index (ENSO-BEST, combining Nino 3.4 SST and the Southern Oscillation Index [*Smith and Sardeshmukh*, 2000]); (2) the Tropical Southern Atlantic sea-surface temperature (SST) anomaly (TSA, SST anomaly is calculated in the box 30°W - 10°E, 20°S - 0° [*Enfield and Mestas-Nunez*, 1999]); (3) the SunSpot Number index (SSN, [*Clette et al.*, 2014]); and (4) the Pacific decadal Oscillation index (PDO, the leading EOF of mean November through March SST anomalies for the Pacific Ocean to the north of 20°N [*Mantua and Hare*, 2002]). All climate indices except TSA are available for the time interval between 1940 and 2015; the use of the TSA index was limited to the time interval between 1956 and 2015 (Table 5.2). All time series available for the time interval between 1940 and 2015 (normalized discharge anomaly and climate indices) are shown in Figure 5.2 (see Appendix A3 for the time series relevant to the time interval between 1956 and 2015, Figure A3.1).

5.2.2 DATA PREPARATION

First, the daily observations of discharge were converted into mean monthly discharge values. Short data gaps in the time series of mean monthly discharge (at most 10% of data were missing) were filled using synthetic values obtained by standard linear regression with the time series of the neighboring station with the highest correlation coefficient [*World Meteorological Organization*, 2011].

The monthly discharge time series were filtered by subtracting the long-term mean monthly values over the entire time-series length and by dividing the resulting monthly anomaly by the long-term monthly standard deviation, to attenuate the annual cycle, which is mainly controlled by the South American Monsoon System (SAMS; see chapter 2, section 2.3, for a general description of SAMS). Below, I will refer to the filtered time series of discharge as *the time series of normalized discharge anomaly* (Table 5.2).

	Time interval 1940-2015	Time interval 1956-2015
Discharge time series	SA0693	SA0693, SA0604, SA0629, and JU0016
Climate indices	ENSO, SSN, and PDO	ENSO, TSA, SSN, and PDO

Table 5.2 Time series for both normalized discharge anomaly and climate indices for the two considered time intervals between September 1940 and August 2015 (Figure 5.2) and between September 1956 and August 2015 (Figure A3.1).

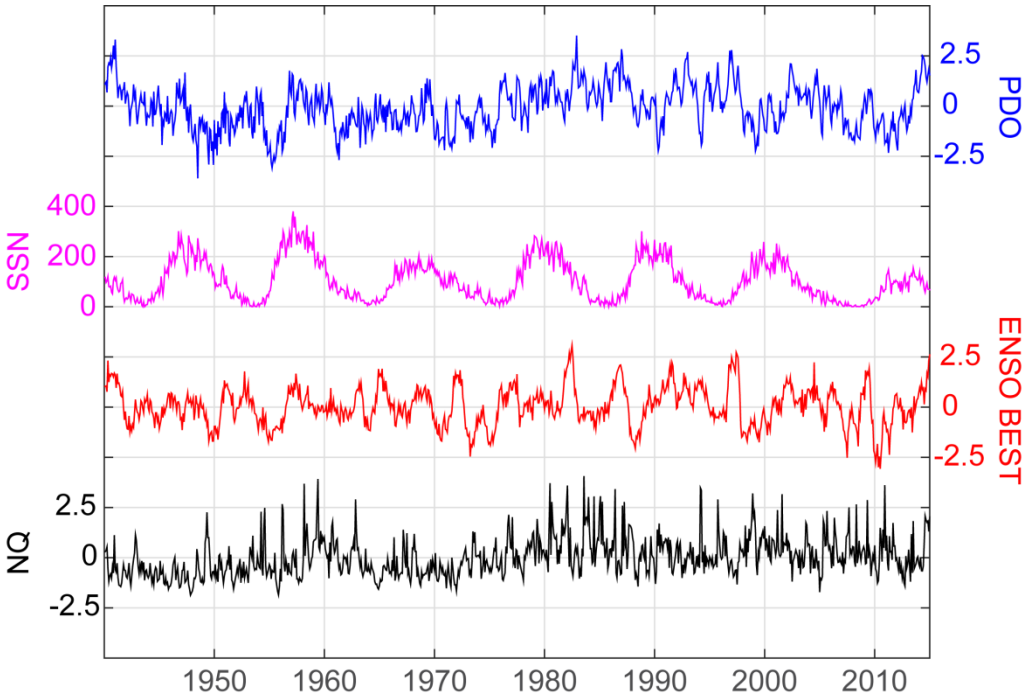

Figure 5.2 Time series of the normalized discharge anomaly (NQ, SA0693, black), El-Niño Southern Oscillation BEST index (ENSO BEST, red), SunSpot Number index (SSN, magenta), and the Pacific decadal Oscillation index (PDO, blue) for the time interval between 1940 and 2015.

5.2.3 METHODS

The time series (normalized discharge anomaly and climate indices) were decomposed using the Ensemble Empirical Mode Decomposition (EEMD, [*Wu et al.*, 2004; *Wu and Huang*, 2009]), which is an enhanced Empirical Mode Decomposition [*Huang et al.*, 1998]. Subsequently, the link between normalized discharge and climate indices was analyzed using the Time-Dependent Intrinsic Correlation [*Chen et al.*, 2010].

The Empirical Mode Decomposition (EMD)

The EMD is based on the assumption that a time series results from different intrinsic modes of oscillations, whose energy can be associated with different timescales.

Each of these oscillatory modes is represented by an intrinsic mode function (IMF) constrained by the following conditions: (1) in the entire time series, the number of extrema and the number of zero-crossings must either be equal or differ by, at most, one; and (2) at any point, the mean value of the envelope defined by the local maxima and the envelope defined by the local minima is zero [*Huang et al.*, 1998]. The IMFs represent an *a-posteriori*-defined basis, which is intrinsically non-linear and non-stationary in amplitude and frequency.

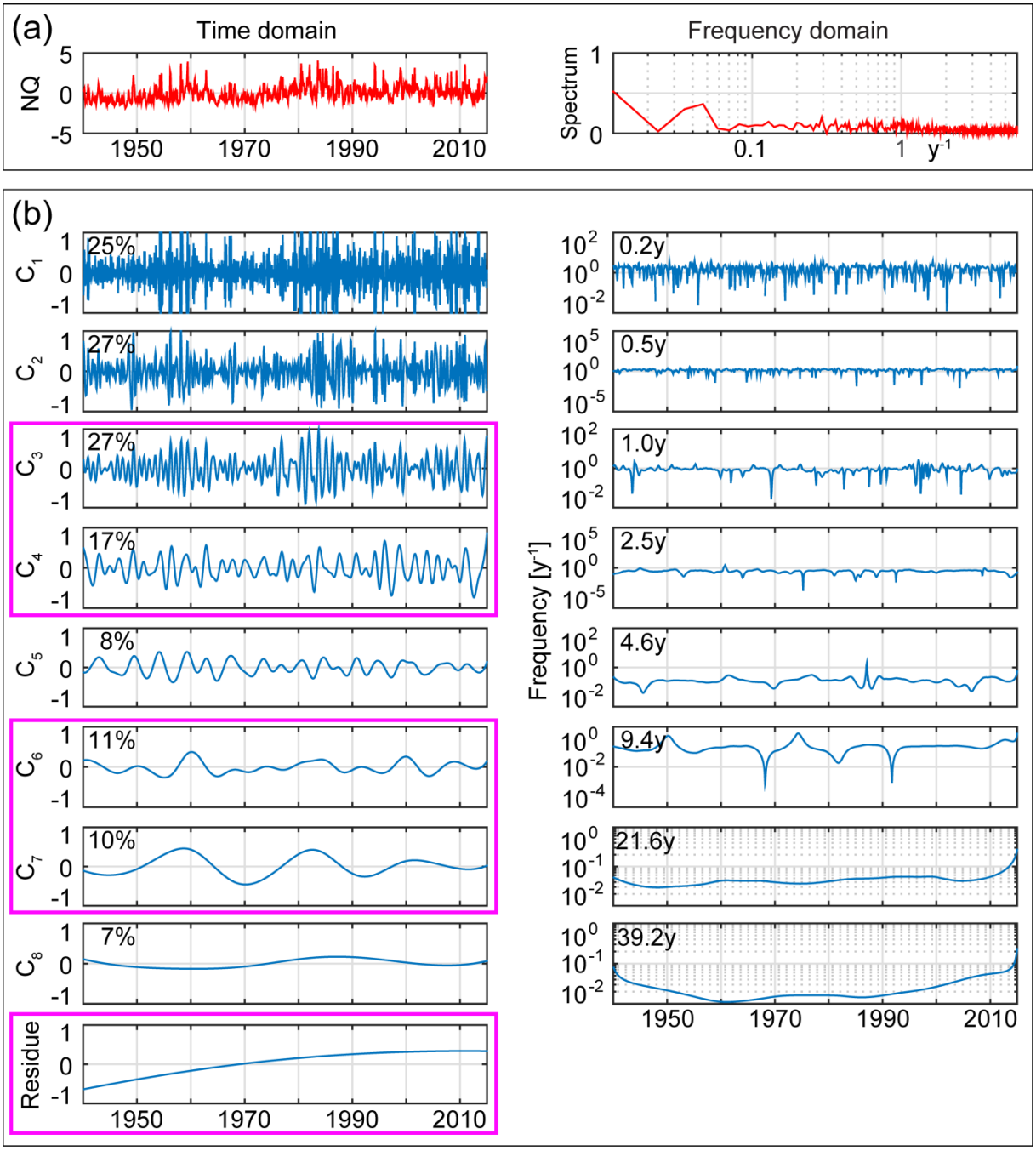

Figure 5.3 (a) Monthly normalized discharge anomaly for hydrological station SA0693 (left) and the amplitude of its Fourier spectrum [s^{-1}] (right). Magenta rectangles indicate statistically significant IMFs (c.f., Figure 5.4); (b) IMFs obtained applying the EEMD method to the monthly normalized discharge anomaly (left). Eight IMFs and one residue have been obtained. Percentage represents the explained variance for each IMF. Since the IMFs obtained by EEMD do not constitute a basis of non-independent elements, the sum of all IMF explained variances can be higher than 100%. The right panel shows the instantaneous frequency of each IMF obtained by HSA; mean period $\overline{T}$ for the whole time series (1940-2015) is also reported.

This is in contrast with standard spectral decomposition generating *a-priori* harmonic functions with constant amplitude and frequency. The IMF are generated from an arbitrary time series x(t) through a technique known as the 'sifting process', which can be summarized as follows:

1. all local extrema of x(t) are identified; subsequently all local maxima are connected by a cubic spline to form the upper envelope; the same is done for all local minima to form the lower envelope. The upper and lower envelopes encompass all data between them. The mean of these two envelopes is a function of time and designated as $m_1(t)$. The difference $h_1(t)$ between x(t) and the mean $m_1(t)$ is computed:

$$h_1(t) = x(t) - m_1(t) \tag{5.1}$$

2. $h_1(t)$ represents the proto-IMF, but it potentially does not satisfy the building constraints (new extrema may be generated due to changing the local zero from a rectangular to a curvilinear coordinate system [*Huang and Shen*, 2014]). Therefore, in the next step $h_1(t)$ is treated as it were the data:

$$h_{11}(t) = h_1(t) - m_{11}(t), \tag{5.2}$$

where $m_{11}(t)$ is the mean of the two envelopes generated from $h_1(t)$. The sifting process is repeated k times, until the number of zero crossings and extrema of $h_{1k}(t)$ function, defined as:

$$h_{1k}(t) = h_{1(k-1)}(t) - m_{1k}(t) \tag{5.3}$$

satisfy the following two conditions: (1) are equal or, at most, differ by one; (2) stay the same S consecutive times. Here, a critical decision must be made: the stoppage criterion, i.e. the value of S. For a review of the different criteria historically used for determining S, I refer to the relevant literature [*Huang et al.*, 1998, 2003; *Huang and Shen*, 2014]; I point out that *Huang et al.*, [2003] suggested S-values between 4 and 8 for optimal siftings. After defining the stoppage criterion, the first IMF is designated at k iteration $h_{1k}(t)$ of the x(t) time series:

$$C_1(t) = h_{1k}(t) \tag{5.4}$$

corresponding to the finest timescale or shortest period component of the time series.

3. The residue $r_1(t)$:

$$r_1(t) = x(t) - C_1(t) \tag{5.5}$$

still potentially contains longer period variations. Therefore, $r_1(t)$ is treated as the new time series and the steps from 1 to 3 are repeated n times until the

final $r_n(t)$ residue either is smaller than an *a priori*-fixed threshold or becomes a monotonic function from which no more IMFs can be extracted.

Once the EMD procedure is terminated, the x(t) time series can be represented as the sum of all IMFs and the final residue:

$$x(t) = C_1(t) + C_2(t) + \dots + C_n(t) + r_n(t) \quad (5.6)$$

The residue is commonly interpreted as the long timescale trend [*Wu et al.*, 2007].

One recognized limitation of EMD is the mode-mixing problem, arising when a clear spectral separation of the modes is not attained [*Huang et al.*, 1999, 2003]. The causes of mode mixing are related to signal intermittency, generating not only aliasing in the time-frequency distribution, but also rendering the physical meaning of individual IMF ambiguous. To overcome this limitation, the Ensemble Empirical Mode Decomposition (EEMD) was introduced, defining the final IMF components of the x(t) time series as the mean of an ensemble of IMFs obtained by N trials, constituted by adding white noise of fixed amplitude to the x(t) time series [*Wu and Huang*, 2009]. It is widely accepted that EEMD largely overcomes the mode-mixing problem, improving greatly the consistency of the decompositions of slightly different pairs of datasets [*Zhang et al.*, 2010; *Wang et al.*, 2012].

It is important to mention that, although these advances have resulted in satisfying the requirements of most practical applications, a rigorous mathematical foundation of the EMD technique, necessary for making the empirical approach more robust, is not available yet. Although much effort has been devoted to improving its mathematical foundation, the implementation of EMD is still empirical and *ad hoc [Wang et al., 2010]*. However, since its introduction, EMD has been used in a wide range of applications, providing particularly useful insights in climate and atmospheric studies [*Wu et al.*, 2007, 2008; *Chang et al.*, 2011; *Franzke*, 2012; *Massei and Fournier*, 2012; *Wilcox et al.*, 2013; *Antico and Torres*, 2015].

Here, I applied the EEMD for each time series (normalized discharge and climate indices) using equally populated ensembles of 200 members and a white-noise amplitude equal to 0.5.

Hilbert spectral analysis (HSA)

In addition, the Hilbert spectral analysis (HSA), was applied to each IMF mode to characterize the time-frequency distribution of the IMF mode, extracting the local frequency information [*Huang et al.*, 1998; *Huang and Wu*, 2009]. With this method, the analytical signal $\acute{C}(t)$ can be described using the Hilbert transform,

$$\bar{C}(t) = C(t) + j\frac{1}{\pi}P\int_{-\infty}^{+\infty}\frac{C(t')}{t-t'}dt' , \tag{5.7}$$

where P is the Cauchy-principle value [*Huang et al.*, 1998]. Eq. 5.7 can be expressed also using the complex-valued analytic formulation, as:

$$\bar{C}(t) = A(t)e^{j\theta(t)} \tag{5.8}$$

with $A(t) = |\bar{C}(t)|$ is the modulus and $\theta(t) = arctan\left(\frac{I(\bar{C}(t))}{R(\bar{C}(t))}\right)$ is the instantaneous phase function [*Huang et al.*, 1998; *Huang and Wu*, 2009]. From Eq. 5.8 the instantaneous frequency can be estimated as:

$$\omega(t) = \frac{1}{2\pi}\frac{d\theta(t)}{dt} \tag{5.9}$$

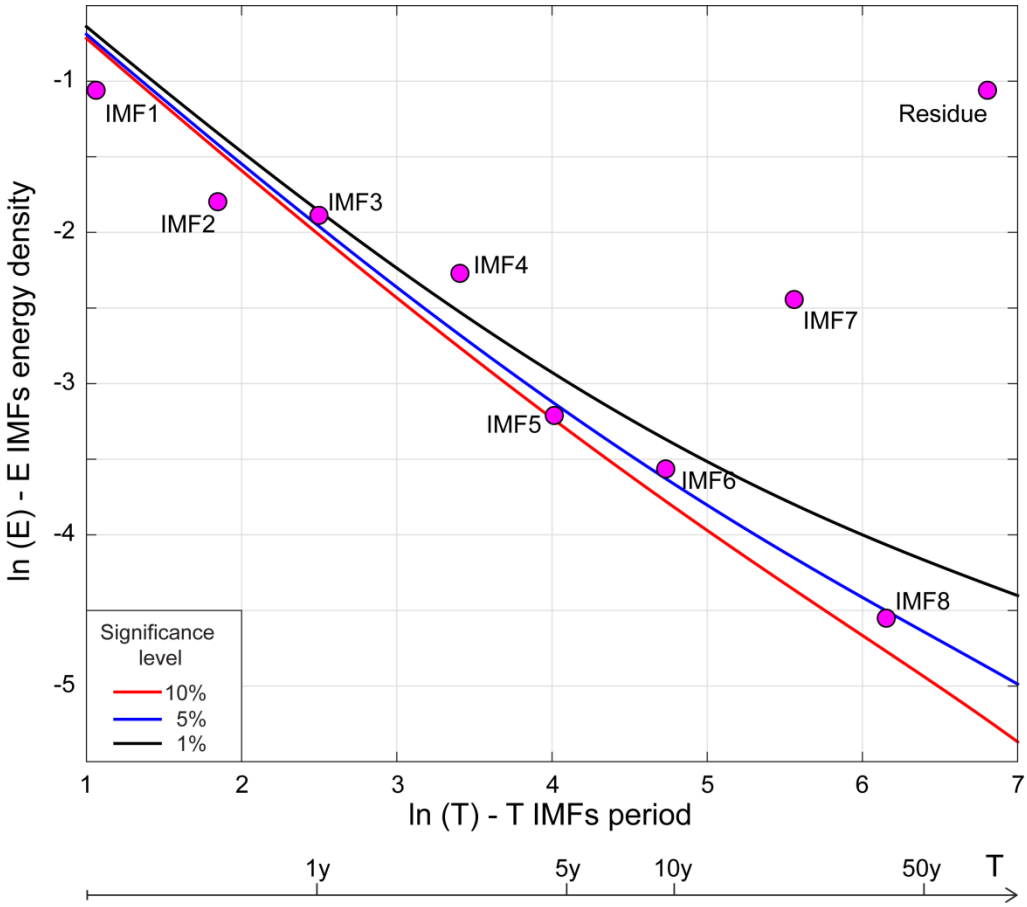

Figure 5.4 Statistical significance test results for the IMFs of the normalized discharge anomaly (Figure 5.3), based on the comparison between the energy density and spread functions obtained by white noise; lines correspond to the 90% (red), 95% (blue), and 99% (black) confidence interval superior extremes. Magenta circles represent energy density as a function of the mean period $\overline{T}$ for each IMF [*Wu et al.*, 2004]. Each value above the blue line indicates an IMF that is statistically different from white noise at the 5% level. IMF3 ($\overline{T}$ = 1y), IMF4 ($\overline{T}$ = 2.5y), IMF6 ($\overline{T}$ = 9.4y), IMF7 ($\overline{T}$ = 21.6y), and the residue result to be statistically significant.

The Hilbert method provides a viable estimation of the instantaneous frequency [*Huang et al.*, 2009], but alternative methods are also available, e.g., the direct quadrature and teager energy operator [*Huang et al.*, 2010, 2011]. The combination of the EMD and HSA is the Hilbert–Huang Transform [*Huang*, 2005]. In this study I applied the HHT Matlab™ provided by *Huang and Wu*, [2009], including the statistical significance test.

Statistical significance test

The EMD method provides a dyadic filter bank through numerical experiments on fractional Gaussian noise and white noise [*Flandrin et al.*, 2004; *Wu et al.*, 2004]. It has been also observed that the IMF components of pure white noise are normally distributed, their Fourier spectra are identical and the product of their energy density and the corresponding mean period are constant. These properties were used to develop the statistical significance test for IMFs obtained by EMD, to distinguish pure noise derived IMF components from IMF components with physically meaningful information [*Wu et al.*, 2004]. Once the significance level has been determined, the confidence intervals of the test are estimated applying EMD to Gaussian white noise in a Monte Carlo simulation, to generate the spread function of mean energy density as a function of the mean period for all IMFs components. Thus, an IMF component of a x(t) time series is statistically significant at the significance level, whenever its energy density lies outside the confidence interval obtained for pure white noise [*Wu et al.*, 2004]. In this study I applied the statistical significance test to determine whether the IMF components of the normalized discharge and the climate indices time series contain physically meaningful information at the 5% significance level.

The Time-Dependent Intrinsic Correlation (TDIC)

When applied to non-stationary time series, the classical, time-independent definition of the correlation may distort correlation information between the signals and provide an unphysical interpretation [*Hoover*, 2003; *Rodó and Rodríguez-Arias*, 2006; *Chen et al.*, 2010].

Alternatively and consistent with the non-stationarity of the time series, the correlation coefficient can be estimated using a sliding window or a scale-dependent correlation technique. The estimation of the correlation between time series may use window sizes defined by the local characteristic scale given by the data itself. Recently, *Chen et al.*, [2010] proposed to use the EMD to estimate an adaptive window to calculate the Time-Dependent Intrinsic Correlation (TDIC).

The TDIC of each pair of statistically significant IMFs is defined as:

$$R_{ij}(t_k^n|t_w^n) = Corr\left(C_{1,i}(t_w^n)C_{2,j}(t_w^n)\right) \quad (5.10)$$

at any t_k, where *Corr* is the correlation coefficient of two time series and t_w^n is the sliding window size, defined as follows:

$$t_w^n = [t_k - n\,t_d/2 : t_k + n\,t_d/2] \quad (5.11)$$

The minimum sliding window size for the local correlation estimation is chosen as $t_d = max\left(T_{1,i}(t_k), T_{2,j}(t_k)\right)$ where $T_{1,i}$ and $T_{2,j}$ are the instantaneous periods $T = \omega^{-1}$,and n is any positive real number [*Chen et al.*, 2010].

This method has been applied in several studies to characterize the relation between different time series [e.g., *Chen et al.*, 2010; *Huang and Schmitt*, 2014]. Here I used TDIC to evaluate correlations between normalized discharge and the climate indices.

5.3 RESULTS

The Hilbert-Huang Transform (HHT) analysis was applied to the normalized discharge anomaly and the climate indices for two time intervals: from 1940 to 2015, and from 1956 to 2015. In the following two sections, the results will be presented for each of these two time intervals. Each section firstly presents the results of EEMD analysis applied to the time series of the normalized discharge anomaly, including the results of the Hilbert spectral analysis. Subsequently, EEMD outcomes obtained from the climate indices are shown. Finally, time-independent Pearson correlation and time-dependent intrinsic correlation (TDIC) are shown for pairs combining both the entire time series and the IMFs of the normalized discharge anomaly and the climate indices.

		$\bar{T}$ [y]			
		NQ SA0693	ENSO BEST	SSN	PDO
Time series components	IMF1	-	-	-	-
	IMF2	-	-	-	0.6
	IMF3	1.0	1.3	-	1.1
	IMF4	2.5	3.0	-	2.6
	IMF5	-	6.1	-	5.2
	IMF6	9.4	10.9	11.2	11.3
	IMF7	21.6	25.9	-	25.7
	IMF8	-	-	-	-

Table 5.3 Summary of EEMD analysis for the normalized discharge anomaly NQ (hydrological station SA0693, Figure 5.1 and Table 5.1), ENSO-BEST, SSN, and PDO for the time interval 1940-2015. For each statistically significant IMF, the value of its mean period $\bar{T}$ [y] is indicated; no mean period values are indicated for non-significant IMFs.

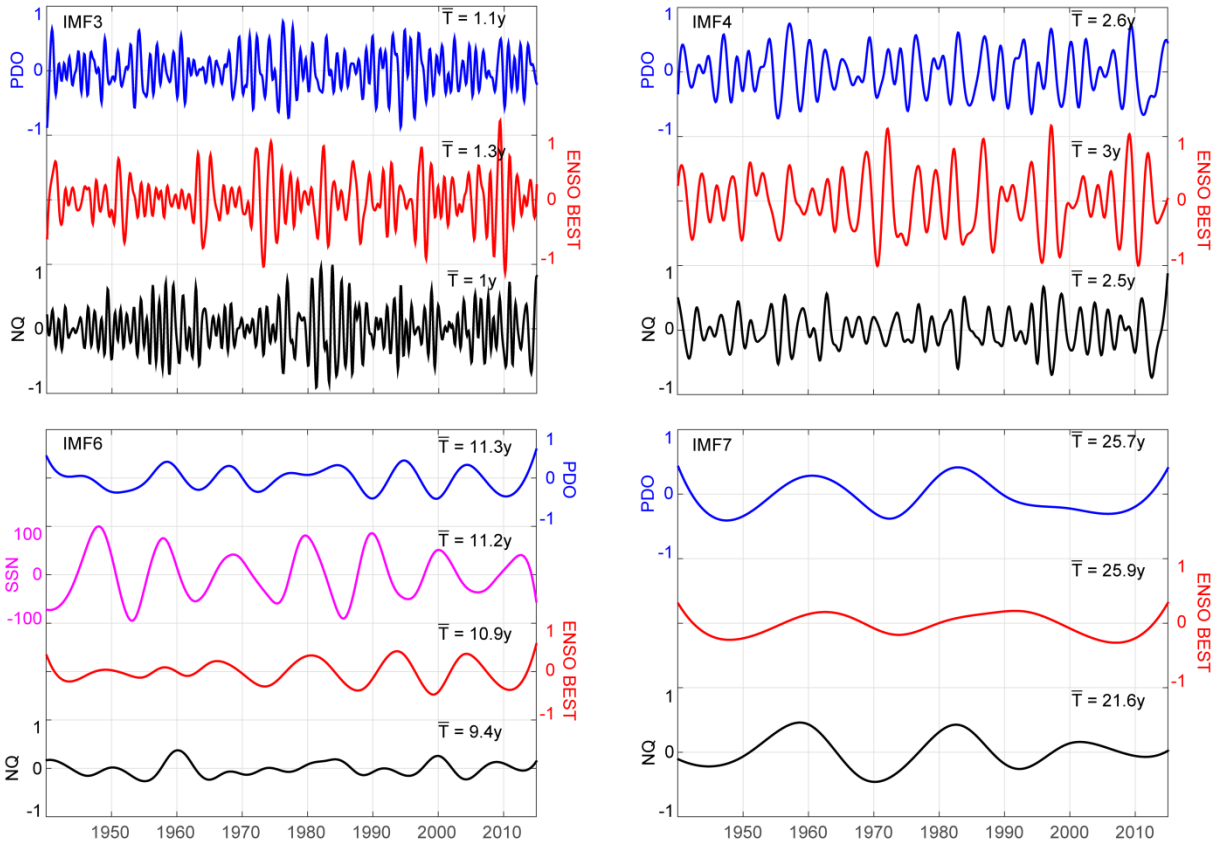

Figure 5.5 EEMD results for the time interval between 1940 and 2015. Shown are each statistically significant IMF of NQ (black) (Table 5.3) and statistically significant IMFs of the used climate indices (ENSO BEST: red, PDO: blue, and SSN: magenta). The mean period $\overline{T}$ of each IMF is also indicated.

5.3.1 Time interval from 1940 to 2015

Results for this time interval refer to station SA0693. EEMD resulted in eight IMFs and a residue (Figure 5.3), among which four IMFs (IMF3 ($\overline{T}$ = 1y), IMF4 ($\overline{T}$ = 2.5y), IMF6 ($\overline{T}$ = 9.4y), IMF7 ($\overline{T}$ = 21.6y)) and the residual (monotonic increasing) are statistically significant at the 5% level (Figure 5.4).

		ENSO BEST	SSN	PDO
NQ SA0693	Entire time series	-	-	0.086
	IMF3	0.111	-	-0.132
	IMF4	-0.176	-	-0.143
	IMF6	-0.186	-	-
	IMF7	0.178	-	0.639

Table 5.4 Time-independent Pearson correlation values between the normalized discharge anomaly (NQ) and the available climate indices for the time interval between 1940 and 2015, for the entire time series and each IMF match. Only statistically significant correlation values are shown ($p<0.05$).

I observed that most of the discharge-anomaly variance was explained by high-frequency modes of oscillation ($\overline{T} \leq 1$y), associated with the SAMS and intra-annual variability. The rest of the variance of NQ was explained by IMF4 (17%) and by IMF6 and IMF7 (11% and 10%, respectively). The instantaneous frequencies associated with the statistically significant IMFs were nearly constant and close to the mean frequency. Few localized oscillations around the mean value, whose duration did not exceed a few months, resulted in a local phase shift of the associated IMF (e.g., for IMF4 in 1975, Figure 5.3).

I observed that these oscillations were not synchronized for all IMFs. For example, for IMF4, the larger oscillation occurred during 1975, whereas for IMF6 two major oscillations of similar magnitude were observed in 1968 and 1992, respectively.

Importantly, I also observed that the amplitude of the oscillations of IMF3 of NQ strongly increased from the middle 1970s to the late 1990s (Figure 5.5); to a lesser degree, a similar behavior was observed from the early 1950s to the middle 1960s. These local increases of IMF3 appeared to be synchronous with one period of oscillation of IMF7, whereas the remaining IMFs did not exhibit similar changes (Figure 5.5).

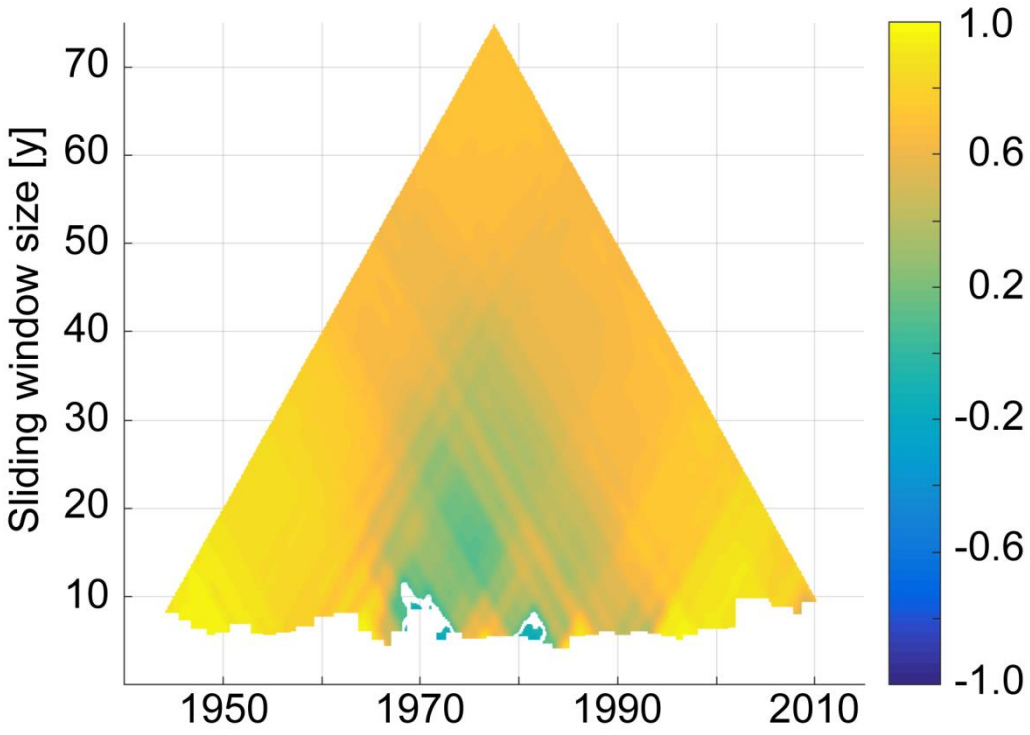

Figure 5.6 Time-Dependent Intrinsic Correlation (TDIC) analysis of the correlation of IMF4 between ENSO BEST (mean period $\overline{T}$ = 5.8y) and PDO (mean period $\overline{T}$ = 5.0y) for the time interval from 1940 to 2015. For each instant (i.e. month) for which the TDIC has to be estimated, the correlation between the two time series is calculated for different time-window sizes, defined by Eq. 5.11. The same procedure is applied for each instant of the time series and the time-dependent correlation is obtained. Except for the time interval between approximately 1970 and 1990, a strong positive correlation is found for most sliding window sizes.

Monthly time series of ENSO BEST, SSN, and PDO for this time interval were also analyzed using EEMD.

Table 5.3 and Figure 5.5 summarize the statistically significant IMFs with the relevant mean period for each index, including normalized discharge anomaly. I observed that the ENSO-BEST index was associated with five IMFs (IMF3-7), the SSN index with one IMF (IMF6), and the PDO index with six IMFs (IMF2-7). Individual results from EEMD, Hilbert spectral analysis, and statistical significance testing are documented in Appendix A3.

To evaluate possible links between the normalized discharge anomaly and the selected climate indices, I estimated the standard time-independent Pearson correlation (Table 5.4). Low correlation values were found (absolute values of correlation less than 0.2), except for the IMF7 match between the normalized discharge anomaly (mean period $\bar{T}$ = 21.6y) and PDO (mean period $\bar{T}$ = 25.7y) (0.639) (Table 5.3 and Table 5.4). In a second step, time-dependent intrinsic correlation (TDIC) analysis was applied; the results obtained for the IMF4 pair of ENSO BEST and PDO indices are shown in Figure 5.6. This example of the outcome of the TDIC documented generally high correlation values for any sliding window size, except for the time interval between the late 1960s and 1985 for sliding window sizes smaller than 40 years.

Figure 5.7 illustrates the TDIC results for the pairs of IMF4, IMF6, and IMF7 of the normalized discharge anomaly (statistically significant IMFs for the time series from the hydrological station SA0693) and the climate indices for the time interval between 1940 and 2015 (ENSO BEST, SSN, and PDO). The outcomes for IMF3 (mean period $\bar{T} \approx$ 1y) were relevant to the annual cycle and are mainly controlled by the SAMS.

For IMF4 (mean period $\bar{T}$ = 2.5y), until approximately 1980 the correlation between NQ and ENSO BEST showed a similar structure to that obtained by correlating NQ and PDO, with generally low correlation values (both positive and negative). After 1980, the ENSO BEST index continued to exhibit low correlation values with the normalized discharge anomaly, but the PDO index resulted highly anti-correlated with the normalized discharge anomaly (Figure 5.7). For short sliding window sizes (< 10y) I also observed short time intervals (≈ 5y long) at approximately 15y recurrence-time intervals for which a strong positive correlation was found until the early 1990s. This behavior was due to the fact that the frequencies of both IMF4 (e.g., of NQ and ENSO BEST) were nearly constant, with close, but different values, generating a quasi-periodic short time interval during which the two IMF4 were locally in phase (i.e., strongly correlated).

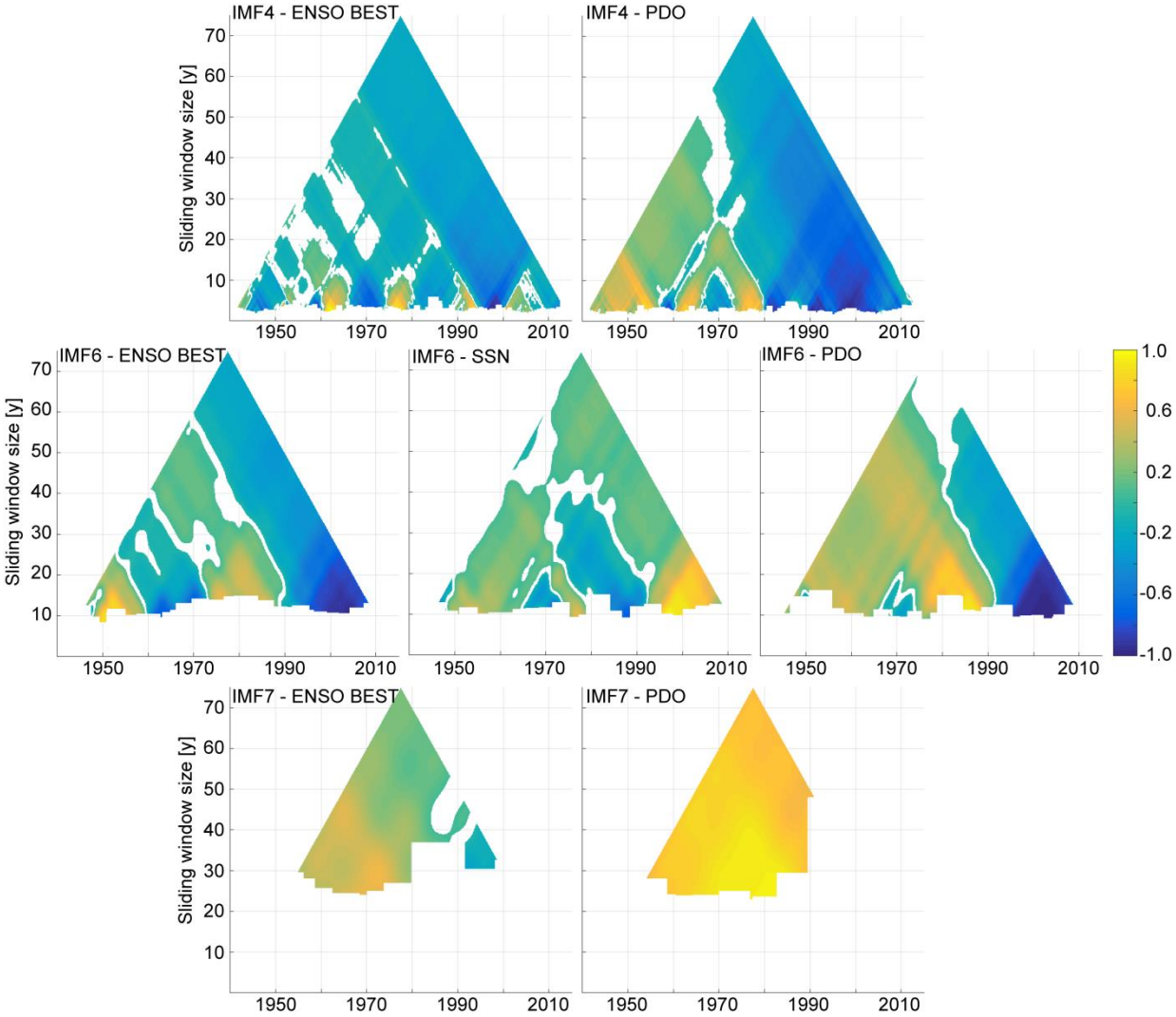

Figure 5.7 TDIC results obtained from pairs of same order IMFs of normalized discharge anomaly of station SA0693 and the processed climate indices for the time interval between 1940 and 2015. Top: IMF4 ($\overline{T}$ = 2.5y) matches between NQ and (left) ENSO BEST and (right) PDO. Middle: IMF6 ($\overline{T}$ = 9.4y) matches between NQ and (left) ENSO BEST, (center) SST, and (right) PDO. Bottom: IMF7 ($\overline{T}$ = 21.6y) matches between NQ and (left) ENSO BEST and (right) PDO.

For IMF6 (mean period $\overline{T}$ = 9.4y) TDIC exhibited rather similar correlations between the pairs of normalized discharge anomaly and ENSO BEST and PDO indices, respectively. Except for locally high positive values, especially for PDO at about 1980, relatively low values were found until approximately 1990 and a strong anti-correlation afterwards. In contrast, SSN correlation with the normalized discharge anomaly resulted in a generally opposite behavior, with strong positive values starting in the early 1990s. For IMF7 (mean period $\overline{T}$ = 21.6y), the normalized discharge anomaly showed a generally strong positive correlation with PDO. In comparison to NQ-PDO pair, ENSO BEST correlation with normalized discharge anomaly resulted generally in smaller correlation values with for IMF7. Finally, ENSO BEST and PDO

indices exhibited strong correlation at all timescales, whereas SSN and PDO showed a strong correlation until approximately 1980 and a strong anti-correlation since then (Figure A3.24 and Figure A3.25).

5.3.2 TIME INTERVAL FROM 1956 TO 2015

For this time interval, four time series of the normalized discharge anomaly were available from different hydrological stations (JU0016, SA0604, SA0629, and SA0693).

Table 5.5 summarizes the results obtained applying EEMD analysis. As for the time interval between 1940 and 2015, EEMD resulted in eight IMFs and one residue for all hydrological stations and the climate-indices time series. For all time series of normalized discharge anomaly, a monotonically increasing residue was obtained (Figure 5.8).

I observed that each time series of the normalized discharge anomaly was composed of a set of IMFs which differs from the others in terms of the mean period $\bar{T}$, i.e. regarding the associated timescale (Table 5.5). For example, the time series of NQ from station SA0604 exhibited one statistically significant IMF (IMF7, mean period $\bar{T}$ = 22.1y), whereas from station SA0629 it presented two IMFs (IMF5 and IMF7, with mean period equal to 4.3y and 23.3y, respectively). Also, station JU0016 was associated with five statistically significant IMFs (IMF3-7) (Figure 5.8).

		$\bar{T}$ [y]							
		NQ SA0693	NQ SA0604	NQ SA0629	NQ JU0016	ENSO BEST	TSA	SSN	PDO
Time series components	IMF1	-	-	-	-	-	-	-	-
	IMF2	-	-	-	-	-	-	-	0.6
	IMF3	1.0	-	-	1.0	1.4	1.2	-	1.1
	IMF4	2.1	-	-	2.4	3.0	2.6	-	2.7
	IMF5	-	-	4.3	5.4	5.8	5.4	-	5.0
	IMF6	11.6	-	-	9.2	12.5	11.8	11.2	11.4
	IMF7	19.7	22.1	23.3	19.8	(30.6)	19.9	-	(32.8)
	IMF8	-	-	-	-	-	-	-	-

Table 5.5 Summary of EEMD analysis for the normalized discharge anomaly NQ (hydrological station SA0693, SA0604, SA0629, JU0016), ENSO BEST, SSN, and PDO for the time interval 1956-2015. For each statistically significant IMF, the value of its mean period $\bar{T}$ [y] is indicated; mean period values are indicated only for statistically significant IMFs; mean periods in parenthesis are associated with IMFs considered unreliable, although statistically significant, because their mean period is greater than half of a time-series length (i.e., less than three cycles occurred during the time interval of the time series).

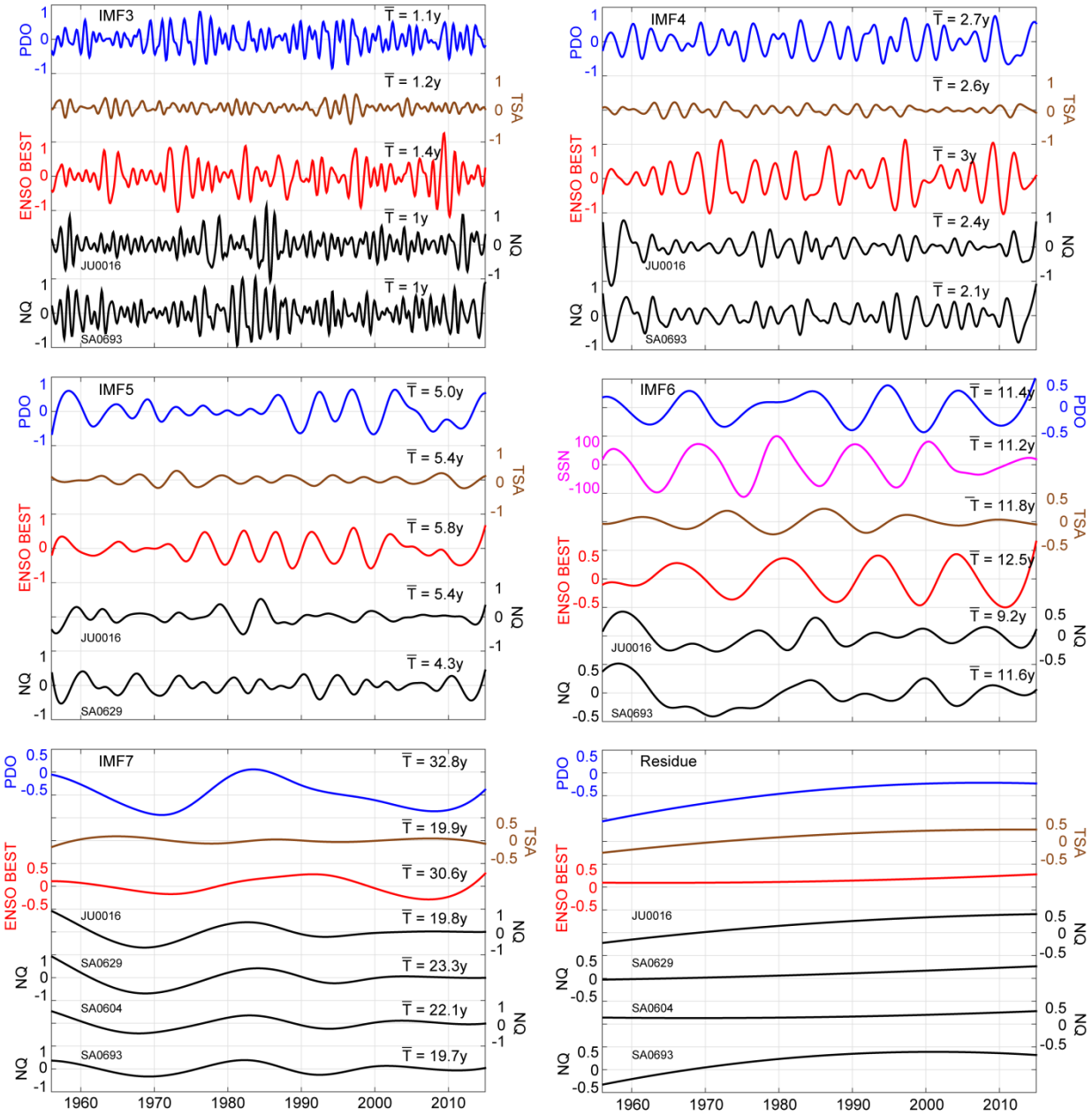

Figure 5.8 EEMD results for the time interval between 1956 and 2015. For each statistically significant IMF of normalized discharge anomaly (Table 5.5), all relevant statistically significant IMFs of the available climate indices are shown. IMFs mean periods $\overline{T}$ are also indicated. The residue for each time series is also shown.

Furthermore, in case that different time series of NQ were composed of an IMF associated with the same timescale, the mean periods $\overline{T}$ had relatively close values (Table 5.5). In addition, for the time interval between 1956 and 2015, the time series from station SA0693 revealed the same set of four IMFs as for the time interval between 1940 and 2015 (Table 5.3 and Table 5.5). Importantly, I observed the local increase of the amplitude of the oscillations of IMF3 of NQ from the middle 1970s to the late 1990s. This was already discussed for the time interval between 1940 and 2015, in association with one period of oscillation of IMF7 (Figure 5.8); in this case,

the time series were not long enough to evaluate the same behavior for the time interval between the early 1950s and the middle 1960s.

To a lesser degree, the IMF4 (~2.3y) and IMF5 (~5y) of NQ presented locally increased amplitudes of the oscillations from the middle 1970s to the late 1990s (Figure 5.8). As for the time interval between 1940 and 2015, it can be noticed that the instantaneous frequency associated with each IMF of the normalized discharge anomaly had approximately constant values around the mean frequency value (see Appendix 3, Figure A3.8-15). Monthly time series of ENSO BEST, TSA, SSN, and PDO for this time interval were also analyzed using the EEMD. In addition to the normalized discharge anomaly, Table 5.5 includes the statistically significant IMFs for each index. It emerged that the ENSO BEST index was associated with five IMFs (IMF3-7), the SSN index with one IMF (IMF6), and the PDO index with six IMFs (IMF2-7). Note that for both ENSO BEST and PDO indices, the IMF7 presented less than two cycles during this time interval and, although statistically significant, results for these two indices of IMF7 could not be considered reliable.

For the time interval between 1956 and 2016, especially for the high frequency IMFs (IMF2-4), the instantaneous frequency showed rather constant values for the climate indices, except for local short and large oscillations around the mean frequency. The outcomes of EEMD, Hilbert spectral analysis, and statistical significance testing are documented in Appendix A3.

For the original time series, the time-independent Pearson correlation analysis of the normalized discharge anomaly and each climate index showed generally low values (absolute correlation values lower than 0.14, Table 5.4). In the case of IMFs pairs, time-independent Pearson correlation values remained small except for the IMF7 for station-to-station pairs or station-to-PDO pairs (Appendix 3, Table A3.1-5 for each IMF).

		Original Time series						
		NQ SA0604	NQ SA0629	NQ JU0016	ENSO BEST	TSA	SSN	PDO
Original time series	NQ SA0693	0.782	0.740	0.623	-	0.124	-	-
	NQ SA0604		0.709	0.501	-	0.083	0.140	-
	NQ SA0629			0.580	-	0.107	0.140	-
	NQ JU0016				-	0.127	-	0.094
	ENSO BEST					-0.087	-	0.444
	TSA						-0.288	-
	SSN							-

Table 5.6 Pearson correlation values between the normalized discharge anomaly (NQ) and the available climate indices for the time interval between 1956 and 2015, for the complete time series (TS). The Pearson correlation values for each IMF match are available in Appendix 3 (Tables A3.1-5). Only statistically significant correlation values are shown ($p<0.05$).

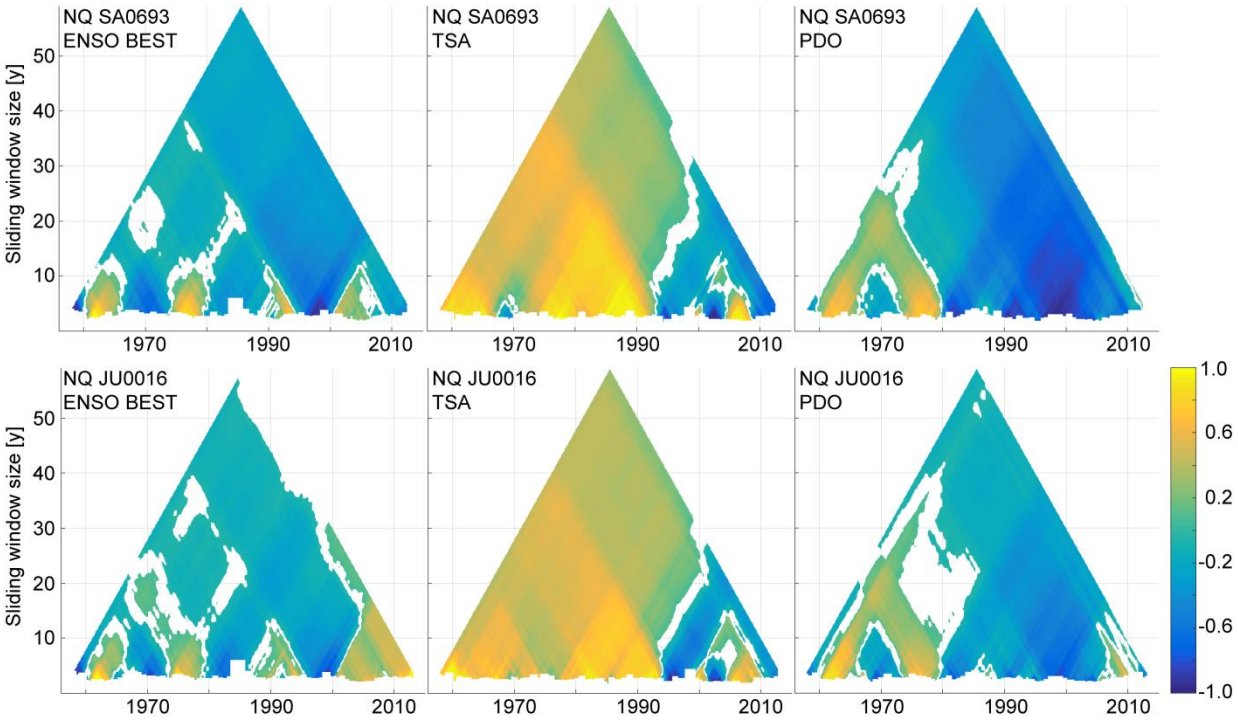

Figure 5.9 TDIC results obtained by matching IMF4 of normalized discharge anomaly from stations SA0693 and JU0016, and the available climate indices for the time interval from 1956 to 2015. Top: SA0693 ($\overline{T}$ = 2.1y) matches between NQ and (left) ENSO BEST, (center) TSA, and (right) PDO. Bottom: JU0016 ($\overline{T}$ = 2.4y) matches between NQ and (left) ENSO BEST (center) TSA, and (right) PDO.

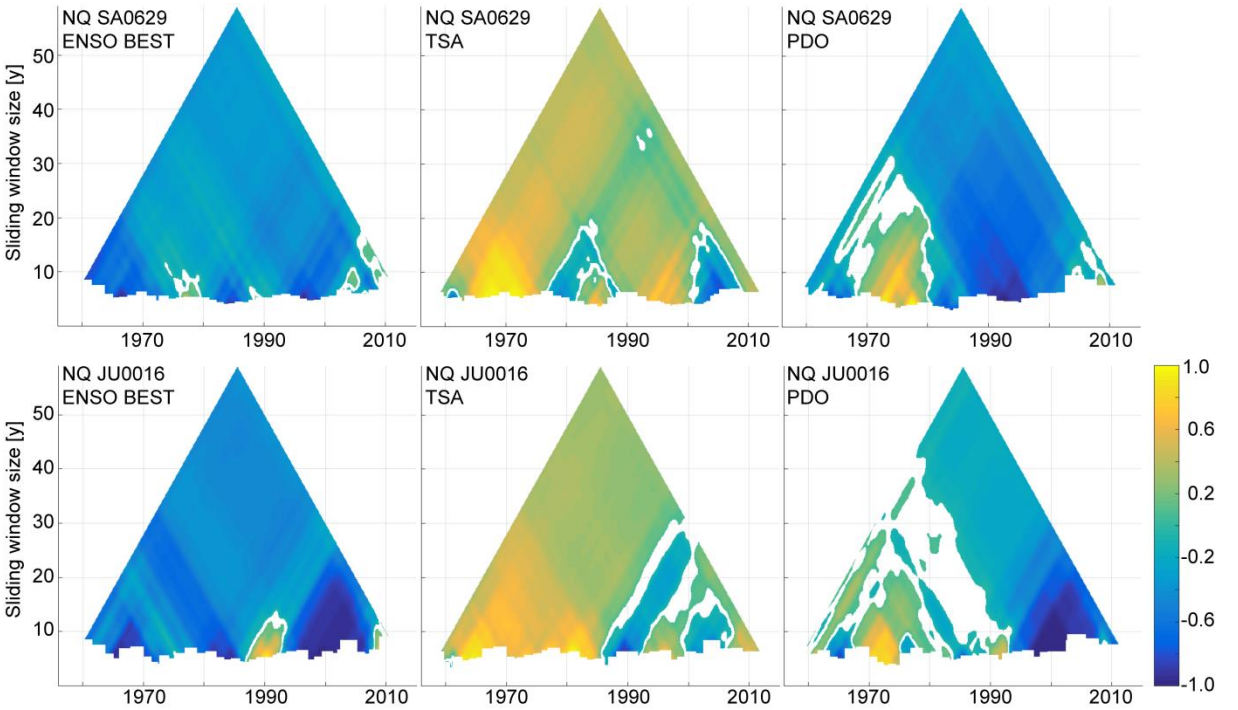

Figure 5.10 TDIC results obtained by matching IMF5 of normalized discharge anomaly from stations SA0629 and JU0016, and the available climate indices for the time interval from 1956 to 2015. Top: SA0629 ($\overline{T}$ = 4.3y) matches between NQ and (left) ENSO BEST, (center) TSA, and (right) PDO. Bottom: JU0016 ($\overline{T}$ = 5.4y) matches between NQ and (left) ENSO BEST (center) TSA, and (right) PDO.

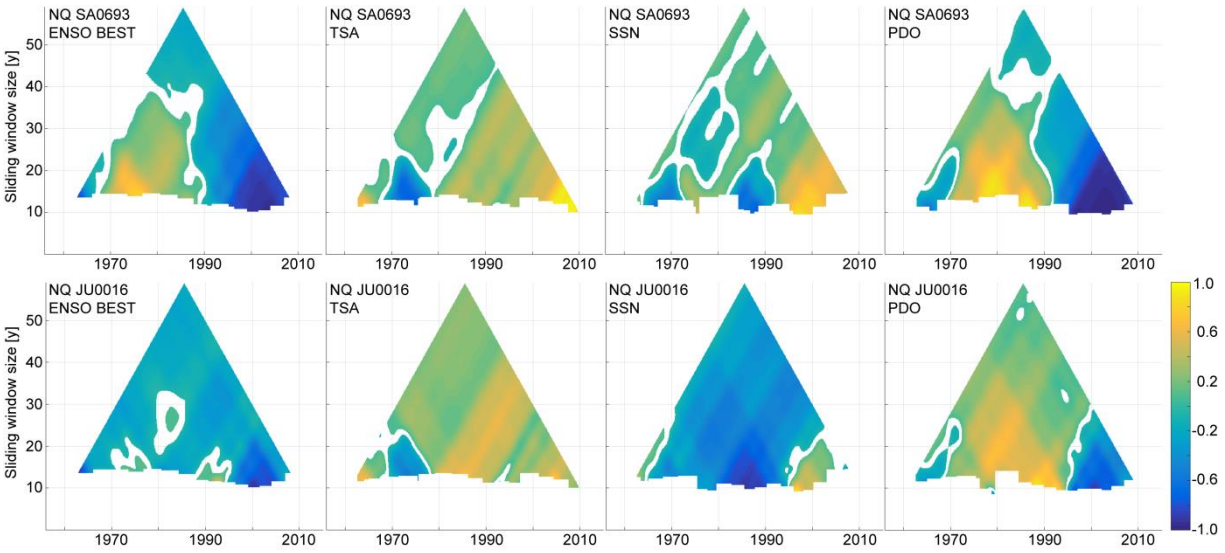

Figure 5.11 TDIC results obtained by matching IMF6 of NQ of hydrological stations SA0693 and JU0016, and the available climate indices for the time interval from 1956 to 2015. Top: SA0693 ($\overline{T}$ = 11.6y) matches between NQ and (left) ENSO BEST, (center-left) TSA, (center-right) SSN, and (right) PDO. Bottom: JU0016 ($\overline{T}$ = 9.2y) matches between NQ and (left) ENSO BEST (center-left) TSA, (center-right) SSN, and (right) PDO.

Concerning the time-dependent intrinsic correlation (TDIC), I observed that for the IMF4 pairs ($\overline{T}$ ~2.3y), TDIC exhibited for short sliding window sizes (< 10y) a behavior similar to that observed for the time interval between 1940 and 2015 for ENSO and PDO correlations with NQ (Figure 5.7). This behavior was due to the fact that the frequencies of both IMF4s (e.g., of NQ and ENSO BEST) were nearly constant, with close, but different values, generating a quasi-periodic short-time interval during which the two IMF4 were locally in phase (i.e., strongly correlated).

Importantly, these high correlation values could not always be associated with positive or negative ENSO or PDO phases. Interestingly, for the IMF4 pair of normalized discharge anomaly and TSA index, both available time series of normalized discharge anomaly (SA0693 and JU0016) exhibited very high correlation values until 1990, whereas after the middle 1990s, high heterogeneity was observed in TDIC. On the contrary, for the pair of normalized discharge anomaly and PDO index, TDIC showed strong anti-correlation for the time series from station SA0693 after approximately 1980.

For IMF5 ($\overline{T}$ ~5y), TDIC mostly showed a strong anti-correlation between normalized discharge anomaly and ENSO BEST index for both available time series (SA0629 and JU0016). The IMF5 pair of normalized discharge anomaly and TSA index instead revealed generally high positive correlation values, especially between approximately 1960 and the middle 1980s for sliding-window sizes smaller than 20y.

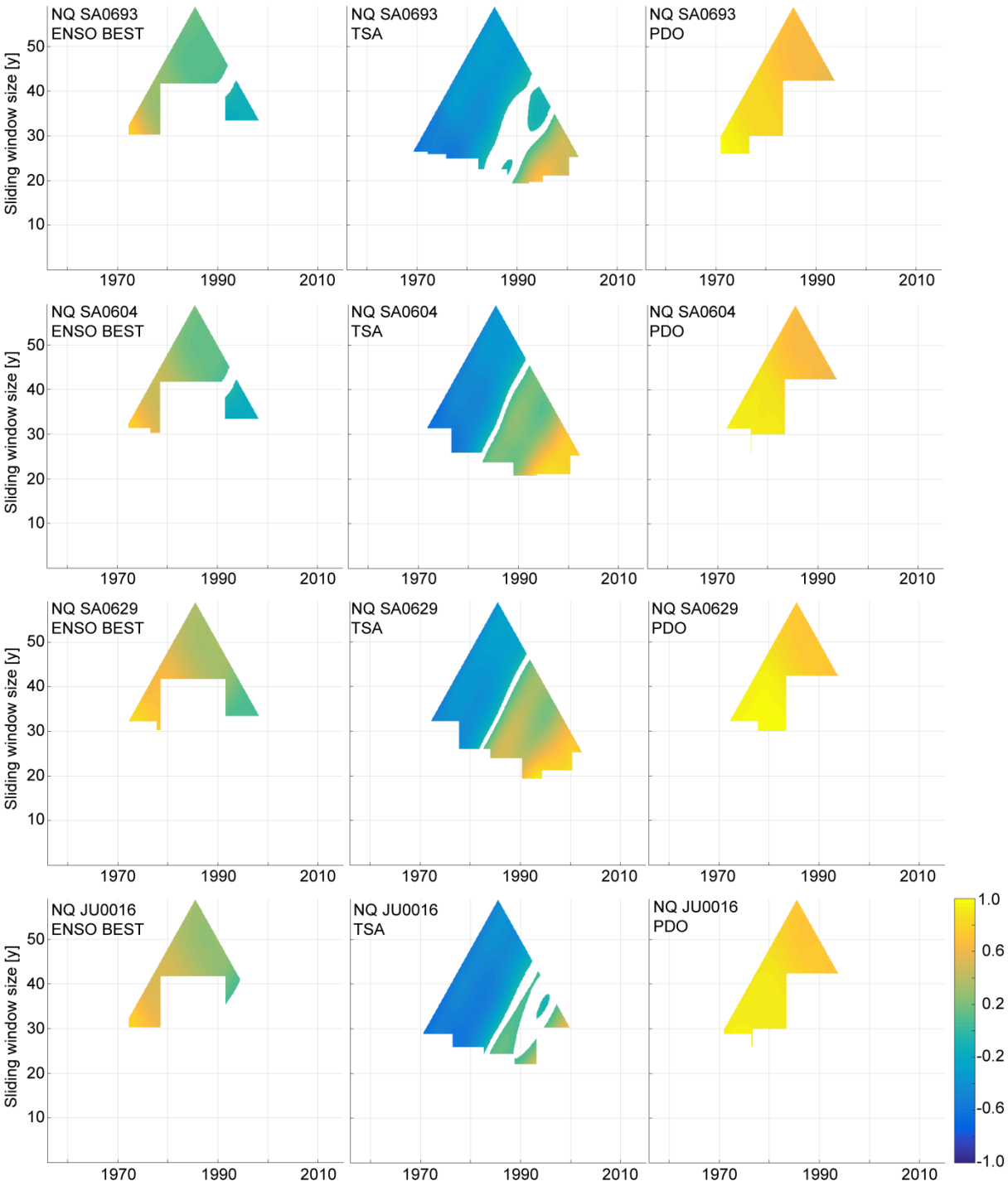

Figure 5.12 TDIC results obtained by matching IMF7 of NQ of hydrological stations SA0693, SA0604, SA0629 and JU0016, and the available climate indices for the time interval from 1956 to 2015. From top to bottom: SA0693 ($\overline{T}$ = 19.7y) matches between NQ and (left) ENSO BEST, (center) TSA, and (right) PDO; SA0604 ($\overline{T}$ = 22.1y) matches between NQ and (left) ENSO BEST, (center) TSA, and (right) PDO; SA0629 ($\overline{T}$ = 23.3y) matches between NQ and (left) ENSO BEST, (centre) TSA, and (right) PDO; JU0016 ($\overline{T}$ = 19.8y) matches between NQ and (left) ENSO BEST (center) TSA, and (right) PDO.

In contrast, the IMF5 pairs of normalized discharge anomaly and PDO index showed a weak relationship until 1990 but strong anti-correlation afterwards.

For IMF6 ($\bar{T}$ ~10y), pronounced heterogeneous results were observed for the hydrological stations SA0693 and JU0016 (Figure 5.11). For the IMF6 pairs of normalized discharge anomaly and both ENSO BEST and PDO indices, TDIC for the time series from station SA0693 mostly showed a structure of values opposite to that obtained for the IMF6 pairs of NQ and both TSA and SSN indices. There existed a relatively strong correlation until 1990 and a subsequent strong anti-correlation. For the time series from station JU0016 the correlation values between the normalized discharge anomaly and the climate indices was weaker, except for the IMF6 pair of the normalized discharge anomaly and SSN index, which exhibited a relatively high anti-correlation.

For IMF7 ($\bar{T}$ ~20y), although PDO evidenced strong correlation values for any available sliding window size, as it was observed for the time interval between 1940 and 2015, these results could not be considered reliable, since less than two cycles were present for the time interval between 1956 and 2015. Instead, for this timescale ($\bar{T}$ ~20y) TDIC results for the pair of the normalized discharge anomaly and TSA index evidenced until the early 1980s a generally weaker relationship than that obtained for shorter timescales, showing negative values for all four stations, and rather high positive values starting from approximately 1990.

5.4 DISCUSSION

The EEMD analysis proved to be an efficient method to document long-term river-discharge trends and to decipher magnitude and frequency of modes of oscillation of river-discharge variability at different timescales in the southern Central Andes of NW Argentina. In addition, the combination of EEMD and TDIC analyses provided important insights to identify linkages with large-scale modes of climate variability that might have affected river discharge in the study area between 1940 and 2015.

The EEMD analysis showed for both analyzed time intervals (between 1940 and 2015, and 1956 and 2015) that all time series (i.e., five normalized discharge anomaly and four climate indices) could be considered as the combination of eight intrinsic mode functions (IMFs) associated with different mean periods and one residual. In the following, I first discuss the IMFs results and the associated implications about the links of river discharge with large-scale modes of climate variability. In a second step, I address the residuals as long-term trends of river discharge for both considered time intervals, discussing them in a regional perspective.

5.4.1 IMFs

In this study, the EEMD analysis resulted in four statistically significant IMFs for the time series of normalized discharge anomaly from station SA0693, i.e. four IMFs components with physically meaningful information [*Wu et al.*, 2004]. This observation allows one to consider the obtained four IMFs as quasi-periodic modes of variability of the normalized discharge anomaly, which can be linked to large-scale modes of climate variability at similar timescales [*Antico and Kröhling*, 2011; *Massei and Fournier*, 2012; *Antico and Torres*, 2015; *Molina et al.*, 2015; *Wang et al.*, 2015].

For station SA0693, the same statistically significant IMFs (IMF3, IMF4, IMF6, and IMF7) were obtained for both considered time intervals, with similar mean period values $\bar{T}$. Relatively small differences between $\bar{T}$ values of the same IMF obtained for the two time intervals were to be expected, given that the IMFs obtained by the EEMD method are approximations of the true envelope composing the original time series [*Wang et al.*, 2010]. Therefore, observations obtained from the analysis relevant to the time interval between 1940 and 2015 hold true also for the time interval between 1956 and 2015 when the time series was not long enough to allow for analogous analysis.

The results of this study revealed that a complex system of climate and coupled atmosphere-ocean processes control river-discharge variability in the southern Central Andes. This is due to the geographic setting of the study area at the transition between the tropics and subtropics, pronounced topographic and climatic gradients, and various factors controlling rainfall combined with different atmospheric processes, such as the SALLJ, the SACZ, and mountain waves (chapter 2) [*de la Torre and Alexander*, 2005; *Vera et al.*, 2006; *Carvalho et al.*, 2012; *Boers et al.*, 2015b; *de la Torre et al.*, 2015].

Several studies in the past two decades have applied spectral analysis to river-discharge time series for different rivers in South America to associate large-scale climate modes of variability with discharge deviations for these regions [*Robertson and Mechoso*, 1998; *Compagnucci et al.*, 2000, 2014; *Poveda et al.*, 2001; *García and Mechoso*, 2005; *Pasquini and Depetris*, 2007, 2010; *Antico and Kröhling*, 2011; *Antico et al.*, 2014; *Apaéstegui et al.*, 2014; *Antico and Torres*, 2015]. Different methodologies have been applied, from the classical Fourier Transform [*Robertson and Mechoso*, 1998; *Poveda et al.*, 2001; *García and Mechoso*, 2005; *Pasquini and Depetris*, 2010] to more complex techniques such as wavelet analysis [*Compagnucci et al.*, 2000, 2014; *Pasquini and Depetris*, 2007; *Apaéstegui et al.*, 2014] and Empirical Mode Decomposition (EMD) [*Antico and Kröhling*, 2011; *Antico et al.*, 2014; *Antico and Torres*, 2015; *Molina et al.*, 2015]. In the following sections, I discuss the results in light of these previous findings, referring to the timescales on ~2 – 5y, ~10y, and ~20y as the *multi-annual*, *decadal*, and *multi-decadal timescales*, respectively.

Multi-annual timescale (~2-5y)

Some of the previous studies suggested that at multi-annual timescales much of the discharge variability of some major South American rivers (i.e., Uruguay, Paraná, Paraguay, Negro, La Plata) may be linked with ENSO activity [*Robertson and Mechoso*, 1998; *García and Mechoso*, 2005; *Pasquini and Depetris*, 2007] and the North Atlantic Oscillation (NAO) [*Hurrell et al.*, 2003; *Antico et al.*, 2014]. The role of ENSO as a potential driver of river-discharge variability was also documented by *Compagnucci et al.* [2000] for Argentine rivers in the southern subtropical Andes (35° S) and by *Poveda et al.* [2001] for most Colombian rivers.

The results of my study reveal a link between ENSO and normalized discharge anomaly for two drainage basins (SA0629 and JU0016) at multi-annual timescales (~5y) (i.e., positive ENSO phases were associated with lower river discharge and *vice versa*, Figure 5.10). Accordingly, ENSO appears as a potential forcing factor for discharge variability at these timescales. At shorter timescales (~2y), however, there appears to be a weak relationship between ENSO and the normalized discharge anomaly (Figure 5.9).

In contrast, at both ~2y and 5y time scales, anomalies in the Southern Tropical Atlantic ocean SST, characterized by the TSA index, exhibited a relatively strong link with discharge anomaly at least until 1990 (Figure 5.9 and Figure 5.10). These results are partly in agreement with previous findings, suggesting that SST anomalies in the tropical Atlantic control discharge in South American rivers at decadal to multi-decadal timescales [*García and Mechoso*, 2005; *Antico and Torres*, 2015]. Interestingly, I observed that at multi-annual timescales, when the PDO relationship with discharge was weak (before 1990), TSA had a strong link with discharge anomaly. Conversely, when the relationship between the discharge anomaly and PDO was stronger (after 1990), the link between TSA weakened. To my knowledge, no previous study has documented a similar observation. I infer that the PDO and SST anomaly of the southern tropical Atlantic alternately modulate discharge variability in rivers of the southern Central Andes (see also below).

Decadal timescale (~10y)

Recent studies have also linked solar activity (i.e., sunspot number) and motion with decadal variations in streamflow of the Paraná river [*Antico and Kröhling*, 2011; *Compagnucci et al.*, 2014] and subtropical Andean rivers up to 35° S lat [*Compagnucci et al.*, 2014]. Similar evidence coupled with SST anomalies of the southern tropical Atlantic was also provided by *Antico and Torres* [2015] for the Amazon [*Antico and Torres*, 2015]. Previous studies also suggested the Atlantic SST anomaly as a driver for discharge variability in major South American rivers on both decadal and multi-decadal timescales [*Robertson and Mechoso*, 1998; *García and Mechoso*, 2005; *Pasquini and Depetris*, 2007, 2010].

With respect to solar activity, my results also revealed a strong correlation between SSN and TSA indices (Figure 5.8), as previously suggested by *Antico and Torres* [2015]. Furthermore, for the time series from station JU0016, whose catchment includes the climatic transition zone between the humid and semi-arid sectors of the eastern Andean flanks, I found a relatively strong anti-correlation between the normalized discharge anomaly and SSN until approximately until 1990. However, I did not identify a coherent spatial pattern that would have indicated an unambiguous influence of solar activity on river-discharge variability. This finding was also reflected by the results related to TSA analysis, which did not show a clear link between discharge variability and SST anomaly in the southern tropical Atlantic at this timescale. On the other hand, PDO impact on river-discharge variability at decadal timescales appeared to become stronger compared to multi-annual timescales, i.e. associated with a strong correlation until 1990 and a strong anti-correlation afterwards (Figure 5.11). This observation is similar to that documented for the multi-annual timescales, suggesting that the PDO and SST anomalies of the southern tropical Atlantic alternately impact discharge variability in rivers of the southern Central Andes.

Multi-decadal timescale (~20y)

On this timescale, PDO showed a particularly strong link with the discharge anomaly, resulting likely from a first-order control of discharge variability in the southern Central Andes (Figure 5.7). This finding is in agreement with *Marengo* [2009, 2012] who suggested that the observed rainfall and discharge trends in the Amazon basin can be explained by multi-decadal modes of climate variability, such as PDO, for example. A similar result was also found by, who proposed a link at multi-decadal timescales between the Pacific ocean SST variability and streamflow of the Paraná river, in southeastern South America (Figure 2.5). However, I emphasize that, in place of the PDO index, *Antico et al.* [2014] used in their study the Interdecadal Pacific Oscillation (IPO) index that includes also southern Pacific SST changes [*Parker et al.*, 2007].

5.4.2 TRENDS OF NORMALIZED DISCHARGE ANOMALY AND THE 1976-77 CLIMATE SHIFT

The EEMD method interprets the residual obtained from decomposing a time series as the long-term trend [*Huang et al.*, 1998; *Wu et al.*, 2007]. For the normalized discharge anomaly (NQ), although with different magnitude, monotonically increasing, statistically significant trends were found for all hydrological stations and time intervals (Figure 5.8). In particular, I observed that

including or excluding the first 16 years of the hydrological station SA0693 does not influence the overall trends. In addition, the mean increase value for both time intervals (from 1940 to 2015 and from 1956 to 2915) was approximately 10% of the standard deviation per decade. In a previous study, trends of the same hydrological stations were evaluated, using a different method based on standard and quantile regression on the time interval between 1940 and 1999, i.e. excluding the last 16 years (Chapter 4 and *Castino et al.* [2016]). *Castino et al.* [2016] found a mean increase of the normalized discharge anomaly by approximately 8.5% per decade, which is in good agreement with the outcomes of this study. Similar results of long-term trend values obtained by different methods and different lengths of the time series (i.e., excluding or not excluding the first or last decades) demonstrates the robustness of these trend results for NQ.

In addition, *Castino et al.* [2016] documented a change point towards higher discharge values from 1971 to 1977 in agreement with previous studies [*García and Vargas*, 1998; *Genta et al.*, 1998; *Robertson and Mechoso*, 1998; *Compagnucci et al.*, 2000; *García and Mechoso*, 2005]. These authors associated the change point in river discharge in southern Central Andes with the 1976-77 global climate shift [*Graham*, 1994; *Miller et al.*, 1994; *Kayano et al.*, 2009; *Marengo*, 2009; *Carvalho et al.*, 2011; *Jacques-Coper and Garreaud*, 2015], highlighting an intensification of the hydrological cycle. In their study, *Castino et al.* [2016] further documented a statistically significant decrease in discharge following the large increase corresponding with the change point, which suggests an oscillatory component in the normalized discharge anomaly.

The EEMD results document that beginning the middle 1970s to the early 1990s the amplitude of most modes of oscillation of discharge largely increased (see sections 5.3.1 and 5.3.2). I hypothesize that this increase is linked to a multi-decadal PDO phase and, to a lesser degree, SST anomalies of the southern tropical Atlantic variability at multi-annual timescales, respectively. In particular, it can be noticed that the local increase of IMF3 (annual timescale) appeared to be synchronized with one period of oscillation of IMF7 (multi-decadal timescale) (Figure 5.5). Since IMF3 represents the mode of oscillation mainly associated with the SAMS, one possible explanation is that the positive phase of PDO modulated the intensity of the SAMS, which in turn resulted in enhanced discharge on multi-decadal timescales.

Therefore, based on the results of the EEMD analysis, I hypothesize that the discharge change point between 1971 and 1977 [i.e., *Castino et al.,* 2016] likely resulted from the superposition of a long-term positive trend observed for the time interval 1940-2015 and the modes of discharge variability, whose amplitudes were enhanced by a PDO change of phase on multi-decadal timescales, and the TSA variability on multi-annual timescales.

Partly, similar explanations have been also proposed by *Zhang et al.* [2016]. These authors analyzed the multi-decadal trend towards wetter conditions in southeastern South America (SESA) during the 20th century, which was followed by a decadal drying trend by the beginning of the 21st century. Interestingly, *Castino et al.* [2016] observed the drying trend in the southern Central Andes already starting in the early 1980s. However, despite some differences in the amplitude of the changes between model estimations and observations, in their model-based study, *Zhang et al.* [2016] showed that the trend toward wetter conditions is likely driven by radiative forcing associated with increasing greenhouse gases, which would have caused the southward tropical expansion. SESA is located underneath the subtropical descending branch of the Hadley cell, which usually suppresses convection activity and forces dry conditions at the surface. According to *Zhang et al.* [2016], the southward tropical expansion would have moved the subtropical descending branch of the Hadley cell away from SESA, resulting in a rainfall increase in this region. *Zhang et al.* [2016] also proposed that the drying trends observed at the beginning of the 21st century are mainly attributable to internal climate variability, such as the Pacific Decadal Variability (PDV) [*Mantua and Hare*, 2002] and the Atlantic Multi-decadal Oscillation (AMO) [*Enfield et al.*, 2001].

5.5 CONCLUSIONS

I analyzed trends and modes of oscillation in discharge anomaly from small to medium montane drainage basins (10^2-10^4 km^2) in the southern Central Andes of NW Argentina. These catchments are characterized by transitions from predominantly humid, low elevations to semi-arid medium-high elevations environments.

I relied on daily discharge observations to generate five time series of the monthly normalized discharge anomaly (NQ); one for the time interval between 1940 and 2015, and four for the time interval between 1956 and 2015.

In my analysis I applied the Hilbert-Huang Transform to the monthly NQ time series and obtained four key results:

1. Although with different magnitude, monotonically increasing statistically significant trends were found for all hydrological stations and time intervals. This result is in agreement with similar findings from previous studies in this region and documents an overall intensification of the hydrological cycle.
2. The Ensemble Empirical Mode Decomposition analysis revealed that discharge variability in this region can be described by five quasi-periodic, statistically significant oscillatory modes, with mean periods varying from 1y to ~20y and different variable magnitude.
3. Discharge variability is mostly linked to PDO phases at multi-decadal (~20y) timescales and, to a lesser degree, to the SST anomaly of the southern

tropical Atlantic at multi-annual timescale. In addition, I observed that PDO and SST anomaly of the southern tropical Atlantic might interfere by modulating discharge variability in southern Central Andean rivers, especially at multi-annual timescales. To a lesser degree, discharge variability also exhibited evidence for a link with ENSO and solar activity.

4. It is hypothesized that the discharge change point observed between 1971 and 1977, and previously associated with the 1976-77 climate shift, was the result of the combination of the long-term increasing trend and the periodic enhancement of discharge that occurred between the middle 1970s and the early 1990s. This appears to have been associated with the multi-decadal PDO phase and multi-annual TSA variability.

AKNOWLEDGMENTS

This study was supported by the Leibniz Fund of the German Science foundation (DFG) to M.S. (STR373/19-1) and the German Federal Ministry of Education and Research project PROGRESS (Climate Change, Georisk and Sustainability initiative at Potsdam University) to M.S. and B.B. The authors thank the Subsecretaría de Recursos Hídricos (BDHI), Argentina, for providing discharge time series. The authors thank D. Cielak (BDHI), R. N. Alonso (UN Salta), A. Villanueva (UN Tucumán), and E. Marigliano (EVARSA, Argentina) for their valuable support during this study. The Matlab™ packages for HHT and TDIC analyses were provided by Dr. Huang and his research group at the Research Center for Adaptive Data Analysis and may be downloaded from http://rcada.ncu.edu.tw/intro.html.

APPENDIX A3

The supporting information of this chapter is available in the attached CD.

CHAPTER 6

DETERMINATION LIMITS FOR COSMOGENIC ^{10}BE AND THEIR IMPORTANCE FOR GEOMORPHIC APPLICATIONS

Sara Savi[1], Stefanie Tofelde[1, 2], Hella Wittmann[2], *Fabiana Castino*[1] and Taylor F. Schildgen[1,2]

[1] Institute of Earth and Environmental Science, University of Potsdam
[2] Helmholtz Centre Potsdam, GFZ German Research Centre for Geosciences

Submitted for publication to Quaternary Research, in review

ABSTRACT

When using cosmogenic nuclides to determine exposure ages or denudation rates in rapidly evolving landscapes, challenges arise related to the small number of nuclides that have accumulated in surface materials. Improvements in accelerator mass spectrometry have enabled analysis of samples with low ^{10}Be content (<10^5 atoms), such that it is timely to discuss how technical limits of nuclide determination, effects of laboratory cleanliness, and overall sample preparation quality affect lower blank limits. Here we describe an approach that defines a lower threshold above which samples with low ^{10}Be content can be statistically distinguished from laboratory blanks. In general, this threshold depends on the chosen confidence interval. In detail, however, we show that depending on which method of blank correction is applied (three of which we describe here), significant differences can arise with respect to when a sample can be distinguished from a blank. This in turn dictates whether the sample can be used to determine an exposure age or denudation rate, or when it only constrains a maximum age or minimum denudation rate. Based on a dataset of 57 samples and 61 blank measurements obtained in one laboratory, we demonstrate how these different approaches may influence the interpretation of the data.

KEYWORDS

Cosmogenic nuclides, blank corrections, threshold, limit of detection, limit of quantification

6.1 INTRODUCTION

In the last two decades, the use of *in situ*-produced cosmogenic nuclides for the quantification of denudation processes and the determination of exposure ages of landforms has seen a fast and broad expansion [*Balco*, 2011; *Granger et al.*, 2013]. This development is due to advances in the technique and to the wide range of geological environments in which the method can be applied. Comprehensive summaries of the method can be found in *Anderson et al.* [1996], *Bierman et al.*, [1996], *Granger et al.* [1996], *von Blanckenburg* [2005], *Balco* [2011], and *Granger et al.* [2013]. Among the group of cosmogenic nuclides that can be used to study geomorphic processes (e.g., ^{10}Be, ^{26}Al, ^{36}Cl, ^{3}He, and ^{21}Ne), *in situ*-produced ^{10}Be is the most widely used, especially for the quantification of denudation rates [*von Blanckenburg*, 2005]. For simplicity and clarity, we will focus our discussion on *in situ* ^{10}Be produced in the target mineral quartz only, although similar concepts can be applied to other cosmogenic nuclides. The broad expansion of ^{10}Be applications has included studies that extend the limits of the technique by analyzing nuclide concentrations in environments where some of the assumptions inherent to the method are not always satisfied. These studies explore, for example, landscapes that are not in erosional steady-state [*Wittmann et al.,* 2007; *Yanites et al.*, 2009; *Kober et al.,* 2012], settings where different rock types do not contribute quartz equally [e.g., *Torres Acosta et al.,* 2015], and environments prone to mass failures or with non-uniform sediment supply [*Niemi et al.,* 2005; *Binnie et al.,* 2006; *Yanites et al.,* 2009; *Kober et al.,* 2012; *McPhillips et al.,* 2014; *Savi et al.,* 2014; *Schildgen et al.,* 2016]. Particularly challenging is the application of these techniques in environments where the cosmogenic nuclide content is low. For example, the occurrence of deep-seated landslide or debris-flow events in rapidly eroding landscapes may result in admixing of low cosmogenic nuclide concentration material into fluvial sediments [*Niemi et al.,* 2005; *Yanites et al.,* 2009; *Kober et al.,* 2012; *Savi et al.,* 2014]. Likewise, recently exposed bedrock surfaces contain low ^{10}Be due to their short exposure time to cosmic rays [*Licciardi et al.,* 2009; *Schaefer et al.,* 2009; *Schimmelpfenning et al.,* 2014; *Savi et al.,* in press]. In other cases, scarcity of the target mineral within the collected material can limit the total amount of nuclides in the sample. Difficulties encountered with low ^{10}Be-content samples are related to (1) the technical limits of the Accelerator Mass Spectrometer (AMS), which can precisely measure ^{10}Be/^{9}Be ratios down to 10^{-15} or 10^{-16} (Stone, 1998), and (2) technical limits and cleanliness issues related to the laboratory where the samples are prepared [e.g., *Balco,* 2011].

Many AMS facilities already provide the lower limit at which they can precisely measure nuclide ratios [e.g., *Rood et al.,* 2010]. However, this number does not account for laboratory cleanliness and contamination that may be introduced during sample preparation and chemical procedures, which are reflected in laboratory blanks. Nevertheless, several recent studies demonstrated that it is possible to date very young landforms (such as moraines of the Little Ice Age) if a series of strict sampling and laboratory standards (including low laboratory blank measurements) are met [*Licciardi et al.,* 2009; *Schaefer et al.,* 2009; *Schimmelpfenning et al.,* 2014]. As such, the adoption of a standardized procedure for performing blank correction and defining measurement thresholds is timely and valuable in the field of geomorphic studies. Despite the existence of a procedure commonly used in analytical chemistry to define a statistically significant threshold for low-concentration samples, there have been so far no clear guidelines on how to apply this procedure to cosmogenic nuclide data. In this paper, we describe this method and evaluate its application for ^{10}Be studies. The method is based on laboratory blank measurements, so that it not only accounts for the AMS detection limit, but also for the cleanliness and contamination that may occur in the laboratory. As an example, we use the ^{10}Be measurements of 57 samples and 61 laboratory blanks to address (1) the influence of blank quality and blank corrections when calculating the number of ^{10}Be atoms in a sample, and (2) the determination of statistically significant limits that define the lower threshold for quantifying exposure ages or denudation rates.

6.2 State of the Art

6.2.1 Cosmogenic nuclide techniques in Earth Surface Sciences

In situ cosmogenic nuclides are produced when secondary cosmic rays (formed by nuclear reactions in the atmosphere) collide with target minerals at or near the Earth's surface [*Nishiizumi et al.,* 1989; *Lal,* 1991; *Brown,* 1992; *von Blanckenburg,* 2005; *Dunai,* 2010]. Being a rare cosmogenic radioactive isotope with a half-life of 1.39 Myr [*Chmeleff et al.,* 2010, *Korschinek et al.,* 2010], ^{10}Be is not naturally present in Earth surface materials. Because the production rate of ^{10}Be decreases approximately exponentially with depth, nuclide accumulation mostly occurs within the upper few meters of the surface [*Lal,* 1991; *Dunai,* 2010]. For this reason, ^{10}Be is widely used for two main categories of geomorphological research: (1) dating of exposed or buried surfaces and sediment [e.g., *Ivy-Ochs and Kober,* 2008; *Granger,* 2006] and (2) quantification of recent (typically millennial-scale) denudation rates [*von Blanckenburg,* 2005; *Granger et al.,* 2013]. In these applications, the ^{10}Be content is measured in a sample collected from an exposed surface (e.g., bedrock or a large boulder) or shielded deposit, or from a sample of sediment collected from a river-bed or sedimentary deposit [*Dunai et al.,* 2000; *Gosse*

and Phillips, 2001; *von Blankenburg,* 2005; *Nishiizumi et al.* 2007; *Dunai,* 2010]. The ^{10}Be concentration of a sample is directly related to the time that the sample has been exposed to cosmic rays (minus those lost from decay) and is inversely related to the erosion rate [*Nishiizumi et al.,* 1989; *Lal,* 1991]. Hence, the ^{10}Be content of a sample depends on both the concentration and the mass of the target mineral (e.g., quartz) from which Be is extracted.

6.2.2 FROM AMS RATIOS TO DENUDATION RATES AND EXPOSURE AGES

Once Be is extracted from the sample, the ^{10}Be (and ^{9}Be) atoms contained in a target mineral are detected with AMS. This instrument uses a source of accelerated ions and a series of magnets to separate different chemical elements with similar atomic masses [e.g. *Dewald et al.,* 2013], which can be interpreted in terms of a ^{10}Be/^{9}Be ratio based on a known measurement standard [*Rugel et al.,* 2016]. To calculate the number of ^{10}Be atoms in a sample, the derived ^{10}Be/^{9}Be ratio is multiplied by the amount of ^{9}Be in the sample, which is normally the known amount added as ^{9}Be carrier during sample preparation. In most rock types, the trace metal ^{9}Be contained is in the lower ppm-range [*Rudnick and Gao,* 2004], which makes the total contribution of natural ^{9}Be negligible relative to the amount added by the carrier. Several studies, however, have demonstrated that in some rock types the natural ^{9}Be is high enough that it must be quantified and included when converting ^{10}Be/^{9}Be ratios to ^{10}Be content [e.g., *Portenga et al.,* 2015; *Corbett et al.,* 2016].

Common chemical preparation procedures include the processing of one or more procedural blanks (referred to as *laboratory blanks* hereafter), containing the ^{9}Be carrier only, to help quantify any contamination that may occur during sample preparation and to account for any ^{10}Be within the carrier. To obtain the number of ^{10}Be atoms in the sample related to *in-situ* production, a *blank correction* or *blank subtraction* is commonly performed. This entails subtracting the average number of ^{10}Be atoms contained in the blanks from the number of ^{10}Be atoms in the sample. This subtraction is particularly important when the number of ^{10}Be atoms in the sample is very low and similar to those in the blanks.

6.2.3 BLANK TYPES AND BLANK CORRECTIONS

Laboratory blanks are typically introduced during the Be separation stage right before total sample dissolution. Samples are likely to undergo different preparation histories (e.g. different amounts of acid used for dissolution, different time-spans needed for evaporation, and so on) that could result in differing amounts of ^{10}Be contamination [*Balco,* 2011], which are reflected in the laboratory blanks (see Appendix A4). Also, the amount of ^{10}Be contamination introduced with the ^{9}Be carrier is, for commercially produced Be solutions, not negligible [*Balco,* 2011; *Granger et al.,*

2013]. *Merchel et al.* [2008] reported $^{10}Be/^{9}Be$ ratios between 10^{-14} to 10^{-15} for a range of commercially available Be solutions that may be used as carrier. Deep-mined phenakite or beryl minerals can alternatively be used to produce carrier solutions, in which case $^{10}Be/^{9}Be$ ratios in the range of 10^{-16} have been obtained [e.g. *Stone,* 1998; *Schaefer et al.,* 2009; *Merchel et al.,* 2013; *Portenga et al.,* 2015; *Corbett et al.,* 2016].

Machine or *instrument blanks* (generally related to AMS measurements) indicate the precision at which the AMS can measure the $^{10}Be/^{9}Be$ ratio [*Balco,* 2011]. This latter kind of blank is uninfluenced by contamination that occurs during the chemical procedure in the laboratory and can provide information about the sensitivity of the measuring process. In accelerator mass spectrometry, a recent study has demonstrated that cross-contamination due to long-term memory of the AMS measurements is in the order of 0.1‰ [Rugel et al., 2016], so that the machine background is commonly neglected [*Currie,* 2008]. It follows that most of the contamination comes from the laboratory processing of the samples [*Balco,* 2011] and, as such, we focus only on *laboratory blanks* hereafter.

Blank corrections

When the number of ^{10}Be atoms in a sample is significantly greater than in the blanks, variability of blank measurements has little impact on the blank-corrected result. However, in the case of low ^{10}Be content in a sample, the blank correction constitutes a large subtraction and the variance among blanks becomes important.

Some ^{10}Be in the blank may originate from processes that would affect an entire batch, such as the ^{10}Be contained in the carrier or in the stock chemicals used. In these cases, a single blank per batch probably provides a good measure of the ^{10}Be contamination. Other sources, such as cross-contamination from poor laboratory practices or insufficient cleaning of reusable labware, result in variable contamination between samples of the same batch and using a single blank per batch may thus be inadequate. *Bierman et al.* [2002] provide details of replicate blank measurements from 53 batches of samples measured from cosmogenic-nuclide target preparation laboratories of the University of Vermont, where two blanks were measured per batch. The good agreement between these blank pairs suggests, at least in that laboratory, that inter-batch contamination is not an issue. However, this is a point that needs to be addressed for each laboratory and perhaps at the individual-user level.

6.3 DETERMINATION LIMITS

6.3.1 GENERAL STATISTICAL BACKGROUND

Following the *International Union of Pure and Applied Chemistry* (IUPAC) definition, there is a minimum sample concentration that can be determined to be statistically different from an analytical blank in every analytical procedure [*Long and*

Winefordner, 1983]. The term "statistically different" implies the application of a statistical approach that tries to answer the question "what is the lowest sample concentration that can be reliably distinguished from a blank?" [*Currie,* 1968; *Long and Winefordner,* 1983; *McKillup and Darby Dyar,* 2010; *Schrivastava and Gupta,* 2011; *Bernal,* 2014]. This question can also be formulated as "what is the upper value within the blank distribution (i.e. the distribution of all available ^{10}Be measurements for the laboratory blanks) that ensures a reliable distinction between blank and sample amounts?"

The common statistical method used to answer this question is to define a *testing hypothesis* (i.e., "Population A is greater than Population B") and compare the distribution of the two populations [*McKillup and Darby Dyar,* 2010]. For cosmogenic studies, this can be translated into the following *null hypothesis* (Figure 6.1): "The number of ^{10}Be atoms in a given sample is not distinguishable from that within the blank", which must be tested at a fixed confidence intervals. Here, we give the example of a 1-tail test, because we are interested in defining an upper limit for the blank distribution, and, vice versa, a lower limit for the sample distribution. In this case, the sample distribution refers to all available sample ^{10}Be measurements after performing a blank correction on each measurement. For variables that are normally distributed, the most common values used for confidence intervals are $\pm k\sigma$, with k = 1, 2, or 3 [*McKillup and Darby Dyar,* 2010], and with σ being the standard deviation of the dataset. Whenever the amount of ^{10}Be in the sample lies outside of a chosen confidence interval, the null hypothesis can be rejected, and we can infer that the sample is statistically distinguishable from the blank (Figure 6.1A). It follows that the choice of the confidence interval to use for the definition of a statistically distinguishable value defines the determination limits [*McKillup and Darby Dyar,* 2010].

6.3.2 LIMITS OF DETECTION (LOD) AND QUANTIFICATION (LOQ)

The IUPAC and ACS committees, generalizing the formulas first introduced by Currie in 1968, recommend calculating the limits of determination with the following equation:

$$Limit = \mu_{Blk} + k\sigma_{Blk} \tag{6.1}$$

where μ_{Blk} and σ_{Blk} are the mean and standard deviation of a normal blank distribution, respectively. When k=3, Eq. 6.1 defines the LOD (Limit of Detection), known as "*the lowest concentration, or amount, of an analyte that can be detected with reasonable confidence for a given analytical procedure*" [*Analytical Methods Committee,* 1987; *Mocak et al.,* 1997]:

$$LOD = \mu_{Blk} + 3\sigma_{Blk}\,. \tag{6.2}$$

This definition of the LOD fixes the confidence interval for the blank distribution, assumed as a Gaussian, at 3σ (99.9% for 1-tail test), resulting in a very low probability of an α-type error (α = 0.1%). Accordingly, a blank value has a 0.1% probability of being considered as a sample (being above the LOD), but a sample with a very low ^{10}Be content could have a very high probability (β-type error) of being considered as blank (when its ^{10}Be content is lower than the LOD; Figure 6.1b) [*Mocak et al.,* 1997].

With higher confidence intervals (e.g., 6σ or 10σ), the probability of incurring an α-type error is strongly reduced, but conversely, the probability of incurring a β-error could drastically increase (Figure 6.1b). The IUPAC and ACS committees recommend using k=10, thereby defining the LOQ (Limit of Quantification) as the lower limit above which every analytical sample can be used in a quantitative way with a confidence interval close to 100%:

$$LOQ = \mu_{Blk} + 10\sigma_{Blk}\,. \tag{6.3}$$

However, having a probability of an α-type error of nearly zero results in a high probability of dismissing samples with low ^{10}Be content because they would fall below the LOQ (Figure 6.1b). Whereas the LOD represents a qualitative indication that an element has truly been detected in the sample, the LOQ represents the limit at which the estimated ^{10}Be atoms can be quantitatively used [*Bernal,* 2014].

As we have already described, the probability of a β-type error strongly depends on both blank and sample distributions. We emphasize that for any sample distribution, the choice of the determination limits will dictate the number of samples falling below or above the limits and, in general, the probability of incurring a β-type error will always increase when increasing the chosen confidence interval.

6.3.3 Determination limits (i.e, LOD and LOQ) for cosmogenic ^{10}Be

For ^{10}Be measurements, the blank values represent the lower limit that can be measured, or the most accurate values that take into account possible contamination. To be able to statistically distinguish a sample with low ^{10}Be content from a blank, the proper confidence interval needs to be chosen and related to the statistics of the laboratory blanks and the risk associated with the β-error of the sample distribution.

Because the definition of the determination limits is based on statistical parameters, if the number of blanks used for their calculation is low (e.g., less than 20), or if the distribution of the measured blank values is not normal, the use of μ and

σ for the calculation of the LOD and LOQ values may be not appropriate [*Long and Winefordner,* 1983; *Analytical Methods Committee,* 1987; *Currie,* 1968; 1972; Bernal, 2014]. In the first case, low number of blank measurements, the problem could be solved using a long-term average blank from the laboratory (which is statistically constrained); however a larger number of blanks could introduce larger scatter if the variance among the blank values is large. If the number of blanks cannot be increased, Eqs. 6.2 and 6.3 may be the only option for the calculation of the determination limits.

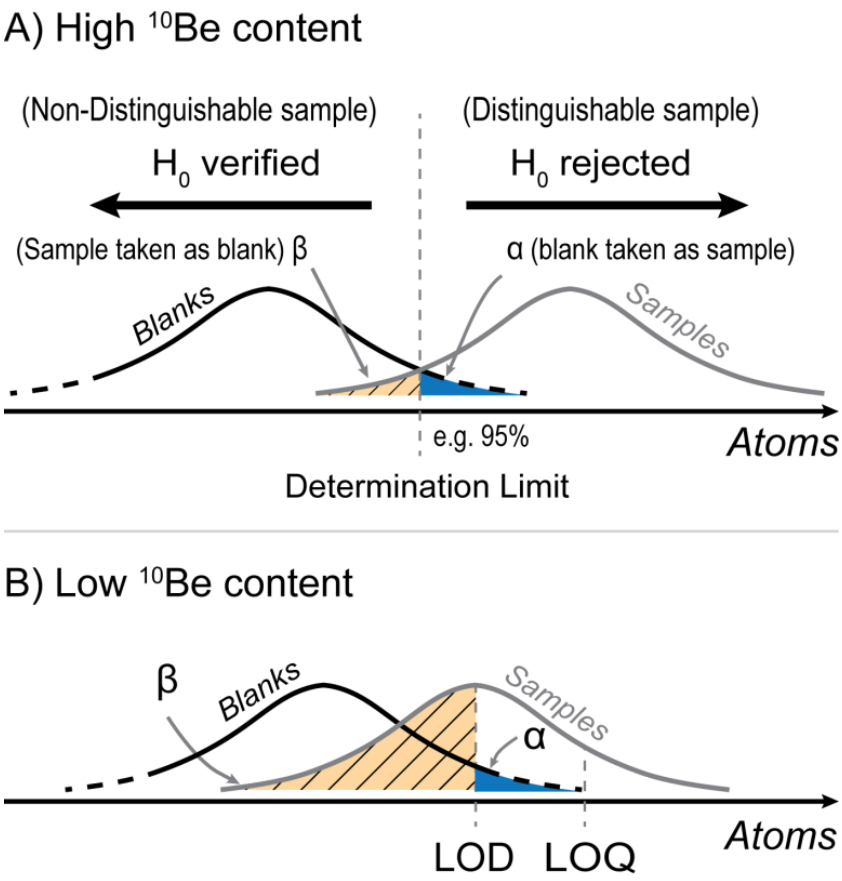

Figure 6.1 Examples of samples with high (A) and low (B) 10Be content. A confidence interval of 95% sets the determination limit. Values below the determination limit are consistent with the null hypothesis (H0), and as such, they cannot be distinguished from the blanks; in contrast, values above the limit will reject the null hypothesis, thus being statistically distinguishable from the blanks. A) For high 10Be content, blank and sample distributions have a relatively small area of overlap, resulting in a relatively low probability of accepting H0. B) For low 10Be content, the probability of having samples below the determination limit is larger and it increases when increasing the chosen confidence interval for the blank distribution. In the figure, the samples not distinguishable from the blanks are 50% for the LOD (see definition in the text), whereas they drastically increase for the LOQ (the hatched area would extend up to the LOQ value). Note that in all the illustrations, the colored areas under the curves are exaggerated to ease visualization.

In this case, and when the blank distribution is non-normal, the calculations of the confidence intervals may be incorrect. In 1987, the *Analytical Method Committee* suggested following the IUPAC recommendations (i.e., Eqs. 6.2 and 6.3) regardless of the shape of the blank distribution. This recommendation was most likely related to the assumption that data are generally normally distributed. When dealing with low concentrations or amounts of an analyte, however, this is rarely the case [*Currie,* 1972; *Bernal,* 2014], and using the IUPAC recommendations for a non-normal distribution would result in slightly different (generally reduced) confidence intervals. For example, considering the blanks in Table 6.1, the Limit of Detection assuming a normal distribution (LOD_N) calculated with Eq. 6.2 would correspond to an actual confidence interval of 98.9% rather than 99.9%, because the blanks are not normally distributed (Figure 6.2).

When the blank statistics indicate a non-normal distribution, a slightly different approach is required. Because AMS-derived counts tend to follow a Poisson distribution with a positive skew, the number of atoms calculated from low blank ratios is likely to create a similar distribution. As such, one approach to calculate a determination limit is to identify which distribution best describes the measured blank data and subsequently calculate the percentile of that distribution relative to the chosen confidence interval. For example, if the best-fit to the blank data is represented by a *Negative Binomial* distribution, fixing a probability of an α-error to 0.1% (equivalent to the LOD) would require that the only samples with a number of ^{10}Be atoms above the 99.9th percentile (corresponding to the 99.9% confidence interval) of the blank distribution can be considered as significantly different from the blanks. Once having determined the probability distribution that best describes the blank and the sample assemblages, the determination limits are given by the percentiles equivalent to the fixed α-value (desired confidence level).

6.4 TESTING THE METHOD

Either using the IUPAC recommendation, or calculating the percentiles for a particular distribution, the LOD defines the threshold above which samples can be distinguished from blanks at the 99.9% confidence interval. To test our approach and evaluate its implications for geomorphic studies, we use one set of 61 blank values (Table 6.1) and one set of 57 sample values (Table A4.1). Blanks and samples were prepared at the Helmholtz Laboratory of the Geochemistry of Earth Surface (HELGES) at GFZ Potsdam [*von Blanckenburg et al.,* 2016] between July 2013 and May 2016. The set of 61 blanks include eight blanks simultaneously processed with the batches of samples over a few 1-month periods between 2014 and 2016. These eight blanks were processed by the same operator, whereas the long-term blanks were prepared by different users. After having calculated the ^{10}Be atoms for blanks and samples, we next performed different blank corrections (see next section), and finally

calculated the LOD and LOQ values for the different blank distributions. These values were then used to assess the reliability of the measured samples.

6.4.1 BLANK CORRECTION METHODS

Here, we describe three different procedures for blank correction: (1) a single-batch blank correction, (2) an average blank correction, derived from multiple blanks averaged from several batches, and (3) a long-term laboratory blank correction. For the single-batch blank correction, the number of ^{10}Be atoms calculated from a single blank processed within the batch is subtracted from each of the samples within the batch.

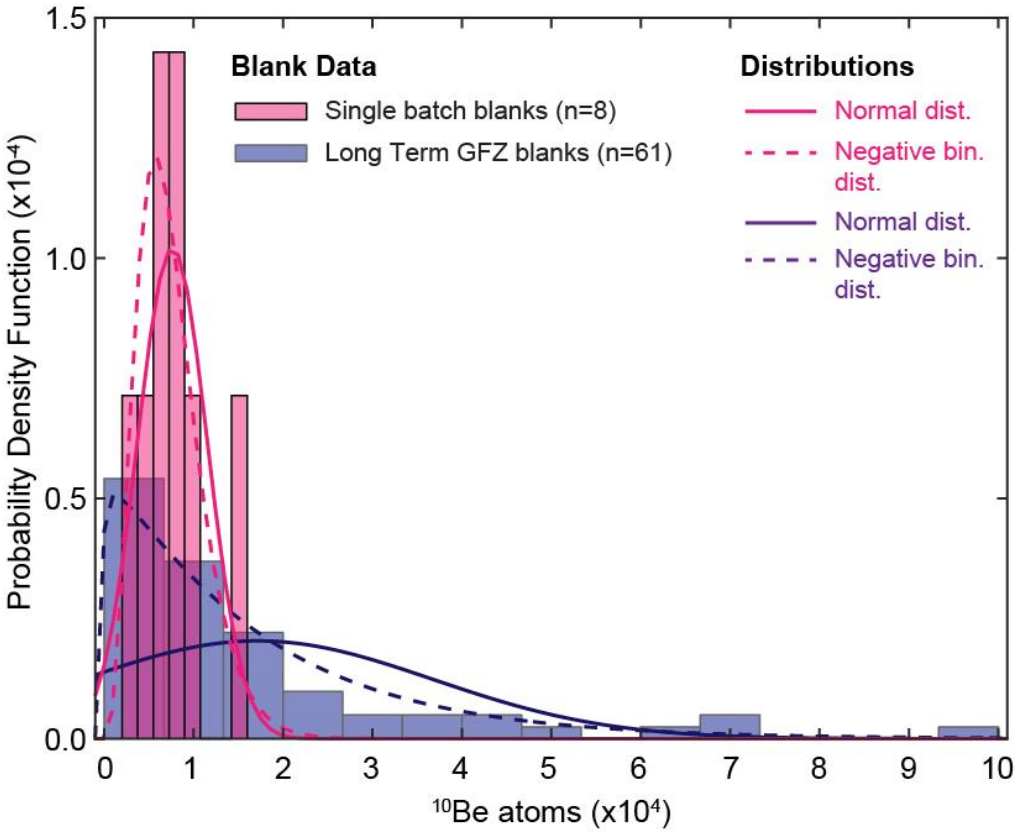

Figure 6.2 Probability density function (PDF) and normalized frequency of the eight single blanks (in pink, histogram) approximated with a normal distribution (in pink, solid line) and with a negative binomial distribution (in pink, dashed line). PDF and normalized frequency of the 61 long-term blanks from the GFZ (in violet, histogram) represented through both a normal distribution (violet, solid line) and a negative binomial distribution (violet, dashed line). Probability distribution parameters associated with the normal distribution are (in 10Be atoms): μ = (0.7630 ± 0.1382) x 104 for the single batch blank method; μ = (1.7154 ± 0.2514) x 104 for the long-term GFZ blanks. When using the Negative-Binomial distribution, the rate of success is R = 4.37 ± 2.11 and the probability is P = (57 ± 29) x 10-5 for the eight blanks, and R = 1.06 ± 0.17 and the probability is P = (6 ± 1) x 10-5 for the long-term GFZ values. The Best fit test with the Akaike Information Criterion (AIC) indicates that both the blank datasets are better described by a negative binomial distribution (smaller AIC). For the 8 blanks: AIC (normal distribution) = 161.19, AIC (negative binomial distribution) = 159.64 for the negative binomial. For the 61 long-term blanks: AIC (normal distribution) = 1.38 x 103, AIC (negative binomial distribution) = 1.31 x 103.

Number of Blanks	$^{10}Be/^{9}Be$	^{10}Be atoms from carrier	1σ [%]	Number of Blanks	$^{10}Be/^{9}Be$	^{10}Be atoms from carrier	11σ [%]
1	5.96E-16	5974	50.1	32	1.68E-15	16822	26.9
2	3.14E-16	3152	70.8	33	1.00E-15	10025	71.1
3	6.11E-16	6125	44.8	34	5.62E-16	5634	70.6
4	9.86E-17	988	100.0	35	5.21E-16	5227	50.1
5	1.08E-15	10807	44.8	36	6.23E-15	62446	12.7
6	3.05E-16	3059	70.8	37	7.30E-15	73222	12.0
7	1.05E-15	10528	18.4	38	6.90E-16	6915	44.8
8	1.94E-15	19451	13.6	39	6.84E-15	68561	15.9
9	1.00E-16	1002	100.0	40	3.06E-15	30686	19.5
10	2.48E-16	2486	70.8	41	1.95E-15	19579	23.1
11	4.24E-16	4251	57.8	42	9.65E-15	96781	11.6
12	7.27E-16	7286	40.9	43	6.58E-16	6591	57.8
13	1.55E-15	15579	31.8	44	3.82E-15	38245	31.8
14	6.56E-16	6576	50.1	45	4.21E-15	42165	31.8
15	3.86E-16	3866	70.8	46	4.57E-15	45824	19.5
16	7.32E-16	7340	40.9	47	2.34E-15	23418	21.5
17	4.46E-16	4473	57.8	48	1.61E-15	16090	27.9
18	1.24E-15	12471	37.9	49	3.49E-15	35027	40.9
19	5.32E-16	5328	50.1	50	3.15E-15	31549	18.2
20	7.62E-16	7642	31.7	51	7.76E-16	7781	70.8
21	1.44E-15	14466	37.9	52	1.71E-15	17153	26.9
22	9.16E-16	9184	37.9	53	2.51E-15	25163	23.1
23	2.41E-16	2420	70.8	54	1.51E-15	15138	33.5
24	2.60E-16	2602	50.1	55	5.62E-16	5638	57.8
25	9.00E-17	902	100.0	56	2.23E-15	22326	29.0
26	9.94E-16	9967	33.5	57	1.77E-15	17724	33.5
27	9.45E-16	9473	40.9	58	4.66E-16	4669	57.8
28	1.15E-16	1155	100.0	59	5.11E-15	51258	21.5
29	1.25E-15	12571	44.8	60	7.94E-16	7959	50.1
30	3.52E-16	3528	70.8	61	9.25E-16	9277	50.1
31	2.28E-15	22847	25.2				

Table 6.1 Long-term blank measurements at the German Research Center (GFZ) from July 2013 to May 2016. A carrier addition of ca. 0.15 mg (in accordance with the laboratory protocols) was used for the calculation of the ^{10}Be atoms. The average blank value is 17154 atoms, with σ = 19601.

In the average-blank correction, all the blanks processed in multiple batches by one operator over a limited time frame (in our case, the eight blanks processed by the same operator) are averaged to a mean number of ^{10}Be atoms contained in the blanks, which is then subtracted from all samples. This approach accounts for operator-specific abilities and any temporal component of the laboratory background, but does not account for differences that may occur among different sample batches.

The long-term laboratory blank correction subtracts a blank ^{10}Be value averaged from all the blanks measured at the laboratory over a longer time span from each sample (in our case, the average of the 61 blank values). This approach has the advantage of being based on many measurements (and hence is statistically well constrained), but because it includes variability associated with different operators and potential variations among batches, it may overestimate the variability associated with a single operator processing a single batch of samples.

We performed the three different blank correction procedures to determine three distinct sets of blank-corrected ^{10}Be values for all the samples (Table A4.3 in the Appendix A4). Next, the LOD and LOQ values were calculated based on the distribution of blanks, i.e., for the eight blanks processed together with the samples, and for the 61 long-term blank values processed in the laboratory. Subsequently, we assessed which samples (i.e, blank-corrected ^{10}Be values) fall below the various LOD and LOQ values.

6.4.2 Determination limits

We calculated the LOD and LOQ for the eight blanks that were processed together with the samples (Table 6.1) using Eqs. 6.2 and 6.3, which assume a Guassian distribution, as well as by fitting a negative binomial curve to the blank distribution using the Matlab Distribution Fitting toolbox (dfittol) and calculating percentiles. We performed the same procedure for the 61 blanks processed by multiple operators over a longer time periods at the GFZ assuming both a normal distribution (using Eqs. 6.2 and 6.3) and a negative binomial distribution. With this approach, we can evaluate the effects of following the IUPAC recommendations despite having non-normal blank distributions (Figure 6.2).

6.5 Results

6.5.1 Blank corrections and error propagation

For the *single-batch blank correction*, we subtracted the ^{10}Be content of a single blank from each sample within its associated batch, and we used the uncertainty on the individual blank measurement for our error propagation. In contrast, for the *average blank correction* and the *long-term laboratory blank correction*, the average ^{10}Be content of the blank distribution was subtracted from each sample, and we used the average value of the uncertainties for our error propagation. The average blank value obtained considering all the 61 blanks is $\mu = 1.71 \times 10^4$ ^{10}Be atoms with $\sigma = 1.96 \times 10^4$ ^{10}Be atoms, whereas the average blank value of the sub-set of eight blanks is smaller, with $\mu = 0.76 \times 10^4$ ^{10}Be atoms and $\sigma = 0.39 \times 10^4$ ^{10}Be atoms.

	LOD_N atoms	LOQ_N atoms	LOD_{NB} atoms	LOQ_{NB} atoms
Average intra-batch blanks (n=8)	19355	46713	2 3958	4 7936
GFZ long-term blanks (n=61)	75957	213164	11 4522	3 02202
Confidence interval	3σ	10σ	3 σ	6σ
Value in %	99.9%	~100%	99.9%	~100%
Number of Samples < Limit				
Single-batch blank correction	3	10	3	11
Value in %	5.3%	17.5%	5.3%	19.3%
Average Blank Correction	3	12	3	12
Value in %	5.3%	21.1%	5.3%	21.1%
Long Term Blank Correction	18	28	21	29
Value in %	31.6%	49.1%	36.8%	50.9%

Table 6.2 Limit of Detection (LOD) and Limit of Quantification (LOQ) for the average eight single-batch blanks and the 61 GFZ long-term average. The subscript "N" after LOD and LOQ refers to the normal distribution whereas the "NB" refers to the negative-binomial distribution.

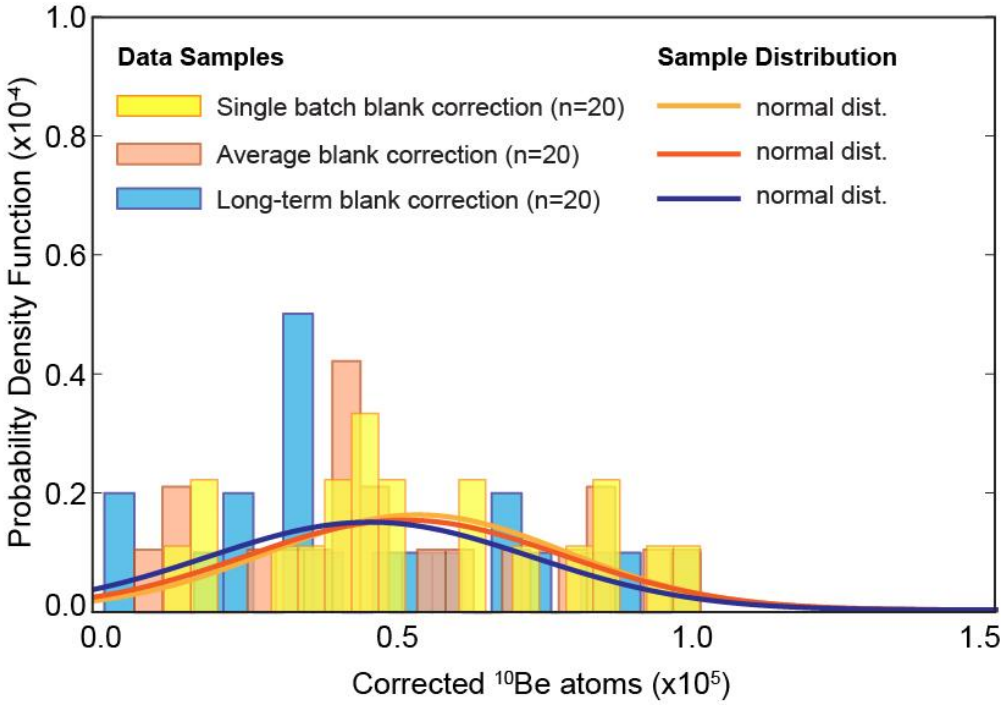

Figure 6.3 Difference between the three correction methods applied to the first 20 samples of our dataset. Shown here are only the samples with low ^{10}Be content to allow the visualization of the differences obtained when the three correction methods (yellow: single batch blank correction; orange: average blank correction; blue: long term blank correction) are applied. Statistical parameters (in ^{10}Be atoms): $\mu = (0.52620 \pm 0.05600) \times 10^5$ (for Single batch blank correction), $\mu = (0.50535 \pm 0.05928) \times 10^5$ (for Average Blank Correction), and $\mu = (0.44545 \pm 0.06069) \times 10^5$ (for Long Term Blank Correction).

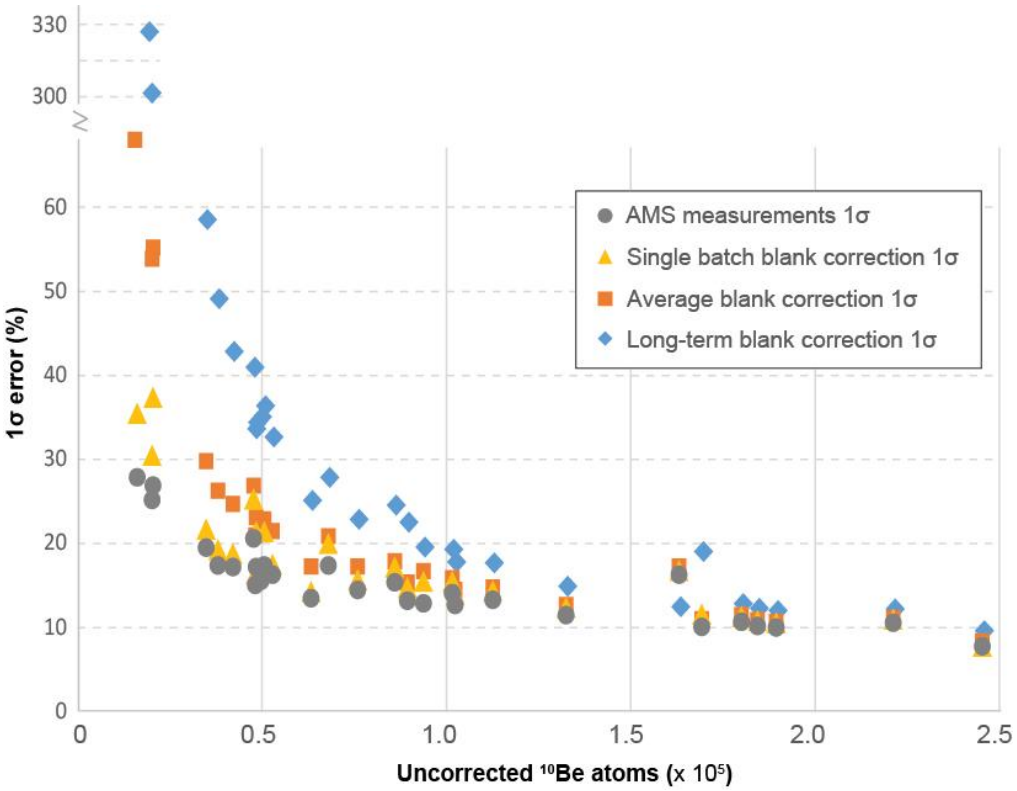

Figure 6.4 Graph of the propagated errors (1σ, in percent) resulting from the different correction methods in comparison with the AMS errors. All the values are plotted against the uncorrected ^{10}Be atoms obtained from the AMS (grey symbols) to allow for a direct comparison between samples. The samples > 2.5 x 10^5 ^{10}Be atoms are excluded from the graph to allow the visualization of the differences between samples with low ^{10}Be content. The y-axis is not continuous to allow for the visualization of higher errors.

Because the *single-batch blank* correction and the *average blank correction* use the same eight blanks, and because these blanks show little variance, the difference between these two blank correction methods is small (Figure 6.3). In contrast, because the 61 blanks processed at the GFZ show large variance with a higher average ^{10}Be content, the blank subtraction is larger, resulting in smaller blank-corrected ^{10}Be contents for the samples (Figure 6.3, Table A4.3). Samples with the lowest ^{10}Be content have the highest uncertainties, which are reflected by large differences in the blank corrections (Fig. 4, Table S2). In addition, for all blank correction methods, the error propagation of the blank-correction procedure results in uncertainties that are particularly large for samples with low ^{10}Be content (i.e., < 50,000 atoms), and are much larger than the analytical (i.e. AMS) uncertainties (Fig. 4). This is particularly the case when the *long-term blank correction* is applied, where uncertainties reach up to 300% and result even in one (meaningless) negative ^{10}Be content (first sample in Table S2). The same samples show error values above 50% when corrected with the *average blank correction*, and values between 30 and 37% when corrected with the *single-batch correction*, thus only in this latter case being similar to the uncertainties commonly reported for low concentration samples (Figure 6.4, Table A4.3).

6.5.2 DETERMINATION LIMITS AND RELIABILITY OF THE SAMPLES

After performing the blank corrections according to the three different methods, we next assess whether or not the samples can be statistically distinguished from the blanks. Because methods to calculate determination limits (LOD and LOQ) rely on a distribution of blanks, we perform these calculations on two sets of blanks: (1) the set of eight blanks processed by a single operator who also processed the samples, and (2) the set of 61 blanks obtained by multiple users over a longer time period.

Following the IUPAC recommendations (subscript "_N" for "normal distribution"), for the eight blanks processed with the samples we obtained values of LOD_{8_N} = 1.94 x 10^4 ^{10}Be atoms, and LOQ_{8_N} = 4.67 x 10^4 ^{10}Be atoms (Table 6.2). For the 61 long-term blanks, we obtained values of LOD_{61_N} = 7.60 x 10^4 ^{10}Be atoms and LOQ_{61_N} = 21.32 x 10^4 ^{10}Be atoms. Using instead a negative binomial distribution (subscript "_NB") (Table 6.2), we obtained values of LOD_{8_NB} = 2.30 x 10^4 ^{10}Be atoms, and LOQ_{8_NB} = 4.78 x 10^4 ^{10}Be atoms for the 8 blank distribution, and values of LOD_{61_NB} = 11.45 x 10^4 ^{10}Be atoms, and LOQ_{61_NB} = 30.22 x 10^4 ^{10}Be atoms for the long-term blank distribution. Incidentally, for the long-term blank distribution, the LOD_{61_N} calculated with Eq. 6.2 (which assumes a normal distribution) corresponds to an actual confidence interval of 98.9% rather than 99.9%, because the blanks are not normally distributed (i.e., best fit represented by the negative binomial distribution; Figure 6.2). The same is true for the LOD_{8_N}, which corresponds to a probability of 99.3% (rather than 99.9%) when the samples are non-normal distributed (best fit represented by the negative binomial distribution).

The applied blank correction method, which changes the statistics of the sample distribution, directly influences the number of samples falling below the relevant determination limits (Figure 6.5, Table 6.2). In particular, when we use the single-batch blank correction or the average blank correction, we assess the reliability of the samples with respect to the LOD_8 and LOQ_8 (values calculated for the set of 8 blanks). When using the IUPAC recommendations (i.e., Eqs. 6.2 and 6.3, and assuming a normal distribution), for the single-batch blank correction, 3 samples are below the LOD_{8_N} and 10 samples are below the LOQ_{8_N} (Table 6.2). These numbers of samples correspond to 5% and 17% of our sample dataset (Figure 6.5). For samples corrected with the average blank correction, 3 samples are below the LOD_{8_N} and 12 samples are below the LOQ_{8_N}, corresponding to 5% and 21% of the sample dataset. When calculating the LOD_8 and LOQ_8 through percentiles (i.e., assuming a negative binomial distribution), these numbers remain basically the same, with only one additional sample falling below the LOQ_{8_NB} (which increases the percentage of undistinguishable samples to 19% – Table 6.2).

When we apply the long-term blank correction, we assess the samples' reliability with respect to the LOD_{61} and LOQ_{61} (values calculated for the set of 61 blanks). In this case, 18 samples (32% of the dataset) are below the LOD_{61_N} and 28 (49% of the dataset) are below the LOQ_{61_N} when the distribution is assumed to be Gaussian, whereas 21 samples (37% of the dataset) are below the LOD_{61_NB} and 28 samples (51% of the dataset) are below the LOQ_{61_NB} values when the limits are calculated through the distributions' percentiles (Figure 6.5, Table 6.2).

6.6 Discussion

Our results highlight that whether or not a sample measurement lies above the chosen determination limit depends on: 1) the distribution of blanks and samples, 2) the applied blank correction procedure, and 3) the type of applied determination limit (LOD or LOQ). All samples whose ^{10}Be content is lower than the chosen determination limit cannot be considered as reliably distinguishable from the laboratory blanks.

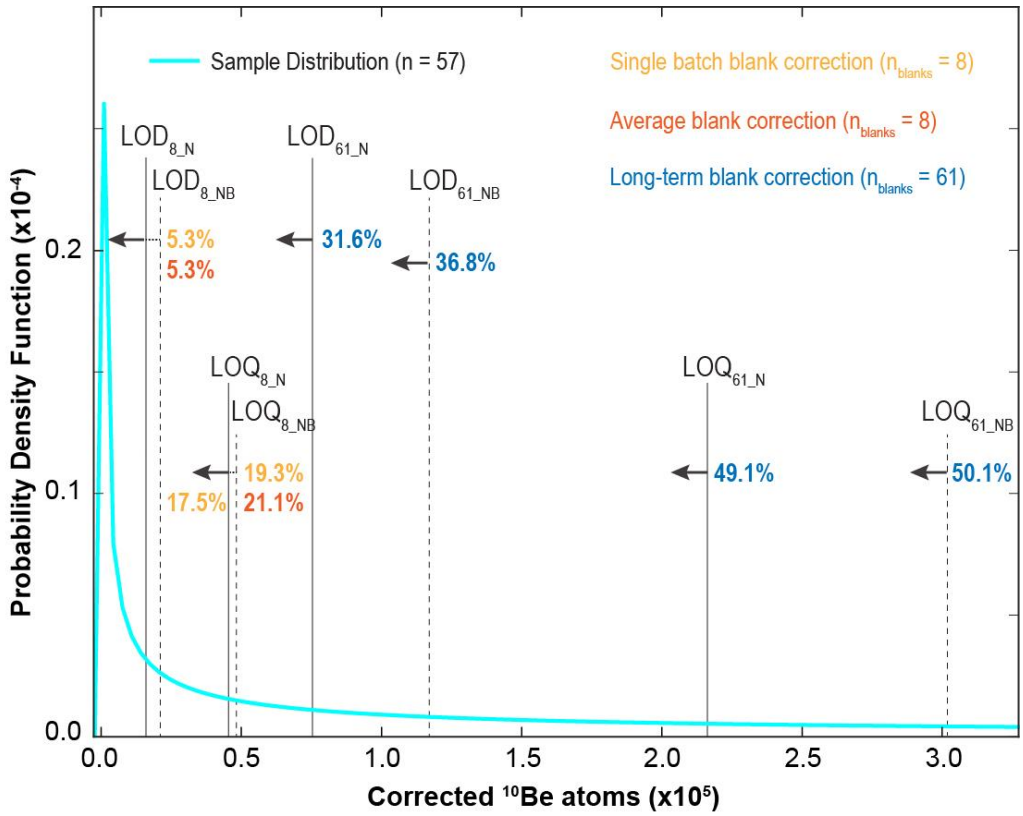

Figure 6.5 Probability Density Function (PDF) of the 57 samples with calculated determination limits. Note that the samples are best represented by a negative binomial distribution (blue curve; displaying only values <2.5 x 10^5 atoms for better visibility of the limits). Numbers at the side of the arrows represent the percentage of samples falling below the assigned limit (colors of the number follow the colors of the corrected distributions; see text for explanation). LOD and LOQ are calculated using Eqs. 6.2 and 6.3 when the distributions are assumed to be Gaussian (subscript "N"), and at the 99.9th and at nearly the 100th percentiles when the distributions are assumed to be Negative Binomial (subscript "NB"; see Table 6.2 for relative values).

Therefore, these values can only be used to limit the age (i.e., younger than the youngest detectable age) or denudation rate (i.e., faster than the fastest detectable rate) recorded by a sample.

6.6.1 CARRIER QUALITY AND BLANK CORRECTIONS

When samples with low ^{10}Be content are expected, the effort and/or expense of acquiring low ^{10}Be/^{9}Be carrier, which typically poses the lower limit attainable for the laboratory blank measurements, is most likely worthwhile. Also, in the specific case of low ^{10}Be content, processing at least two or more blanks per sample-batch would provide a better characterization of the laboratory cleanliness and more robust statistics for the calculation of the determination threshold (Figure 6.6).

The results of our analysis highlight that the blank correction is among the most important factors in defining the final results and the number of samples that can be statistically distinguished from the blanks. In particular, for the average blank correction method on our dataset, average blank values are relatively low, and corresponding LOD_8 and LOQ_8 values are also low. As such, most of the samples lie above the determination limits. Also, the choice of the type of distribution (i.e., Gaussian or Negative Binomial) seems to have little impact on the final value of the determination limits. These determination limits, being based on only eight blanks, are representative of the individual operator's ability and of the contamination that occurred during the processing of the samples, but do not show the intra-batch variability. In contrast, the long-term laboratory blanks have a large scatter and show values spanning several orders of magnitude. As such, the high average blank value results in a large blank correction, and the relatively high LOD_{61} and LOQ_{61} values imply that most of the samples cannot be reliably distinguished from the average blank (Figure 6.5). Also, the type of distribution chosen to fit the blank values seems to have a larger impact of the final values of the determination limits.

In general, if the long-term laboratory blanks show small variance between the measurements, using the long-term average for the blank correction guarantees more robust values for the statistics of the blank distribution and for the calculation of the limits. On the other hand, if the long-term blanks show a large scatter, the single-batch blank correction or the average blank correction may be favored. In these circumstances, however, a small number of blanks may result in determination limits that do not accurately describe the cleanliness of the laboratory. As such, and especially when samples with low ^{10}Be content are expected, processing more than one blank per batch would guarantee to have statistically constrained determination limits [i.e., based on at least 20 blank values; *Bernal,* 2014]. In any case, when determining average blank values and determination limits, it also important to consider whether a classical approach (assuming a Gaussian distribution) can be used, or if an alternative distribution with percentile calculations is more accurate.

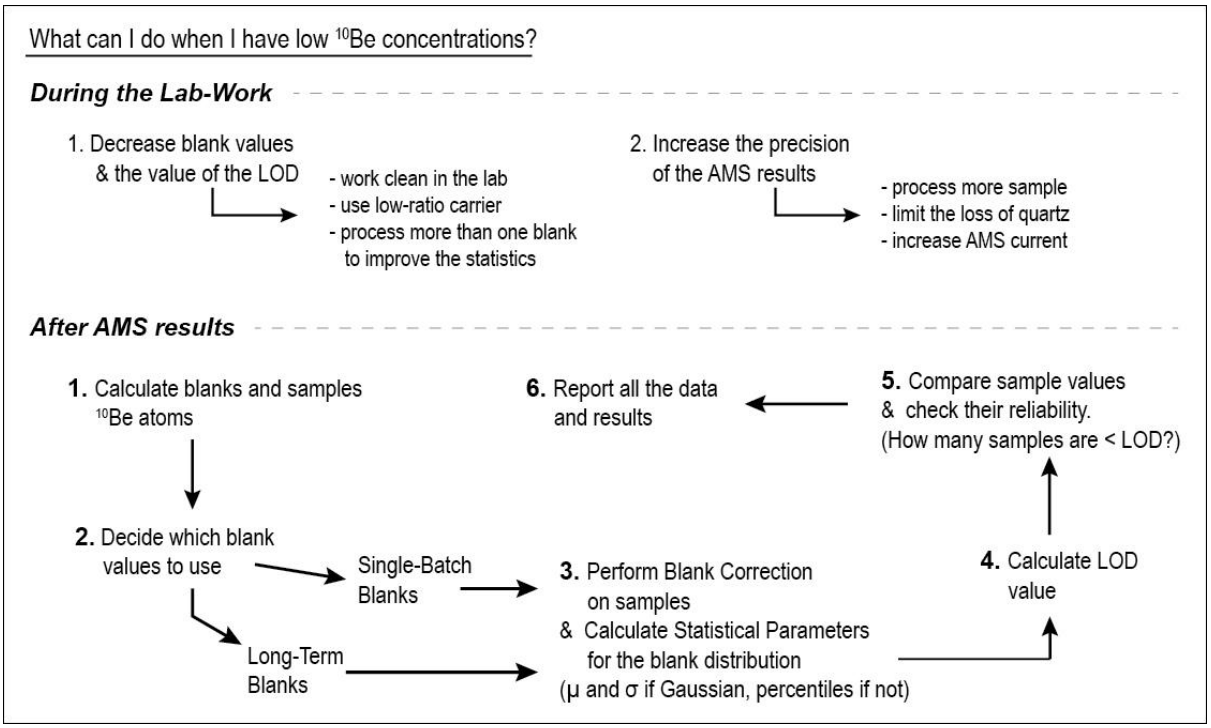

Figure 6.6 Schematic view of the steps to perform in case of samples with low ^{10}Be content. Decreasing the blank values and increasing the precision of the AMS measurements allow to have less overlap between the blank and sample distributions.

6.6.2 INCREASING THE PRECISION OF THE AMS MEASUREMENTS

In general, samples with larger uncertainties are more sensitive to the chosen blank correction method (Figure 6.4, Table A4.3). Accordingly, apart from improvements in laboratory cleanliness, another way to decrease the impact of the blank correction would be to increase the precision of the AMS measurement. This could be done by increasing the amount of sample processed during the chemical procedure, by reducing the loss of quartz during the chemical treatment of the samples (see Appendix A4), or by increasing the AMS current during the measurements [*Schaefer et al.,* 2009; *Rugel et al.,* 2016] (Figure 6.6). Whether to increase the amount of sample to process, or to use specific techniques to minimize quartz loss during Be-purification, may depend on the laboratory standards, costs, processing-times, and the feasibility of acquiring large amounts of sample.

6.6.3 WHICH LIMIT DO I USE?

Given the high confidence intervals that are often necessary in particular applications of chemistry, such as when dealing with contaminants [*McKillup and Darby Dyar,* 2010], the IUPAC and ACS have defined the LOQ as the limit for the quantitative use of the sample data. However, for cosmogenic studies, there is little need for such high confidence intervals and consequently conservative interpretations.

As such, the choice of the LOD as the lower threshold is probably reasonable, and would still allow users to distinguish samples from blanks with a reliability of 99.9%. In general, due to the strong dependency of the determination limits on the blank and sample distributions and on the applied blank correction method, each case should be evaluated individually.

6.6.4 IMPACTS ON GEOMORPHIC APPLICATIONS

With our blank and sample datasets, we demonstrated that, depending on which blank correction method is applied, the number of samples that can reliably be distinguished from blanks may vary strongly. In particular, considering only the LOD values (both for the 8 and 61 subsets of blanks), we showed that the percentage of samples that cannot be reliably distinguished from the blanks varies between 5% and 37%. This range shows, for geomorphic applications, that the precision of the measurements and the cleanliness of the laboratory can have a strong impact on the final interpretations of the data. For example, using low-ratio carrier and increasing the AMS current, Schaefer et al. (2009) were able to obtain very low and precise blank values (between 6,000 and 26,000 atoms with a 1σ error < 10%) and very precise sample measurements (between 70,000 and 1,000,000 atoms with a 1σ error < 10%). As such, their blank and sample distributions did not overlap. Indeed, applying the IUPAC recommendations to this dataset, the calculation of the LOD would give a value around 58,500 ^{10}Be atoms, implying that all the samples would be statistically distinguishable from the blanks with a confidence of 99.9%. With these highly precise results, the authors measured exposure ages as young as 150 ± 15 years, dating moraines of the Little Ice Age.

In a case of similarly young boulders and rapidly denuding tributary catchments on an alluvial fan, *Savi et al.,* [in press] showed that depending on which correction method is applied, the propagated error in the final exposure ages or denudation rates can vary up to 20%. This resulted in 3 samples (almost one fifth of a first set of processed samples) that could not be distinguished from the blanks, and could only be used to limit the exposure ages or denudation rates. However, by increasing the amount of sample processed during the chemical procedure for the following set of samples, and thus increasing the precision of the AMS measurements, all the remaining samples could be statistically distinguished from the blanks at a confidence of 99.9%. This resulted in quantifiable exposure ages as low as 50 ± 8 years, and denudation rates as fast as 13.8 ± 2.6 mm/yr. These results highlight how, using the appropriate techniques in the laboratory and being aware of the method's limitation, it would be possible to measure incredibly young ages and fast denudation rates. This may open a whole set of new possibilities for the use of cosmogenic nuclide techniques in geomorphic studies.

6.7 CONCLUSIONS

In this paper we have discussed the challenges related to the use of cosmogenic nuclide techniques in the case of low ^{10}Be content, which are typically found in samples collected from rapidly eroding landscapes, young surfaces, or when a very limited amount of the target mineral is available for analysis. By adapting a method commonly used in analytical chemistry, we describe an approach to define a lower threshold above which samples with low ^{10}Be content can be used in a quantitative way, accounting for laboratory cleanliness and contamination that may occur during the chemical procedure. This approach can be applied by the end-user of AMS measurements based on a number of different options for characterizing laboratory blanks.

Our analysis demonstrates the importance of producing low, precise, and reproducible blank measurements, as they reduce the differences among various blank-correction procedures and decrease the value of the various determination limits, therefore increasing the number of samples that are distinguishable from laboratory blanks. When the different blank-correction methods result in substantial differences, we suggest calculating and reporting the results of all three methods (single-batch-blank correction, average-blank correction, and long-term average correction) to better quantify the influence of uncertainties on the results. Particularly for samples with low ^{10}Be content, it is important to report detailed information about the laboratory protocols, blank measurements (including both the measured ratios and the amount of added carrier, in order to calculate the number of ^{10}Be atoms), the applied blank correction, and the value of the chosen determination limit (i.e., LOD).

ACKNOWLEDGMENTS

This work has been funded by the Swiss National Science Foundation (grants PBBEP2_146196 and P300P2_151344 awarded to S. Savi), the Alexander von Humboldt Foundation (awarded to S. Savi) and the Emmy Noether program of the German Science Foundation (grant SCHI 1241/1-1, awarded to T. Schildgen). We greatly acknowledge the helpful and detailed discussions with S. A. Binnie of the University of Cologne and the detailed comments of Lee Corbett and of an anonymous reviewer on an earlier version of this manuscript.

APPENDIX A4

The supporting information of this chapter is available in the attached CD.

CHAPTER 7
DISCUSSION AND CONCLUSIONS

The main aim of this study was to decipher spatiotemporal variability and trend patterns of rainfall and discharge in the subtropical southern Central Andes of NW Argentina during the past seven decades. Particular emphasis was devoted to documenting the rates and magnitudes of changes of extreme hydro-meteorological events in this region. The rationale for this choice was to improve our knowledge of hydrologic and geomorphic processes that shape landscapes in high-elevation mountains, but also for implementing effective measures anticipating future environmental impacts and mitigating the socio-economic effects of a changing climate.

The southern Central Andes encompass low-elevation to medium-elevation, wet and densely vegetated areas on the eastern flanks of the orogen, and high-elevation, sparsely vegetated arid regions to the west (Figures 2.3 and 2.4). Together, both end-member regions constitute an integral part of the pronounced E-W gradient in topography, rainfall, and surface-processes across the Andean orogen; these conditions are particularly well expressed by differences in stream-power and depositional characteristics, which make this region a premier target for studying climate variability and its impacts in a high-elevation environment.

To test if and to which degree rainfall and river discharge have changed in this region over the ultimate seven decades (from 1940 to 2015) I set out to evaluate if hydrological changes were related to variations in magnitude and/or frequencies of extreme hydro-meteorological events. Furthermore, the link between river discharge and large-scale modes of climate variability, such as the El Niño Southern Oscillation [*Horel and Wallace*, 1981; *Ropelewski and Halpert*, 1987], was investigated on different timescales, to decipher possible forcing mechanisms of hydro-meteorological variables in the semi-arid, highly vulnerable high-mountain environment during the past decades. Finally, having hypothesized that variations in extreme hydro-meteorological events represent the climatic driver of widespread aggradation in the intermontane drainage basins of the southern Central Andes, I contributed to improve the quantitative evaluation of cosmogenic-nuclide derived erosion rates in this high-mountain environment.

I addressed these topics in four independent, yet thematically linked studies in chapters 3 through 6. Here, I summarize and integrate the main key findings, focusing on the hydro-meteorological aspects, and discuss them in a regional perspective.

7.1 RAINFALL AND RIVER-DISCHARGE TRENDS DURING THE LAST SEVEN DECADES

In this part of the study, I distinguished between three geographic areas characterized by pronounced topographic, environmental, and climatic differences: (1) the *low elevations* (< 0.5 km) east of the NW Argentine Andes, with low topographic slopes and low relief values; (2) the *intermediate elevations* or mountain-front area - an area characterized by a highly dynamic surface-process regime, with steep slopes and high relief values with elevations between about 0.5 and 3 km; and (3), the *high elevations* above 3 km to the west of the mountain front, with steep slopes and high relief.

The analysis of rainfall variability and trend patterns in NW Argentina was based on daily rain-gauge observations (40 gauges, from 1950 to 2014), mostly located at low and intermediate elevations on the eastern flank of the Andes (Figure 3.2). In addition, two gridded datasets (CPC-uni, from 1979 to 2014 [*Xie et al.*, 2007], and TRMM 3B42 V7 data from 1998 to 2014 [*Huffman et al.*, 2007]), were also used to achieve higher spatiotemporal resolution. For the analysis of rainfall variability, three different time intervals were investigated: 1950-2014, 1979-2014, and 1998-2014, depending on availability. For river discharge, I used daily time series (from 1940 to 2015) from small to medium-size river catchments (10^2-10^4 km^2) located in the intermediates elevations of the study area (Figure 4.1). The trend analysis was performed on two different time intervals and using two different methods: from 1940 to 1999 I applied quantile regression [*Koenker and Bassett Jr.*, 1978], and from 1940 to 2015 I worked with the Hilbert-Huang Transform analysis [*Huang*, 2005]. This choice was taken to test the robustness of the trend analysis and it was determined by data availability and quality. In the following sections, I integrate the key results of rainfall and river-discharge time series analysis focussed on two different time intervals, from 1940 to 2015 and from 1979 to 2014. I refer to these intervals as the *long-term interval* and the *interval after the change point*, respectively. I emphasize that, due to data availability, for each of these two time intervals, rainfall and river-discharge time series are relevant to different portions of the entire time interval (e.g., for the long-term interval rainfall time series are available from 1950 to 2014, whereas river discharge is available from 1940 to 2015).

7.1.1 THE LONG-TERM INTERVAL (1940-2015)

For the long-term interval, only station data were available (n=13) for the rainfall analysis, resulting in low spatial resolution, especially at high-elevation regions. Robust findings were obtained at intermediate elevations, characterized by the highest rainfall station density and by the presence of streamflow-gauging stations.

For the interval between 1950 and 2014 I identified an increase in the annual total rainfall amount and wet-days frequency at the transition between the low and intermediate elevations. This result agrees with previous studies documenting positive rainfall trends in Argentina and in all of South America during approximately the same time intervals [e.g., *Barros et al.*, 2000; *Haylock et al.*, 2006]. Importantly, my study revealed that low and high elevations did not exhibit any spatially coherent long-term trend pattern.

Interestingly, while analyzing the daily rainfall-frequency distribution, I often observed small or no changes in median values of the rainfall magnitude, whereas the extreme rainfall events (≥95th percentiles) exhibited a significant tendency towards local intensification or attenuation. At seasonal scale, a trend for a wetter wet season and, to a lesser degree, a drier dry season was also found. In addition, during the wet season extreme events (> 95th percentile) underwent a significant increase in magnitude, but not in frequency at the transition zone between the low and intermediate elevations. Despite the limited availability of time series at high elevations for the long-term interval (only two time series were available), I also found evidence for increasing magnitudes of extreme rainfall events in the northernmost sector of the high elevations of my study area (chapter 3). This observation agrees with previous studies in Argentina and South America, showing increasing trends in heavy precipitation on approximately during the same time interval [*Penalba and Robledo*, 2010; *Skansi et al.*, 2013].

River discharge time-series analysis, based on the quantile regression [*Koenker and Bassett Jr.*, 1978] and the Hilbert-Huang Transform analysis [*Huang*, 2005]), revealed a spatially coherent and statistically significant increase in discharge for the time interval between 1940 and 2015, for drainage basins located at the intermediate elevations (chapters 4 and 5). In addition, higher trends were documented for the uppermost percentiles (chapter 4). This long-term increase of river discharge is in good agreement with the findings of the rainfall time-series analysis at intermediate elevations, documenting the robustness of this result, which highlights an intensification of the hydrological cycle in NW Argentina between 1940 and 2015 (Figure 7.1).

I furthermore documented a rapid increase in the amount of discharge during the period 1971-1977, most likely linked to the 1976-77 climate shift [*Graham*, 1994; *Miller et al.*, 1994]. This finding agrees with the study of *Jacques-Coper and Garreaud* [2015], who showed a pronounced positive shift of mean precipitation between periods of ten years before 1975 and ten years after 1979 east of the southern Central Andes. In addition, I found most pronounced trends for high percentiles (>70th) of daily river discharge in agreement with the outcomes of the rainfall time series analysis. For example, in the upper Rio Bermejo basin of the northernmost Argentine Andes the quantitative evaluation of the changes in water volumes across

the change point revealed that the mean annual discharge increased by 40% ± 15% over seven years.

7.1.2 THE INTERVAL AFTER THE CHANGE POINT (1979-2014)

For the time interval after the change point, a higher, yet uneven, density characterized the rainfall-station dataset with respect to the long-term time interval. However, this limitation was overcome by integrating station-data time series with CPC and TRMM gridded datasets, resulting in high spatiotemporal resolution in the study area, including high elevations.

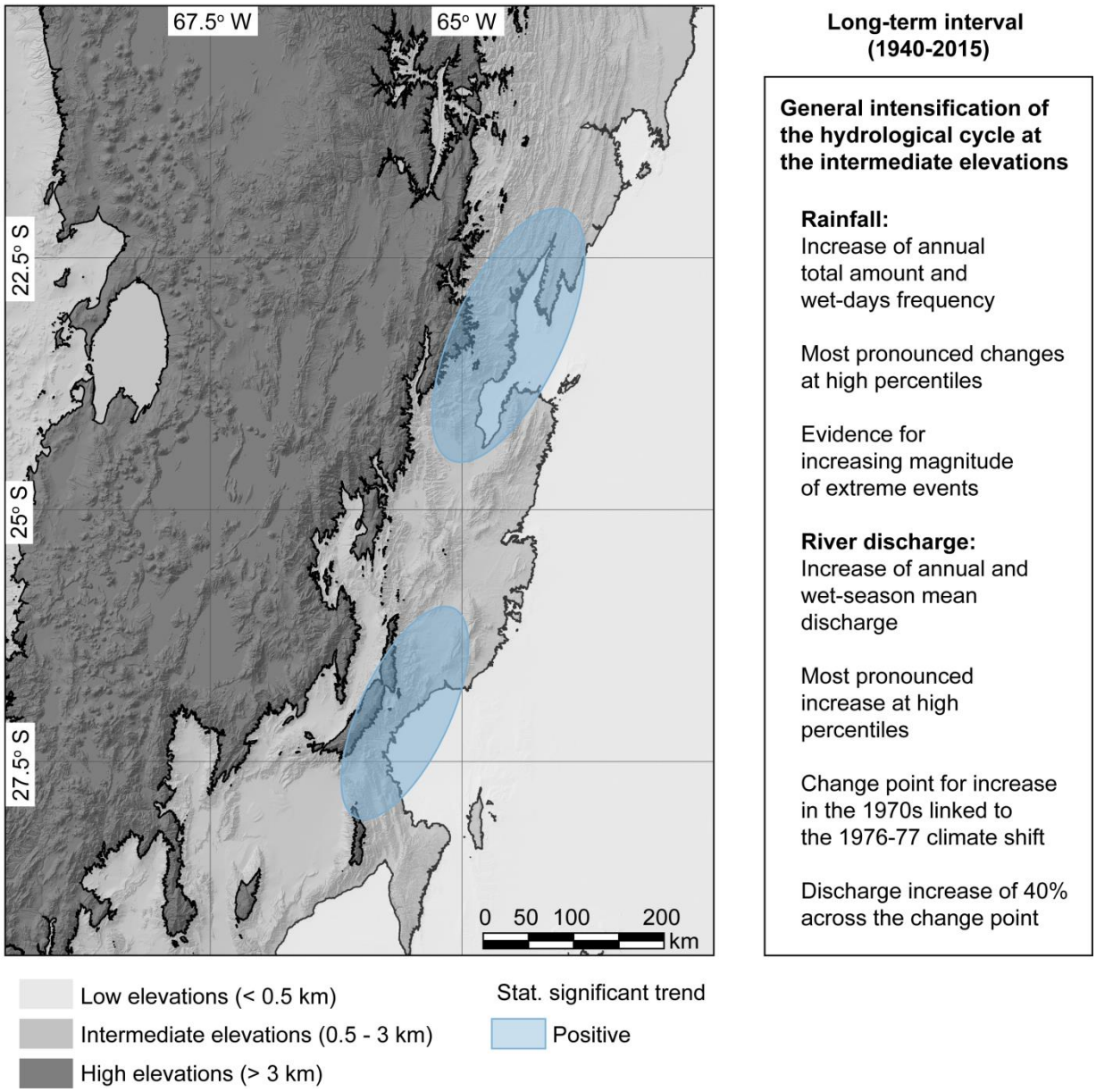

Figure 7.1 Overview of the study region with the described three main topographic areas (low, intermediate, and high elevations, see text) and the key results of the rainfall and river discharge long-term (between 1950 and 2014 for rainfall, and 1940 and 2015 for river discharge) trend analysis, showing an overall intensification of the hydrological cycle at intermediate elevation sectors (0.5 – 3 km asl).

For the time interval between 1979 and 2014, both rain-gauge measurements and the CPC dataset revealed a significant trend towards decreasing annual rainfall total amounts at low elevations. This is also confirmed by TRMM data during the time interval between 1998 and 2014. Instead, at high elevations, extensive areas on the arid southern Andean Plateau (Puna de Atacama) have recorded increasing annual rainfall total amounts and, to a lesser degree, frequency of wet days during the time interval between 1979 and 2014 (Figure 7.2). In addition, my analysis revealed that extensive areas at high elevations on the Puna de Atacama Plateau have experienced increasing magnitudes of extreme rainfall events, at least from 1979, as suggested by CPC data analysis and TRMM data from 1998 (chapter 3). Although the frequency of extreme rainfall events did not show any statistically significant trends, I interpreted the previous results to indicate significant changes, particularly in the magnitude of rainstorms affecting the southern Central Andes.

The outcomes of the rainfall time-series analysis were partly in good agreement with the results of river-discharge analysis also for the time interval between 1979 and 2014. Apart from the extremely pronounced and spatially coherent increase of river discharge across the change point (between 1967 and 1981), negative trends after the change point were found at most percentiles of daily river discharge, both at annual scale and for the wet season. Importantly, high percentiles (>70th) of daily river discharge exhibited the most pronounced trends; similarly, rainfall extreme events (>95th percentile) showed generally the highest rate of change from 1979. In addition, as in the case of river discharge, I observed a rainfall-trend reversal starting in 1979 towards decreasing rainfall amounts in the topographic transition zone between the low (<0.5km) and the intermediate elevations (0.5 - 3 km) to the west.

Few previous studies associated the abrupt increase of rainfall and river discharge in several major South American river basins with the 1976-77 climate shift [e.g., *Minetti and Vargas*, 1998; *Rusticucci and Penalba*, 2000; *Labat et al.*, 2004; *Carvalho et al.*, 2011; *Jacques-Coper and Garreaud*, 2015]. However, to my knowledge, only *Zhang et al.* [2016] documented a trend reversal in annual rainfall total amounts in southeastern South America (SESA), even though this trend started at the beginning of 21st century, and not after the 1970s change point.

Interestingly, by testing the hypothesis if the rainfall trend reversal observed in the southern Central Andes was related to the 1976-77 climate shift, I did not find a spatiotemporally coherent change signal in the rainfall pattern. This is in contrast with the river-discharge trend analysis, documenting a pronounced widespread increase during 1971-1977. Therefore, it was not possible to unambiguously identify the 1976-77 climate shift as a forcing factor responsible for the changing rainfall trend in the study region (Appendix A1). I attributed this limitation to the high spatiotemporal stochasticity and intermittency of rainfall-related processes, associated with sparse and disparately distributed rainfall stations. Therefore, in contrast with the river-

discharge gauging system, the rainfall network does not fully capture the small spatiotemporal scale of convective cells that partially control the rainfall pattern at the topographic transition zone at intermediate elevations during the wet season [*Romatschke and Houze*, 2010; *Rasmussen and Houze*, 2011; *Rohrmann et al.*, 2014]. In this context, it is conceivable that, despite the fact that the trend reversal is also observed in the rainfall pattern, the timing and magnitude of the 1971-1977 change point were not properly detected by rainfall time-series analysis (Appendix A2).

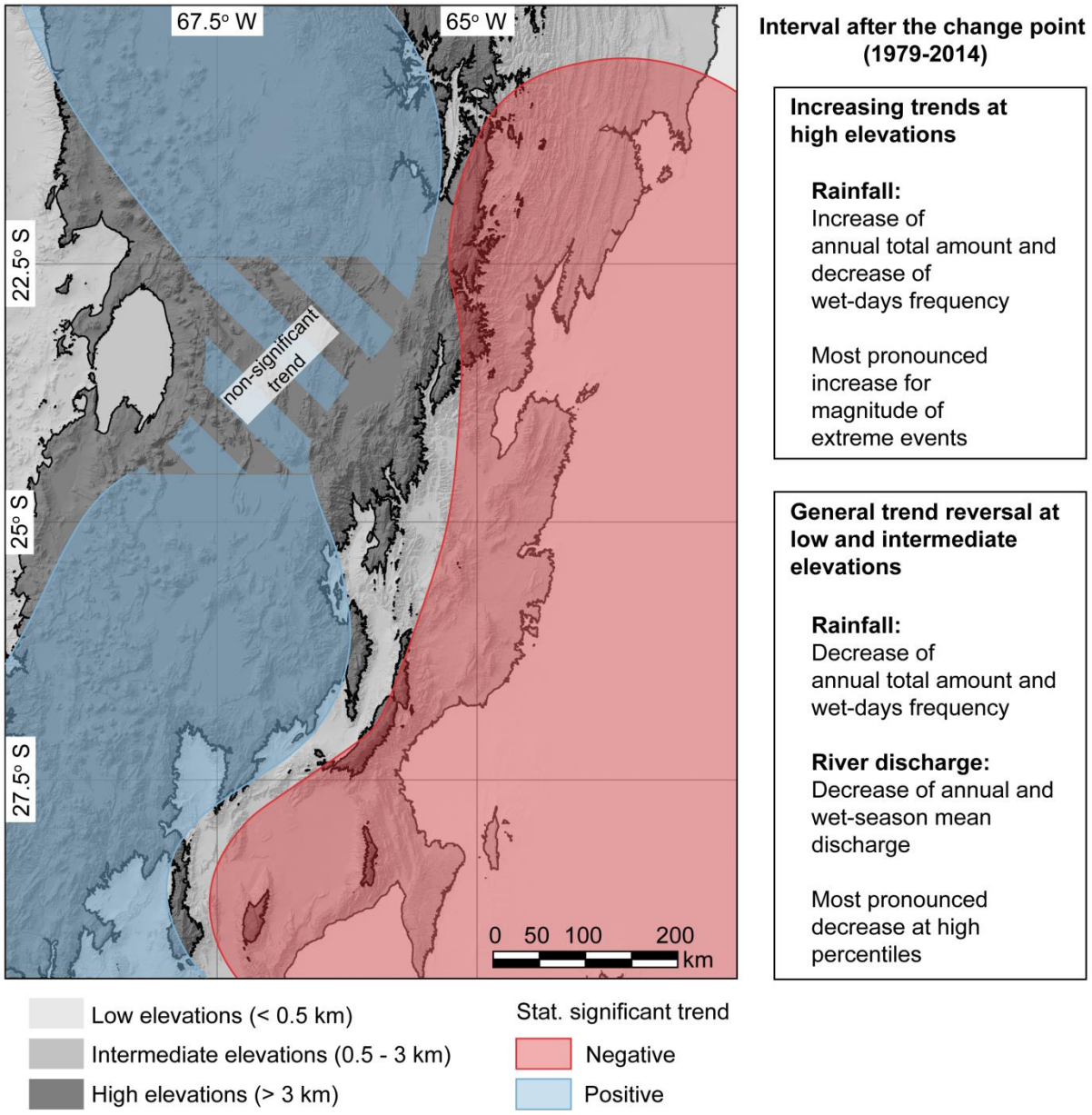

Figure 7.2 Overview of the study region with the described three main topographic areas (low, intermediate, and high elevations) and the key results of the rainfall and river-discharge trend analysis for the period after the change point (between 1979 and 2014 for rainfall, and 1978 and 1999 for river discharge). In comparison with the long-term trends (Figure 7.1), a general trend reversal is observed at low and intermediate elevations, whereas high-elevation regions exhibit increased magnitude of rainfall total amount and extreme events.

7.2 OSCILLATIONS OF RIVER DISCHARGE IN THE SOUTHERN CENTRAL ANDES AND LARGE-SCALE MODES OF CLIMATE VARIABILITY

In addition to the trend evaluation, I analyzed modes of oscillation of discharge anomalies from a set of drainage basins located on the eastern flank of the Andes of NW Argentina from 1940 to 2015. By decomposing monthly time series of the normalized discharge anomaly with the Hilbert-Huang Transform [*Huang*, 2005], I observed that in the study region discharge variability can be described by five quasi-periodic statistically significant oscillatory modes, with mean periods varying from 1y to ~20y.

Most of the river-discharge variability is associated with the South American Monsoon System on annual timescale, but still longer timescales (multi-annual and multi-decadal) may explain large parts of the river-discharge variance. In light of the fact that the physical processes controlling changes in the hydrologic system in South America have remained unclear [*Robertson and Mechoso*, 1998; *Marengo*, 2004; *García and Mechoso*, 2005; *Antico and Kröhling*, 2011; *Antico and Torres*, 2015], I tested for a possible link between river-discharge variations and large-scale climate modes of variability, using different indices describing Pacific and Atlantic Oceans climate variability (i.e., ENSO BEST, TSA, SSN, and PDO, see chapter 5 for acronym definitions). The choice of these indices is important because they are associated with ocean-atmosphere coupling processes, taking into account various modes of variability of both Pacific and Atlantic Ocean basins.

In summary, this analysis clearly showed that discharge variability is primarily linked to Pacific Ocean variability (PDO phases) at multi-decadal timescales (~20y) and, to a lesser degree, to TSA variability at multi-annual timescales (~2-5y). Less pronounced manifestations were also documented for a link between discharge variability in the study area and both, ENSO and solar activity.

Importantly, the length of the available time series (75y) allowed me to decompose them into oscillatory modes associated with timescales encompassing no more than 20-30y. Hence, longer time series could help deciphering linkages between river-discharge variations and modes of climate variability at timescales longer than 20-30 years (e.g., the Atlantic Multi-Decadal Oscillation (AMO), typically associated with timescales of ~70y [*Enfield et al.*, 2001; *Antico and Torres*, 2015]).

Interestingly, some previous studies suggested ENSO as a primary control of river-discharge variability of some major South American rivers (i.e., Uruguay, Paraná, Paraguay, Negro, La Plata) [*Robertson and Mechoso*, 1998; *García and Mechoso*, 2005; *Pasquini and Depetris*, 2007] as well as for Argentine rivers in the subtropical Andes (35°S) [*Compagnucci et al.*, 2000]. In contrast, my analysis

revealed a relatively weaker link between ENSO and river-discharge variability in the southern Central Andes between 1940 and 2015, whereas PDO phases and SST anomalies of the tropical Atlantic represent a relatively stronger driver.

The multi-decadal link with PDO phases was already suggested by *Marengo* [2009] and *Marengo et al.* [2012] following their analysis of discharge variability of the Amazon river. In addition, *Antico et al.* [2014] proposed a link between the sea-surface temperature variability of the Pacific Ocean and streamflow of the Paraná river. Linkages between SST anomalies in the tropical Atlantic and discharge of several South American rivers were also observed by *García and Mechoso* [2005] and *Antico and Torres* [2015], although at decadal and multi-decadal timescales.

Finally, with this study I showed that the discharge change point observed from 1971 and 1977 and associated with the 1976-77 climate shift can be interpreted as the result of the combination of the following phenomena: (1) the long-term increasing trend between 1940 and 2015, and (2) the periodic enhancement of discharge occurred between the middle 1970s and the early 1990s linked to the PDO phase transition and TSA variability at multi-decadal and multi-annual timescales, respectively.

7.3 Concluding Remarks

This study revealed that low-, intermediate, and high elevations in the Andes of NW Argentina respond differently to changing climate conditions. In particular, in the long-term I documented statistically significant changes at the transition zone between low and intermediate elevations at the eastern flank of the Andes.

The observed increase in rainfall, both in total amount and extreme-event intensity, is consistent with the findings by Hsu et al. [2011]. These authors showed that total monsoon precipitation has had statistically significant positive trends during the past 30 years related to an increase in global mean-surface temperatures. Carvalho and Cavalcanti [2016] observed that the reanalysis products (CFSR and NCEP/NCAR) indicate a progressive increase in low-level tropospheric temperatures over tropical South America during the monsoon season. This can potentially alter ocean-land differential heating affecting monsoonal circulation and moisture transport from the tropics to the subtropics. Enhanced monsoonal circulation could affect the strength of the SALLJ and/or the SACZ, which are the most important phenomena controlling moisture advection in the subtropics and the precipitation systems affecting the southern Central Andes [*Gandu and Silva Dias*, 1998; *Marengo et al.*, 2012, and references cited within].

Interestingly, in their model-based study *Zhang et al.* [2016] proposed an additional explanation for the multi-decadal trend towards wetter conditions during the 20th century in SESA. Despite some differences in the amplitude of the changes between model estimations and observations, *Zhang et al.* [2016] showed that the

observed trend toward wetter conditions is likely driven by radiative forcing associated with increasing greenhouse gases, which would cause the southward tropical expansion. SESA is located underneath the subtropical descending branch of the Hadley cell, which usually suppresses convection activity and forces dry conditions at the surface. According to *Zhang et al.* [2016], the southward tropical expansion would have moved the subtropical descending branch of the Hadley cell away from SESA, resulting in the observed rainfall increase. Similar mechanisms could potentially explain the enhancement of rainfall magnitude, particularly for rainstorm events, during the last seven decades in the NW Argentine Andes.

Against the backdrop of changing climate, these hypotheses (i.e., enhancement of the monsoonal circulation and/or expansion of the tropics, and the linkage with increasing radiative forcing and a trend toward wetter conditions) are crucial for anticipating future environmental impacts on the environment and mitigating the effects of a warming climate on society.

Importantly, the CMPI5 projections for rainfall in South America for the end of this century showed a continued poleward intensification of the SAMS south of 20°, associated with a positive trend in the frequency of heavy and extreme rainfall events in southern and southeastern Brazil and the La Plata basin [*Carvalho and Cavalcanti*, 2016]. Furthermore, although an overall relatively weak signal of change for the entire wet season (October-March) was found for the Andean plateau, the study of *Carvalho and Cavalcanti* [2016] predicted for the end of this century a positive significant trend signal in the Argentine sector of the Andean plateau.

Despite the significant advance and improvement of future climate model projections, it has been also recognized that several process affecting climate variability (e.g., teleconnections with coupled modes of climate variability such as the Madden-Julian Oscillation (MJO) [*Madden and Julian*, 1971; *Jones et al.*, 2004], ENSO, or PDO) still need to be properly simulated to produce realistic scenarios of climate change in the SAMS. This is particularly true for the low- and intermediate elevations in NW Argentine Andes, where my study revealed a strong link between PDO phases and river-discharge variability at multi-decadal timescales. These new insights into climate variability and the hydrological cycle in the southern Central Andes can help advance our understanding of past climate changes as well as improving future predictions of variations in the hydrological cycle, particularly with respect to extreme hydro-meteorological events and their impact on the surface-process regime.

In fact, based on the evidence provided by this study, I suggest that the widespread abrupt increase in river discharge observed during the 1970s in the intermediate elevations of the NW Argentine Andes resulted partly from the cyclic enhancement of discharge linked to the PDO phase transition and TSA variability

during the 1970s. I also showed that, in association with this sudden increase of river discharge, the most pronounced changes in rainfall affected large-magnitude events (high rainfall percentiles). This relationship leads me to hypothesize a link between hydro-meteorological drivers and sediment-transport processes in this semi-arid environment. Accordingly, the increase in discharge, particularly in the case of large-magnitude events, has resulted in increased hillslope destabilization and erosion, followed by massive sediment transfer through the fluvial system. However, the subsequent decrease of river discharge observed after the 1970s would have ultimately caused aggradation in low-elevation areas, as the fluvial system was overwhelmed by the sustained influx of coarse sediment, causing infrastructural damage and the loss of agricultural land [*Rivelli*, 1999; *Cencetti and Rivelli*, 2011; *Marcato et al.*, 2012].

Finally, I recall that, during the time span considered in my study, extreme hydro-meteorological events exhibit pronounced variations not only at intermediate elevations, but also in the arid, high-elevation southern Andean plateau, suggesting that this region responds more readily to changes in large-scale circulation. However, it still remains unclear which processes ultimately drive the differential trend pattern observed in rainfall between low-intermediate (decreasing trend) and high elevations (increasing trend) following the sudden increase during the 1970s. This is due to the limited availability of both rainfall and river-discharge observations in terms of station density and time-series length. Therefore, future studies should strive to implement methodologies alternative to long-term trend analysis and mode decomposition, such as the evaluation of reanalysis products and/or regional climate models outputs [*Kalnay et al.*, 1996; *Skamarock et al.*, 2005; *Bosilovich et al.*, 2008; *Norris et al.*, 2016]. With this approach, it might be eventually possible to further test the trend toward wetter conditions observed at high elevations and to decipher the causes of differential trend patterns in the low elevations of the eastern flank of the NW Argentine Andes.

REFERENCES

AghaKouchak, A., and N. Nasrollahi (2010), Semi-parametric and parametric inference of extreme value models for rainfall data, *Water Resour. Manag.*, *24*(6), 1229–1249, doi:10.1007/s11269-009-9493-3.

Agosta, E. A., and R. H. Compagnucci (2008), The 1976/77 austral summer climate transition effects on the atmospheric circulation and climate in Southern South America, *J. Clim.*, *21*(17), 4365–4383, doi:10.1175/2008JCLI2137.1.

Alexander, M. A., I. Bladé, M. Newman, J. R. Lanzante, N. C. Lau, and J. D. Scott (2002), The atmospheric bridge: The influence of ENSO teleconnections on air-sea interaction over the global oceans, *J. Clim.*, *15*(16), 2205–2231, doi:10.1175/1520-0442(2002)015<2205:TABTIO>2.0.CO;2.

Alonso, R. N., T. E. Jordan, K. T. Tabbutt, and D. S. Vandervoort (1991), Giant evaporite belts of the Neogene central Andes, *Geology*, *19*(4), 401, doi:10.1130/0091-7613(1991)019<0401:GEBOTN>2.3.CO;2.

Analytical Methods Committee, 1987. Recommendations for the Definition, Estimation and Use of the Detection Limit. Analyst, 112.

Anderson, R.S., Repka, J.L., Dick, G.S., 1996. using in situ 10Be and 26Al. Geology, 24(1), 47–51.

Antico, A., and D. M. Kröhling (2011), Solar motion and discharge of Paraná River, South America: Evidence for a link, *Geophys. Res. Lett.*, *38*(19), 1–5, doi:10.1029/2011GL048851.

Antico, A., and M. E. Torres (2015), Evidence of a decadal solar signal in the Amazon River: 1903 to 2013, *Geophys. Res. Lett.*, *42*, doi:10.1002/2015GL066089.

Antico, A., G. Schlotthauer, and M. E. Torres (2014), Analysis of hydroclimatic variability and trends using a novel empirical mode decomposition: Application to the Paraná River Basin, *J. Geophys. Res. Atmos.*, *119*, 1218–1233, doi:10.1002/2013JD020420.

Antolini, G., L. Auteri, V. Pavan, F. Tomei, R. Tomozeiu, and V. Marletto (2015), A daily high-resolution gridded climatic data set for Emilia-Romagna, Italy, during 1961-2010, *Int. J. Climatol.*, n/a-n/a, doi:10.1002/joc.4473.

Apaéstegui, J. et al. (2014), Hydroclimate variability of the northwestern Amazon Basin near the Andean foothills of Peru related to the South American Monsoon System during the last 1600 years, *Clim. Past*, *10*(6), 1967–1981, doi:10.5194/cp-10-1967-2014.

Auer, I. et al. (2007), HISTALP – historical instrumental climatological surface time series of the Greater Alpine Region Ingeborg, *Int. J. Climatol.*, *27*, 17–46, doi:10.1002/joc.1377.

Balco G., 2011. Contributions and unrealized potential contributions of cosmogenic-nuclide exposure dating to glacier chronology, 1990-2010. Quaternary Science Reviews, 30, 3-27.

Bandyopadhyay, J., D. Kraemer, R. Kattelmann, and Z. W. Kundzewicz (1997), Highland waters: A resource of global significance, in *Mountains of the World: A Global Priority*, edited by B. Messerli and J. Ives, pp. 131–155, Parthenon, New York.

Barnett, T. P., J. C. Adam, and D. P. Lettenmaier (2005), Potential impacts of a

warming climate on water availability in snow-dominated regions., *Nature*, *438*(7066), 303–309, doi:10.1038/nature04141.

Barros, V., M. E. Castañeda, and M. Doyle (2000), Recent Precipitation Trends in Southern South America East of the Andes: An Indication of Climatic Variability, in *Southern Hemisphere Paleo- and Neoclimates*, pp. 187–206.

Barros, V., T. F. Stocker, D. Qin, D. J. Dokken, K. L. Ebi, M. D. Mastrandrea, K. J. Mach, S. K. Allen, and M. Tignor (2012), IPCC, 2012 - Glossary of Terms, *Manag. Risks Extrem. Events Disasters to Adv. Clim. Chang. Adapt.*, 555–564, doi:10.1177/1403494813515131.

Barros, V., R. Clarke, and P. Silva Dias (2013), *Climate Change in the La Plata Basin*.

Barros, V. R., J. A. Boninsegna, I. A. Camilloni, M. Chidiak, G. O. Magrín, and M. Rusticucci (2015), Climate change in Argentina: Trends, projections, impacts and adaptation, *Wiley Interdiscip. Rev. Clim. Chang.*, *6*(2), 151–169, doi:10.1002/wcc.316.

Beniston, M. (2003), Climatic change in mountain regions: A review of possible impacts, *Clim. Change*, *59*(1–2), 5–31, doi:10.1023/A:1024458411589.

Beniston, M. (2012), Is snow in the Alps receding or disappearing?, *Wiley Interdiscip. Rev. Clim. Chang.*, *3*(4), 349–358, doi:10.1002/wcc.179.

Beniston, M., D. G. Fox, S. Adhikary, R. Andressen, A. Guisan, J. Holten, J. Innes, J. Maitima, M. Price, and L. Tessier (1996), Impacts of climate change on mountain regions, in *Second Assessment Report of the Intergovernmental Panel on Climate Change (IPCC)*, pp. 191–213, Cambridge University Press.

Beniston, M., H. F. Diaz, and R. S. Bradley (1997), Climatic change at high elevation sites: an overview, *Clim. Change*, *36*, 233–251, doi:10.3406/rga.2005.2342.

Beniston, M., M. Stoffel, and M. Hill (2011), Impacts of climatic change on water and natural hazards in the Alps: Can current water governance cope with future challenges? Examples from the European "ACQWA" project, *Environ. Sci. Policy*, *14*(7), 734–743, doi:10.1016/j.envsci.2010.12.009.

Berbery, E. H., and V. R. Barros (2002), The Hydrologic Cycle of the La Plata Basin in South America, *J. Hydrometeorol.*, *3*(6), 630–645.

Bernal, E., 2014. Limit of Detection and Limit of Quantification Determination in Gas Chromatography, Advances in Gas Chromatography. Dr Xinghua Guo (Ed.), ISBN: 978-953-51-1227-3, InTech, DOI: 10.5772/57341.

Bhutiyani, M. R., V. S. Kale, and N. J. Pawar (2008), Changing streamflow patterns in the rivers of northwestern Himalaya: Implications of global warming in the 20th century, *Curr. Sci.*, *95*(5), 618–626.

Bianchi, A. R., and C. E. Yañez (1992), *Las precipitaciones en el Noroeste Argentino, Inst. Nac. Tecnol. Agropecu. Estac´ıon Exp.*, edited by A. Agropecuaria Salta.

Bierman, P., and E. J. Steig (1996), Estimating rates of denudation using cosmogenic isotope abundances in sediment, *Earth Surf. Process. Landforms*, *21*(2), 125–139.

Bierman, P., E. J. Steig, I. Received, and I. January (1996), Estimating Rates of Denudation Using Cosmogenic Isotope Abundances in Sediment, *Earth Surf. Process. Landforms*, *21*, 125–139.

Bierman, P.R., Caffee, M.W., Davis, P.T., Marsella, K., Pavich, M., Colgan, P., Mickelson, D., Larsen, J., 2002. Rates and Timing of Earth Surface Processes From In Situ-Produced Cosmogenic Be-10. Rev. Mineral. Geochemistry 50, 147–205. doi:10.2138/rmg.2002.50.4

Binnie, S. A., Phillips, W.M., Summerfield, M. a., Keith Fifield, L., 2006. Sediment mixing and basin-wide cosmogenic nuclide analysis in rapidly eroding mountainous environments. Quat. Geochronol. 1, 4–14. doi:10.1016/j.quageo.2006.06.013

Binnie, S. A., Dunai, T.J., Voronina, E., Goral, T., Heinze, S., Dewald, A., 2015. Separation of Be and Al for AMS using single-step column chromatography. Nuclear Instruments and Methods in Physics Research B. doi: http://dx.doi.org/10.1016/j.nimb.2015.03.069

von Blanckenburg, F., Hewawasam, T., Kubik, P.W., 2004. Cosmogenic nuclide evidence for low weathering and denudation in the wet, tropical highlands of Sri Lanka. J. Geophys. Res. 109, F03008. doi:10.1029/2003JF000049

von Blanckenburg, F. (2005), The control mechanisms of erosion and weathering at basin scale from cosmogenic nuclides in river sediment, *Earth Planet. Sci. Lett.*, *237*(3–4), 462–479, doi:10.1016/j.epsl.2005.06.030.

von Blanckenburg, F., Wittmann, H., Schuessler, J.A., 2016. HELGES: Helmholtz Laboratory for the Geochemistry of the Earth Surface. Journal of Large-Scale Research Facilities 2, A84.

Bocchiola, D. (2014), Long term (1921-2011) hydrological regime of Alpine catchments in Northern Italy, *Adv. Water Resour.*, *70*, 51–64, doi:10.1016/j.advwatres.2014.04.017.

Boers, N., B. Bookhagen, N. Marwan, J. Kurths, and J. A. Marengo (2013), Complex networks identify spatial patterns of extreme rainfall events of the South American Monsoon System, *Geophys. Res. Lett.*, *40*(16), 4386–4392, doi:10.1002/grl.50681.

Boers, N., R. V. Donner, B. Bookhagen, and J. Kurths (2014a), Complex network analysis helps to identify impacts of the El Niño Southern Oscillation on moisture divergence in South America, *Clim. Dyn.*, doi:10.1007/s00382-014-2265-7.

Boers, N., B. Bookhagen, H. Barbosa, N. Marwan, and J. Kurths (2014b), Prediction of extreme floods in the Central Andes by means of Complex Networks, *Nat. Commun.*, *5*(5199), doi:10.1038/ncomms6199.

Boers, N., A. Rheinwalt, B. Bookhagen, H. M. J. Barbosa, N. Marwan, J. A. Marengo, and J. Kurths (2014c), The South American rainfall dipole: A complex network analysis of extreme events, *Geophys. Res. Lett.*, *41*(20), 7397–7405, doi:10.1002/2014GL061829.

Boers, N., B. Bookhagen, J. A. Marengo, N. Marwan, J.-S. von Storch, and J. Kurths (2015a), Extreme Rainfall of the South American Monsoon System: A Dataset Comparison Using Complex Networks, *J. Clim.*, *28*(3), 1031–1056, doi:10.1175/JCLI-D-14-00340.1.

Boers, N., B. Bookhagen, N. Marwan, and J. Kurths (2015b), Spatiotemporal characteristics and synchronization of extreme rainfall in South America with focus on the Andes Mountain range, *Clim. Dyn.*, doi:10.1007/s00382-015-2601-6.

Bolch, T. et al. (2012), The State and Fate of Himalayan Glaciers, *Science (80-.).*, *336*(6079), 310–314, doi:10.1126/science.1215828.

Bombardi, R. J., L. M. V Carvalho, and C. Jones (2013), Simulating the influence of the South Atlantic dipole on the South Atlantic convergence zone during neutral ENSO, *Theor. Appl. Climatol.*, 1–19, doi:10.1007/s00704-013-1056-0.

Bookhagen, B., and D. W. Burbank (2010), Toward a complete Himalayan hydrological budget: Spatiotemporal distribution of snowmelt and rainfall and

their impact on river discharge, *J. Geophys. Res.*, *115*(F3), F03019, doi:10.1029/2009JF001426.

Bookhagen, B., and M. R. Strecker (2008), Orographic barriers, high-resolution TRMM rainfall, and relief variations along the eastern Andes, *Geophys. Res. Lett.*, *35*(6), L06403, doi:10.1029/2007GL032011.

Bookhagen, B., and M. R. Strecker (2011), Modern Andean Rainfall Variation during ENSO Cycles and its Impact on the Amazon Drainage Basin, in *Amazonia: Landscape and Species Evolution: A look into the past*, edited by C. Hoorn and F. P. Wesselingh, pp. 223–241, Blackwell Publishing, Oxford, UK.

Bookhagen, B., and M. R. Strecker (2012), Spatiotemporal trends in erosion rates across a pronounced rainfall gradient: Examples from the southern Central Andes, *Earth Planet. Sci. Lett.*, *327–328*, 97–110, doi:10.1016/j.epsl.2012.02.005.

Bookhagen, B., R. C. Thiede, and M. R. Strecker (2005), Abnormal monsoon years and their control on erosion and sediment flux in the high, arid northwest Himalaya, *Earth Planet. Sci. Lett.*, *231*(1–2), 131–146, doi:10.1016/j.epsl.2004.11.014.

Bosilovich, M. G., J. Chen, F. R. Robertson, and R. F. Adler (2008), Evaluation of Global Precipitation in Reanalyses, *J. Appl. Meteorol. Climatol.*, *47*(9), 2279–2299, doi:10.1175/2008JAMC1921.1.

Bradley, R. S., M. Vuille, H. F. Diaz, and W. Vergara (2006), Threats to Water Supplies in the Tropical Andes, *Science (80-.).*, *312*, 1755–1756.

Brown, E.T., Brook, E.J., Raisbeck, G.M., Yiou, F., Kurz, M.D., 1992. Effective attenuation lengths of cosmic rays producing 10Be and 26Al in quartz: implications for exposure age dating. Geophys. Res. Lett. 19, 369–372. doi:10.1029/92GL00266

Brown, E.T., Edmond, J.M., Raisbeck, G.M., Yiou, F., Kurz, M.D., Brook, E.J., 1991. Examination of surface exposure ages of Antarctic moraines using in situ produced 10Be and 26Al. Geochim. Cosmochim. Acta 55, 2269–2283. doi:10.1016/0016-7037(91)90103-C

Brunetti, M., M. Maugeri, and T. Nanni (2001), Changes in total precipitation, rainy days and extreme events in Northeastern Italy, *Int. J. Climatol.*, *21*(7), 861–871, doi:10.1002/joc.660.

Brunetti, M., M. Maugeri, T. Nanni, I. Auer, R. B??hm, and W. Sch??ner (2006), Precipitation variability and changes in the greater Alpine region over the 1800-2003 period, *J. Geophys. Res. Atmos.*, *111*(11), 1–29, doi:10.1029/2005JD006674.

Cade, B., and B. Noon (2003), A gentle introduction to quantile regression for ecologists, *Front. Ecol. Environ.*, *1*(8), 412–420.

Caine, N. (1980), The Rainfall Intensity: Duration Control of Shallow Landslides and Debris Flows, *Geogr. Ann. Ser. A, Phys. Geogr.*, *62*(1/2), 23–27, doi:10.2307/520449.

Callede, J., J. L. Guyot, J. Ronchail, Y. L'Hote, H. Niel, and E. De Oliveira (2004), Evolution of the River Amazon's discharge at Obidos from 1903 to 1999, *Hydrol. Sci. Journal-Journal Des Sci. Hydrol.*, *49*(1), 85–97, doi:10.1623/hysj.49.1.85.53992.

Campetella, C. M., and C. S. Vera (2002), The influence of the Andes mountains on the South American low-level flow, *Geophys. Res. Lett.*, *29*(17), 1826, doi:10.1029/2002GL015451.

Carrasco, J. F., R. Osorio, and G. Casassa (2008), Secular trend of the equilibrium-line

altitude on the western side of the southern Andes, derived from radiosonde and surface observations, *J. Glaciol.*, *54*(186), 538–550, doi:10.3189/002214308785837002.

Carretier, S. et al. (2012), Slope and climate variability control of erosion in the Andes of central Chile, *Geology*, *41*(2), 195–198, doi:10.1130/G33735.1.

Carvalho, L. M. V., and I. F. A. Cavalcanti (2016), The South American Monsoon System (SAMS), in *The Monsoon and Climate Change*, edited by L. M. V. Carvalho and C. Jones, pp. 219–267, Springer.

Carvalho, L. M. V., and C. Jones (2016), *The Monsoons and Climate Change*, Springer C., edited by L. M. V. Carvalho and C. Jones, Springer.

Carvalho, L. M. V., C. Jones, and B. Liebmann (2004), The South Atlantic Convergence Zone: Intensity, Form, Persistence, and Relationships with Intraseasonal to Interannual Activity and Extreme Rainfall, *J. Clim.*, *17*(1), 88–108.

Carvalho, L. M. V., C. Jones, A. E. Silva, B. Liebmann, and P. L. Silva Dias (2011), The South American Monsoon System and the 1970s climate transition, *Int. J. Climatol.*, *31*(8), 1248–1256, doi:10.1002/joc.2147.

Carvalho, L. M. V., C. Jones, A. N. D. Posadas, R. Quiroz, B. Bookhagen, and B. Liebmann (2012), Precipitation Characteristics of the South American Monsoon System Derived from Multiple Datasets, *J. Clim.*, *25*(13), 4600–4620, doi:10.1175/JCLI-D-11-00335.1.

Casassa, G., P. López, B. Pouyaud, and F. Escobar (2009), Detection of changes in glacial run-off in alpine basins: examples from North America, the Alps, central Asia and the Andes, *Hydrol. Process.*, *23*, 31–41, doi:10.1002/hyp.

Castino, F., B. Bookhagen, and M. R. Strecker (2017), Rainfall variability and trends of the past six decades (1950–2014) in the subtropical NW Argentine Andes, *Clim. Dyn.*, *48*, 1049–1067, doi:10.1007/s00382-016-3127-2.

Castino, F., B. Bookhagen, and M. R. Strecker (2016), River Discharge Dynamics in the Southern Central Andes and the 1976-77 Global Climate Shift, *Geophys. Res. Lett.*, doi:10.1002/2016GL070868.

Cencetti, C., and F. R. Rivelli (2011), Landslides Dams Induced by Debris Flows in Quebrada Del Toro (Province of Salta, Argentina), in *5th International Conference on Debris-Flow Hazards Mitigation: Mechanics, Pre- diction and Assessment*, pp. 645–650, Casa Editrice Università La Sapienza, Padua, Italy.

Chang, C. P., Y. Zhang, and T. Li (2000), Interannual and Interdecadal Variations of the East Asian Summer Monsoon and Tropical Pacific SSTs. Part 1: Roles of the Subtropical Ridge C.-P. Chang, Yongsheng Zhang and Tim Li, *J. Clim.*, *13*, 4310–4325, doi:10.1175/1520-0442(2000)013<4310:IAIVOT>2.0.CO;2.

Chang, C. Y., J. C. H. Chiang, M. F. Wehner, A. R. Friedman, and R. Ruedy (2011), Sulfate aerosol control of tropical atlantic climate over the twentieth century, *J. Clim.*, *24*(10), 2540–2555, doi:10.1175/2010JCLI4065.1.

Chen, M., W. Shi, P. Xie, V. B. S. Silva, V. E. Kousky, R. W. Higgins, and J. E. Janowiak (2008), Assessing objective techniques for gauge-based analyses of global daily precipitation, *J. Geophys. Res. Atmos.*, *113*(4), 1–13, doi:10.1029/2007JD009132.

Chen, S. et al. (2013), Evaluation of the successive V6 and V7 TRMM multisatellite precipitation analysis over the Continental United States, *Water Resour. Res.*, *49*(12), 8174–8186, doi:10.1002/2012WR012795.

Chen, X., Z. WU, and N. E. HUANG (2010), *The Time-Dependent Intrinsic*

Correlation Based on the Empirical Mode Decomposition.

Chevallier, P., B. Pouyaud, W. Suarez, and T. Condom (2011), Climate change threats to environment in the tropical Andes: Glaciers and water resources, *Reg. Environ. Chang.*, *11*(SUPPL. 1), 179–187, doi:10.1007/s10113-010-0177-6.

Chevallier, P., B. Pouyaud, M. Mojaïsky, M. Bolgov, O. Olsson, M. Bauer, and J. Froebrich (2012), Trends for snow cover and river flows in the Pamirs (Central Asia), *Hydrol. Earth Syst. Sci. Discuss.*, *9*(1), 29–64, doi:10.5194/hessd-9-29-2012.

Chmeleff, J., von Blanckenburg, F., Kossert, K., Jakob, D., 2010. Determination of the 10Be half-life by multicollector ICP-MS and liquid scintillation counting. Nucl. Instruments Methods Phys. Res. Sect. B Beam Interact. with Mater. Atoms 268, 192–199. doi:10.1016/j.nimb.2009.09.012

Christensen, J. H. et al. (2013), Climate Phenomena and their Relevance for Future Regional Climate Change, in *Climate Change 2013: The Physical Science Basis. Contribution of Working Group I to the Fifth Assessment Report of the Intergovernmental Panel on Climate Change*, edited by T. F. Stocker, D. Qin, G.-K. Plattner, M. Tignor, S. K. Allen, J. Boschung, A. Nauels, Y. Xia, V. Bex, and P. M. Midgley, pp. 1217–1308, Cambridge University Press, Cambridge, United Kingdom and New York, NY, USA.

Christl, M., Vockenhuber, C., Kubik, P.W., Wacker, L., Lachner, J., Alfimov, V., Synal, H. a., 2013. The ETH Zurich AMS facilities: Performance parameters and reference materials. Nucl. Instruments Methods Phys. Res. Sect. B Beam Interact. with Mater. Atoms 294, 29–38. doi:10.1016/j.nimb.2012.03.004

Clette, F., L. Svalgaard, J. M. Vaquero, and E. W. Cliver (2014), Revisiting the Sunspot Number: A 400-Year Perspective on the Solar Cycle, *Space Sci. Rev.*, *186*(1–4), 35–103, doi:10.1007/s11214-014-0074-2.

COBINABE (2010), *Generación y Transporte de Sedimentos en la Cuenca Binacional del Río Bermejo*, Buenos Aires.

Cogley, J. G., J. S. Kargel, G. Kaser, and V. van der Veen (2010), Tracking the Source of Glacier Misinformation, *Science (80-.).*, *327*, 552.

Cohen, J. C. P., M. A. F. Silva Dias, and C. A. Nobre (1995), Environmental Conditions Associated with Amazonian Squall Lines: A Case Study, *Mon. Weather Rev.*, *123*(11), 3163–3174.

Compagnucci, R. H., and W. M. Vargas (1998), Inter-annual variability of the Cuyo rivers' streamflow in the Argentinean Andean mountains and ENSO events, *Int. J. Climatol.*, *18*(14), 1593–1609, doi:10.1002/(SICI)1097-0088(19981130)18:14<1593::AID-JOC327>3.0.CO;2-U.

Compagnucci, R. H., S. A. Blanco, M. A. Figliola, and P. M. Jacovkis (2000), Variability in subtropical Andean Argentinean Atuel river; a wavelet approach, *Environmetrics*, *11*(June 1998), 251–269, doi:10.1002/(SICI)1099-095X(200005/06)11:3<251::AID-ENV405>3.0.CO;2-0.

Compagnucci, R. H., A. L. Berman, V. Velasco Herrera, and G. Silvestri (2014), Are southern South American Rivers linked to the solar variability?, *Int. J. Climatol.*, *34*(5), 1706–1714, doi:10.1002/joc.3784.

Condom, T., P. Rau, and J. C. Espinoza (2011), Correction of TRMM 3B43 monthly precipitation data over the mountainous areas of Peru during the period 1998-2007, *Hydrol. Process.*, *25*(12), 1924–1933, doi:10.1002/hyp.7949.

Cook, E. R., K. J. Anchukaitis, B. M. Buckley, R. D. D'Arrigo, G. C. Jacoby, and W. E. Wright (2010), Asian monsoon failure and megadrought during the last millennium., *Science*, *328*(5977), 486–9, doi:10.1126/science.1185188.

Coppus, R., and a. C. Imeson (2002), Extreme events controlling erosion and sediment transport in a semi-arid sub-Andean valley, *Earth Surf. Process. Landforms*, *27*(13), 1365–1375, doi:10.1002/esp.435.

Corbett, L.B., Bierman, P.R. and Rood, D.H., An approach for optimizing in situ cosmogenic 10Be sample preparation. Quaternary Geochronology, in press.

Currie, L. A., 1968. Limits for qualitative detection and quantitative determination: Application to radiochemistry. Anal. Chem. 40, 586–593. doi:10.1021/ac60259a007

Currie, L. A., 1972. The measurement of environmental levels of rare gas nuclides and the treatment of very low-level counting data. In Nuclear Science, IEEE Transactions on , 19(1), 119-126. doi: 10.1109/TNS.1972.4326496

Currie, L. A., 2008. Detection and quantification capabilities in nuclear analytical measurements. In Analysis of Environmental Radionuclides, Radioactivity in the Environments, 11, Elsevier, doi: 10.1016/S1569-4860(07)11003-2

Dai, A., I. Y. Fung, and A. D. Del Genio (1997), Surface observed global land precipitation variations during 1900-88, *J. Clim.*, *10*(11), 2943–2962.

Daly, C. (2006), Guidelines for assessing the suitability of spatial climate data sets, *Int. J. Climatol.*, *26*(6), 707–721, doi:10.1002/joc.1322.

Daly, C., R. P. Neilson, and D. L. Phillips (1994), A Statistical-Topographic Model for mapping climatological precipitation over mountainous terrain, *J. Appl. Meteorol.*, *33*, 140–158.

Dee, D. P. et al. (2011), The ERA-Interim reanalysis: Configuration and performance of the data assimilation system, *Q. J. R. Meteorol. Soc.*, *137*(656), 553–597, doi:10.1002/qj.828.

Dewald, A., Heinze, S., Jolie, J., Zilges, A., Dunai, T., Rethemeyer, J., Melles, M., Staubwasser, M., Kuczewski, B., Richter, J., Radtke, U., von Blanckenburg, F., Klein, M., 2013. Cologne AMS, a dedicated center for accelerator mass spectrometry in Germany. Nuclear Instruments and Methods in Physics Research Section B: Beam Interactions with Materials and Atoms 294, 18-23.

Diaz, H., M. Grosjean, and L. Graumlich (2003), Climate Variability and Change in High Elevation Regions: Past, Present and Future, *Clim. Change*, *59*(1), 1.

Diaz, H. F., M. P. Hoerling, and J. K. Eischeid (2001), Enso variability, teleconnections and climate change, *Int. J. Climatol.*, *21*(15), 1845–1862, doi:10.1002/joc.631.

Dimri, A. P., and S. K. Dash (2012), Wintertime climatic trends in the western Himalayas, *Clim. Change*, *111*(3), 775–800, doi:10.1007/s10584-011-0201-y.

Dunai, T.J., 2000. Scaling factors for production rates of in situ produced cosmogenic nuclides: a critical reevaluation. Earth Planet. Sci. Lett. 176, 157–169. doi:10.1016/S0012-821X(99)00310-6

Dunai, T.J., 2010. Cosmogenic Nuclides. Cambridge University Press, UK.

Dunne, T., and K. L. A. Mertes (2007), Rivers, in *The Physical Geography of South America*, edited by T. Veblen, K. Young, and A. R. Orme, pp. 76–90, Oxford University Press.

Durkee, J. D., T. L. Mote, and J. M. Shepherd (2009), The contribution of mesoscale convective complexes to rainfall across subtropical South America, *J. Clim.*, *22*(17), 4590–4605, doi:10.1175/2009JCLI2858.1.

Easterling, D. R., G. A. Meehl, C. Parmesan, S. a Changnon, T. R. Karl, and L. O. Mearns (2000), Climate extremes: observations, modeling, and impacts.,

Science, *289*(September), 2068–2074, doi:10.1126/science.289.5487.2068.

Enfield, D. B., and A. M. Mestas-Nunez (1999), How ubiquitous is the dipole relationship in tropical Atlantic sea surface temperatures?, *Jounral Geophys. Res.*, *40*, 7841–7884, doi:10.1029/1998JC900109.

Enfield, D. B., A. M. Mestas-Nunez, and P. J. Trimble (2001), The Atlantic Multidecadal Oscillation and its relation to rainfall and river flows in the continental U.S., *Geophys. Res. Lett.*, *28*(10), 2077–2080, doi:10.1029/2000GL012745.

Ensor, L. A., and S. M. Robeson (2008), Statistical characteristics of daily precipitation: Comparisons of gridded and point datasets, *J. Appl. Meteorol. Climatol.*, *47*(9), 2468–2476, doi:10.1175/2008JAMC1757.1.

Espinoza, J. C., M. Lengaigne, J. Ronchail, and S. Janicot (2012), Large-scale circulation patterns and related rainfall in the Amazon Basin: A neuronal networks approach, *Clim. Dyn.*, *38*(1–2), 121–140, doi:10.1007/s00382-011-1010-8.

Espinoza, J. C., S. Chavez, J. Ronchail, C. Junquas, K. Takahashi, and W. Lavado (2015), Rainfall hotspots over the southern tropical Andes: Spatial distribution, rainfall intensity, and relations with large-scale atmospheric circulation, *Water Resour. Res.*, *6*(4), 446, doi:10.1002/2014WR016273.

Evans, S. G., and J. J. Clague (1994), Recent climatic change and catastrophic geomorphic processes in mountain environments, *Geomorphology*, *10*(1–4), 107–128, doi:10.1016/0169-555X(94)90011-6.

Evans, W. D. (1942), The standar error of percentiles, *J. Am. Stat. Assoc.*, *37*(219), 367–376.

Field, C. B. et al. (2014), *Technical summary*.

Flandrin, P., P. Gonçalves, and G. Rilling (2004), Detrending and denoising with empirical mode decompositions, *Proc. 12th Eur. Signal Process. Conf.*, (3), 1581–1584.

Francou, B. (2003), Tropical climate change recorded by a glacier in the central Andes during the last decades of the twentieth century: Chacaltaya, Bolivia, 16°S, *J. Geophys. Res.*, *108*(D5), 1–12, doi:10.1029/2002JD002959.

Franzke, C. (2012), Nonlinear trends, long-range dependence, and climate noise properties of surface temperature, *J. Clim.*, *25*(12), 4172–4183, doi:10.1175/JCLI-D-11-00293.1.

Frei, C., and C. Schär (2001), Detection probability of trends in rare events: Theory and application to heavy precipitation in the Alpine region, *J. Clim.*, *14*(7), 1568–1584.

Füssel, H. M., and R. J. T. Klein (2006), Climate change vulnerability assessments: An evolution of conceptual thinking, *Clim. Change*, *75*(3), 301–329, doi:10.1007/s10584-006-0329-3.

Gandu, A., and J. Geisler (1991), A primitive equations model study of the effect of topography on the summer circulation over tropical South America, *J. Atmos. Sci.*, *48*(16), 1822–1836.

Gandu, A. W., and P. L. Silva Dias (1998), Impact of tropical heat sources on the South American tropospheric upper circulation and subsidence, *J. Geophys. Res.*, *103*(D6), 6001, doi:10.1029/97JD03114.

García, N. O., and C. R. Mechoso (2005), Variability in the discharge of South American rivers and in climate / Variabilité des débits de rivières d'Amérique du

Sud et du climat, *Hydrol. Sci. J.*, *50*(3), 37–41, doi:10.1623/hysj.50.3.459.65030.

García, N. O., and W. M. Vargas (1998), The temporal climatic variability in the "Rio de la Plata" Basin displayed by the river discharges, *Clim. Change*, *38*, 359–379, doi:10.1023/A:1005386530866.

Gardelle, J., E. Berthier, and Y. Arnaud (2012), Slight mass gain of Karakoram glaciers in the early twenty-first century, *Nat. Geosci.*, *5*(5), 322–325, doi:10.1038/ngeo1450.

Garg, V., and V. Jothiprakash (2008), Estimation of useful life of a reservoir using sediment trap efficiency, *J. Spat. Hydrol.*, *8*(2), 1–14, doi:10.1017/CBO9780511806049.

Garreaud, R. (2000), Cold Air Incursions over Subtropical South America: Mean Structure and Dynamics, *Mon. Weather Rev.*, *128*(7), 2544–2559.

Garreaud, R., and P. Aceituno (2001), Interannual rainfall variability over the South American Altiplano, *J. Clim.*, *14*, 2779–2789.

Garreaud, R., and D. Battisti (1999), Interannual (ENSO) and Interdecadal (ENSO-like) Variability in the Southern Hemisphere Tropospheric Circulation*, *J. Clim.*, *12*, 2113–2123.

Garreaud, R., M. Vuille, and A. C. Clement (2003), The climate of the Altiplano: observed current conditions and mechanisms of past changes, *Palaeogeogr. Palaeoclimatol. Palaeoecol.*, *194*(1–3), 5–22, doi:10.1016/S0031-0182(03)00269-4.

Garreaud, R. D., M. Vuille, R. Compagnucci, and J. Marengo (2009), Present-day South American climate, *Palaeogeogr. Palaeoclimatol. Palaeoecol.*, *281*(3–4), 180–195, doi:10.1016/j.palaeo.2007.10.032.

Garreaud, R. D., A. Molina, and M. Farias (2010), Andean uplift, ocean cooling and Atacama hyperaridity: A climate modeling perspective, *Earth Planet. Sci. Lett.*, *292*(1–2), 39–50, doi:10.1016/j.epsl.2010.01.017.

Genta, J. L., G. Perez-Iribarren, and C. R. Mechoso (1998), A Recent Increasing Trend in the Streamflow of Rivers in Southeastern South America, *J. Clim.*, *11*, 2858–2862.

Giorgi, F., and P. Lionello (2008), Climate change projections for the Mediterranean region, *Glob. Planet. Change*, *63*(2–3), 90–104, doi:10.1016/j.gloplacha.2007.09.005.

Giovannettone, J. P., and A. P. Barros (2009), Probing Regional Orographic Controls of Precipitation and Cloudiness in the Central Andes Using Satellite Data, *J. Hydrometeorol.*, *10*(1), 167–182, doi:10.1175/2008JHM973.1.

Gloor, M., R. J. W. Brienen, D. Galbraith, T. R. Feldpausch, J. Schöngart, J. L. Guyot, J. C. Espinoza, J. Lloyd, and O. L. Phillips (2013), Intensification of the Amazon hydrological cycle over the last two decades, *Geophys. Res. Lett.*, *40*(9), 1729–1733, doi:10.1002/grl.50377.

Gobiet, A., S. Kotlarski, M. Beniston, G. Heinrich, J. Rajczak, and M. Stoffel (2014), 21st century climate change in the European Alps-A review, *Sci. Total Environ.*, *493*, 1138–1151, doi:10.1016/j.scitotenv.2013.07.050.

Gosse, J.C., Phillips, F.M., 2001. Terrestrial in situ cosmogenic nuclides:theory and application. Quat. Sci. Rev. 20, 1475–1560. doi:10.1016/S0277-3791(00)00171-2

Gosset, W. S. (1908), The Probable Error of a Mean, *Biometrika*, *6*, 1–24.

Goswami, B. N., V. Venugopal, D. Sengupta, M. S. Madhusoodanan, and P. K. Xavier

(2006), Increasing Trend of Extreme Rain Events Over India in a Warming Environment, *Science (80-.).*, *314*(December), 1442–1445, doi:10.1126/science.1132027.

Graham, N. E. (1994), Decadal-scale climate variability in the tropical and North Pacific during the 1970s and 1980s: observations and model results, *Clim. Dyn.*, *10*(3), 135–162, doi:10.1007/BF00210626.

Granger, D., J. Kirchner, and R. Finkel (1996), Spatially averaged long-term erosion rates measured from in situ-produced cosmogenic nuclides in alluvial sediment, *J. Geol.*, *104*(3), 249–257.

Granger, D.E., 2006. A review of burial dating methods using 26Al and 10Be. In: L.L. Siame, D.L. Bourlès, E.T. Brown (eds.), In Situ-Produced Cosmogenic Nuclides and Quantification of Geological Processes. Geol. Soc. Am. Spec. Paper 415, 1-16.

Granger D.E., Lifton N.A., Willenbring J.K., 2013. A cosmic trip: 25 years of cosmogenic nuclides in geology. Geological Society of America Bullettin, doi: 10.1130/B30774.1.

Hallet, B., L. Hunter, and J. Bogen (1996), Rates of erosion and sediment evacuation by glaciers: A review of field data and their implications, *Glob. Planet. Change*, *12*(1–4), 213–235, doi:10.1016/0921-8181(95)00021-6.

Halloy, S. (1982), Contribucíon al estudio de la zona de Huaca huasi, Cumbres Calchaquíes (Tucumán Argentina), Univ. Nac., Tucumán.

Hänggi, P., and R. Weingartner (2012), Variations in Discharge Volumes for Hydropower Generation in Switzerland, *Water Resour. Manag.*, *26*(5), 1231–1252, doi:10.1007/s11269-011-9956-1.

Hanshaw, M. N., and B. Bookhagen (2014), Glacial areas, lake areas, and snow lines from 1975 to 2012: status of the Cordillera Vilcanota, including the Quelccaya Ice Cap, northern central Andes, Peru, *Cryosphere*, *8*(1), 1–18, doi:10.5194/tc-8-1-2014.

Hare, W. L., W. Cramer, M. Schaeffer, A. Battaglini, and C. C. Jaeger (2011), Climate hotspots: Key vulnerable regions, climate change and limits to warming, *Reg. Environ. Chang.*, *11*(SUPPL. 1), 1–13, doi:10.1007/s10113-010-0195-4.

Hartmann, D. L. et al. (2013), Observations: Atmosphere and Surface, in *Climate Change 2013: The Physical Science Basis. Contribution of Working Group I to the Fifth Assessment Report of the Intergovernmental Panel on Climate Change*, edited by T. F. Stocker, D. Qin, G.-K. Plattner, M. Tignor, S. K. Allen, J. Boschung, A. Nauels, Y. Xia, V. Bex, and P. M. Midgley, pp. 159–254, Cambridge University Press, Cambridge, United Kingdom and New York, NY, USA.

Haselton, K., G. Hilley, and M. R. Strecker (2002), Average Pleistocene climatic patterns in the southern central Andes: Controls on mountain glaciation and paleoclimate implications, *J. Geol.*, *110*, 211–226.

Haylock, M., and N. Nicholls (2000), Trends in extreme rainfall indices for an updated high quality data set for Australia, 1910-1998, *Int. J. Climatol.*, *20*(13), 1533–1541.

Haylock, M. R. et al. (2006), Trends in total and extreme South American rainfall in 1960-2000 and links with sea surface temperature, *J. Clim.*, *19*(8), 1490–1512, doi:10.1175/JCLI3695.1.

Heidinger, H., C. Yarlequé, A. Posadas, and R. Quiroz (2012), TRMM rainfall correction over the Andean Plateau using wavelet multi-resolution analysis, *Int. J. Remote Sens.*, *33*(14), 4583–4602, doi:10.1080/01431161.2011.652315.

Held, I. M., and B. J. Soden (2006), Robust responses of the hydrological cycle to

global warming, *J. Clim.*, *19*(21), 5686–5699, doi:10.1175/JCLI3990.1.

Henley, W. F., M. a. Patterson, R. J. Neves, and a. D. Lemly (2000), Effects of Sedimentation and Turbidity on Lotic Food Webs: A Concise Review for Natural Resource Managers, *Rev. Fish. Sci.*, *8*(April), 125–139, doi:10.1080/10641260091129198.

Higgins, R. W., W. Shi, E. Yarosh, and R. Joyce (2000), *Improved United States Precipitation Quality Control System and Analysis - Atlas No. 7.*

Holland, P. W., and R. E. Welsch (1977), Robust regression using iteratively reweighted least-squares, *Commun. Stat. - Theory Methods*, *6*(9), 813–827, doi:10.1080/03610927708827533.

Hoover, K. D. (2003), Nonstationary time series, cointegration, and the principle of the common cause, *Br. J. Philos. Sci.*, *54*(4), 527–551, doi:10.1093/bjps/54.4.527.

Horel, J. D., and Wallace (1981), Planetary-Scale Atmospheric Phenomena Associated with the Southern Oscillation, *Mon. Weather Rev.*, *109*, 813–829, doi:10.1175/1520-0493(1982)110<1495:COSAPA>2.0.CO;2.

Houston, J. (2006), The great Atacama flood of 2001 and its implications for Andean hydrology, *Hydrol. Process.*, *20*(3), 591–610, doi:10.1002/hyp.5926.

Houze, R. A., K. L. Rasmussen, S. Medina, S. R. Brodzik, and U. Romatschke (2011), Anomalous atmospheric events leading to the summer 2010 floods in Pakistan, *Bull. Am. Meteorol. Soc.*, *92*(3), 291–298, doi:10.1175/2010BAMS3173.1.

Hsu, P. C., T. Li, and B. Wang (2011), Trends in global monsoon area and precipitation over the past 30 years, *Geophys. Res. Lett.*, *38*(January), 1–5, doi:10.1029/2011GL046893.

Huang, N. E. (2005), Introduction to the Hilbert Huang Transform, *Transform*, *5*, 1–26, doi:doi:10.1142/9789812703347_0001.

Huang, N. E., and S. S. P. Shen (2014), *Hilbert-Huang transform and its applications*, edited by N. E. Huang and S. S. P. Shen, World Scientific Publishing, Singapore.

Huang, N. E., and Z. Wu (2009), Ensemble Empirical Mode Decomposition: a Noise-Assisted Data Analysis Method, *Adv. Adapt. Data Anal.*, *1*(1), 1, doi:10.1142/S1793536909000047.

Huang, N. E., Z. Shen, S. R. Long, M. C. Wu, H. H. Shih, Q. Zheng, N.-C. Yen, C. C. Tung, and H. H. Liu (1998), The empirical mode decomposition and the Hilbert spectrum for nonlinear and non-stationary time series analysis, *Proc. R. Soc. A Math. Phys. Eng. Sci.*, *454*, 903–995, doi:10.1098/rspa.1998.0193.

Huang, N. E., Z. Shen, and S. R. Long (1999), A new view of nonlinear water waves: The Hilbert Spectrum 1, *Annu. Rev. Fluid Mech.*, *31*(1), 417–457, doi:10.1146/annurev.fluid.31.1.417.

Huang, N. E., M.-L. C. Wu, S. R. Long, S. S. P. Shen, W. Qu, P. Gloersen, and K. L. Fan (2003), A confidence limit for the empirical mode decomposition and Hilbert spectral analysis, *Proc. R. Soc. A Math. Phys. Eng. Sci.*, *459*(2037), 2317–2345, doi:10.1098/rspa.2003.1123.

Huang, N. E., Z. Wu, S. R. Long, K. C. Arnold, X. Chen, and K. Blank (2009), on Instantaneous Frequency, *Adv. Adapt. Data Anal.*, *1*(2), 177–229, doi:10.1142/S1793536909000096.

Huang, Y., and F. G. Schmitt (2014), Time dependent intrinsic correlation analysis of temperature and dissolved oxygen time series using empirical mode decomposition, *J. Mar. Syst.*, *130*, 90–100, doi:10.1016/j.jmarsys.2013.06.007.

Huang, Y. X., F. G. Schmitt, Z. M. Lu, P. Fougairolles, Y. Gagne, and Y. L. Liu (2010), Second-order structure function in fully developed turbulence, *Phys. Rev. E - Stat. Nonlinear, Soft Matter Phys.*, *82*(2), 1–7, doi:10.1103/PhysRevE.82.026319.

Huang, Y. X., F. G. Schmitt, J. P. Hermand, Y. Gagne, Z. M. Lu, and Y. L. Liu (2011), Arbitrary-order Hilbert spectral analysis for time series possessing scaling statistics: Comparison study with detrended fluctuation analysis and wavelet leaders, *Phys. Rev. E - Stat. Nonlinear, Soft Matter Phys.*, *84*(1), 1–13, doi:10.1103/PhysRevE.84.016208.

Huber, P. J. (1981), *Robust statistics*, edited by J. & S. I. Wiley, Wiley, New York.

Huffman, G. J., D. T. Bolvin, E. J. Nelkin, D. B. Wolff, R. F. Adler, G. Gu, Y. Hong, K. P. Bowman, and E. F. Stocker (2007), The TRMM Multisatellite Precipitation Analysis (TMPA): Quasi-Global, Multiyear, Combined-Sensor Precipitation Estimates at Fine Scales, *J. Hydrometeorol.*, *8*(1), 38–55, doi:10.1175/JHM560.1.

Huntington, T. G. (2006), Evidence for intensification of the global water cycle: Review and synthesis, *J. Hydrol.*, *319*(1–4), 83–95, doi:10.1016/j.jhydrol.2005.07.003.

Hurrell, J. W., Y. Kushnir, and G. Ottersen (2003), An overview of the North Atlantic oscillation, *Clim. Significance Environ. Impact*, (134), 1–35, doi:10.1029/134GM01.

Immerzeel, W. W., L. P. H. van Beek, and M. F. P. Bierkens (2010), Climate Change Will Affect the Asian Water Towers, *Science (80-.).*, *328*, 1382–1385.

Insel, N., C. Poulsen, and T. Ehlers (2010), Influence of the Andes Mountains on South American moisture transport, convection, and precipitation, *Clim. Dyn.*, *35*(7), 1477–1492, doi:10.1007/s00382-009-0637-1.

Isotta, F. A. et al. (2014), The climate of daily precipitation in the Alps: Development and analysis of a high-resolution grid dataset from pan-Alpine rain-gauge data, *Int. J. Climatol.*, *34*(5), 1657–1675, doi:10.1002/joc.3794.

Ivy-Ochs S., Kober F., 2008. Surface exposure dating with cosmogenic nuclides. Eiszeitalter und Gegenwart Quaternary Science Journal, 57 (1-2), 179-209.

Jacques-Coper, M., and R. D. Garreaud (2015), Characterization of the 1970s climate shift in South America, *Int. J. Climatol.*, *35*(8), 2164–2179, doi:10.1002/joc.4120.

Jansson, P., R. Hock, and T. Schneider (2003), The concept of glacier storage: A review, *J. Hydrol.*, *282*(1–4), 116–129, doi:10.1016/S0022-1694(03)00258-0.

JeŽek, P., A. Willner, F. AceÑolaza, and H. Miller (1985), The Puncoviscana trough—a large basin of Late Precambrian to Early Cambrian age on the Pacific edge of the Brazilian shield, *Geol. Rundschau*, *74*(3), 573–584.

Jones, C., and L. M. V Carvalho (2014), Sensitivity to Madden-Julian Oscillation variations on heavy precipitation over the contiguous United States, *Atmos. Res.*, *147–148*, 10–26, doi:10.1016/j.atmosres.2014.05.002.

Jones, C., D. Waliser, K.-M. Lau, and W. Stern (2004), Global occurrences of extreme precipitation and the Madden-Julian Oscillation: Observations and predictability, *J. Clim.*, 4575–4589.

Jones, C., L. M. V Carvalho, and B. Liebmann (2012), Forecast skill of the South American monsoon system, *J. Clim.*, *25*(6), 1883–1889, doi:10.1175/JCLI-D-11-00586.1.

Kääb, A., E. Berthier, C. Nuth, J. Gardelle, Y. Arnaud, A. Kaab, E. Berthier, C. Nuth, J. Gardelle, and Y. Arnaud (2012), Contrasting patterns of early twenty-first-

century glacier mass change in the Himalayas, *Nature*, *488*(7412), 495–498, doi:10.1038/nature11324.

Kalnay, E. et al. (1996), The NCEP/NCAR 40-Year Reanalysis Project, *Bull. Am. Meteorol. Soc.*, *77*(3), 437–471.

Katz, R. W., and B. G. Brown (1992), Extreme events in a changing climate: Variability is more important than averages, *Clim. Change*, *21*(3), 289–302, doi:10.1007/BF00139728.

Kayano, M. T., C. Pestrelo de Oliveira, and R. V. Andreoli (2009), Interannual relations between South American rainfall and tropical sea surface temperature anomalies before and after 1976, *Int. J. Climatol.*, *29*, 1439–1448, doi:10.1002/joc.1824.

Keiler, M., J. Knight, and S. Harrison (2010), Climate change and geomorphological hazards in the eastern European Alps., *Philos. Trans. A. Math. Phys. Eng. Sci.*, *368*(1919), 2461–2479, doi:10.1098/rsta.2010.0047.

Kendall, M. G. (1948), *Rank correlation methods*, Griffin, London, UK.

Kendon, E., N. Roberts, and H. Fowler (2014), Heavier summer downpours with climate change revealed by weather forecast resolution model, *Nat. Clim. Chang.*, *4*(June), 1–7, doi:10.1038/NCLIMATE2258.

Kessler, M. (2002), The elevational gradient of Andean plant endemism: Varying influences of taxon-specific traits and topography at different taxonomic levels, *J. Biogeogr.*, *29*(9), 1159–1165, doi:10.1046/j.1365-2699.2002.00773.x.

Khaliq, M. N., T. B. M. J. Ouarda, J. C. Ondo, P. Gachon, and B. Bobée (2006), Frequency analysis of a sequence of dependent and/or non-stationary hydro-meteorological observations: A review, *J. Hydrol.*, *329*(3–4), 534–552, doi:10.1016/j.jhydrol.2006.03.004.

Kirchner, J. W., R. C. Finkel, C. S. Riebe, D. E. Granger, J. L. Clayton, J. G. King, W. F. Megahan, and F. Sites (2001), Mountain erosion over 10 yr, 10 k.y., and 10 m.y. time scales, *Geology*, *29*(7), 591–594.

Kober, F., Hippe, K., Salcher, B., Ivy-Ochs, S., Kubik, P.W., Wacker, L., Hahlen, N., 2012. Debris-flow-dependent variation of cosmogenically derived catchment-wide denudation rates. Geology 40, 935–938. doi:10.1130/G33406.1

Koenker, R., and G. Bassett Jr. (1978), Regression Quantiles, *Econometrica*, *46*(1), 33–50, doi:10.2307/1913643.

Kohl, C.P., Nishiizumi, K., 1992. Chemical isolation of quartz for measurement of in-situ-produced cosmogenic nuclides. Geochim. Cosmochim. Acta 56, 3583–3587. doi:10.1016/0016-7037(92)90401-4

Kormann, C., A. Bronstert, T. Francke, T. Recknagel, and T. Graeff (2016), Model-Based Attribution of High-Resolution Streamflow Trends in Two Alpine Basins of Western Austria, *Hydrology*, *3*(1), 7, doi:10.3390/hydrology3010007.

Korschinek, G., Bergmaier, A., Faestermann, T., Gerstmann, U.C., Knie, K., Rugel, G., Wallner, A., Dillmann, I., Dollinger, G., von Gostomski, C.L., Kossert, K., Maiti, M., Poutivtsev, M., Remmert, A., 2010. A new value for the half-life of 10Be by Heavy-Ion Elastic Recoil Detection and liquid scintillation counting. Nucl. Instruments Methods Phys. Res. Sect. B Beam Interact. with Mater. Atoms 268, 187–191. doi:10.1016/j.nimb.2009.09.020

Korup, O., and J. J. Clague (2009), Natural hazards, extreme events, and mountain topography, *Quat. Sci. Rev.*, *28*(11–12), 977–990, doi:10.1016/j.quascirev.2009.02.021.

Krishna Kumar, K., K. Rupa Kumar, R. G. Ashrit, N. R. Deshpande, and J. W. Hansen (2004), Climate impacts on Indian agriculture, *Int. J. Climatol.*, *24*(11), 1375–1393, doi:10.1002/joc.1081.

Krishnamurthy, C. K. B., U. Lall, and H.-H. Kwon (2009), Changing Frequency and Intensity of Rainfall Extremes over India from 1951 to 2003, *J. Clim.*, *22*(18), 4737–4746, doi:10.1175/2009JCLI2896.1.

Kummerow, C., W. Barnes, T. Kozu, J. Shiue, and J. Simpson (1998), The Tropical Rainfall Measuring Mission (TRMM) sensor package, *J. Atmos. Ocean. Technol.*, *15*, 809–817.

Kummerow, C. et al. (2000), The Status of the Tropical Rainfall Measuring Mission (TRMM) after Two Years in Orbit, *J. Appl. Meteorol.*, *39*(12), 1965–1982.

de la Torre, A., and P. Alexander (2005), Gravity waves above Andes detected from GPS radio occultation temperature profiles: Mountain forcing?, *Geophys. Res. Lett.*, *32*(17), 1–4, doi:10.1029/2005GL022959.

de la Torre, A., H. Pessano, R. Hierro, J. R. Santos, P. Llamedo, and P. Alexander (2015), The influence of topography on vertical velocity of air in relation to severe storms near the Southern Andes Mountains, *Atmos. Res.*, *156*, 91–101, doi:10.1016/j.atmosres.2014.12.020.

Labat, D., J. Ronchail, J. Callede, J. L. Guyot, E. De Oliveira, and W. Guimarães (2004), Wavelet analysis of Amazon hydrological regime variability, *Geophys. Res. Lett.*, *31*(2), L02501, doi:10.1029/2003GL018741.

Lal, D. (1991), Cosmic ray labeling of erosion surfaces: in situ nuclide production rates and erosion models, *Earth Planet. Sci. Lett.*, *104*(2–4), 424–439, doi:10.1016/0012-821X(91)90220-C.

Latif, M., and T. P. Barnett (1994), Causes of Decadal Climate Variability over the North Pacific and North America., *Science*, *266*(5185), 634–637, doi:10.1126/science.266.5185.634.

Lavado Casimiro, W. S., D. Labat, J. Ronchail, J. C. Espinoza, and J. L. Guyot (2013), Trends in rainfall and temperature in the Peruvian Amazon-Andes basin over the last 40 years (1965-2007), *Hydrol. Process.*, *27*(20), 2944–2957, doi:10.1002/hyp.9418.

Licciardi, J. M., Schaefer, J. M., Taggart, J. R., Lund, D. C., 2009. Holocene Glacier Fluctuations in the Peruvian Andes Indicate Northern Climate Linkages. Science, 325, 1677. doi: 10.1126/science.1175010

Liebmann, B., and D. Allured (2005), Daily Precipitation Grids for South America, *Bull. Am. Meteorol. Soc.*, *86*(11), 1567–1570, doi:10.1175/BAMS-86-11-1567.

Liniger, H., R. Weingartner, and M. Grosjean (1998), *Mountains of the world - Water towers for the 21st century*, Bern.

Lliboutry, L. (1998), Glaciers of Chile and Argentina, in *Glaciers of South Amrica USGS Professional Paper 1386-I*, edited by R. S. Williams and J. Ferrigno, pp. 109–206, USGS, Denver.

Long, G. L., Winefordner, J. D., 1983. Limit of Detection: A closer look at the IUPAC definition. Analitical Chemistry, 55(7), 712–724.

Longobardi, A., and P. Villani (2009), Trend analysis of annual and seasonal rainfall time series in the Mediterranean area, *Int. J. Climatol.*, doi:10.1002/joc.2001.

Madden, R. a., and P. R. Julian (1971), Detection of a 40–50 Day Oscillation in the Zonal Wind in the Tropical Pacific, *J. Atmos. Sci.*, *28*, 702–708.

Maddox, R. A., C. F. Chappell, and L. R. Hoxit (1979), Synoptic and mesoscale aspects of flash flood events, *Bull. Am. Meteorol. Soc.*, *60*, 115–123.

Madsen, H., D. Lawrence, M. Lang, M. Martinkova, and T. R. Kjeldsen (2014), Review of trend analysis and climate change projections of extreme precipitation and floods in Europe, *J. Hydrol.*, *519*(PD), 3634–3650, doi:10.1016/j.jhydrol.2014.11.003.

Malik, N., B. Bookhagen, N. Marwan, and J. Kurths (2011), Analysis of spatial and temporal extreme monsoonal rainfall over South Asia using complex networks, *Clim. Dyn.*, *39*(3–4), 971–987, doi:10.1007/s00382-011-1156-4.

Malik, N., B. Bookhagen, and P. J. Mucha (2016), Spatiotemporal patterns and trends of Indian monsoonal rainfall extremes, *Geophys. Res. Lett.*, 1–22, doi:10.1002/2016GL067841.

Mann, H. B. (1945), Nonparametric tests against trend, *Econometrica*, *13*(3), 245–259.

Mantua, N., and S. Hare (2002), The Pacific decadal oscillation, *J. Oceanogr.*, *58*, 35–44.

Marcato, G., a. Pasuto, and F. R. Rivelli (2009), Mass movements in the Rio Grande Valley (Quebrada de Humahuaca, Northwestern Argentina): a methodological approach to reduce the risk, *Adv. Geosci.*, *22*, 59–65.

Marcato, G., G. Bossi, F. Rivelli, and L. Borgatti (2012), Debris flood hazard documentation and mitigation on the Tilcara alluvial fan (Quebrada de Humahuaca, Jujuy province, North-West Argentina), *Nat. Hazards Earth Syst. Sci.*, *12*(6), 1873–1882, doi:10.5194/nhess-12-1873-2012.

Marengo, J. A. (1995), Variations and change in south American streamflow, *Clim. Change*, *31*(1), 99–117, doi:10.1007/BF01092983.

Marengo, J. A. (2004), Interdecadal variability and trends of rainfall across the Amazon basin, *Theor. Appl. Climatol.*, *78*(1–3), 79–96, doi:10.1007/s00704-004-0045-8.

Marengo, J. A. (2009), Long-term trends and cycles in the hydrometeorology of the Amazon basin since the late 1920s, *Hydrol. Process.*, *23*, 3236–3244, doi:10.1002/hyp.7396.

Marengo, J. A., C. A. Nobre, J. Tomasella, M. D. Oyama, G. Sampaio de Oliveira, R. de Oliveira, H. Camargo, L. M. Alves, and I. F. Brown (2008), The Drought of Amazonia in 2005, *J. Clim.*, *21*(3), 495–516, doi:10.1175/2007JCLI1600.1.

Marengo, J. A., R. Jones, L. M. Alves, and M. C. Valverde (2009), Future change of temperature and precipitation extremes in South America as derived from the PRECIS regional climate modeling system, *Int. J. Climatol.*, *29*, 2241–2255, doi:10.1002/joc.

Marengo, J. A. et al. (2012), Recent developments on the South American monsoon system, *Int. J. Climatol.*, *32*(1), 1–21, doi:10.1002/joc.2254.

Marshall, J., Y. Kushnir, D. Battisti, P. Chang, A. Czaja, R. Dickinson, J. Hurrell, M. McCartney, R. Saravana, and M. Visbeck (2001), North Atlantic Climate Variability: Phenomena, Impacts and Mechanisms, *Int. J. Climatol.*, *21*, 1863–1898, doi:10.1002/joc.693.

Martinelli, G. (2007), Mountain biodiversity in Brazil, *Rev. Bras. Botânica*, *30*(4), 587–597, doi:10.1590/S0100-84042007000400005.

Massei, N., and M. Fournier (2012), Assessing the expression of large-scale climatic fluctuations in the hydrological variability of daily Seine river flow (France)

between 1950 and 2008 using Hilbert-Huang Transform, *J. Hydrol.*, *448–449*, 119–128, doi:10.1016/j.jhydrol.2012.04.052.

Matsuo, K., and K. Heki (2010), Time-variable ice loss in Asian high mountains from satellite gravimetry, *Earth Planet. Sci. Lett.*, *290*(1–2), 30–36, doi:10.1016/j.epsl.2009.11.053.

McKillup, S., Darby Dyar, M., 2010. Geostatistics explained: An introductory guide for earth scientists. Cambridge University Press, UK.

McPhillips, D., Bierman, P.R., Rood, D.H., 2014. Millennial-scale record of landslides in the Andes consistent with earthquake trigger. Nat. Geosci 7, 925–930. doi:10.1038/ngeo2278

Melack, J. M., E. M. L. M. Novo, B. R. Forsberg, M. T. F. Piedade, and L. Maurice (2009), Floodplain ecosystem processes, *Geophys. Monogr. Ser. 186*, 525–541.

Merchel, S., Arnold, M., Aumaître, G., Benedetti, L., Bourlès, D.L.L., Braucher, R., Alfimov, V., Freeman, S.P.H.T.P.H.T., Steier, P., Wallner, a., 2008. Towards more precise 10Be and 36Cl data from measurements at the 10-14 level: Influence of sample preparation. Nucl. Instruments Methods Phys. Res. Sect. B Beam Interact. with Mater. Atoms 266, 4921–4926. doi:10.1016/j.nimb.2008.07.031

Merchel, S., Bremser, W., Bourlès, D.L., Czeslik, U., Erzinger, J., Kummer, N. -a., Leanni, L., Merkel, B., Recknagel, S., Schaefer, U., 2013. Accuracy of 9Be-data and its influence on 10Be cosmogenic nuclide data. J. Radioanal. Nucl. Chem. 298, 1871–1878. doi:10.1007/s10967-013-2746-x

Miller, A., D. Cayan, T. Barnett, N. Graham, and J. Oberhuber (1994), The 1976-77 Climate Shift of the Pacific Ocean, *Oceanography*, *7*(1), 21–26, doi:10.5670/oceanog.1994.11.

Miller, J. D., W. W. Immerzeel, and G. Rees (2012), Climate Change Impacts on Glacier Hydrology and River Discharge in the Hindu Kush – Himalayas A Synthesis of the Scientific Basis, *Mt. Res. Dev.*, *32*(4), 461–467, doi:10.1659/MRD-JOURNAL-D-12-00027.1.

Minetti, J. L., and W. M. Vargas (1998), Trends and jumps in annual precipitation in South America, south of the 15°S, *Atmosfera*, *11*, 205–211.

Minvielle, M., and R. D. Garreaud (2011), Projecting rainfall changes over the South American Altiplano, *J. Clim.*, *24*(17), 4577–4583, doi:10.1175/JCLI-D-11-00051.1.

Mocak, J., Bond, A. M., Mitchell, S., Scollary, G., 1997. A statistical overview of standard (IUPAC and ACS) and new procedures for determining the limits of detection and quantification: application to voltammetric and stnpping techniques. Pure & Appl. Chern., 69(2), 297-328.

Molina, A., V. Vanacker, E. Brisson, D. Mora, and V. Balthazar (2015), Multidecadal change in streamflow associated with anthropogenic disturbances in the tropical Andes, *Hydrol. Earth Syst. Sci.*, *19*(10), 4201–4213, doi:10.5194/hess-19-4201-2015.

Moors, E. J. et al. (2011), Adaptation to changing water resources in the Ganges basin, northern India, *Environ. Sci. Policy*, *14*(7), 758–769, doi:10.1016/j.envsci.2011.03.005.

Nerini, D., Z. Zulkafli, L.-P. Wang, C. Onof, W. Buytaert, W. Lavado-Casimiro, and J.-L. Guyot (2015), A Comparative Analysis of TRMM–Rain Gauge Data Merging Techniques at the Daily Time Scale for Distributed Rainfall–Runoff Modeling Applications, *J. Hydrometeorol.*, *16*(5), 2153–2168, doi:10.1175/JHM-D-14-0197.1.

Niemi, N.A., Oskin, M., Burbank, D.W., Heimsath, A.M., Gabet, E.J., 2005. Effects of bedrock landslides on cosmogenically determined erosion rates. Earth Planet. Sci. Lett. 237, 480–498. doi:10.1016/j.epsl.2005.07.009

Nishiizumi, K., E. L. Winterer, C. P. Kohl, J. Klein, R. Middleton, D. Lal, and J. R. Arnold (1989), Cosmic ray production rates of 10Be and 26Al in quartz from glacially polished rocks, *ournal Geophys. Res. Solid Earth*, *94*(B12), 2156–2202, doi:10.1029/JB094iB12p17907.

Nishiizumi, K., Imamura, M., Caffee, M.W., Southon, J.R., Finkel, R.C., McAninch, J., 2007. Absolute calibration of 10Be AMS standards. Nucl. Instruments Methods Phys. Res. Sect. B Beam Interact. with Mater. Atoms 258, 403–413. doi:10.1016/j.nimb.2007.01.297

Norris, J., L. M. V. Carvalho, C. Jones, F. Cannon, B. Bookhagen, E. Palazzi, and A. A. Tahir (2016), The spatiotemporal variability of precipitation over the Himalaya: evaluation of one-year WRF model simulation, *Clim. Dyn.*, doi:10.1007/s00382-016-3414-y.

Nourani, V., M. Komasi, and A. Mano (2009), A multivariate ANN-wavelet approach for rainfall-runoff modeling, *Water Resour. Manag.*, *23*(14), 2877–2894, doi:10.1007/s11269-009-9414-5.

Palazzi, E., J. Von Hardenberg, and A. Provenzale (2013), Precipitation in the hindu-kush karakoram himalaya: Observations and future scenarios, *J. Geophys. Res. Atmos.*, *118*(1), 85–100, doi:10.1029/2012JD018697.

Papalexiou, S. M., and D. Koutsoyiannis (2013), Battle of extreme value distributions: A global survey on extreme daily rainfall, *Water Resour. Res.*, *49*(1), 187–201, doi:10.1029/2012WR012557.

Parker, D., C. Folland, A. Scaife, J. Knight, A. Colman, P. Baines, and B. Dong (2007), Decadal to multidecadal variability and the climate change background, *J. Geophys. Res. Atmos.*, *112*(18), 1–18, doi:10.1029/2007JD008411.

Pasquini, A. I., and P. J. Depetris (2007), Discharge trends and flow dynamics of South American rivers draining the southern Atlantic seaboard: An overview, *J. Hydrol.*, *333*(2–4), 385–399, doi:10.1016/j.jhydrol.2006.09.005.

Pasquini, A. I., and P. J. Depetris (2010), ENSO-triggered exceptional flooding in the Paraná River: Where is the excess water coming from?, *J. Hydrol.*, *383*(3–4), 186–193, doi:10.1016/j.jhydrol.2009.12.035.

Penalba, O. C., and F. A. Robledo (2010), Spatial and temporal variability of the frequency of extreme daily rainfall regime in the La Plata Basin during the 20th century, *Clim. Change*, *98*(3), 531–550, doi:10.1007/s10584-009-9744-6.

Pepin, E., J. L. Guyot, E. Armijos, H. Bazan, P. Fraizy, J. S. Moquet, L. Noriega, W. Lavado, R. Pombosa, and P. Vauchel (2013), Climatic control on eastern Andean denudation rates (Central Cordillera from Ecuador to Bolivia), *J. South Am. Earth Sci.*, *44*, 85–93, doi:10.1016/j.jsames.2012.12.010.

Pepin, N. et al. (2015), Elevation-dependent warming in mountain regions of the world, *Nat. Clim. Chang.*, *5*(5), 424–430, doi:10.1038/nclimate2563.

Piovano, E. L., D. Ariztegui, and S. D. Moreiras (2002), Recent environmental changes in Laguna Mar Chiquita (central Argentina): A sedimentary model for a highly variable saline lake, *Sedimentology*, *49*(6), 1371–1384, doi:10.1046/j.1365-3091.2002.00503.x.

Plate, E. J. (2002), Flood risk and flood management, *J. Hydrol.*, *267*(1–2), 2–11, doi:10.1016/S0022-1694(02)00135-X.

Portenga, E.W., Bierman, P.R., Duncan, C., Corbett, L.B., Kehrwald, N.M., Rood, D.H.,

2015. Erosion rates of the Bhutanese Himalaya determined using in situ-produced 10Be. Geomorphology 233, 112–126. doi:10.1016/j.geomorph.2014.09.027.

Poveda, G., A. Jaramillo, M. M. Gil, N. Quiceno, and R. I. Mantilla (2001), Seasonality in ENSO-related precipitation, river discharges, soil moisture, and vegetation index in Colombia, *Water Resour. Res.*, *37*(8), 2169–2178, doi:10.1029/2000WR900395.

Rabatel, A. et al. (2013), Current state of glaciers in the tropical Andes: A multi-century perspective on glacier evolution and climate change, *Cryosphere*, *7*(1), 81–102, doi:10.5194/tc-7-81-2013.

Rajczak, J., P. Pall, and C. Schär (2013), Projections of extreme precipitation events in regional climate simulations for Europe and the Alpine Region, *J. Geophys. Res. Atmos.*, *118*(9), 3610–3626, doi:10.1002/jgrd.502972013.

Ramírez, E., B. Francou, P. Ribstein, M. Descloitres, R. Guérin, J. Mendoza, R. Gallaire, B. Pouyaud, and E. Jordan (2001), Small glaciers disappearing in the Tropical Andes. A case study in Bolivia; the Chacaltaya Glacier (16° S), *J. Glaciol.*, *47*, 187–194, doi:10.3189/172756501781832214.

Rao, V. B., S. H. Franchito, C. M. E. Santo, and M. A. Gan (2015), An update on the rainfall characteristics of Brazil: seasonal variations and trends in 1979-2011, *Int. J. Climatol.*, n/a-n/a, doi:10.1002/joc.4345.

Rasmussen, K. L., and R. A. Houze (2011), Orogenic Convection in Subtropical South America as Seen by the TRMM Satellite, *Mon. Weather Rev.*, *139*(8), 2399–2420, doi:10.1175/MWR-D-10-05006.1.

Richardson, S. D., and J. M. Reynolds (2000), An overview of glacial hazards in the Himalayas, *Quat. Int.*, *65–66*, 31–47, doi:10.1016/S1040-6182(99)00035-X.

Rienecker, M. M. et al. (2011), MERRA: NASA's modern-era retrospective analysis for research and applications, *J. Clim.*, *24*(14), 3624–3648, doi:10.1175/JCLI-D-11-00015.1.

Rivelli, F. R. (1999), El aluvionamiento en los ríos de la Quebrada de Humahuaca (Jujuy, Argentina), in *I Congreso Argentino del Cuaternario y Geomorfología*, pp. 47 – 50, Universidad Nacional de La Pampa, Santa Rosa, La Pampa, Argentina.

Rivelli, R. F., and E. Manuela (2009), Protection de margenes en el Rio Grande, Tramo Las Quebradas Trancas - Tilcara, in *Cuarto Simposio sobre Hidraulica de Rios. Salta, Argentina, 2009*, pp. 1–4.

Robertson, A. W., and C. R. Mechoso (1998), Interannual and Decadal Cycles in River Flows of Southeastern South America, *J. Clim.*, *11*, 2570–2581.

Robledo, F. A., C. Vera, and O. C. Penalba (2015), Influence of the large-scale climate variability on daily rainfall extremes over Argentina, *Int. J. Climatol.*, n/a-n/a, doi:10.1002/joc.4359.

Rodda, J. C. (2011), Guide to Hydrological Practices, *Hydrol. Sci. J.*, *56*(168), 196–197, doi:10.1080/02626667.2011.546602.

Rodó, X., and M. Á. Rodríguez-Arias (2006), A new method to detect transitory signatures and local time/space variability structures in the climate system: The scale-dependent correlation analysis, *Clim. Dyn.*, *27*(5), 441–458, doi:10.1007/s00382-005-0106-4.

Roe, G. H. (2003), Orographic precipitation and the relief of mountain ranges, *J. Geophys. Res.*, *108*(B6), 1–12, doi:10.1029/2001JB001521.

Rohmeder, W. (1943), Observaciones meterológicas en la región encumbrada de las Sierras de Famatina y del Aconquija (republica Argentina)., *An. Soc. Cient. Arg.*, *136*, 97–124.

Rohrmann, A., M. R. Strecker, B. Bookhagen, A. Mulch, D. Sachse, H. Pingel, R. N. Alonso, T. F. Schildgen, and C. Montero (2014), Can stable isotopes ride out the storms? The role of convection for water isotopes in models , records , and paleoaltimetry studies in the central Andes, *Earth Planet. Sci. Lett.*, *407*, 187–195, doi:10.1016/j.epsl.2014.09.021.

Romatschke, U., and R. A. Houze (2010), Extreme Summer Convection in South America, *J. Clim.*, *23*(14), 3761–3791, doi:10.1175/2010JCLI3465.1.

Romatschke, U., and R. A. Houze (2013), Characteristics of Precipitating Convective Systems Accounting for the Summer Rainfall of Tropical and Subtropical South America, *J. Hydrometeorol.*, 120927133830006, doi:10.1175/JHM-D-12-060.1.

Romatschke, U., S. Medina, and R. A. Houze (2010), Regional, Seasonal, and Diurnal Variations of Extreme Convection in the South Asian Region, *J. Clim.*, *23*(2), 419–439, doi:10.1175/2009JCLI3140.1.

Rood D.H., Hall S., Guilderson T.P., Finkel R.C., Brown T.A., 2010. Challenges and opportunities in high-precision Be-10 measurements at CAMS. Nuclear Instruments and Methods in Physics Research B, 268, 730–732.

Ropelewski, C. F., and M. S. Halpert (1987), Global and Regional Scale Precipitation Patterns Associated with the El Niño/Southern Oscillation, *Mon. Weather Rev.*, *115*(8), 1606–1626, doi:10.1175/1520-0493(1987)115<1606:GARSPP>2.0.CO;2.

Roy, S. Sen, and R. C. Balling (2004), Trends in extreme daily precipitation indices in India, *Int. J. Climatol.*, *24*(4), 457–466, doi:10.1002/joc.995.

Rudnick, R.L. and Gao, S., 2004. Composition of the Continental Crust. In: D.H. Heinrich and K.T. Karl (Editors), Treatise on Geochemistry. Elsevier, Amsterdam, pp. 1-64.

Rugel, G., Pavetich, S., Akhmadaliev, S., Enamorado Baez, S.M., Scharf, A., Ziegenrücker, R., Merchel, S. 2016. The first four years of the AMS-facility DREAMS: Status and developments for more accurate radionuclide data. Nuclear Instruments and Methods in Physics Research B, 370, 94–100.

Ruscica, R. C., A. A. Sörensson, and C. G. Menéndez (2014), Hydrological links in Southeastern South America: Soil moisture memory and coupling within a hot spot, *Int. J. Climatol.*, *3653*(February), 3641–3653, doi:10.1002/joc.3930.

Rusticucci, M., and O. Penalba (2000), Interdecadal changes in the precipitation seasonal cycle over Southern South America and their relationship with surface temperature, *Clim. Res.*, *16*(1), 1–15, doi:10.3354/cr016001.

Ryan, P. A. (1991), Environmental effects of sediment on New Zealand streams: A review, *New Zeal. J. Mar. Freshw. Res.*, *25*(2), 207–221, doi:10.1080/00288330.1991.9516472.

Sahai, H., Khurshid, A., 1993. Confidence Intervals for the Mean of a Poisson Distribution. Biometrics J. 35, 857–867.

Saji, N. H., B. N. Goswami, P. N. Vinayachandran, and T. Yamagata (1999), A dipole mode in the tropical Indian Ocean, *Nature*, *401*(6751), 360–363, doi:10.1038/43854.

Salfity, J. A., and R. A. Marquillas (1994), Tectonic and sedimentary evolution of the Cretaceous-Eocene Salta group basin, Argentina, in *Cretaceous tectonics of the Andes*, edited by J. A. Salfity, pp. 266–315, Braunschweig, Germany.

Salio, P., M. Nicolini, and A. C. Saulo (2002), Chaco low-level jet events characterization during the austral summer season, *J. Geophys. Res. Atmos.*, *107*(24), 4816, doi:10.1029/2001JD001315.

Savi, S., Norton, K., Picotti, V., Brardinoni, F., Akçar, N., Kubik, P.W., Delunel, R., Schlunegger, F., 2014. Effects of sediment mixing on 10Be concentrations in the Zielbach catchment, central-eastern Italian Alps. Quat. Geochronol. 19, 148–162. doi:10.1016/j.quageo.2013.01.006

Savi, S., T. . Schildgen, S. Tofelde, H. Wittmann, D. Scherler, J. Mey, R. Alonso, and M. R. Strecker (accepted), Climatic modulation of sedimentary processes: The Del Medio debris-flow fan, NW Argentina, *Jounral Geophys. Res. Earth Surf.*

Schaefer, J.M., Denton, G.H., Kaplan, M., Putnam, A., Finkel, R.C., Barrell, D.J. a, Andersen, B.G., Schwartz, R., Mackintosh, A., Chinn, T., Schlüchter, C., 2009. High-frequency Holocene glacier fluctuations in New Zealand differ from the northern signature. Science 324, 622–625. doi:10.1126/science.1169312

Schaller, M., von Blanckenburg, F., Hovius, N., Kubik, P.W., 2001. Large-scale erosion rates from in situ-produced cosmogenic nuclides in European river sediments. Earth and Planetary Science Letters, 188, 441-458.

Scherler, D., B. Bookhagen, and M. R. Strecker (2011), Spatially variable response of Himalayan glaciers to climate change affected by debris cover, *Nat. Geosci.*, *4*(3), 156–159, doi:10.1038/ngeo1068.

Schildgen, F. T., Robinson, R. A. J., Savi, S., Phillips, W. M., Spencer J. Q. G., Bookhagen, B., Scherler, D., Tofelde, S., Alonso, R. N., Kubik, P. W., Binnie, S. A., Strecker, M. R., in press. Landscape response to late Pleistocene climate change in NW Argentina: Sediment flux modulated by basin geometry and connectivity. Journal of Geophysical Research: Earth Surface.

Schimmelpfennig, I., Schaefer, J.M., Akçar, N., Koffman, T., Ivy-Ochs, S., Schwartz, R., Finkel, R.C., Zimmerman, S., Schlüchter, C., 2014. A chronology of Holocene and Little Ice Age glacier culminations of the Steingletscher, Central Alps, Switzerland, based on high-sensitivity beryllium-10 moraine dating. Earth Planet. Sci. Lett. 393, 220–230. doi:10.1016/j.epsl.2014.02.046

Schmidli, J., and C. Frei (2005), Trends of heavy precipitation and wet and dry spells in Switzerland during the 20th century, *Int. J. Climatol.*, *25*(6), 753–771, doi:10.1002/joc.1179.

Schneider, C., M. Schnirch, C. Acuña, G. Casassa, and R. Kilian (2007), Glacier inventory of the Gran Campo Nevado Ice Cap in the Southern Andes and glacier changes observed during recent decades, *Glob. Planet. Change*, *59*(1–4), 87–100, doi:10.1016/j.gloplacha.2006.11.023.

Shrivastava, A., Gupta, V., 2011. Methods for the determination of limit of detection and limit of quantitation of the analytical methods. Chronicles Young Sci. 2, 21. doi:10.4103/2229-5186.79345

Schwerdtfeger, W. (1976), *Climates of Central and South America - World Surv. Climatol. - Vol. 12*, Elsevier Sci., New York.

Seiler, C., R. W. A. Hutjes, and P. Kabat (2013), Climate variability and trends in bolivia, *J. Appl. Meteorol. Climatol.*, *52*(1), 130–146, doi:10.1175/JAMC-D-12-0105.1.

Seluchi, M., and A. Saulo (2003), The northwestern Argentinean low: A study of two typical events, *Mon. Weather …*, 2361–2378.

Seluchi, M. E., and J. A. Marengo (2000), Tropical – Midlatitude Exchange of Air Masses During Summer and Winter in South America : Climatic Aspects, *Int. J. Climatol.*, *1190*(20), 1167–1190.

Sen, Z., and Z. Habib (2000), Spatial analysis of monthly precipitation in Turkey, *Theor. Appl. Climatol.*, *67*(1–2), 81–96, doi:10.1007/s007040070017.

Seneviratne, S. I. et al. (2012), Changes in climate extremes and their impacts on the natural physical environment, in *Managing the Risks of Extreme Events and Disasters to Advance Climate Change Adaptation. A Special Report of Working Groups I and II of the Intergovernmental Panel on Climate Change (IPCC)*, edited by C. B. Field et al., pp. 109–230, Cambridge, UK, and New York, NY, USA,.

Serinaldi, F., and C. G. Kilsby (2014), Rainfall extremes: Toward reconciliation after the battle of distributions, *Water Resour. Res.*, *50*(1), 336–352, doi:10.1002/2013WR014211.

Shahzad Khattak, M., M. S. Babel, and M. Sharif (2011), Hydro-meteorological trends in the upper Indus River basin in Pakistan, *Clim. Res.*, *46*(2), 103–119, doi:10.3354/cr00957.

Sharif, M., D. R. Archer, H. J. Fowler, and N. Forsythe (2013), Trends in timing and magnitude of flow in the Upper Indus Basin, *Hydrol. Earth Syst. Sci.*, *17*(4), 1503–1516, doi:10.5194/hess-17-1503-2013.

Sheffield, J., K. M. Andreadis, E. F. Wood, and D. P. Lettenmaier (2009), Global and continental drought in the second half of the twentieth century: Severity-area-duration analysis and temporal variability of large-scale events, *J. Clim.*, *22*(8), 1962–1981, doi:10.1175/2008JCLI2722.1.

Sillmann, J., V. V. Kharin, F. W. Zwiers, X. Zhang, and D. Bronaugh (2013), Climate extremes indices in the CMIP5 multimodel ensemble: Part 2. Future climate projections, *J. Geophys. Res. Atmos.*, *118*(6), 2473–2493, doi:10.1002/jgrd.50188.

Silva, A. da, and L. de Carvalho (2007), Large-scale index for South America Monsoon (LISAM), *Atmos. Sci. Lett.*, doi:10.1002/asl.

Silva, V. B. S., V. E. Kousky, W. Shi, and R. W. Higgins (2007), An Improved Gridded Historical Daily Precipitation Analysis for Brazil, *J. Hydrometeorol.*, *8*(4), 847–861, doi:10.1175/JHM598.1.

Skamarock, W., J. Klemp, and J. Dudhia (2005), *A description of the advanced research WRF version 2*, Boulder, Colorado, USA.

Skansi, M. de los M. et al. (2013), Warming and wetting signals emerging from analysis of changes in climate extreme indices over South America, *Glob. Planet. Change*, *100*(December 2015), 295–307, doi:10.1016/j.gloplacha.2012.11.004.

Smith, C. a., and P. D. Sardeshmukh (2000), The effect of ENSO on the intraseasonal variance of surface temperatures in winter, *Int. J. Climatol.*, *20*(13), 1543–1557, doi:10.1002/1097-0088(20001115)20:13<1543::AID-JOC579>3.0.CO;2-A.

Sorg, A., T. Bolch, M. Stoffel, O. Solomina, and M. Beniston (2012), Climate change impacts on glaciers and runoff in Tien Shan (Central Asia), *Nat. Clim. Chang.*, *2*(10), 725–731, doi:10.1038/nclimate1592.

SSRH (2004), *Estadística Hidrológica de la República Argentina.*, Subsecretaría de Recursos Hídricos, Buenos Aires, Argentina.

Stager, J. C., D. B. Ryves, B. M. Chase, and F. S. R. Pausata (2011), Catastrophic drought in the Afro-Asian monsoon region during Heinrich event 1., *Science*, *331*(6022), 1299–302, doi:10.1126/science.1198322.

Stocker, T. F. et al. (2013), Technical Summary, in *Climate Change 2013: The Physical Science Basis. Contribution of Working Group I to the Fifth Assessment Report of the Intergovernmental Panel on Climate Change*, pp. 31–115.

Stone, J., 1998. A rapid fusion method for separation of beryllium-10 from soils and silicates. Geochimica et Cosmochimica Acta, 62, 555e561.

Strecker, M. R., R. N. Alonso, B. Bookhagen, B. Carrapa, G. E. Hilley, E. R. Sobel, and M. H. Trauth (2007), Tectonics and Climate of the Southern Central Andes, *Annu. Rev. Earth Planet. Sci.*, *35*(1), 747–787, doi:10.1146/annurev.earth.35.031306.140158.

Tank, A. K., F. W. Zwiers, and X. Zhang (2009), *Guidelines on Analysis of extremes in a changing climate in support of informed decisions for adaptation, WCDMP-No. 72*, WMO.

Taylor, W. A. (2000), Change-Point Analysis: A Powerful New Tool For Detecting Changes, *Analysis*, 1–19.

Thibeault, J., A. Seth, and G. Wang (2012), Mechanisms of summertime precipitation variability in the bolivian altiplano: Present and future, *Int. J. Climatol.*, *32*(September 2011), 2033–2041, doi:10.1002/joc.2424.

Thibeault, J. M., a. Seth, and M. Garcia (2010), Changing climate in the Bolivian Altiplano: CMIP3 projections for temperature and precipitation extremes, *J. Geophys. Res. Atmos.*, *115*(8), 1–18, doi:10.1029/2009JD012718.

Tilman (2002), Agriculture sustainability and intensive production practices, , *418*(August).

Torrence, C., and P. J. Webster (1999), Interdecadal changes in the ENSO-monsoon system, *J. Clim.*, *12*(8 PART 2), 2679–2690, doi:10.1175/1520-0442(1999)012<2679:ICITEM>2.0.CO;2.

Torres-Acosta, V., Schildgen, T.F., Clarke, B.A., Scherler, D., Bookhagen, B., Wittmann, H., von Blanckenburg, F., Strecker, M.R., 2015. Effect of vegetation cover on millennial-scale landscape denudation rates in East Africa. Lithosphere 7, 408–420. doi:10.1130/L402.1

Trenberth, K. E. (2011), Changes in precipitation with climate change, *Clim. Res.*, *47*(1–2), 123–138, doi:10.3354/cr00953.

Trenberth, K. E., A. Dai, R. M. Rasmussen, and D. B. Parsons (2003), The changing character of precipitation, *Bull. Am. Meteorol. Soc.*, *84*(9), 1205–1217+1161, doi:10.1175/BAMS-84-9-1205.

Trussart, S., D. Messier, V. Roquet, and S. Aki (2002), Hydropower projects: A review of most effective mitigation measures, *Energy Policy*, *30*(14), 1251–1259, doi:10.1016/S0301-4215(02)00087-3.

Tucci, C. E. M., and R. T. Clarke (1998), Environmental Issues in the la Plata Basin, *Int. J. Water Resour. Dev.*, *14*(2), 157–173, doi:10.1080/07900629849376.

Urrutia, R., and M. Vuille (2009), Climate change projections for the tropical Andes using a regional climate model: Temperature and precipitation simulations for the end of the 21st century, *J. Geophys. Res.*, *114*(D2), D02108, doi:10.1029/2008JD011021.

Vera, C. et al. (2006), Toward a unified view of the American monsoon systems, *J. Clim.*, *19*(20), 4977–5000, doi:10.1175/JCLI3896.1.

Vergara, W., A. M. Deeb, A. M. Valencia, R. S. Bradley, B. Francou, A. Zarzar, A. Grünwaldt, and S. M. Haeussling (2007), Economic Impacts of Rapid Glacier Retreat in the Andes, *Eos, Trans. Am. Geophys. Union*, *88*(25), 261, doi:10.1029/2007EO250001.

Verschuren, D., K. R. Laird, and B. F. Cumming (2000), Rainfallanddroughtinequatorialeast Africa during the past 1 , 100 years, *Sol.*

Cells, *403*(January).

Viala, E. (2008), Water for food, water for life a comprehensive assessment of water management in agriculture, *Irrig. Drain. Syst.*, *22*, 127–129, doi:10.1007/s10795-008-9044-8.

Viviroli, D., H. H. Dürr, B. Messerli, M. Meybeck, and R. Weingartner (2007), Mountains of the world, water towers for humanity: Typology, mapping, and global significance, *Water Resour. Res.*, *43*(7), 1–13, doi:10.1029/2006WR005653.

Viviroli, D. et al. (2011), Climate change and mountain water resources: Overview and recommendations for research, management and policy, *Hydrol. Earth Syst. Sci.*, *15*(2), 471–504, doi:10.5194/hess-15-471-2011.

Vizy, E. K., and K. H. Cook (2007), Relationship between Amazon and high Andes rainfall, *J. Geophys. Res. Atmos.*, *112*(7), 1–14, doi:10.1029/2006JD007980.

Vörösmarty, C. J., P. Green, J. Salisbury, and R. B. Lammers (2000), Global Water Resources: Vulnerability from Climate Change and Population Growth, *Science (80-.).*, *289*(5477), 284–288, doi:10.1126/science.289.5477.284.

Vuille, M., and F. Keimig (2004), Interannual Variability of Summertime Convective Cloudiness and Precipitation in the Central Andes Derived from ISCCP-B3 Data, *J. Clim.*, *17*(17), 3334–3348.

Vuille, M., R. S. Bradley, and F. Keimig (2000), Climate Variability in the Andes of Ecuador and Its Relation to Tropical Pacific and Atlantic Sea Surface Temperature Anomalies, *J. Clim.*, *13*(Hastenrath 1981), 2520–2535, doi:10.1175/1520-0442(2000)013<2520:CVITAO>2.0.CO;2.

Vuille, M., R. S. Bradley, M. Werner, and F. Keimig (2003), 20Th Century Climate Change in the Tropical Andes : Observations and Model Results, *Clim. Change*, *59*, 75–99.

Vuille, M., B. Francou, P. Wagnon, I. Juen, G. Kaser, B. G. Mark, and R. S. Bradley (2008), Climate change and tropical Andean glaciers: Past, present and future, *Earth-Science Rev.*, *89*(3–4), 79–96, doi:10.1016/j.earscirev.2008.04.002.

Vuille, M., E. Franquist, R. Garreaud, W. Sven, W. S. Lavado Casimiro, and B. Cáceres (2015), Impact of the global warming hiatus on Andean temperature, *J. Geophys. Res. Atmos.*, *120*(9), 3745–3757, doi:10.1002/2015JD023126.

Wang, B., R. Wu, and X. Fu (2000), Pacific-East Asian teleconnection: How does ENSO affect East Asian climate?, *J. Clim.*, *13*(9), 1517–1536, doi:10.1175/1520-0442(2000)013<1517:PEATHD>2.0.CO;2.

Wang, G., X.-Y. Chen, F.-L. Qiao, Z. Wu, and N. E. Huang (2010), On Intrinsic Mode Function, *Adv. Adapt. Data Anal.*, *2*(3), 277–293, doi:10.1142/S1793536910000549.

Wang, T., M. Zhang, Q. Yu, and H. Zhang (2012), Comparing the applications of EMD and EEMD on time-frequency analysis of seismic signal, *J. Appl. Geophys.*, *83*, 29–34, doi:10.1016/j.jappgeo.2012.05.002.

Wang, W. chuan, K. wing Chau, D. mei Xu, and X. Y. Chen (2015), Improving Forecasting Accuracy of Annual Runoff Time Series Using ARIMA Based on EEMD Decomposition, *Water Resour. Manag.*, *29*(8), 2655–2675, doi:10.1007/s11269-015-0962-6.

Webster, P. J., and S. Yang (1992), Monsoon and Enso: Selectively Interactive Systems, *Q. J. R. Meteorol. Soc.*, *118*(507), 877–926, doi:10.1002/qj.49711850705.

Webster, P. J., V. E. Toma, and H. M. Kim (2011), Were the 2010 Pakistan floods predictable?, *Geophys. Res. Lett.*, *38*(4), 1–5, doi:10.1029/2010GL046346.

Wilcox, L. J., E. J. Highwood, and N. J. Dunstone (2013), The influence of anthropogenic aerosol on multi-decadal variations of historical global climate, *Environ. Res. Lett.*, *8*(2), 24033, doi:10.1088/1748-9326/8/2/024033.

Wittmann, H., von Blanckenburg, F., Kruesmann, T., Norton, K.P. and Kubik, P.W., 2007. Relation between rock uplift and denudation from cosmogenic nuclides in river sediment in the Central Alps of Switzerland. Journal of Geophysical Research-Earth Surface, 112(F4).

WMO (2008), *Guide to Hydrological Practices*, 6th ed., edited by WMO.

Wolman, M., and J. Miller (1960), Magnitude and frequency of forces in geomorphic processes, *J. Geol.*, *68*(1), 54–74.

World Meteorological Organization (2011), *Guide to Climatological Practices WMO-No. 100*, WMO., edited by WMO, WMO, Geneva.

Wu, Z., and N. E. Huang (2009), Ensemble Empirical Mode Decomposition : A Noise Assisted Data Analysis Method, *Adv. Adapt. Data Anal.*, *1*(1), 1–41, doi:10.1142/S1793536909000047.

Wu, Z., N. E. Huang, and B. W. Zhaohua (2004), A study of the characteristics of white noise using the empirical mode decomposition method, *Proc. R. Soc. A Math. Phys. Eng. Sci.*, *460*, 1597–1611, doi:10.1098/rspa.2003.1221.

Wu, Z., N. E. Huang, S. R. Long, and C.-K. Peng (2007), On the trend, detrending, and variability of nonlinear and nonstationary time series, *Proc. Natl. Acad. Sci. U. S. A.*, *104*(38), 14889–14894, doi:10.1073/pnas.0701020104.

Wu, Z., E. K. Schneider, B. P. Kirtman, E. S. Sarachik, N. E. Huang, and C. J. Tucker (2008), The modulated annual cycle: An alternative reference frame for climate anomalies, *Clim. Dyn.*, *31*(7–8), 823–841, doi:10.1007/s00382-008-0437-z.

Wulf, H., B. Bookhagen, and D. Scherler (2010), Seasonal precipitation gradients and their impact on fluvial sediment flux in the Northwest Himalaya, *Geomorphology*, *118*(1–2), 13–21, doi:10.1016/j.geomorph.2009.12.003.

Wulf, H., B. Bookhagen, and D. Scherler (2012), Climatic and geologic controls on suspended sediment flux in the Sutlej River Valley, western Himalaya, *Hydrol. Earth Syst. Sci.*, *16*(7), 2193–2217, doi:10.5194/hess-16-2193-2012.

Wulf, H., B. Bookhagen, and D. Scherler (2016), Differentiating between rain, snow, and glacier contributions to river discharge in the western Himalaya using remote-sensing data and distributed hydrological modeling, *Adv. Water Resour.*, *88*, 152–169, doi:10.1016/j.advwatres.2015.12.004.

Xie, P., M. Chen, S. Yang, A. Yatagai, T. Hayasaka, Y. Fukushima, and C. Liu (2007), A Gauge-Based Analysis of Daily Precipitation over East Asia, *J. Hydrometeorol.*, *8*(3), 607–626, doi:10.1175/JHM583.1.

Xu, X., C. Lu, X. Shi, and S. Gao (2008), World water tower: An atmospheric perspective, *Geophys. Res. Lett.*, *35*(20), 1–5, doi:10.1029/2008GL035867.

Xue, X., Y. Hong, A. S. Limaye, J. J. Gourley, G. J. Huffman, S. I. Khan, C. Dorji, and S. Chen (2013), Statistical and hydrological evaluation of TRMM-based Multi-satellite Precipitation Analysis over the Wangchu Basin of Bhutan: Are the latest satellite precipitation products 3B42V7 ready for use in ungauged basins?, *J. Hydrol.*, *499*, 91–99, doi:10.1016/j.jhydrol.2013.06.042.

ACKNOWLEDGMENTS

This study could have not been possible without the support of many people.

First, I sincerely thank my supervisor, Manfred R. Strecker, who helped, trusted, and supported me along this challenging experience. By difficult moments, when it was complicated to find my way, his words have always suggested me how to move and helped me in renewing the motivation for my research study.

I thank my advisor, Bodo Bookhagen, for having provided me with a solid, constant guidance along this venture. I am grateful to Bodo for having supported me, showing always a deep respect for the work of others.

I would like to deeply thank Stefano Parolai and Helmut Echtler, for having suggested me to visit the Institute in Golm and let this venture start.

Special thanks go to Ines Münch and the secretary team, Tanja Klaka-Tauscher, Martina Heidemann, and Cornelia Becker, who have been always very helpful solving small and not-so small problems. Particularly, I thank Tanja, whose warm smile and smart irony are unique gifts.

I am very grateful to Sara Savi, for having involved me in her research project. Discussions with Sara were often stimulating further investigation. I thank Paolo Ballato and Rasmus Thiede, to whom I am deeply indebted for the insightful discussions and having helped in orienting myself during this venture. A special thank also goes to Simon Riedl, for scientific discussions and helping me solving technical programming issues.

I would like to thank the Argentine friends and collegues, who have accompanied me in discovering a wonderful place. Many thanks to Ricardo Alonso, Arturo Villanueva, Ricardo Mon, Carolina Montero, Daniel Cielak, Eduardo Marigliano, and Janina Rojo.

I would also like to thank Stefanie Tofelde and Heiko Pingel for good scientific discussions. I am also thankful to them for having helped me in different occasions with the German version of my documents.

I would like to thank the 'Smurfs' for having welcomed me and for the insightful discussions during the group seminar. Being an outsider, these moments were particularly important for me to widen my perspectives.

I thank my room-mates, former and current ones, for their patience and support. Time with you was very nice and I keep delightful memories. Here they are: Jan, Marlene, Bernd, Xia, Johannes, Jürgen, Fred, Veronica, Patricia, Stephanie, Anke, Sebastian, Magda, and Flavia. I am also grateful for having had the opportunity to meet many interesting people and shared relaxing moment with them, during lunch or in free-time. The 'kitchen-group' has provided me with an irreplaceable amusing support: Lidia, Paolo, Giuditta, Iris, Nico, Amaury, Alessia, Silvio, Julien, Viktoria, and many others.

I would like to thank Luciana, Barbara, Antonella, Barbara, and Alessandra, my best friends, for their infinite patience and valuable advices.

Last but not least, I am grateful to my family, Mom and Dad, who taught me to keep going. And to my little one, Marí, and my big one, Dino, for the strength they give me and the patience they have, but also for being there.